

# Characterization and Optimization of the new Imaging Fourier Transform Spectrometer GLORIA

Zur Erlangung des akademischen Grades eines  
DOKTORS DER NATURWISSENSCHAFTEN  
von der Fakultät für Physik

genehmigte

DISSERTATION  
von

Mahesh Kumar Sha

aus Kalkutta, Indien

Referent: Prof. Dr. Herbert Fischer  
Korreferent: Prof. Dr. Johannes Orphal

Tag der mündlichen Prüfung: 20.12.2013



# Abstract

The upper troposphere and lower stratosphere (UTLS) region plays a crucial role in the present climate change. The present climate models and observing systems do not have the capabilities of improving our knowledge about the processes which occur at mesoscale distances, in narrow atmospheric layers and in short timescales. In order to provide high resolution observations of the UTLS region, a new imaging Fourier transform spectrometer (IFTS) called Gimballed Limb Observer for Radiance Imaging of the Atmosphere (GLORIA) has been developed. The GLORIA spectrometer is equipped with a large focal plane array (FPA) measuring the emission of the earth's atmosphere in the mid-infrared spectral region. The instrument is gimbal mounted to allow measurements of the atmosphere in limb- and nadir-sounding geometry. It is operated on board the high altitude aircraft M55-Geophysica and HALO (High Altitude and Long Range Research Aircraft). The measurements performed with GLORIA provide high resolution information about the dynamics and chemistry of the UTLS region. A proper characterization of the instrument is necessary in order to analyze the data, to define the errors of the measured parameters and to interpret the results of the measurements. The work presented in this thesis focuses on the radiometric and spectrometric characterization and optimization of GLORIA. The characterization work also provides the instrument parameters for the calibration.

The first part of this work focuses on the radiometric characterization of the GLORIA spectrometer. In particular a characterization method for determining the responsivity and sensitivity of the detector is presented. The operating parameters of the detector are optimized. Based on the characterization results, a judgment on the quality of the detectors has been made. The nonlinearity of the detector system is quantified and a method for the correction is presented with its application to flight data. A theoretical noise model for GLORIA is presented which quantifies and identifies the sources contributing to the measured signal. The model also allows to give an estimate on several instrument parameters. The good agreement between the measured and theoretically calculated noise equivalent spectral radiance (NESR) values verifies the nominal performance of the instrument. A qualitative analysis of the imaging quality of the GLORIA optics is presented next. Parasitic images which are found due to multiple reflections are characterized and quantified.

In the second part, the focus is laid on the spectrometric characterization of the GLORIA spectrometer. A method for the determination of the spectral calibration parameters is presented and applied to measurements performed with GLORIA both on ground and in flight. It is found that deep space measurements are better suited for finding the spectral calibration parameters than nominal atmospheric measurements, if the signal to noise ratio is sufficient. The parameters are found to be slowly changing with the thermal drift of the interferometer. The spectral calibration error made by not adjusting the infrared objective (IRO) position corresponding to the change of interferometer temperature is relatively small and well acceptable. The spectral calibration works generally well leaving only a small residual line position error which is acceptable. In the next section, a novel method for the determination of the focus in an IFTS based on the line width is shown. It is found

that the method is sensitive enough to identify a defocusing of approximately 2.4 ‰ of the focal length. Furthermore, a novel method for the determination of the interferometer shear using the Haidinger fringe pattern is presented. The method is used to characterize and quantify the constant, linear and higher order shear values over the interferometer length. The vibrational frequencies due to the relative motion of the instrument optics are quantified. It is found that the magnitudes of the vibrational shear frequencies present during the laboratory measurements are small and not an issue for GLORIA.

In this thesis, the interferometer and detector parameters have been characterized and optimized, helping to better understand the important features of this IFTS instrument. This characterization work makes it possible to perform scientific measurements with optimized instrument parameters. Furthermore, it helps in the analysis and better understanding of the measured scientific data.

# Zusammenfassung

Die Region der oberen Troposphäre und unteren Stratosphäre spielt eine wichtige Rolle bei der aktuellen Klimaänderung. Mit den heutigen Klimamodellen und Beobachtungssystemen ist es jedoch noch nicht möglich, mesoskalige Prozesse in dünnen atmosphärischen Schichten und auf kurzen Zeitskalen zu erforschen. Um hochauflösende Daten in der UTLS Region messen zu können wurde ein neues abbildendes Fourier-Transformations-Spektrometer (FTS) entwickelt, genannt GLORIA (Gimballed Limb Observer for Radiance Imaging of the Atmosphere). Das Spektrometer von GLORIA ist mit einem großen abbildenden Detektor ausgestattet und misst die Eigenemission der Erdatmosphäre im mittleren infraroten Spektralbereich. Das Instrument wird von einem Kardanrahmen gehalten, der atmosphärische Messungen im Horizont- und Nadir- Modus erlaubt. GLORIA wird an Bord der hochfliegenden Flugzeuge M55-Geophysica und HALO (High Altitude and Long Range Research Aircraft) eingesetzt. Durch die Messungen, die mit GLORIA vorgenommen werden, können hochauflösende Informationen über die Dynamik und die Chemie der UTLS Region gewonnen werden. Um die erzielten Daten und Ergebnisse richtig interpretieren zu können, ist es wichtig, dass das Gerät gut charakterisiert ist. Die vorliegende Arbeit beschäftigt sich mit der radiometrischen und spektralen Charakterisierung und Optimierung von GLORIA. Durch die Charakterisierung erhält man unter anderem Instrumentenparameter für die Kalibrierung.

Der erste Teil dieser Arbeit beschäftigt sich mit der radiometrischen Charakterisierung des GLORIA Spektrometers. Insbesondere wird eine Charakterisierungsmethode vorgestellt, mit der die Responsivität und die Empfindlichkeit des Detektors bestimmt werden. Die Betriebsparameter des Detektors werden optimiert. Basierend auf den Charakterisierungsergebnissen wird die Qualität des Detektors beurteilt. Die Nichtlinearität des Detektorsystems wird quantifiziert und es wird eine Korrekturmethode sowie ihre Anwendung auf die Flugdaten präsentiert. Ein theoretisches Rauschmodell für GLORIA wird vorgestellt, das die verschiedenen Rauschquellen identifiziert und quantifiziert, die einen Einfluss auf das gemessene Signal haben. Das Modell erlaubt es auch, einige Instrumentenparameter abzuschätzen. Die gute Übereinstimmung zwischen der gemessenen und der theoretisch vorhergesagten NESR (noise equivalent spectral radiance) bestätigt das nominale Verhalten des Instruments. Eine qualitative Analyse der Bildqualität der Optik von GLORIA wird nachfolgend vorgestellt. Dabei wurden parasitäre Bilder aufgrund von Mehrfachreflexionen gefunden; diese werden charakterisiert und beurteilt.

Im zweiten Teil liegt der Fokus auf der spektralen Charakterisierung des GLORIA Spektrometers. Eine Methode zur Bestimmung der Parameter für die spektrale Kalibrierung wird vorgestellt und auf Messungen, die mit GLORIA sowohl am Boden als auch im Flug durchgeführt wurden, angewandt. Dabei wurde festgestellt, dass zur Bestimmung der spektralen Kalibrierungsparameter aufwärts gerichtete Messungen besser geeignet sind als nominale Atmosphärenmessungen, wenn das Signal-zu-Rausch-Verhältnis hinreichend hoch ist. Die Parameter ändern sich langsam mit den Temperaturänderungen im Spektrometer. Als Folge von Temperaturänderungen verändert sich die Position des Interferometerobjektivs; der dadurch verursachte Fehler in der Spektralkalibrierung ist allerdings

klein und ist deshalb akzeptabel. Die Spektralkalibrierung funktioniert generell gut. Der kleine Restfehler in der Linienposition kann akzeptiert werden. Außerdem wird eine neuartige Methodik zur Ermittlung des Fokus in einem abbildenden FTS basierend auf der Linienbreite vorgestellt. Diese Methode ist ausreichend genau, um eine Defokussierung der Fokallänge von ungefähr 2,4 ‰ feststellen zu können. Des Weiteren wird eine neuartige Methode zur Feststellung des Interferometer-„Shears“ unter Verwendung der Haidinger-Ringe gezeigt. Diese Methode wird verwendet, um einen konstanten, einen linearen und einen „Shear“ höherer Ordnung über den Interferometerpfad hinweg zu charakterisieren und zu quantifizieren. Die Vibrationsfrequenzen, die durch die Bewegungen der optischen Komponenten zueinander entstehen, werden quantifiziert. Hierbei wurde festgestellt, dass die Stärke der Vibrationen, die bei den Labormessungen gefunden wurden, klein und für GLORIA nicht relevant sind.

In dieser Arbeit wurden das Interferometer sowie die Detektorparameter charakterisiert und optimiert. Damit können wichtige Funktionen dieses abbildenden FTS besser verstanden werden. Die Charakterisierung ermöglicht es, wissenschaftliche Messungen mit optimierten Instrumentenparametern durchzuführen. Außerdem trägt sie dazu bei, die gemessenen wissenschaftlichen Daten analysieren, deren Fehler quantifizieren und diese besser verstehen zu können.

# Contents

<b>1. Introduction</b>	<b>1</b>
<b>2. Basic principles</b>	<b>5</b>
2.1. Remote sensing and Fourier Transform Spectrometry . . . . .	5
2.2. The Michelson Interferometer . . . . .	5
2.3. The imaging Fourier Transform Spectrometer . . . . .	11
<b>3. The airborne IFTS GLORIA</b>	<b>13</b>
3.1. Interferometer unit . . . . .	15
3.2. Spectrometer unit . . . . .	15
3.3. Instrument optics . . . . .	18
3.4. Detector unit . . . . .	18
3.5. Reference laser system . . . . .	20
3.6. Radiometric calibration unit . . . . .	21
3.7. Electronic unit . . . . .	22
3.8. Pointing unit . . . . .	23
3.9. GLORIA measurement modes . . . . .	23
3.10. Instrument operation platforms . . . . .	25
<b>4. Data recording and processing</b>	<b>27</b>
4.1. Data recording process . . . . .	27
4.2. Level0 data processing . . . . .	28
4.3. Level1 data processing . . . . .	30
<b>5. Radiometric characterization</b>	<b>33</b>
5.1. Detector characterization . . . . .	33
5.1.1. Noise . . . . .	34
5.1.2. Detector response . . . . .	35
5.1.3. Noise equivalent power . . . . .	37
5.1.4. Detector parameter optimization . . . . .	37
5.1.5. Detector comparison . . . . .	40
5.2. Nonlinearity . . . . .	45
5.3. Noise analysis: Theoretical evaluation . . . . .	53
5.3.1. Photon loads and dark current . . . . .	53
5.3.2. Noise sources . . . . .	54
5.4. Noise analysis: Measurement evaluation . . . . .	56
5.4.1. DC analysis from fixed slide measurements . . . . .	57
5.4.2. Noise analysis from fixed slide measurements . . . . .	58
5.5. Spectral features of the detector and instrument parameters . . . . .	59
5.5.1. Instrument response . . . . .	59
5.5.2. Instrument transmission . . . . .	61
5.5.3. Modulation efficiency . . . . .	61

5.5.4. Detector response . . . . .	63
5.5.5. Detector quantum efficiency . . . . .	64
5.5.6. Detector cutoff . . . . .	65
5.5.7. Noise equivalent spectral radiance . . . . .	65
5.6. Imaging quality over the FPA . . . . .	72
5.7. Parasitic images . . . . .	78
<b>6. Spectrometric characterization</b>	<b>83</b>
6.1. Spectral calibration - Introduction . . . . .	83
6.1.1. Determination of the spectral calibration parameters . . . . .	85
6.1.2. Spectral calibration sources . . . . .	86
6.2. Gas cell measurements . . . . .	87
6.2.1. Laboratory measurement setup . . . . .	87
6.2.2. Simulations . . . . .	88
6.3. Line selection criteria . . . . .	88
6.4. Line position determination methods . . . . .	90
6.4.1. Optimization of the zero filling method for the line position determination . . . . .	92
6.5. Noise effect on the determination of the spectral calibration parameters . . . . .	94
6.6. Optical axis variation with infrared objective movement . . . . .	96
6.7. Spectral calibration from in-flight measurements . . . . .	97
6.8. Focal plane determination using spectral line width . . . . .	111
6.9. Shear analysis . . . . .	116
<b>7. Conclusions and outlook</b>	<b>129</b>
<b>Bibliography</b>	<b>133</b>
<b>Publications of the author</b>	<b>139</b>
<b>Publications of the author in preparation</b>	<b>141</b>
<b>A. Transmission curves of different optics used in GLORIA</b>	<b>143</b>
<b>B. Analysis of parasitic image</b>	<b>147</b>
<b>List of symbols</b>	<b>155</b>
<b>List of abbreviations</b>	<b>157</b>
<b>List of figures</b>	<b>161</b>
<b>List of tables</b>	<b>163</b>
<b>Acknowledgements</b>	<b>165</b>

# 1. Introduction

The climate of the earth is changing. The massive emission of halocarbons since the first half of the twentieth century has led to the formation of the ozone hole in the polar spring over the Antarctic continent, first described by Farman et al. in 1985 [1]. A typically smaller ozone depletion also occurs almost every spring over the Northern hemisphere. An unprecedented Arctic ozone loss was observed in early 2011 [2]. The increase in greenhouse gases since the pre-industrial era has led to an enhancement in the absorption and emission of infrared radiation by gases, leading to an overall warming of the earth's surface [3, 4]. However, there is still uncertainty concerning the amplitude of this effect and its impact on the regional and local scales. The degradation of the air quality, also known as pollution or smog (air pollution in populated areas), has increased in the present times. The pollution has led to global dimming. Studies have shown that the global direct irradiance at the earth's surface has been reduced by an estimated amount of 4 % over the three decades 1960 - 1990 [4]. These effects are all interlinked to one another. The atmosphere is strongly coupled to the other systems of the earth like oceans, vegetation and land, therefore the change in the atmosphere will directly influence other systems.

The upper troposphere and lower stratosphere (UTLS) region (extending over an altitude range of about 6 km to 25 km height, dependent on latitude and season) is the most affected region due to chemical and radiative feedbacks caused by ozone recovery, greenhouse gases and other effects. This region plays a crucial role for the climate system. The earth's thermal radiation can be trapped easily in the UTLS region. The radiation may interact with water vapor, ozone, aerosols and other gases leading to processes which are poorly quantified. The atmospheric circulation and the surface climate are modulated by the coupling effect between radiative, dynamic and chemical feedback processes in the UTLS region on daily to monthly and yearly timescales [5]. To understand the complex characteristics of this region, observations with high spatial and temporal resolution, along with model systems [6] are required. Gettelman et al. [6] has shown that there is a link between the thermal gradient and the dynamic barrier. The dynamic barriers inhibit mixing and give rise to specific trace gas distributions. Therefore, it is extremely important to probe and understand the UTLS layer of the atmosphere.

Some of the processes which are important in the troposphere and the stratosphere are shown in figure 1.1. All processes except the Brewer-Dobson circulation usually occur at mesoscale (<50-200 km), in narrow atmospheric layers (<1-3 km) and in short timescales

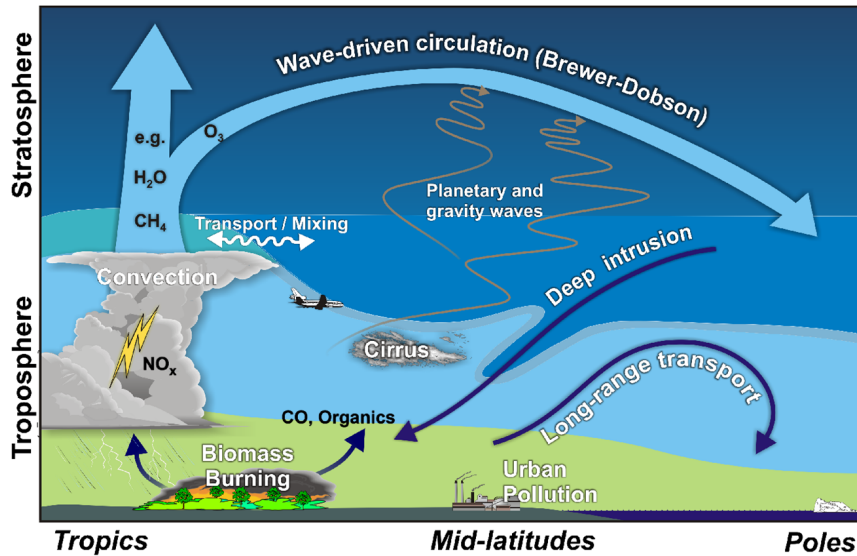


Figure 1.1.: Schematic view of the global structure of the troposphere and lower stratosphere of the earth's atmosphere. The figure illustrates the large-scale and mesoscale interactions which take place in that part of the earth's atmosphere. (source: Peter Preuße, FZJ)

(<1-5 days) [5]. The present climate models and observing systems do not have these resolutions, hence the processes are parameterized in these models. However, high resolution observations of the UTLS region are required in order to understand the processes in this region which are critical to the climate change.

Since the late 1980s, several Fourier transform spectrometers (FTS) have been built for the measurement of the atmosphere. Present day limb scanning instruments and detectors are restricted in their ability to spatially resolve characteristic features of the atmospheric dynamics in the UTLS region. A summary of the FTS instruments operating on-ground or from space has been discussed by Flaud and Orphal [7]. MIPAS (Michelson interferometer for passive atmospheric sounding) is one of the many FTS working in the infrared spectral region [8–11]. MIPAS B2 (balloon version) and MIPAS-STR (aircraft version) have been developed at the Institute for Meteorology and Climate Research (IMK) of the Karlsruhe Institute of Technology (KIT). These limb scanning instruments have single pixel detectors. The imaging Fourier transform spectrometer (IFTS) called Gimballing Limb Observer for Radiance Imaging of the Atmosphere (GLORIA) has been jointly developed by the research centers KIT and Forschungszentrum Jülich (FZJ) for providing more detailed observational data of the UTLS region. The concept and the scientific objectives have been presented in detail in earlier publications [12–15]. High spatial resolution observations made with GLORIA demonstrate that novel information on mesoscale atmospheric dynamics can be obtained [16, 17]. These measurements will be helpful in better understanding the atmosphere and improving weather forecast and climate models on the long term.

The GLORIA spectrometer is equipped with a large focal plane array (FPA) measuring in the infrared emission region ( $780\text{ cm}^{-1}$  to  $1400\text{ cm}^{-1}$ ) of the earth's atmosphere. Moreover, it is capable of both limb- and nadir-sounding of the atmosphere facilitated by its suspension on a gimballing mount. It is capable of operating on various airborne platforms. The measurements performed with GLORIA give information on a number of chemical, dynamical and radiative processes, affecting the physical structure and the composition of the atmosphere. The main focus of the measurements is on the dynamics and chemistry of the UTLS region. The limb sounding mode is used for example to explore the transport processes between different layers of the atmosphere. These processes take place on scales which are hardly resolved by state-of-the-art satellite instruments. The instrument

is flexible in terms of spatial and spectral sampling. On an aircraft it provides sampling in the order of few hundreds of meters vertically and a few tens of kilometers horizontally, thereby probing the different atmospheric layers at the same time [13,15]. The nadir mode is designed for enhancing the horizontal sampling density in the lower and middle troposphere to support research on topics like biomass burning, pollution, methane sources and sinks. Simultaneous measurements of a large number of chemical compounds can be done with GLORIA. Figure 1.2 shows a simulated calculated spectrum at 20 km altitude for a mid latitude July standard atmosphere using GLORIA instrument parameters. The plot shows several trace gases present in the atmosphere which can be detected by GLORIA. An example of the spectra from atmospheric measurements is shown in figure 6.10.

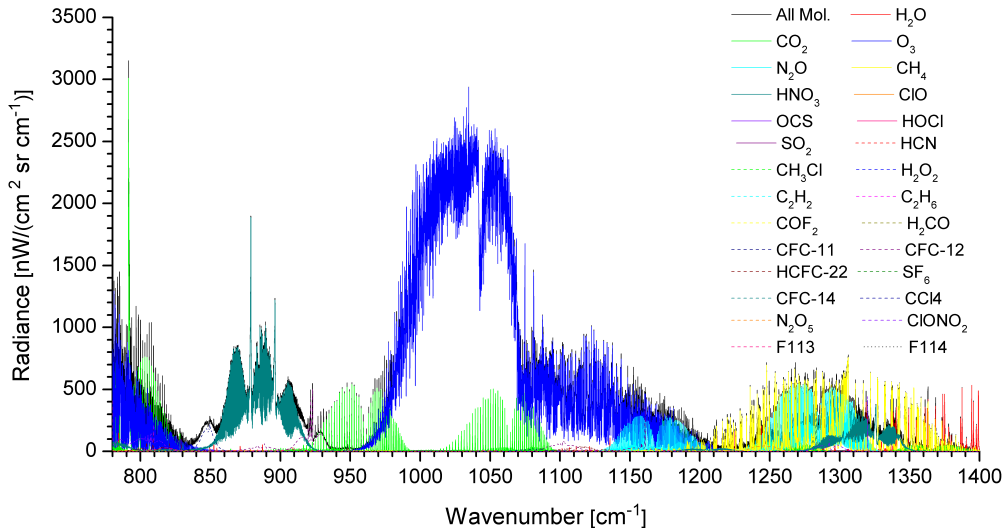


Figure 1.2.: Forward calculated spectra showing several trace gases at 20 km altitude for a mid latitude July standard atmosphere in the spectrally detectable range of GLORIA

In order to analyze the data and interpret the results of the measurements correctly, it is mandatory to have a well characterized instrument. A characterization of the instrument including detector parameters is also needed in order to optimize the operating parameters for the instrument under different measurement conditions and to provide the instrument parameters for the calibration and retrieval process. This thesis focuses on the spectrometric and radiometric characterization and optimization of the GLORIA spectrometer.

In the next chapter basic principles of an FTS related to this study are discussed. The **third chapter** includes the description of GLORIA and its sub-components, the measurement modes and the instrument operation platforms. In the **fourth chapter** an overview of the processing steps starting from the recording of atmospheric emission till the production of spectrally and radiometrically calibrated spectra is given. In the **fifth chapter** results of the *radiometric* characterization measurements of the GLORIA spectrometer and comparisons with theoretical estimates are shown. Instrument parameters, detector parameters, detector operating conditions, nonlinearity, parasitic images and imaging quality over the FPA are discussed. An estimate of the error contribution from the above mentioned sources is provided. In the **sixth chapter** results of the *spectrometric* characterization of the GLORIA spectrometer are shown. It includes a discussion on the choice of the calibration sources, the line determination methods used, the spectral calibration method and its application to the measured data. The focal plane determination using the spectral information of the emission lines, shear and instrument vibration determination from Haidinger fringes are discussed. An estimate of the error contribution from the above mentioned sources is provided. The conclusions and outlook are presented in the **final chapter**.



## 2. Basic principles

The basic concept of Fourier spectroscopy has been described in several books [18–20]. In this chapter the most important aspects which are relevant for the thesis are presented. The main focus is on providing a fundamental background on the aspects of a classical FTS and an IFTS, relevant to the study of atmospheric radiation.

### 2.1. Remote sensing and Fourier Transform Spectrometry

Atmospheric remote sensing refers to the measurement of electromagnetic (EM) radiation emitted by, or reflected from the earth and its atmosphere, or using occultation techniques in one of the several spectral regions. Distant observations of the terrestrial radiative activities are often made by remote sensing instruments deployed on airborne or spaceborne platforms. This thesis will deal with one such airborne remote sensing system used for performing measurements of the atmosphere.

Spectrometry is the detection and measurement of EM radiation and its analysis in terms of frequency and energy distribution. An FTS measures the incoming broadband spectrum from the atmosphere. The measured spectrum gives information about the trace gases present in the atmosphere. The spectrum is not recorded directly by an FTS, but as the Fourier transform of an incoming broadband spectrum which is called an interferogram. In a later processing step, the interferogram is inverse Fourier transformed to get back the spectrum.

### 2.2. The Michelson Interferometer

The Michelson interferometer (MI) is the most common form of an optical interferometer. It is a simple yet powerful tool in the study of Fourier transform spectroscopy. The Michelson interferometers are used either as a four port instrument consisting of two input ports and two output ports, or as a two port instrument with one input and one output port. A two port MI is used in GLORIA.

#### Ideal case

An ideal MI consists of three active components: A moving mirror, a fixed mirror and a beamsplitter which can have a compensator plate if necessary. Figure 2.1 shows the ray propagation in a two port MI. The optical arrangement in a MI has four arms. The light from a source at the object plane of the first arm is collimated and is then divided

into two beams of equal amplitude at the beamsplitter (assuming an ideal beamsplitter having 50% reflectance and 50% transmittance). The reflected and the transmitted beams from the beamsplitter surface travel to the second and the third arms. The second arm has a moving mirror (traveling at a constant velocity), whereas the third arm has a fixed mirror. One of the separated beams gets reflected from the moving mirror while the other beam gets reflected from the fixed mirror. After reflection, these light beams meet at the beamsplitter again, where they are recombined and then split once more. The beam traveling towards the fourth arm, perpendicular to the direction of the input beam, is measured by the detector. The measured intensity is dependent upon the path difference traversed by the two beams before their recombination at the beamsplitter. The difference in the optical paths between the two split beams is created by varying the relative position of the moving mirror to the fixed mirror. The difference in the path lengths ( $x$ ) traveled by these two light beams is called optical path difference (OPD). The OPD position is called the zero path difference (ZPD) when both mirrors are equally apart from the beamsplitter.

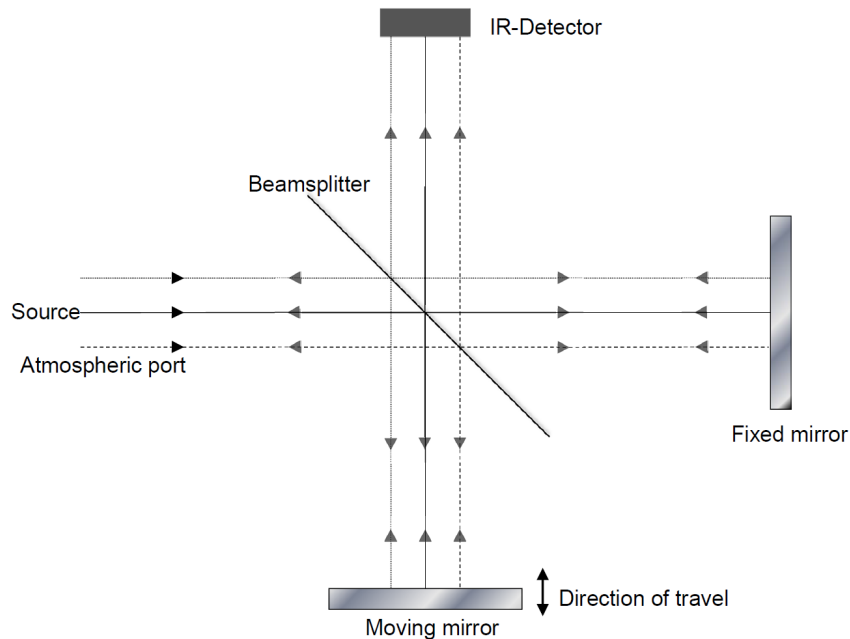


Figure 2.1.: A 2D diagram showing the ray propagation in a two port Michelson interferometer.

The two beams as seen by the detector are in phase at ZPD and are said to interfere constructively. The light from the source goes to the detector and nothing returns to the source. If the moving mirror is displaced by  $\lambda/4$ , making a path difference of  $\lambda/2$ , where  $\lambda$  is the wavelength of the source, the two beams are out of phase and interfere destructively. The light goes back to its source and nothing reaches the detector. As the moving mirror moves by another  $\lambda/4$  the OPD becomes  $\lambda$  and so the two beams are in phase again and interfere constructively leading to a constructive interference. The displacement of the mirror creates an intensity variation on the detector. The intensity reaches its maximum and forms constructive interference when  $x = n\lambda$ , with  $n = 0, 1, 2, \dots$ , and in a similar way, the destructive interference occurs when  $x = (n + \frac{1}{2})\lambda$ . This signal recorded by a detector as a function of the path difference gives an interferogram. The intensity of the interferogram as a function of optical path difference  $x$  for a monochromatic source having a wavelength  $\lambda_0$  (corresponding wavenumber  $\sigma_0$ ) and intensity  $S(\sigma_0)$  is given as

$$I_0(x) = S(\sigma_0)[1 + \cos(\frac{2\pi x}{\lambda_0})] = S(\sigma_0)[1 + \cos(2\pi\sigma_0 x)]. \quad (2.1)$$

The right hand side contains an unmodulated term and a modulated term dependent on the OPD. For a polychromatic source the detector views a superposition of the cosine

functions,

$$I_1(x) = \int_0^{\infty} S(\sigma)(1 + \cos(2\pi\sigma x))d\sigma. \quad (2.2)$$

Subtracting the mean of the interferogram from equation 2.2, the modulated part of the interferogram is expressed as

$$I(x) = I_1(x) - \overline{I_1(x)} = \int_0^{\infty} S(\sigma)\cos(2\pi\sigma x)d\sigma. \quad (2.3)$$

A complete interferogram is generated by moving the mirror along its axis. The interferogram has its maximum intensity centered at the ZPD because all wavelengths of light constructively interfere. The OPD increases as the mirror moves away from the ZPD. Rays at different frequencies are growing more and more out-of-phase. Some are constructively and some are destructively interfering. This results in a rapid decay of the interferogram intensity away from the ZPD. The signal on the right side of equation 2.3 contains all spectral information and is the cosine Fourier transformation of the source distribution  $S(\sigma)$ . The distribution can be recovered by the inverse Fourier transformation,

$$S(\sigma) = \int_0^{\infty} I(x)\cos(2\pi\sigma x)dx. \quad (2.4)$$

Mathematically extending the range of the integration to  $\pm \infty$ , a spectrum at negative wavenumbers  $S(-\sigma)$  is also produced along with the spectrum at positive wavenumbers  $S(\sigma)$ . The image of the actual signal is mirrored at the corresponding negative wavenumbers. We have

$$S(-\sigma) = S^*(\sigma), \quad (2.5)$$

where  $S^*(\sigma)$  is the complex conjugate of  $S(\sigma)$ . Therefore the complex Fourier transformation of equation 2.3 and equation 2.4 becomes

$$I(x) = \int_{-\infty}^{\infty} S(\sigma)e^{i2\pi\sigma x}d\sigma = FT^{+1}\{S(\sigma)\}, \quad (2.6)$$

$$S(\sigma) = \int_{-\infty}^{\infty} I(x)e^{-i2\pi\sigma x}dx = FT^{-1}\{I(x)\}. \quad (2.7)$$

The Fourier transformation pair reveals the fundamental principle of an FTS, which states that the desired spectrum is the Fourier transform of the measured interferogram. The interferogram is a measured quantity and therefore is a real function. But if the interferogram is not perfectly symmetric, its transform  $S(\sigma)$  is a complex function,

$$S(\sigma) = S_r(\sigma) + iS_i(\sigma) = |S(\sigma)|e^{i\phi(\sigma)}. \quad (2.8)$$

The complex spectrum is represented in terms of the real  $S_r(\sigma)$  and the imaginary  $S_i(\sigma)$  parts, or as the product of the amplitude spectrum  $|S(\sigma)|$  and the phase spectrum  $\phi(\sigma)$ . The magnitude spectrum is represented as

$$|S(\sigma)| = \sqrt{(S_r(\sigma))^2 + (S_i(\sigma))^2}, \quad (2.9)$$

and the phase spectrum is the representation of the angle between the real and the imaginary spectrum

$$\phi(\sigma) = \tan^{-1} \left[ \frac{S_i(\sigma)}{S_r(\sigma)} \right]. \quad (2.10)$$

### From the ideal case to measured interferogram

In reality, the measured interferogram is not continuous and does not extend to infinity. The  $x$  in equation 2.7 is in the range  $[-L, L]$ , where  $L$  is the length (one sided) of the interferogram. In addition, the measured interferogram is not continuous but rather sampled at discrete points and digitized.

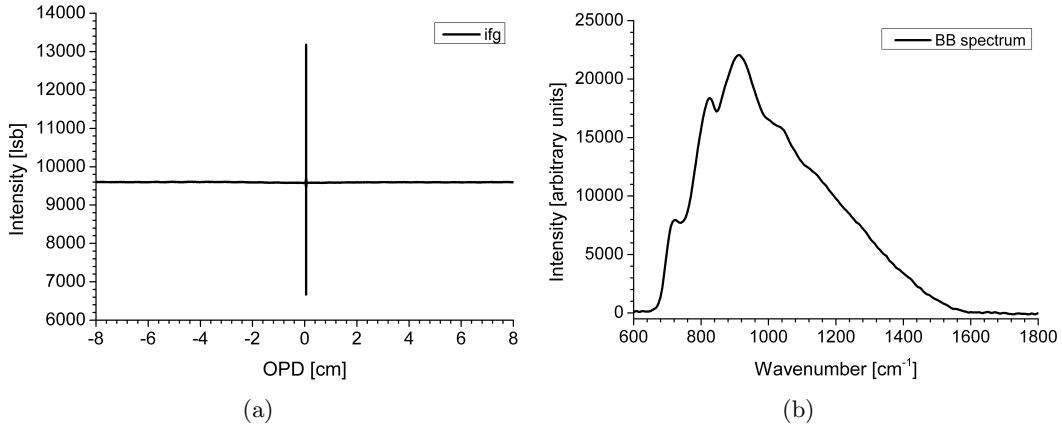


Figure 2.2.: Blackbody interferogram (a) and its corresponding magnitude spectrum (b) from measurement data.

A measured blackbody (BB) interferogram and its corresponding magnitude spectrum are shown in figure 2.2(a) and figure 2.2(b), respectively. The interferogram is bounded in a finite range and has its maximum value at the ZPD due to the constructive interference occurring at the ZPD from all wavelengths. In real life we discretely sampled interferograms and we may not hit the actual interferogram peak. So the sampled maximum is taken as the best proxy of the ZPD. The spectrum is also bounded and has discrete sampling points as well.

### Discrete interferogram

Mathematically, the transformation from a continuous to a discrete interferogram is done by multiplying the continuous interferogram with a Dirac comb sampling function having a width of  $\Delta x$ ,

$$I_{digitized}(x) = I(x) \cdot \text{Dirac}_{\Delta x}(x), \quad (2.11)$$

which contains values only at the points  $x = n\Delta x$ . The convolution theorem states that the Fourier transform of a convolution is the product of the transforms of the individual functions and vice versa.

$$F(\sigma) \cdot G(\sigma) = FT(f(x)) \cdot FT(g(x)) = FT[f(x) \otimes g(x)] \quad (2.12)$$

Using the convolution theorem, the resulting discrete spectrum is the convolution of the desired spectral distribution and a dirac comb of width  $1/\Delta x$ . The FT of a digitized interferogram gives a continuous spectrum which repeats itself at an interval of  $1/\Delta x$ . This effect is known as aliasing. In case of aliasing effects, the final measured spectrum is the sum of all replicas. In order to avoid distortion of the spectrum by aliasing, the maximum frequency in the spectrum should be limited to  $\sigma_{max} = 1/(2\Delta x)$ . Hence, the spectrum in the range of  $[-\sigma_{max}, \sigma_{max}]$  has no loss of information (Nyquist theorem [21]). The maximum wavenumber  $\sigma_{max} = 1/(2\Delta x) = \sigma_{Nyquist}$  is called the Nyquist frequency.

Generalizing the Nyquist theorem one can say that the spectrum can be reproduced when all signals are in the wavenumber range from  $(n-1) \cdot \sigma_{max}/2$  to  $n \cdot \sigma_{max}/2$ . The spectrum

of the discrete interferogram is in the range  $[-\sigma_{max}, 0]$  if  $n$  is an even number and  $[0, \sigma_{max}]$  if  $n$  is an odd number. Therefore, the spectrum can be reconstructed if  $n$  is known.

### Finite interferogram length

The measured interferograms do not have an infinite path difference as shown in equation 2.6, but rather a finite path. The  $x$  is in the range of  $[-L, L]$  instead of  $[-\infty, \infty]$ . This operation is equivalent to multiplying an infinitely long interferogram with a rectangular function ( $\Pi(\frac{x}{2L})$ ). The rectangular function has a value of unity when  $|x| \leq L$  and is zero elsewhere. The FT of a rectangular function is a sinc function ( $FT(\Pi(\frac{x}{2L})) = 2L \cdot sinc(2L\sigma)$ ). The interferogram with a finite path is represented as

$$I_{finite}(x) = I_{infinite}(x) \cdot \Pi\left(\frac{x}{2L}\right). \quad (2.13)$$

In the spectral domain it corresponds to a convolution of the FT of the interferogram with a sinc function having a width of  $1/(2L)$

$$S_{finite}(x) = S_{infinite}(x) \otimes 2L \cdot sinc(2L\sigma). \quad (2.14)$$

From equation 2.14 it can be said that a sharp spectral line (Delta line) is broadened according to the rectangular function when passing through the interferometer. The instrument function<sup>1</sup> in this case is a sinc function,

$$ILS(\sigma) = 2L \cdot sinc(2L\sigma). \quad (2.15)$$

The delta line having infinitesimal width becomes a line of finite width. The full width at half maximum (FWHM) of the line is given as

$$FWHM_{inst.func.} = 1.207\left(\frac{1}{2L}\right). \quad (2.16)$$

The interferogram with a longer path length has a smaller width of the sinc function.

### Discrete spectrum

The numerical FT of the discrete sampled interferogram is calculated on discrete points, making the spectrum discrete as well. This implies that the spectrum is multiplied with a Dirac comb. The spectral sampling is given as

$$\delta\sigma = \frac{1}{2L} = \frac{1}{N\Delta x}, \quad (2.17)$$

where  $2L$  is the interferogram length having  $N$  consecutively sampled values with a sampling interval of  $\Delta x$ . Using the convolution theorem, a multiplication in the spectral domain corresponds to a convolution in the interferogram domain. This implies that the interferogram is repeated with a period of  $2L$ . Aliasing effects are not seen here as the measured interferogram is recorded in the range between  $[-L, L]$ .

---

<sup>1</sup>The instrument function or instrument line shape (ILS) represents the shape of the spectral line resulting from a truly monochromatic input. It gives the degree of the non-ideal nature of the instrument.

### Discrete Fourier transformation

The discrete Fourier transformation (DFT) refers to performing FT with a discrete number of sample points. A DFT of a measured interferogram with  $N$  discrete points will give a complex spectrum with  $N/2$  points. The interferogram and the spectrum expressed in discrete notation are as follows:

$$I(x_j) = \frac{1}{N} \sum_{k=1}^N S(\sigma_k) e^{i2\pi x_j \sigma_k} \quad (2.18)$$

$$S(\sigma_k) = \frac{1}{N} \sum_{j=1}^N I(x_j) e^{-i2\pi x_j \sigma_k} \quad (2.19)$$

### Measured interferogram and spectrum

The measured digital interferogram can be interpreted as the multiplication of the physical continuous interferogram with a rectangular function corresponding to the length of the interferogram  $[-L, L]$ , multiplied by a Dirac comb of width  $\Delta x$  and convolved with a Dirac comb of width  $2L$ :

$$I_{measured}(x) = \left[ I(x) \cdot \Pi\left(\frac{x}{2L}\right) \cdot \text{II}_{\Delta x}(x) \right] \otimes \text{II}_{2L}(x). \quad (2.20)$$

The measured spectrum can be represented as the convolution of the theoretical spectrum with the FT of a rectangular function, convolved with a Dirac comb of width  $1/(\Delta x)$  and multiplied with a Dirac comb of width  $\Delta \sigma$ :

$$S_{measured}(\sigma) = \left[ S(\sigma) \otimes [2L \cdot \text{sinc}(2\pi\sigma L)] \otimes \text{II}_{1/(\Delta x)}(\sigma) \right] \cdot \text{II}_{\Delta\sigma}(\sigma). \quad (2.21)$$

### Interpolation

The spectrum being discrete is made up of a set of  $N$  points which are spaced  $\delta\sigma = 1/(2L)$  apart. The sampling is increased by an interpolation process called zerofilling. In this process, the number of points in the interferogram is increased by adding points with a value of zero symmetric to the ZPD position and until the length of  $L'$ . The spacing in the spectrum becomes  $\delta\sigma' = 1/(2L')$ . This method allows to get the spectrum on a finer grid and find the values for the necessary spectral point (e.g. line maximum determination). Typically, the zerofilling is done such that the number of samples after zerofilling is  $2^n$ , where  $n$  is the zerofilling term. This allows to perform fast Fourier transform (FFT) in contrast to the DFT, thereby reducing the computational time significantly.

### Apodization

Radiation from a monochromatic source upon passing through an interferogram with a finite length produces spectral lines with finite width accompanied by a series of sidelobes. These sidelobes are called ringing. The ringing comes from the sinc function (equation 2.15). If the spectral lines are sharper than the instrument function, the sidelobes of the sinc function are visible. The sidelobes of the sinc function are sometimes disturbing. For example, if the secondary maximum of a strong line overlay on the neighboring weak line, the weak line is hidden under the sidelobe and is not being identified. The abrupt discontinuity at the end of the interferogram is the major source of the ringing and therefore has to be removed. The interferogram is multiplied with a function that reduces the amplitude smoothly to a small value before its end. This function is called an apodization function. Applying the apodization function to the interferogram helps to reduce the sidelobes but it degrades the spectral resolution and broadens the line. The sampling points are not independent after applying apodization to the interferogram. Norton strong apodization [22, 23] function has been used to apodize interferograms in this study.

## 2.3. The imaging Fourier Transform Spectrometer

The advancement of the solid-state detector technology has made the development of large focal plane arrays (FPA) possible. Mercury cadmium telluride (HgCdTe, or MCT) is a commonly used detector semiconductor material for infrared measurements. The MCT detector usually has a wide spectral range and is used to detect atmospheric radiation in the short-wave infrared, mid-wave infrared and long-wave infrared atmospheric windows. It can be operated at temperatures ranging from that of liquid helium to room temperature. The MCT has a direct energy gap, it has the ability to obtain both low and high carrier concentrations; high mobility of electrons and low dielectric constant is possible. In addition, the extremely small change of lattice constant with composition allows to grow high quality layers and graded gap structures [24]. As a result, the MCT can be used for detectors operated at various modes (photodiode, photoconductor or metal-insulator-semiconductor (MIS) detector). Large optical coefficients of the MCT enables high quantum efficiency. The response and the sensitivity of the MCT detectors are high.

An imaging Fourier transform spectrometer uses a spectrometer in combination with an array detector consisting of multiple photosensitive elements. As a result, an IFTS is capable of collecting high resolution spectral images. The advantage of using the FPA is that while performing atmospheric measurements, we can see a large range of the atmosphere at once. The elements of the array detector are usually arranged as rectangle or square and are placed at the focal plane of the IFTS.

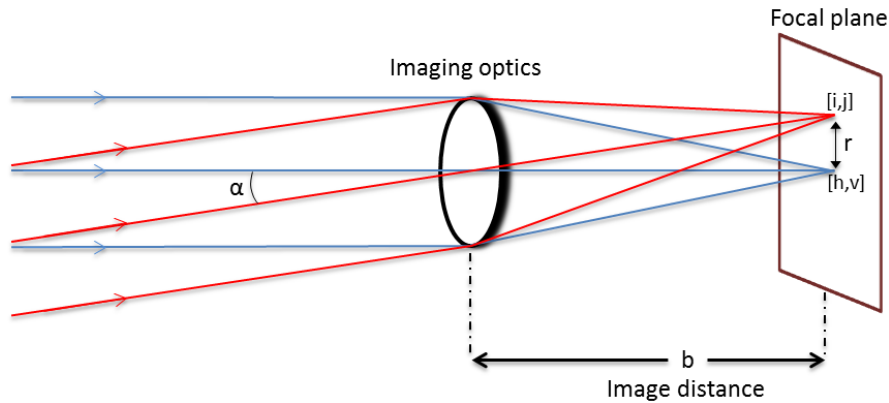


Figure 2.3.: A ray diagram showing projections for the on-axis and an off-axis pixel. The  $(h,v)$  and  $(i,j)$  index represent the position of the on-axis and off-axis pixels,  $r$  is the distance between the two pixels,  $\alpha$  is the off-axis angle and  $b$  represents the image distance.

The interferometer slide defines the optical axis in an IFTS. Rays traveling parallel to the optical axis are incident on the detector surface at the pixel  $(h,v)$ , also called the on-axis pixel. All other pixels receive the rays which travel at an angle  $(\alpha)$  with respect to the optical axis. These pixels are called off-axis pixels. Figure 2.3 shows a ray diagram for the radiation incident on the on-axis and an off-axis pixel. The off-axis pixels have different optical paths depending on their relative position from the on-axis pixel. The OPD for the pixel  $(i,j)$  on the detector array is expressed as

$$x_{i,j} = x_0 \cos(\alpha_{i,j}), \quad (2.22)$$

where

$x_{i,j}$  is the OPD of the pixel  $(i, j)$ ,

$x_0$  is the OPD of the on-axis pixel,

$\alpha_{i,j}$  is the off-axis angle of the pixel  $(i, j)$ .

More effects in relation to the IFTS are discussed further in chapter 5 and chapter 6.

A MCT detector with  $256 \times 256$  pixels with a pitch of  $40 \mu\text{m}$  is used in GLORIA. Depending on the scientific needs only a subset of the full array is used for performing the measurements. The pixel array can be freely configured from  $8 \times 8$  to  $256 \times 256$  pixels. A typical configuration of  $128 \times 128$  pixels is used during laboratory measurements. The alloy of the detector is custom made. The spectral window starts seeing signal at  $680 \text{ cm}^{-1}$  ( $\approx 14.7 \mu\text{m}$ ) and in the higher wavenumber region the signal is limited by the transmission efficiency of the detector window (made of Germanium). The spectral range for scientific data processing is between  $780 \text{ cm}^{-1}$  ( $\approx 12.8 \mu\text{m}$ ) and  $1400 \text{ cm}^{-1}$  ( $\approx 7.1 \mu\text{m}$ ). The selection criterion for the spectral range is discussed in section 5.5.6 and section 5.5.7. The detector is operated in the temperature range of 50 K to 62 K. The FPA used in GLORIA contains two components: A detector array composed of photovoltaic (PV) diodes and a readout integrated circuit (ROIC) which is responsible for reading the generated voltage signal that is proportional to the collected charge from each pixel of the detector array. The signals are then being sent out in a desired sequence to form a two-dimensional FPA image. A block diagram of the detector electronics and the ROIC is shown in figure 5.22.

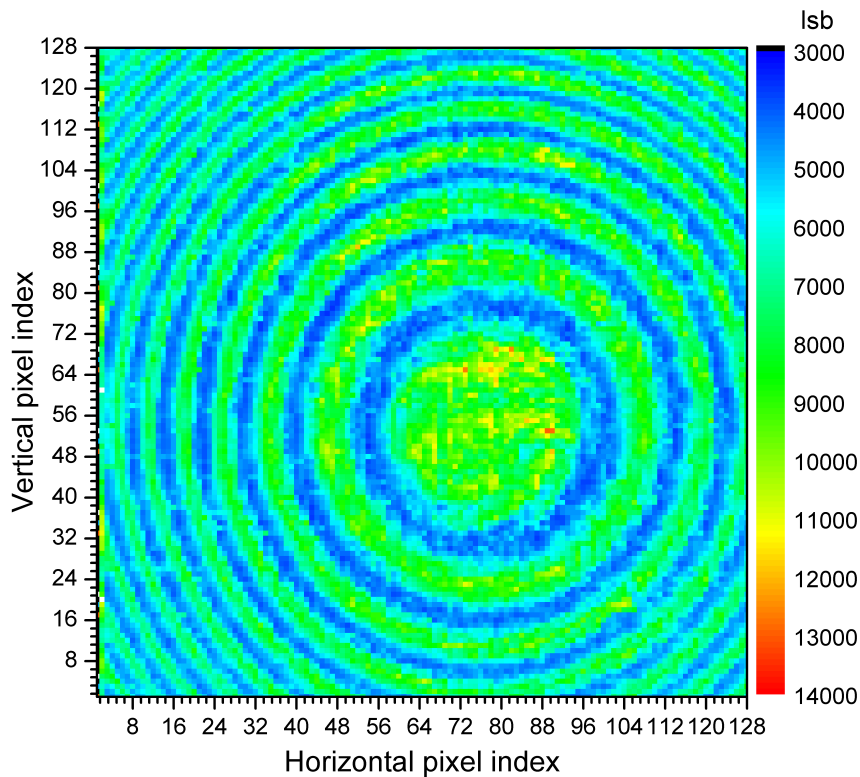


Figure 2.4.: A 2D plot showing the Haidinger fringe pattern over the FPA. The bright (green to yellow) and the dark circles (bluish) correspond to the region with constructive and destructive interference.

A monochromatic source filling the full field of view of an IFTS instrument when imaged on the FPA produces fringes of equal inclination known as Haidinger fringes. Figure 2.4 shows a Haidinger fringe pattern over an  $128 \times 128$  detector array. These fringes are made of alternate dark (low intensity - blue) and bright rings (high intensity - green) formed by constructive and destructive interference of two beams coming from the two arms of the interferometer. An imaging detector gives the opportunity to record an extended picture, whereas a single detector could only detect the central spot.

### 3. The airborne IFTS GLORIA

GLORIA is an IFTS operating in the mid infrared spectral region. The instrument (shown in figure 3.2) is designed to operate in outer compartments on airborne platforms (see figures 3.3 and 3.13) and is exposed to ambient pressure and temperature. The instrument has been designed to operate in a broad temperature range. It consists of an actively cooled spectrometer, two blackbodies used as calibration sources and a three-axis mechanical gimballed frame unit. The gimballed frame unit, the power supply unit and the blackbodies are mounted on a frame (base plate) which is fixed to the aircraft. The three-axis movement with the help of an inertial navigation system provides the pointing and stabilization of the line-of-sight. The spectrometer unit consists of a Michelson interferometer, a cooling system, an infrared detector system with an integrated Stirling cooler and a focusing lens system.

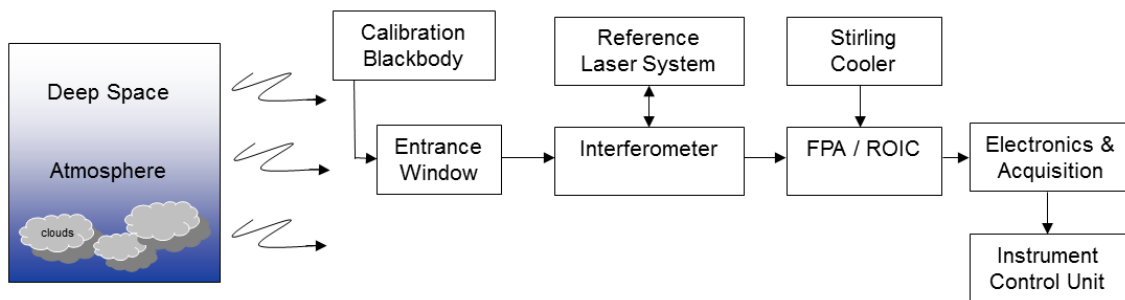


Figure 3.1.: Block diagram showing some of the target sources and different components of GLORIA which are in the path of the IR and the reference laser signal.

A schematic representation of some of the radiation sources and different components of GLORIA in the path of the IR and the reference laser signal is shown in figure 3.1. The radiation sources are the atmosphere, the "deep space" and the blackbodies. The IR radiation enters the spectrometer through the entrance window, passes through the interferometer, the focusing optics and is recorded by the FPA. A reference laser signal is introduced in the interferometer to give information about the position and the velocity of the interferometer drive (slide). The electronic and acquisition unit is responsible for the acquisition of the IR and the reference laser signal. The signals are being recorded in the instrument control unit which is also responsible for controlling the instrument and performing measurements in different modes. In this chapter, a brief description of the components of GLORIA along with its measurement modes and carriers are discussed.

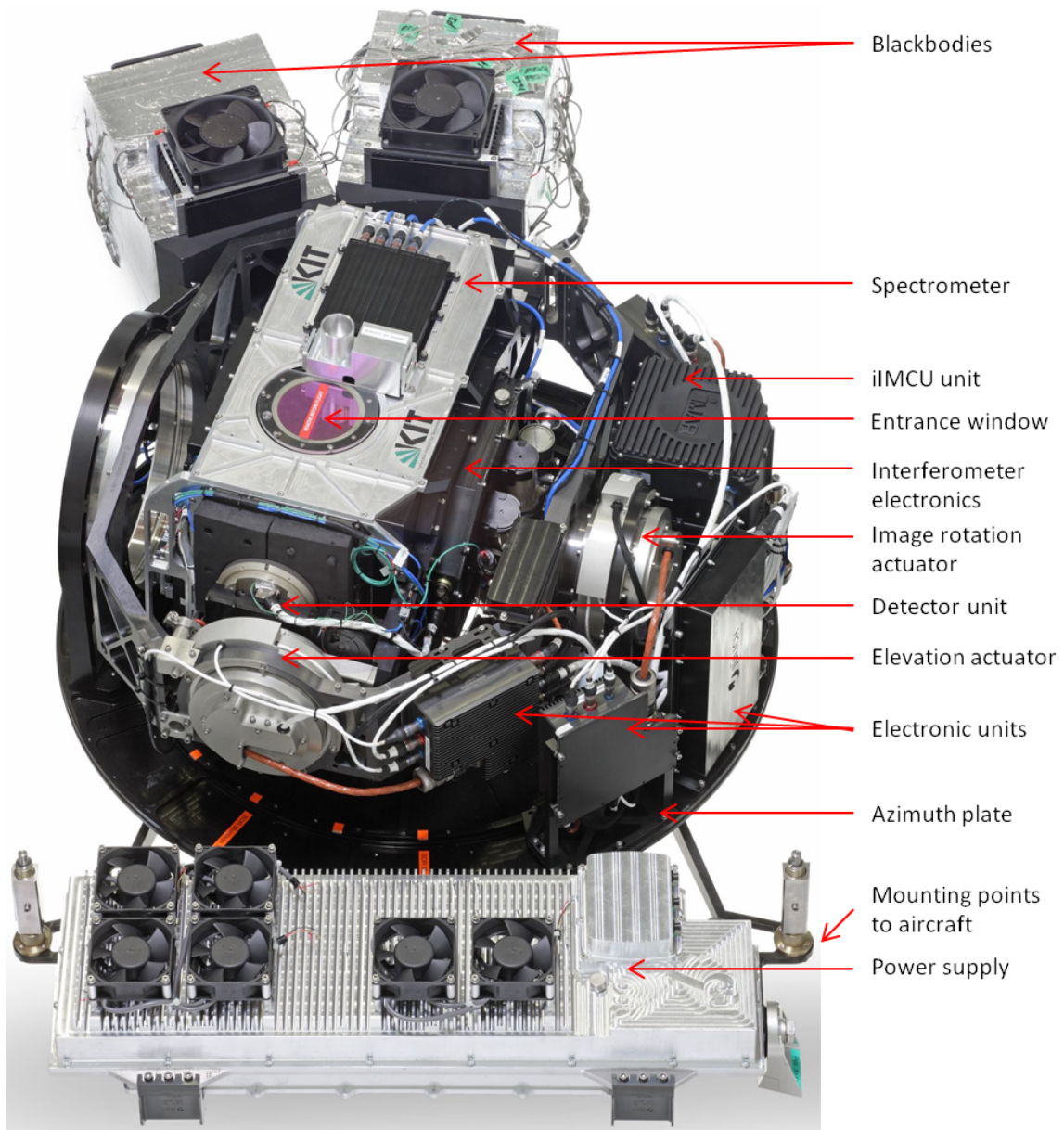


Figure 3.2.: Bottom view of the GLORIA instrument (source: Herbert Schneider, FZJ).

The bottom view of the GLORIA instrument with the spectrometer looking in the direction of the nadir is shown in figure 3.2.

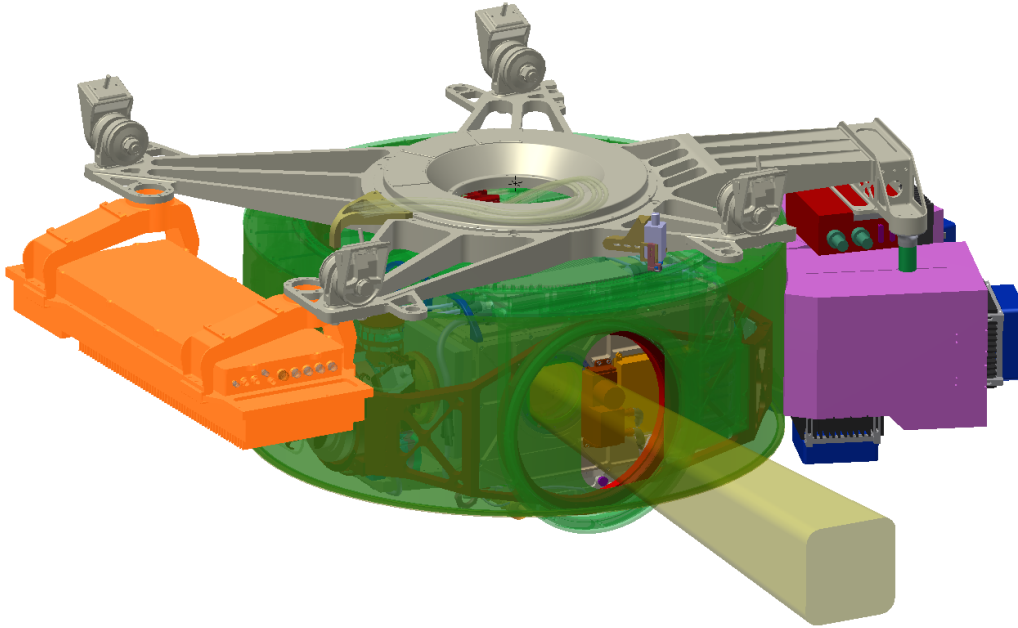


Figure 3.3.: A CAD drawing illustrating the GLORIA instrument. The dimensions of the GLORIA instrument are  $1620 \times 950 \times 680 \text{ mm}^3$  ( $l \times b \times h$ ). (source: ZEA-1, FZJ and Christian Sartorius, KIT).

A CAD drawing of the GLORIA instrument is shown in figure 3.3. The drawing shows the side view of the instrument, where it is in the limb viewing geometry. A protection cover is mounted around the main frame with an opening for the incoming radiation (yellow bundle) falling on the entrance window of the GLORIA spectrometer.

### 3.1. Interferometer unit

The heart of the GLORIA instrument is a classical Michelson interferometer. The interferometer is a single linear slide design with hollow cube corners. It has a maximum optical path difference (MOPD) of  $\pm 8 \text{ cm}$ . Figure 3.4 shows the radiation path with different optical components in the GLORIA interferometer. Point O on the beamsplitter refers to the point where the interference occurs for the central beam. A and B represent the points at the apex of the cube corners where the central beam is reflected. The path difference  $x$  is created by the difference of the optical paths in the two arms of the interferometer. The reference laser unit which is also a part of the interferometer is discussed in section 3.5.

The interferometer is cooled in order to reduce its self emission with the operating temperature range between  $-60 \text{ }^\circ\text{C}$  and  $-45 \text{ }^\circ\text{C}$ . All used optics and mechanics have been designed to work at this temperature range. The components present in the interferometer are shown in a CAD drawing (figure 3.5). Some of the components are discussed in detail in later sections.

### 3.2. Spectrometer unit

The interferometer, the cooling system and the media feedthrough module are placed inside an insulation box. The electrical connection for the components inside the interferometer passes through the media feedthrough module. A cooling reservoir with a volume of about two liters is attached to the base of the interferometer. In order to reduce the heat entering from outside, the above mentioned components are covered with highly efficient Va-Q-Vip vacuum-insulation panels which are in turn encased within an aluminium housing. The housing is open for the entrance window and at the detector side. The lower part of

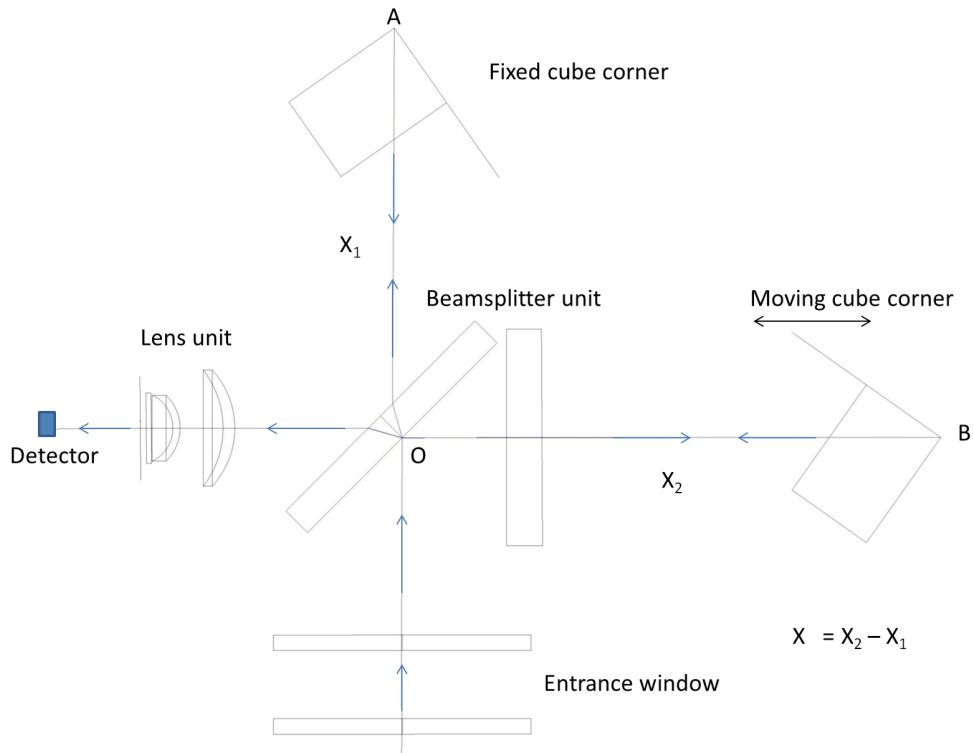


Figure 3.4.: A 2D diagram showing the ray propagation through the different optical components in GLORIA.

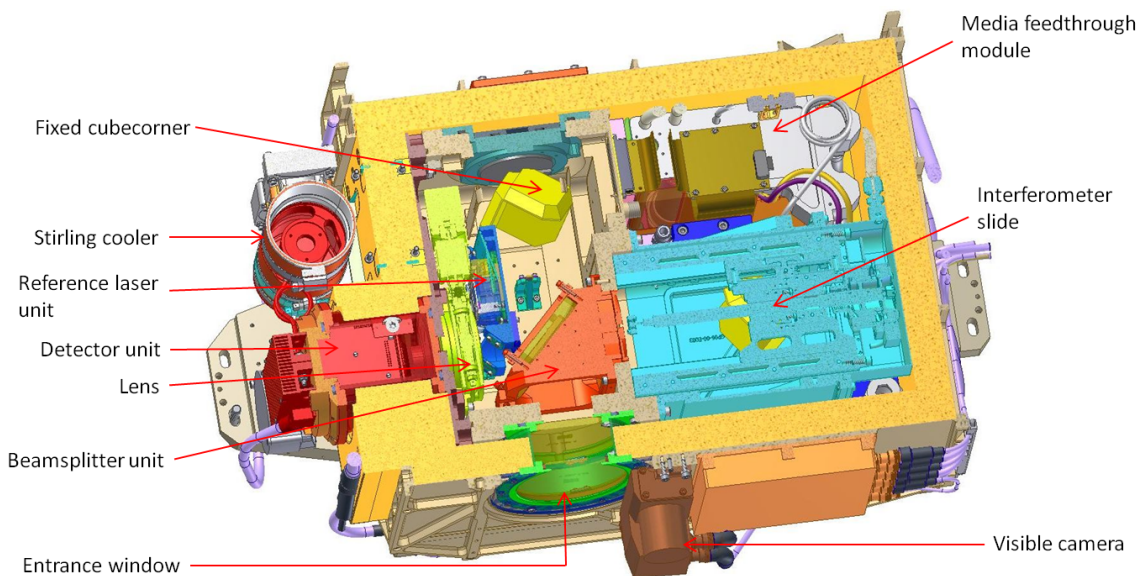


Figure 3.5.: Inside view of the spectrometer showing different components of the GLORIA interferometer. (source: Christian Sartorius, KIT)

the housing consists of the elevation plate on which the interferometer is mounted. The elevation plate is connected to the gimballed frame. For the other side of the housing thin walled aluminium plates are used which mechanically protect the insulation panel from damage and hold several electronic units. The detector side of the housing has a plate on which the infrared objective (IRO), the detector and the compressor have been fixed. All these units together form the spectrometer unit.

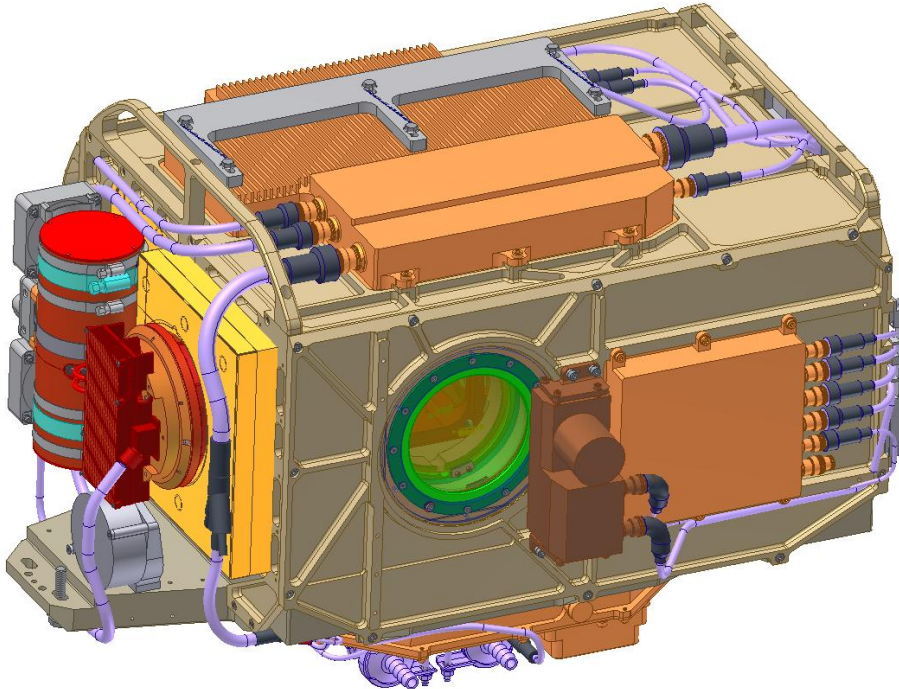


Figure 3.6.: Front view of the spectrometer showing different components. The dimensions of the spectrometer are  $670 \times 460 \times 430 \text{ mm}^3$  ( $l \times b \times h$ ) (source: Christian Sartorius, KIT).

The inside and the front view of the spectrometer are shown in figures 3.5 and 3.6, respectively. Different electronic modules are fixed to the body of the spectrometer. A camera measuring in the visible wavelength range is fixed outside the spectrometer to the right of the entrance window. It has a wider field-of-view (FOV) as compared to the IR detector and is used to record pictures or videos of the same scene and its surrounding as recorded by the IR detector. This gives an additional information of the presence of clouds and their surroundings. Moreover, it gives a reference system for checking the pointing stabilization. The spectrometer is actively cooled with a coolant. For laboratory operations, the instrument is cooled by flushing liquid nitrogen (LN<sub>2</sub>) through the cooler. For flight operations, the cooling reservoir is filled with dry ice (CO<sub>2</sub> snow) produced from CO<sub>2</sub> gas. The total amount of dry ice produced inside the reservoir is about 1.7 kg. At the beginning of the cooling phase with dry ice, the temperature inside the spectrometer can reach as low as -78 °C. It then starts to get warmer as the dry ice starts to sublimate. The instrument is kept cooled for up to about 24 hours. The optical components are cooled by conduction from the refrigerant reservoir placed below the interferometer unit. The interferometer is flushed on-ground with gaseous nitrogen when it is not cooled. Two hydro traps are mounted outside the spectrometer on the bottom of the electronics under the cooling system. The traps are filled with molecular sieves which helps in the process of adsorbing water vapor. The dust from the molecular sieve is prevented from entering the interferometer using a dust filter.

### 3.3. Instrument optics

The orientation of the optical components in the interferometer is shown in figure 3.4. The optical components are made of special materials suitable for the infrared spectral region and are capable of operating at cryogenic temperatures going down to  $-65\text{ }^{\circ}\text{C}$ . The transmissive optical components have wedged surfaces to avoid parallel reflections of light. Some components have the possibility to be heated when necessary in order to avoid damages of the components by avoiding water deposition during instrument warming after cold operating conditions.

The entrance window is made up of two layers of Germanium (Ge). The beamsplitter unit consists of a beamsplitter and a compensator plate. The compensator plate compensates the wavelength dependent dispersion effect of the radiation passing through the beamsplitter substrate. Both plates are made of Potassium Chloride (KCl). The beamsplitter plate has a coating for the IR region and two circular spots with a coating optimized for passing the visible reference laser beam. The hollow cube corner or retro-reflector is an assembly of three reflecting surfaces mutually connected at an angle of  $90^{\circ}$ . They are made of glass ceramic (Zerodur) and are coated with gold. The reflected beam from the ideal cube corner surface is parallel to the incident beam making it insensitive to tilt. Lateral movement of the cube corners and vibration on them produces shear. An analysis of the shear during measurements and appropriate correction procedure is shown in section 6.9).

The infrared objective (IRO) is a lens system consisting of two lenses. The focal length of the IRO is 71.0 mm at  $+23\text{ }^{\circ}\text{C}$  under 1030 mbar pressure and 72.260 mm at  $-63\text{ }^{\circ}\text{C}$  at 1 mbar pressure [25]. Both lenses are aspherical, the smaller and the bigger lens (figure A.1) are made of Zinc Selenide (ZnSe) and Germanium (Ge), respectively. The lenses have an anti-reflective (AR) coating to reduce reflection. The IRO is placed inside a mechanical holder to have the possibility to be adjusted to the focal position corresponding to the instrument operating temperature. The total adjustable length is 4 mm with a stepping of 148 counts per mm. In addition to these components, there are some other optical components built in the reference laser unit which are specifically used in its path. These components are discussed in section 3.5.

### 3.4. Detector unit

A second generation AIM's optical photovoltaic Mercury-Cadmium-Telluride (HgCdTe, MCT) detector is used for GLORIA. The detector is measuring in the long-wavelength infrared (LWIR) spectral range [26]. The HgCdTe detector material is made of an alloy composed of a wide energy-gap semiconductor CdTe and a semimetallic compound HgTe. HgTe is considered as a semiconductor with a negative energy gap. The energy gap of the alloy can be controlled by controlling the relative proportions of HgTe and CdTe. The variable band gap  $\text{Hg}_{1-x}\text{Cd}_x\text{Te}$  (HgCdTe) alloy can be tuned with respect to the mole fraction ratio ( $x$ ) of Cd to Hg. The possibility of tuning the alloy provides an unprecedented degree of freedom in the selection of the detector's spectral window. This has made  $\text{Hg}_{1-x}\text{Cd}_x\text{Te}$  the important material for the detector application in the IR spectral range [27].

The HgCdTe detectors used for GLORIA have been developed on the standard n-on-p technology based on MCT grown by liquid-phase epitaxy (LPE) and involving vacancy doping [28]. The n-type region, where easily excited electrons are desired, is added with a donor type of impurity (such as baron) and the other region of the material is added with an acceptor type of impurity (such as copper) and is called the p-type region. The boundary between the two regions is called the depletion region. When a p-n junction is formed some free electrons in the n-type region are attracted to the p-type region and the

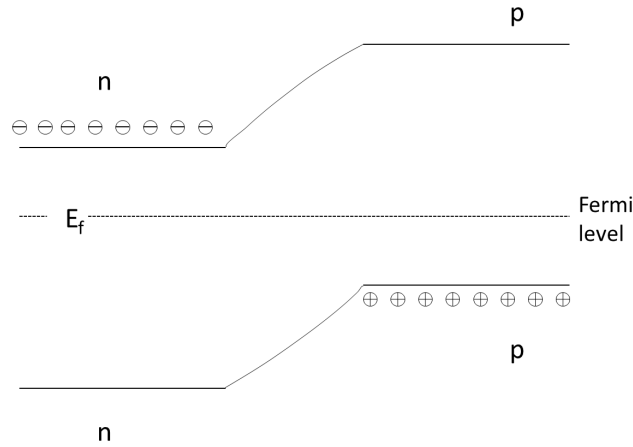


Figure 3.7.: Energy band diagram of a p-n junction [27].

holes drift to the n-type region. The n-type region is left with a net positive charge and the p-type region is left with a net negative charge. Therefore a potential is being developed. Figure 3.7 shows the energy band diagram of a p-n junction. The Fermi levels<sup>1</sup> of each material are aligned to the same energy ( $E_f$ ) when the steady state has been established. If a photon which has sufficient energy is absorbed in or near the depletion region, the electron will gain sufficient energy and will move to the conduction band. The electron will be attracted towards the n-type region, leaving behind a hole that moves towards the p-type region. As a result, the electrodes attached to the detector will see a current flow or voltage difference due to the separation of the electron-hole pair. The number of electrons produced is measured with an appropriate interface or circuitry. The radiation intensity falling on the detector surface can therefore be quantified. The absorption of the radiation is due to the bulk material (HgCdTe) and not the impurities, so the PV detector is still considered as intrinsic<sup>2</sup>.

The detector is offered as Integrated Detector Cooler Assemblies (IDCAs) which comprises of a large focal plane array, dewar, cooler and front-end electronics (FEE) with 14 bit analog-to-digital-converters (ADCs). The Stirling cooler helps cooling down the detector to a temperature range of 62 K to 50 K. Some of the detector parameters provided by the manufacturer (AIM) are given in table 3.1.

Table 3.1.: AIM detector parameter specifications.

Parameter	value
Detector array and full frame readout-frequency	256×256 pixels with 884 Hz
Used detector array and readout-frequency	128×128 pixels with 2665 Hz, 64×128 pixels with 4940 Hz, 48×128 pixels with 6281 Hz
Pitch	40 $\mu\text{m}$
Sensitive area of a pixel	36 $\mu\text{m}$ x 36 $\mu\text{m}$
Detector operating temperature	62 K - 50 K
Detector window	Germanium with AR coating, window has a minimum wedging of 10 arcmin
Detector mass including cooler	4 kg (approx.)

<sup>1</sup>The Fermi level is an energy level where the probability of finding a filled energy state is 50 %. An equal number of filled and vacant levels are both above and below the Fermi level.

<sup>2</sup>Intrinsic semiconductors are those for which the Fermi level is in the center of the forbidden energy gap.

The detector array configuration with  $128 \times 128$  pixels with an interferometer slide velocity of about 0.666 cm/sec has been used for the laboratory characterization. During the first flight of GLORIA it was decided to fly with a configuration of  $64 \times 128$  pixels giving us the opportunity to increase the velocity of the interferometer slide to about 1 cm/sec. Thereby, the relationship between velocity and vibrationally induced velocity errors can be increased. But due to unexpectedly high vibrations encountered on the first flight with the M-55 Geophysica (see section 3.10) aircraft, the interferometer drive velocity was further increased to about 1.28 cm/sec with a detector array configuration of  $48 \times 128$  pixels for the later flights.

A block diagram of the detector electronics is shown in figure 5.22. The detector array is attached to a readout integrated circuit (ROIC). The ROIC has two capacitors for each detector pixel. The detector is operating in stare while scan mode (SWS). One of the capacitors of the ROIC integrates the signal charge, while the other capacitor is used as an in-pixel sampling capacitor. The pixel sampling is controlled by a clock, such that the integration period is identical for all pixels in the array. The readout rate (also called frame rate) of the signal is determined by the pixel array selected for the measurement. The data generated by the detector operating at 2665 Hz, with  $128 \times 128$  detector pixels is about 170 Mbits/sec. The data acquisition system has to be capable of recording data at this rate. The eight ADCs (10 MHz, 14 bit) read the detector data from eight pixels in the vertical direction. The sampling of the data is performed on an equidistant temporal grid. The digital data is time stamped and transferred to the storage computer (the so called CHEFFE) by a fast serial link data cable.

### 3.5. Reference laser system

A temperature stabilized single mode diode is used as a reference laser source in GLORIA. Two gratings (double volume holographic grating (VHG) [29]) stabilize the diode at about 647.5 nm and 656.8 nm and the operating temperatures corresponding to these wavenumbers are about  $-40^\circ\text{C}$  and  $+20^\circ\text{C}$ , respectively. The grating stabilizes the laser diode's drift to approximately  $1/20^{\text{th}}$  of the standard drift, e.g. 0.03 nm/K [30] for a span of 0.5 nm or  $10^\circ\text{C}$ . The temperature of the laser diode is controlled with a Peltier element. This allows to both cool and heat the laser diode such as to stabilize it at a given temperature.

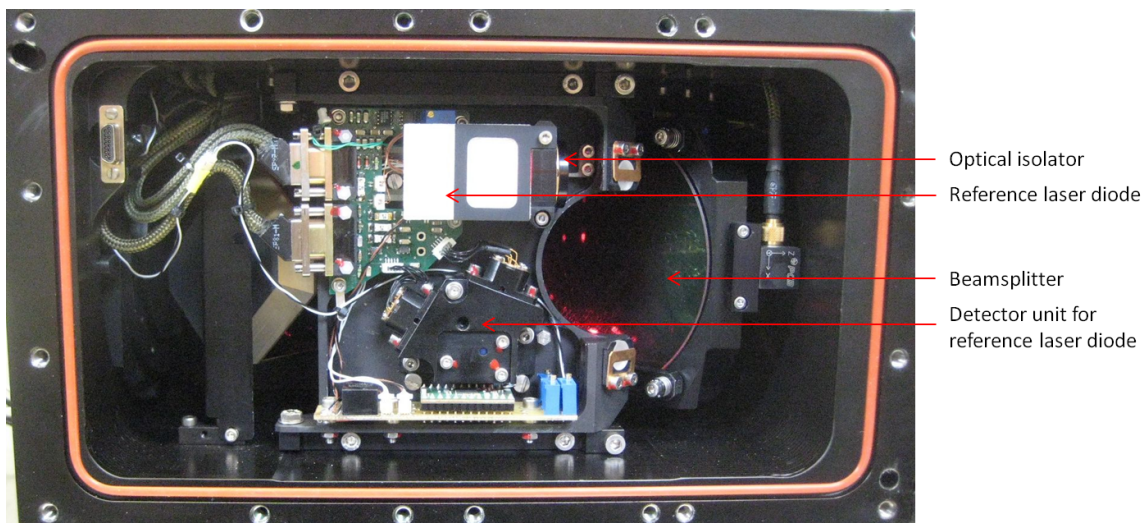


Figure 3.8.: Reference laser diode setup for the GLORIA interferometer.

The setup of the reference laser system used in GLORIA is shown in figure 3.8. The optical components in the path of the laser beam are the optical isolator, beamsplitter unit, cube

corners, a quarter wave plate and a Glan prism. A linearly polarized laser beam is used as the input source. An optical isolator<sup>3</sup> is placed in front of the laser diode to reduce back reflections, thus preventing damage of the laser source, amplitude modulation, mode hops, frequency shifts and spikes in the laser signal. The beam undergoes a phase shift of  $90^\circ$  by passing through a quarter wave plate placed in one arm of the interferometer and is circularly polarized. The output beam after superposition of the beams from the two interferometer arms is separated by the Glan prism into the two polarization components of the circularly polarized light, which are then measured by two photo diode detectors. This signal is referred to as length measuring interferometer (LMI) signal. The rising zero crossings of the laser signal are time-stamped, this gives the information about the velocity and the direction of the drive. The motion control of the drive is accomplished by the encoder on the spindle motor. The space-time relation of the interferometer drive measured by the LMI signal is used to resample the IR data on a space equidistant grid (see chapter 4.2).

### 3.6. Radiometric calibration unit

Two almost identical large area cavity blackbodies and "deep space" measurements performed by looking at  $+10^\circ$  elevation angle are used in GLORIA as calibration sources. The deep space measurements have little contributions from atmospheric measurements present only in some spectral windows, the radiation in the other spectral range can be considered as a radiation of zero intensity. The blackbodies are independently temperature controlled using Peltier elements. For radiometric calibration during flight, one blackbody shall be temperature stabilized at 30 K above ambient temperature (hot-BB) and one at least 10 K below ambient temperature (cold-BB).

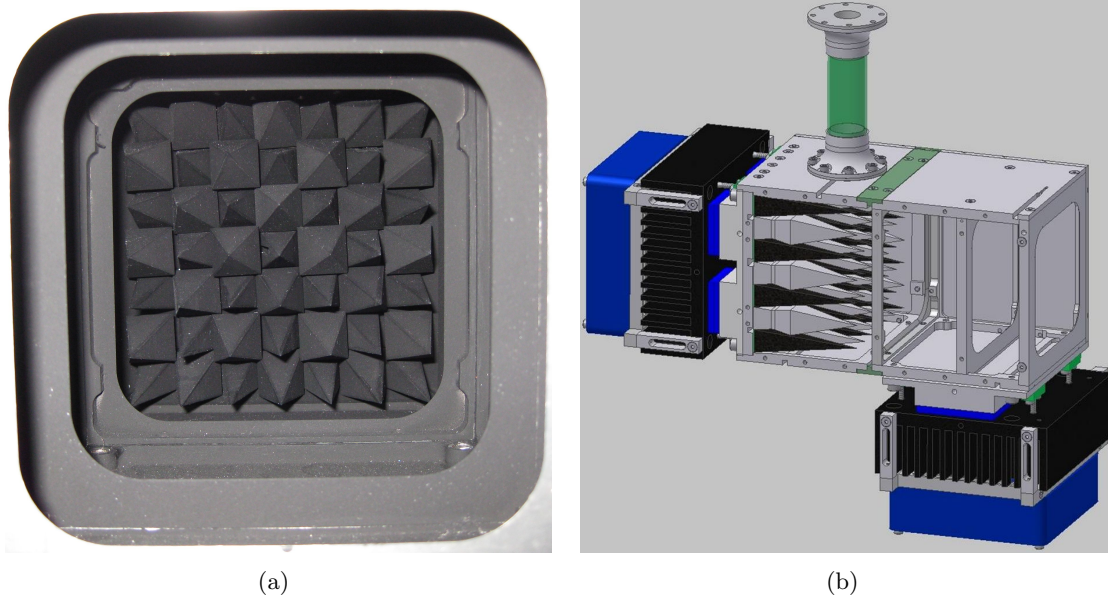


Figure 3.9.: (a): Optical surface of GLORIA blackbody showing pyramids. (b): 3D model of the GLORIA blackbody (source: Friedhelm Olschewski, Bergische Universität Wuppertal).

The blackbodies have an optical surface of  $126\text{ mm} \times 126\text{ mm}$ . The optical surface consists of a pyramid array with 49 peaks (figure 3.9(a)). The pyramids have a steep angle ( $83^\circ$  to  $79^\circ$ ). They are coated with black paint NEXTEL velvet coating 811-21. The

<sup>3</sup>An optical isolator is a passive magneto-optic device that allows light to travel in one direction.

emissivity of the paint is measured to be greater than 0.967 in the spectral range between  $5 \mu\text{m}$  and  $12 \mu\text{m}$  [31]. This structure of the blackbody gives a calculated emissivity of 0.9996 [32]. Platinum resistance thermometers (PRTs) are used for temperature measurements performed at selected pyramids. A 3D model of the blackbody design is shown in figure 3.9(b). The front part of the housing is used as a stray light baffle. This is temperature controlled and is operated at a slightly lower temperature to operate as a water vapor trap thus preventing water vapor condensation on the optical surface.

### 3.7. Electronic unit

The electronic system in GLORIA is based on a modular structure. Figure 3.10 shows the block diagram of the electronic units. The colors are referring to the electronic components in the different gimbal levels of GLORIA. The main power (laboratory or aircraft power) enters GLORIA at the ground plate electronics and is further distributed to different power units for driving the motors, the control units and the data recording systems.

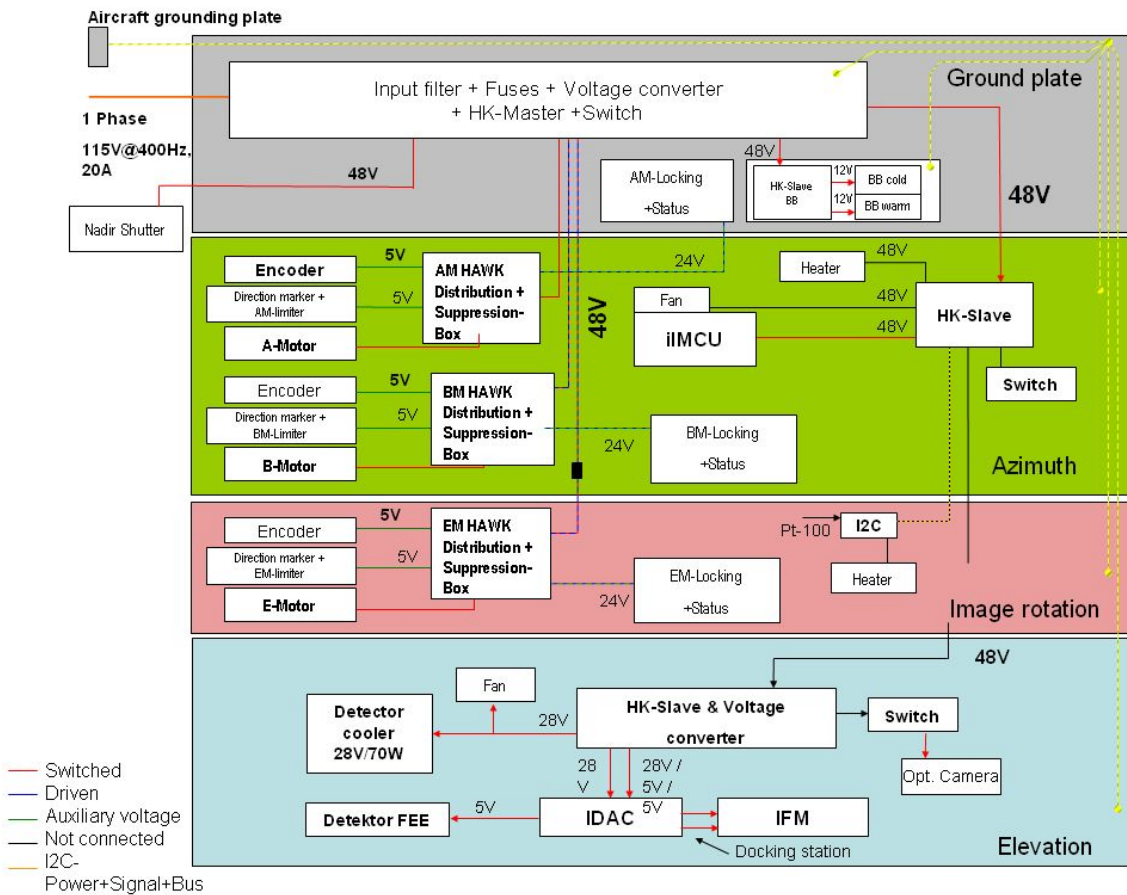


Figure 3.10.: Block diagram for the electronic unit in GLORIA (source: Tom Neubert, FZJ).

### IDAC and CHEFFE

IDAC is the interferometer electronics and data acquisition system. It makes the interface to the interferometer and the infrared detector. It controls the interferometer drive, the reference laser system and the detector FEE (figure 3.11). It provides the time stamps on the IR and the reference laser data which is used for the resampling process. It controls the stepper drive to adjust the IRO to the focal position for variable interferometer operating temperatures (range from  $-70 \text{ }^\circ\text{C}$  to  $+30 \text{ }^\circ\text{C}$ ). CHEFFE controls the instrument operation and is used as a data storage system (figure 3.11). The transfer of data to CHEFFE

is done via fiber optics using a Camera Link interface. A remote control unit with an embedded processor (Embedded Linux) is used for a standardized GBit Ethernet interface to receive telecommands and to transfer data (e.g., housekeeping, service updates). More information on IDAC and CHEFFE and the data recording system of GLORIA can be found in a dedicated paper [33].

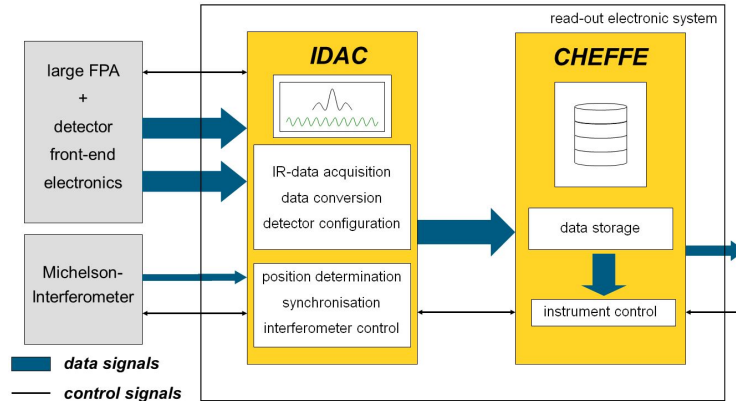


Figure 3.11.: Architecture of read-out electronic system for GLORIA (source: Tom Neubert, FZJ).

### 3.8. Pointing unit

The GLORIA spectrometer is mounted inside a gimbaled frame which ensures agility to rotate the instrument in three axes (elevation, azimuth and image rotation). The gimbaled frame along with the iMAR inertial measurement and control unit (iIMCU) [34] forms the pointing unit. The purpose of the pointing unit is to adjust and stabilize the pointing to the desired target direction and to determine the attitude and position of the instrument. It allows to stabilize the scene on the focal plane array by compensating the aircraft's roll, pitch and yaw changes as well as other (forward, up and down) movements of the aircraft during the measurement. The pointing is achieved in a feedback control loop with a stabilization control unit (SCU) using the information from the inertial measurement unit (IMU), global positioning system (GPS), micro-electro-mechanical system (MEMS) and encoders. The maximum angle of rotation in the elevation, the azimuth and the image rotation are  $115^\circ$ ,  $150^\circ$  and  $25^\circ$ , respectively.

### 3.9. GLORIA measurement modes

The main scientific focus of GLORIA is on the dynamics and chemistry of the UTLS region. It is designed to be operated in two measurement modes. The dynamics mode (DM) measurements are realized with a high spatial resolution but with a low spectral resolution. The measurements in this mode are done by scanning the atmosphere at different azimuth viewing angles in the limb ranging from  $45^\circ$  to  $128^\circ$ . Atmospheric dynamic processes such as tropospheric intrusions and gravity waves can be studied using these measurements. In addition, 3D tomographic retrievals can be done with the data. The chemistry mode (CM) measurements are realized with a high spectral resolution but with a lower horizontal resolution. The measurements are done looking at a given azimuth angle (typically  $80^\circ$  to  $90^\circ$ ) in the limb viewing geometry. In this mode, the main focus is set on understanding the chemical compositions and the reactions happening in different layers of the atmosphere. The instrument can also look in the nadir direction, the measurement is performed by looking at one ground scene while recording one interferogram. These measurements potentially give information on biomass burning, pollution, methane sources and sinks. Table 3.2 gives typical settings and requirements for the dynamics and chemistry mode of operation for GLORIA for an observer at 15 km.

Table 3.2.: Typical setting for the GLORIA measurement parameter for an observer at 15 km.

Requirements	Dynamics mode	Chemistry mode
<b>Geometric</b>		
Lower limit of the FOV	$\sim 4 \text{ km} = -3.27^\circ = -57.1 \text{ mrad}$	
Upper limit of the FOV	$+0.8^\circ = 14 \text{ mrad}$	
Vertical coverage	$4.07^\circ = 71 \text{ mrad}$	
Vertical sampling	140 m @ 10 km = 2'	
Horizontal coverage (one image)	$\sim 6.72 \text{ km} @ 10 \text{ km} = 1.5^\circ = 26 \text{ mrad}$	
Viewing angle to flight direction	45° to 128° in 4° steps	85° (fixed)
<b>Spectrometric</b>		
Spectral sampling	0.625 $\text{cm}^{-1}$	0.0625 $\text{cm}^{-1}$
MOPD	0.8 cm	8 cm
Spectral coverage	780 - 1400 $\text{cm}^{-1}$	780 - 1400 $\text{cm}^{-1}$
Integration time (one IFTS scan)	1.25 s	12.5 s

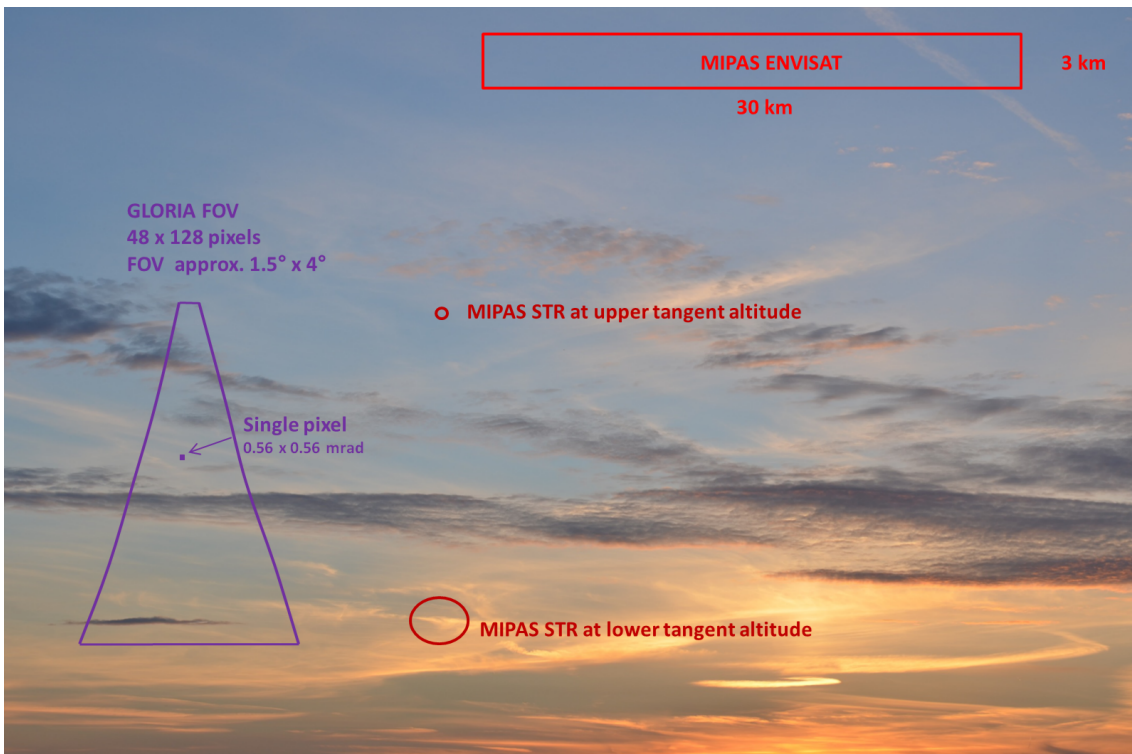


Figure 3.12.: A schematic illustration of the measurement geometry of GLORIA and other FTS instruments. On the picture of the evening sky it is shown how sharp edges of thin clouds can be sampled with GLORIA.

A schematic illustration of the sampling geometry of GLORIA and other FTS instruments is shown in figure 3.12. The field-of-view (FOV) for GLORIA is freely configurable from  $8 \times 8$  up to  $128 \times 128$  pixels. Typically  $48$  (horizontal)  $\times$   $128$  (vertical) pixels corresponding to  $1.5^\circ \times 4^\circ$  FOV are used. A single pixel has a FOV of approximately  $0.56 \text{ mrad} \times 0.56 \text{ mrad}$ . GLORIA can resolve fine structures (e.g., thin cirrus clouds) in the atmosphere. In addition, it has an extended view of the atmosphere per measurement and is able to identify the cloud distribution. The red circles show the pixel size of the limb-sounding MIPAS STR (Michelson Interferometer for Passive Atmospheric Sounding STRatospheric aircraft) [11, 35] at different tangent altitudes. The red box shows the FOV of the measurement made by MIPAS ENVISAT (Michelson Interferometer for Passive Atmospheric

Sounding Environmental Satellite) [10]. These instruments have a large FOV as compared to GLORIA, thereby the fine structures cannot to be resolved.

### 3.10. Instrument operation platforms

GLORIA can be operated from various high altitude research aircrafts. The total weight of the instrument is approximately 265 kg. Up to now GLORIA has flown on two airborne platforms during two scientific campaigns (ESSenCe [36], TACTS/ESMVal [37, 38]) and one certification campaign. The maiden flight was done with the Myasishchev M-55 Geophysica on December 11, 2011. The instrument had been mounted in the nose bay of the aircraft. M-55 Geophysica is a Russian high altitude research aircraft operated by the Myasishchev Design Bureau (MDB). It is capable to carry payloads of up to 2000 kg and can perform flights at altitudes up to 21 km. The cruising ground speed is about 750 km/h. The aircraft flight endurance at a cruising altitude of 17 km is 5 hours 15 minutes and at the altitude 19.7 km it is 4 hours 40 minutes [39]. In 2012 (April and July - August) GLORIA was flown with the new German research aircraft HALO. The aircraft is based on a production G550 business jet from the Gulfstream Aerospace Cooperation and is capable to carry a payload of 3 tons. It has a ceiling altitude of more than 15 km. Its range can be above 10000 km or more than 10 flight hours for transcontinental experiments as well as long duration measurements [40]. GLORIA is mounted in a dedicated belly bay on HALO (figure 3.13).

GLORIA can be operated autonomously on the aircraft. A satellite link (Iridium) to a supervising ground station has been implemented for down link of housekeeping data and uplink of telecommands such as to react to unforeseen problems and adapting the measurement plan. Alternatively, an instrument operator onboard (only possible in HALO) can take care of the instrument operations.



Figure 3.13.: HALO research aircraft with GLORIA in the belly pod. GLORIA is measuring in the limb mode looking to the right side of the flight direction.



## 4. Data recording and processing

This chapter begins with a discussion on the process of recording various data from GLORIA. This comprises of recording the infrared signal and the reference laser signal. A number of other housekeeping data, like temperature, pressure, vibration, etc., coming from various onboard sensors is also simultaneously recorded for subsequent calibration processes. After the data is recorded, it needs to be processed to produce spectrally and radiometrically calibrated spectra. Additionally this involves running various checks on the data. The data processing is done in two levels, which are,

- Level0 data processing - in this processing step the measured interferogram, sampled on a time-equidistant grid, is resampled onto a space-equidistant grid. In addition to the resampling process, a nonlinearity (NL) correction (see section 5.2), a fringe count error (FCE) correction (see section 4.2) and a spectral calibration (see section 6.1) is done.
- Level1 data processing - in this processing step, a Fourier transform of the resampled interferogram is performed to get the spectrum. A complex radiometric calibration using the blackbody and the deep space measurements is performed. The radiometric calibration is done using a two-point calibration approach (section 4.3).

### 4.1. Data recording process

The infrared signal (interferograms corresponding to each pixel) and the reference laser signal (LMI signal) are saved in two separate binary files defined as *cub* and *lxa* files, respectively. The files are marked with an unique time stamp corresponding to the start time of each interferometer scan. The *cub* file contains a three dimensional information of data, the two dimensions correspond to the pixels of the detector surface (horizontal and vertical) and the third dimension is the interferogram signal corresponding to the acquisition time. The 2D data is called a *frame* which contains the measured intensity of the interferogram for each pixel at a given time. The *frames* in a *cub* file are recorded on an equidistant time sampling grid. The *lxa* file contains the times of the rising zero crossings of the interferogram of the reference laser diode signal and information about the direction of the slide movement. The *cub* file together with the corresponding *lxa* file serve as the input for level0 processing. The housekeeping data starting from the power-up of GLORIA until the power-down is saved in a binary file called *flight dat*.

## 4.2. Level0 data processing

The main tasks in level0 processing are explained in this section. It comprises of interferogram resampling, checking for erroneous files, nonlinearity correction, determination of the fringe count error and spectral calibration. In addition, the level0 processing also does a data quality check of the measured signal (both *cub* and *lxa* files).

The level0 code has two versions. One version is an IDL prototype, which is slow but powerful, it does all the needed processing steps mentioned above. The other version is an operational code based on C programming language, which is fast and slim. The operational code is limited in its functionalities. Some additional lookup tables are needed for performing the fast processing. These parameter files have to be generated in advance using the IDL code by processing one pixel for each *cub* file. The single pixel chosen for this step is close to the optical axis, such that the off-axis effects can be neglected.

### Interferogram resampling

The measured interferograms are resampled on a space-equidistant grid. This allows to calculate the spectrum on a wavenumber scale. The velocity variation of the slide is taken care of and the time delay between the infrared signal and the reference laser signal is adjusted upon performing interferogram resampling following Brault's [41] approach.

The measured interferogram gives the time-intensity relation. The space-time relation is extracted from the reference laser signal. The interpolation of the measured interferograms on a space-equidistant grid is done by a resampling process which comprises of the following steps. An equidistant space grid independent of the reference laser wavelength is defined and the corresponding points in time are determined by a linear interpolation of the laser signal. The measured interferogram is then interpolated to this grid by a convolution process. The convolution kernel consists of values corresponding to an apodized sinc function. The convolution is performed by convolving the interferogram with the convolution kernel centered at the interpolation points. A study of the interferogram resampling for GLORIA and its effects has been presented by Kleinert [42]. The resampled interferograms of a *cub* file are saved in a binary form with a file extension as *bif* (Brault-resampled interferogram) file.

### Checking for erroneous files

The time stamps of the frames of the raw interferograms are checked for proper gridding. A *cub* file with equidistant time stamps implies no *frame* loss. The *lxa* file is checked for erroneous zero crossings. They are detected through spikes in the velocity signal. Level0 processing is performed to a *cub* file, only if it has no *frame* loss and the corresponding *lxa* file has no spikes.

### Nonlinearity correction

The infrared signal measured by the detector is nonlinear. A nonlinearity correction has to be applied to the infrared data to map the values onto a linear scale. The nonlinearity determination and correction procedure applied to GLORIA data is discussed in chapter 5.2.

### Determination of fringe count error

A two point calibration approach following the Revercomb method [43] is used for a radiometric calibration of the GLORIA data. The main criterion of this calibration method is that the scene and the calibration spectra must have the same phase. If the ZPD changes then the phase of the interferograms will change accordingly. The interferogram maximum is determined during level0 processing, it is taken as proxy for the ZPD. Ideally the ZPD

position of a given pixel for all *cub* files should be at the same value. If the electronics makes an error in counting the number of rising laser zero crossings or fringes, the ZPD position will vary from measurement to measurement in which case a FCE correction is necessary.

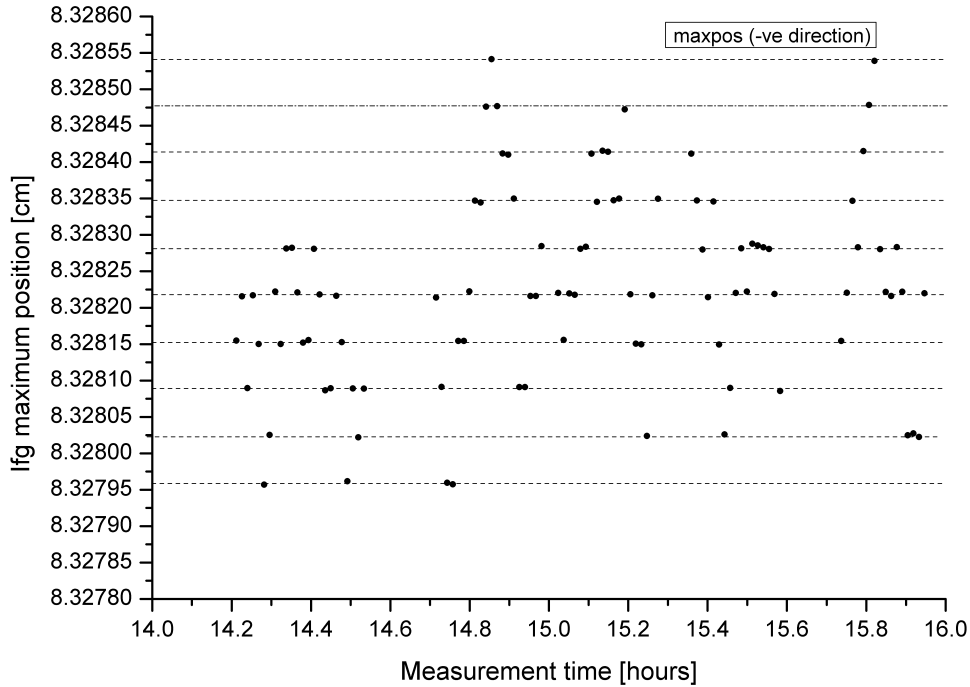


Figure 4.1.: Interferogram maximum plotted for an on-axis pixel of several *cub* files from laboratory measurements. The dotted lines are drawn with a separation of one laser wavelength. The plot shows the FCE accounted during the measurement.

A plot of the maximum position of the interferogram (black points) corresponding to an on-axis pixel from a set of *cub* files measured in the laboratory is shown in figure 4.1. The dotted lines on the plot are separated by one laser wavelength. The plot shows that the interferogram maximum positions do not lie on the same value but are separated by a distance which is a multiple of the reference laser wavelength. The FCE has to be corrected prior to performing radiometric calibration. The fringe count error is compensated during the level0 processing by shifting the abscissa in the interferogram domain. The correction is done for all *cub* files with fringe count errors considering the position for one *cub* file as reference.

### Spectral calibration

Spectral calibration is the process of the application of an appropriate scaling factor to the abscissa of each pixel to correct for the off-axis effect of the detector pixels and for an appropriate reference laser wavelength. A detailed description about the spectral calibration method used is discussed in chapter 6.1. The determination of the spectral calibration parameters can be performed with any chemistry mode measurements. The spectral calibration has to be applied to each measured *cub* file.

### 4.3. Level1 data processing

The level1 data processing deals with the generation of radiometrically calibrated spectra from the space-equidistant, spectrally calibrated, nonlinearity corrected and FCE corrected interferograms. The processing is done with OLAF (Optimierte Level1 Auswertung für Fernerkundung) [44]. The OLAF code is based on IDL.

#### Performing Fourier transformation

The output file (*bif* file) of the level0 process contains resampled interferograms for all pixels. The resampled interferograms of the individual pixels are Fourier transformed to get the corresponding uncalibrated spectra. The real and imaginary part of the spectra are saved in binary files with extensions as *spr* and *spi*, respectively.

#### Performing radiometric calibration

The measured spectrum is calibrated by multiplying it with the gain factor and subtracting the offset term. The calibrated atmospheric spectrum is calculated as

$$A_a = S_a \cdot \underbrace{\frac{L_h - L_c}{S_h - S_c}}_{\text{gain}} - \underbrace{\left( S_c \cdot \frac{L_h - L_c}{S_h - S_c} - L_c \right)}_{\text{offset}} \quad (4.1)$$

where

A is the calibrated spectrum in radiance units,

S is the measured spectrum in arbitrary units,

L is the Planck function of the calibration source,

a : atmospheric, h : hot calibration source, c : cold calibration source.

In the equation 4.1,  $S_a$ ,  $S_h$  and  $S_c$  are complex spectra, therefore  $A_a$  is also a complex spectrum.

The spectrum of the reference calibration sources (e.g., deep space and blackbody) measurements are calculated by performing the Fourier transform of the corresponding interferograms. The gain and the offset can be calculated using the spectra from the calibration sources. No explicit phase correction is done to the data, but it is corrected implicitly during a complex calibration using the Revercomb method [43]. The calibration can be performed using spectra from two blackbodies or a combination of a deep space and a blackbody. The radiometric calibration of the ESSenCe campaign data are performed using the measurements of the two blackbodies. The radiometric calibration of the TACTS data are performed using the measurements of a blackbody and the deep space, due to the reason that the second blackbody had EMC problems.

The real and the imaginary part of the complex calibrated spectra for all pixels are saved as binary files with the extensions as *scr* and *sci*, respectively. Ideally the *scr* file contains the measured signal (typically atmosphere) and the *sci* file only the noise. Figure 4.2 shows an exemplary measurement spectrum from *scr* and *sci* files extracted for a single pixel. The top plot shows the spectrum of the source signal containing atmospheric lines. The bottom plot shows a spectrum containing noise and small unknown low-resolution contribution which is left after the radiometric calibration. The imaginary part (*sci*) of the spectrum is used as an information source for the noise level, phase errors and processing errors. The noise equivalent spectral radiance (NESR) is calculated from the imaginary part of the calibrated spectrum for every pixel using several measurements (section 5.5.7). Since the slow varying slope in the imaginary part of the spectrum is present in all measurements, it does not influence the NESR calculation.

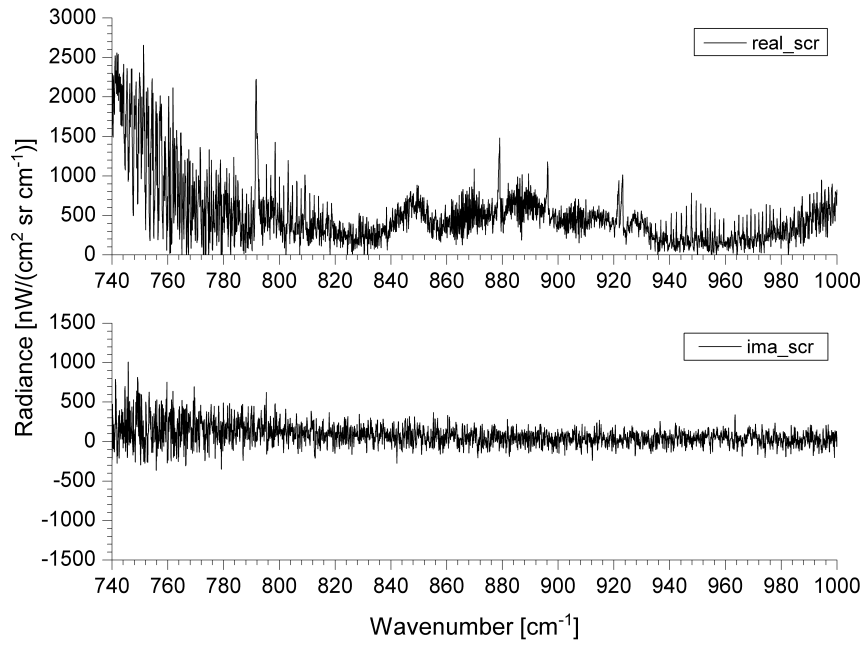


Figure 4.2.: The real and the imaginary part of the radiometrically calibrated atmospheric spectrum for a single pixel for one *cub* file. The ordinate is in  $\text{nW}/(\text{cm}^2 \text{sr cm}^{-1})$  or SRU (spectral radiance units).

The spectrally and radiometrically calibrated atmospheric measurements are used for the retrieval of the temperature and trace gas distribution of the target atmospheric scene. This processing is done in a separate stage (level2) of data processing.



## 5. Radiometric characterization

This chapter begins with a description of the characterization process of the radiometric properties of the detectors used in GLORIA. The responsivity and sensitivity of the detector are determined at first. With reference to these properties, the operating parameters of the detectors are optimized. This process and the results are discussed thereafter. A comparison of the different detectors used in GLORIA is presented subsequently. In the section following this, the nonlinearity effect of the detector system is quantified. A correction method for the nonlinearity is presented along with a discussion on the results of its application. The noise sources in the instruments are discussed next and a theoretical model is presented. This provides an estimation of the theoretical values of the noise equivalent spectral radiance (NESR). The spectral dependency of the detector parameters like response and quantum efficiency are discussed after this. In the next section, the instrument parameters like instrument response, transmission, modulation and NESR are calculated from the laboratory and in-flight data. The NESR value from the measurement is compared to the theoretically expected value. The imaging quality of the system is determined and discussed next. The chapter concludes with a discussion on the optical properties of the system.

### 5.1. Detector characterization

Three second generation 2D infrared MCT detectors (II/1, II/1a and II/2) were supplied by AIM. The detectors were characterized and compared. Table 5.1 gives some detector parameters which are relevant for the detector characterization.

#### Measurement setup

Dedicated laboratory measurements with the detector looking directly into a blackbody were performed in order to characterize the detector. The measurement setup used is shown in figure 5.1. The detector was mounted on top of a blackbody cooled with a silicone oil bath cooler. This setup has the advantage that the radiation coming from the blackbody is directly received by the detector without any optical component (except the detector window) present in its path. The detector is cooled to cryogenic temperatures with the help of a Stirling cooler.

DC measurements were performed at cold and hot blackbody temperatures of approximately 220 K and 262 K. The values selected correspond to the upper boundary of source temperatures seen by GLORIA in the atmosphere and the lower limit of the measurement setup, respectively. The detector temperature and bias voltage were set to 55 K and

Table 5.1.: Parameters relevant for the determination of the radiometric properties of the detector.

Parameter	Value
Single pixel area	$40 \times 40 \mu\text{m}^2$
Effective area ( $A_{pix}$ ) of a single pixel ( $d^2$ )	$36 \times 36 \mu\text{m}^2$ (estimated)
Solid angle of one pixel ( $\Omega_{pix}$ )	0.1876 sr
Specific detector element capacity ( $C_s$ )	$2.3 \times 10^{-15} \text{ F } \mu\text{m}^{-2}$
Detector zero bias resistance-area product (ROA)	800 ohm $\text{cm}^2$
Detector zero bias resistance ( $r_{det}$ )	$\text{ROA}/d^2 = 6.17 \times 10^7 \text{ ohm}$
Detector full well capacity ( $Q_{fw}$ )	$2.326 \times 10^7 \text{ e}^-$ (estimated)
Detector lower cutoff wavenumber ( $\sigma_1$ )	$780 \text{ cm}^{-1}$
Detector upper cutoff wavenumber ( $\sigma_2$ )	$1400 \text{ cm}^{-1}$

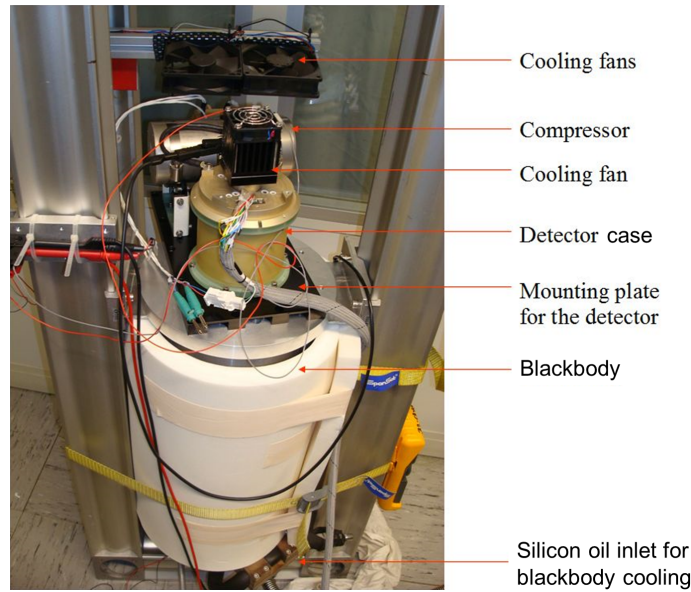


Figure 5.1.: Experimental setup used for the direct blackbody measurements with the detector.

1.32 V, respectively. A detector pixel area of  $256 \times 256$  pixels with an integration time of  $17.1 \mu\text{s}$  has been used. In order to improve the signal-to-noise ratio, the measurement was averaged over 1000 frames.

### 5.1.1. Noise

The standard deviation of the DC values for a given pixel of a measurement gives a measure of the noise in the interferogram domain. The noise ( $\nu$ ) for a given pixel from the measurement data can be calculated as

$$\nu = \sqrt{\frac{1}{N-1} \sum_{i=1}^N (x_i - \bar{x})^2} \quad (5.1)$$

where  $x_i$  represents the individual signal value for the  $i^{\text{th}}$  frame, where  $i$  is ranging from 1 to  $N$  and  $\bar{x}$  is the mean of  $x_i$ .

The noise of each pixel is determined by calculating the standard deviation of 1000 frames of the corresponding pixel in a cub file. Figure 5.2(a) and figure 5.2(b) show a 2D noise distribution and the corresponding histogram plot over the  $256 \times 256$  detector pixels for the

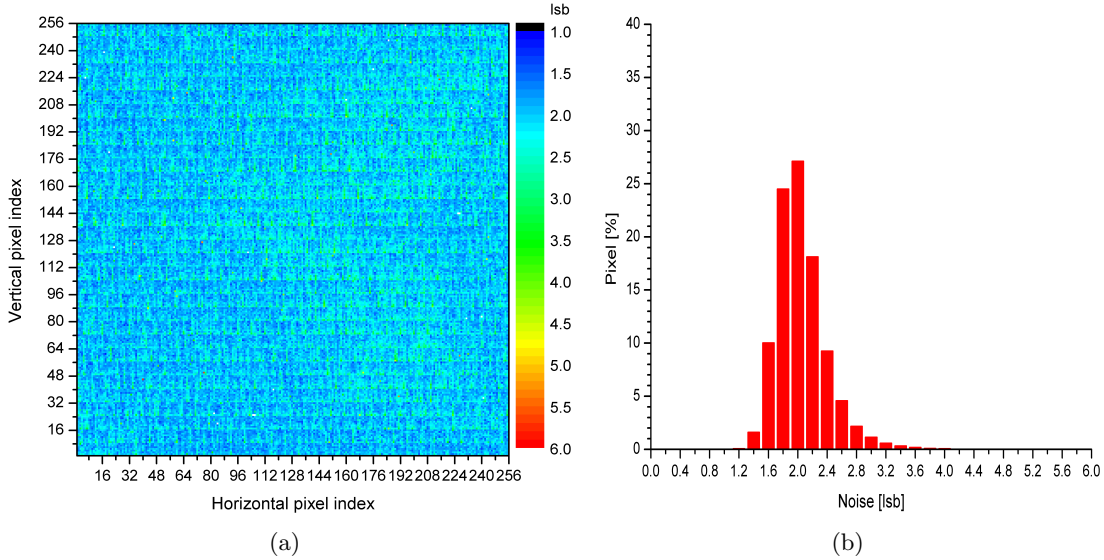


Figure 5.2.: Noise plot for the cold blackbody measured with  $256 \times 256$  detector array. (a) 2D noise plot for detector II/1. (b) Histogram plot showing the corresponding noise distribution.

measurements performed with the blackbody at approximately 220 K. The median of the noise values is 1.996 lsb. The noise distribution over the detector shows horizontal stripes extending over the full line and vertical stripe patterns of eight pixels occurring only at certain positions. The data recording electronics consist of eight ADCs which are running in parallel and record the data in the vertical direction of the detector array. Each ADC has its own linear stage of operational amplifiers with individual offset voltages. The noise properties of these ADCs are also different. It is the noise of these eight ADCs which is seen as the horizontal stripes over the detector array. The plot shows that the first ADC has a higher noise value as compared to the rest. The vertical stripes occur in blocks of eight pixels and at a frequency of  $22 \times 8$  pixels. The data is sampled at 10 MHz. So the frequency of the occurrence of the vertical stripes is 454.5 KHz. The detector front-end-electronics has a DC/DC converter which has a switching frequency between 400 KHz and 500 KHz. The frequency is dependent on the signal load on the detector. Laboratory measurements give a switching frequency of 450 KHz for the DC/DC converter [45]. The operational amplifiers have a high input impedance (about  $3 \text{ K}\Omega$ ) and act as an antenna. These amplifiers are disturbed at this frequency. So the signal recorded by the eight ADCs at the same time are affected at the switching frequency.

### 5.1.2. Detector response

The detector response is a measure of how sensitive the detector reacts to the incoming signal. A higher response implies a better detector performance. It is a spectrally dependent function, with units of  $\text{W}^{-1}\text{cm}$ . The spectral dependence of the detector response is addressed in section 5.5.4. The integral of the response over the spectral range has the units of  $\text{W}^{-1}$ . Thus, the detector response allows deduction of the incident radiant power on the detector from the measured signal.

The DC signal measured by the detector for the measurement setup used is given as [18]

$$DC = A_{pix} \Omega_{pix} \int_{\sigma_{min}}^{\sigma_{max}} \tau_{EW}(\sigma) R_D(\sigma) L(\sigma, T) d\sigma \quad (5.2)$$

where

$\sigma_{min}$  and  $\sigma_{max}$  are the lower ( $780 \text{ cm}^{-1}$ ) and upper ( $1400 \text{ cm}^{-1}$ ) cutoff wavenumbers,

$\tau_{EW}$  is the transmittance of the detector window,  
 $R_D$  is the detector response,  
 $L$  is the spectral radiance<sup>1</sup>,  
 $T$  is the temperature of the blackbody.

The integral response is directly measured with the measurement setup. Using equation 5.2 for blackbody measurements performed at the hot and the cold temperatures, assuming the integral transmittance value of the detector window to be unity (neglecting small deviations from unit in the start and end of the cutoff wavenumber region and also deviations due to temperature changes) and rearranging the terms, the integral detector response over the spectral range of GLORIA for a given detector integration time can be calculated as

$$R_D = \frac{(DC_{bbh} - DC_{bbc})}{A_{pix}\Omega_{pix}(L(T_{bbh}) - L(T_{bbc}))} \quad (5.4)$$

where

$L(T)$  is the integrated spectral radiance over the spectral range of GLORIA,  
 $bbc, bbh$  are the indices for the blackbody at cold and hot temperatures.

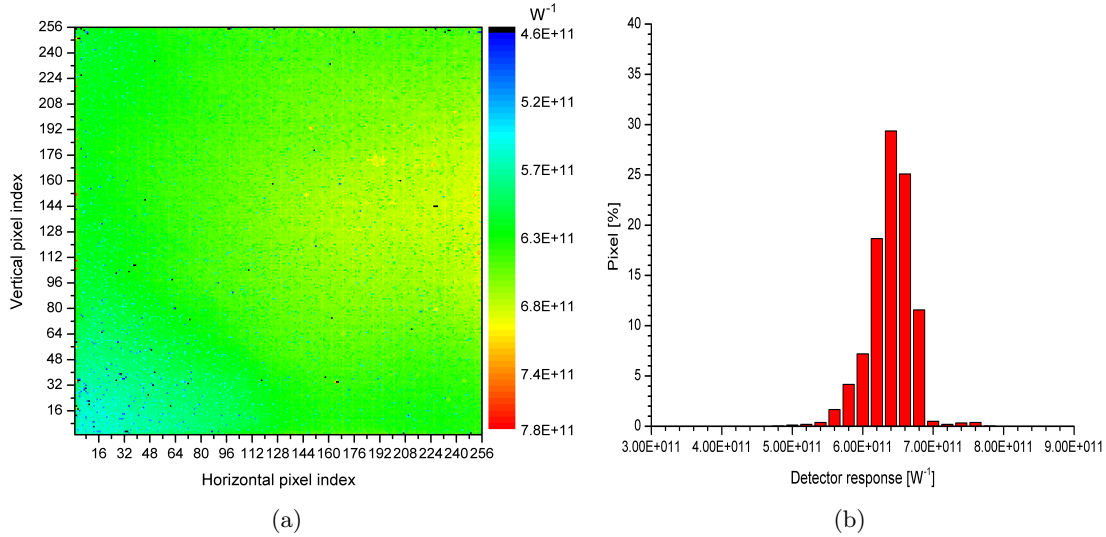


Figure 5.3.: Response plot calculated using cold and hot blackbody measured with  $256 \times 256$  detector array. (a) 2D response plot for detector II/1. (b) Histogram plot showing the corresponding response distribution.

A 2D integral detector response distribution and the corresponding histogram plot over the  $256 \times 256$  detector pixels for the blackbody measurements performed at cold and hot temperatures are shown in figure 5.3(a) and figure 5.3(b), respectively. The response distribution over the detector array shows a variation of about 20% between the lower left corner and the middle right side. This feature is particular to this detector material. The median response value is  $6.4 \times 10^{11}$   $W^{-1}$ .

<sup>1</sup>The spectral radiance is the amount of radiation that is emitted or passes through a unit area and falls within a unit solid angle in a specified direction. The spectral radiance for a blackbody is given by Planck's law

$$L(\sigma, T) = 2h_p c^2 \sigma^3 \frac{1}{e^{\frac{h_p c \sigma}{K_B T}} - 1} \quad (5.3)$$

where  $h_p$  is the Planck constant,  $c$  is the speed of light and  $K_B$  is the Boltzmann constant.

### 5.1.3. Noise equivalent power

The noise equivalent power (NEP) is defined as the amount of the radiant power incident on the detector that yields a signal-to-noise level of one. The NEP is a measure of the sensitivity of the detector. A small value of the NEP represents a sensitive detector. It has the units of  $\text{Ws}^{0.5}$  and is calculated as follows [46]

$$NEP = \frac{\nu}{R_D \sqrt{1/(2t_{samp})}} \quad (5.5)$$

where  $t_{samp}$  is the detector sampling time.

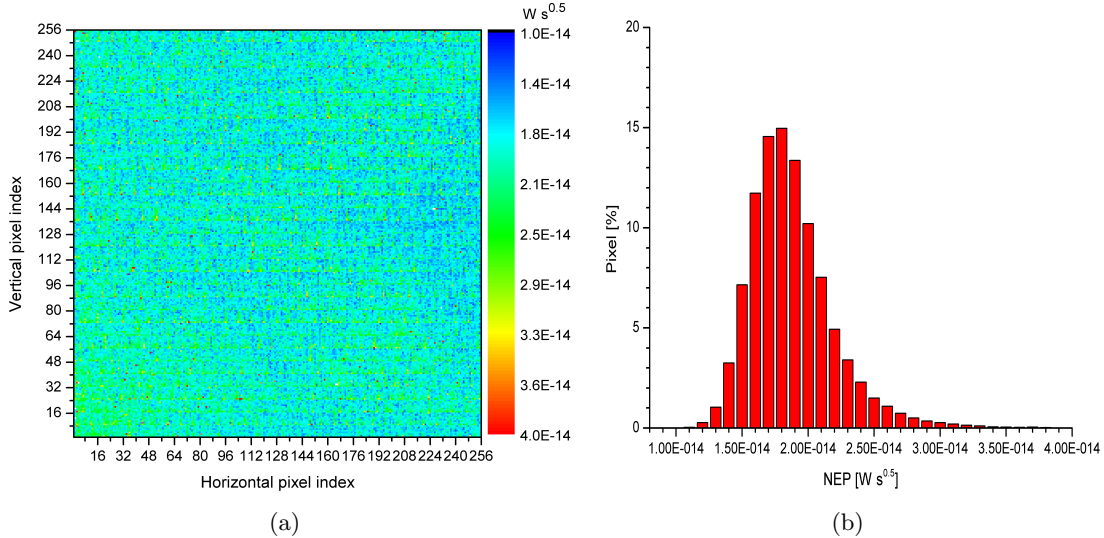


Figure 5.4.: NEP plot calculated using a cold blackbody measured with  $256 \times 256$  detector array. (a) 2D NEP plot for detector II/1. (b) Histogram plot showing the corresponding NEP distribution.

A 2D NEP distribution and the corresponding histogram plot over the  $256 \times 256$  detector pixels for the blackbody measurements performed at the cold temperature are shown in figure 5.4(a) and figure 5.4(b), respectively. The NEP plot is a combination of the noise and response plots. It reflects the noise pattern showing stripes as well as the response variation over the detector array. The median of the NEP value is  $1.83 \times 10^{-14} \text{ W s}^{0.5}$ .

### 5.1.4. Detector parameter optimization

The detectors used in GLORIA can be operated at different bias voltages (in a range between 1.24 V and 1.40 V) and temperatures (in a range between 50 K and 62 K). The optimal bias voltage and operating temperature for the best detector performance has to be determined. The measurement setup used is the same as the one discussed at the beginning of section 5.1. The operating conditions with respect to the blackbody temperatures, detector area and integration time for the DC measurements were the same as discussed before. The results shown in this section are from detector II/1.

#### Detector bias voltage optimization

The measurements were done at three bias voltages: 1.24 V (lower most range), 1.32 V (middle range), 1.40 V (upper most range). The measurements were done at a detector temperature of 55 K.

DC measurements with 1000 frames were analyzed. The noise values for the three cases of bias voltages for all pixels were calculated for the blackbody measurements at 218 K and

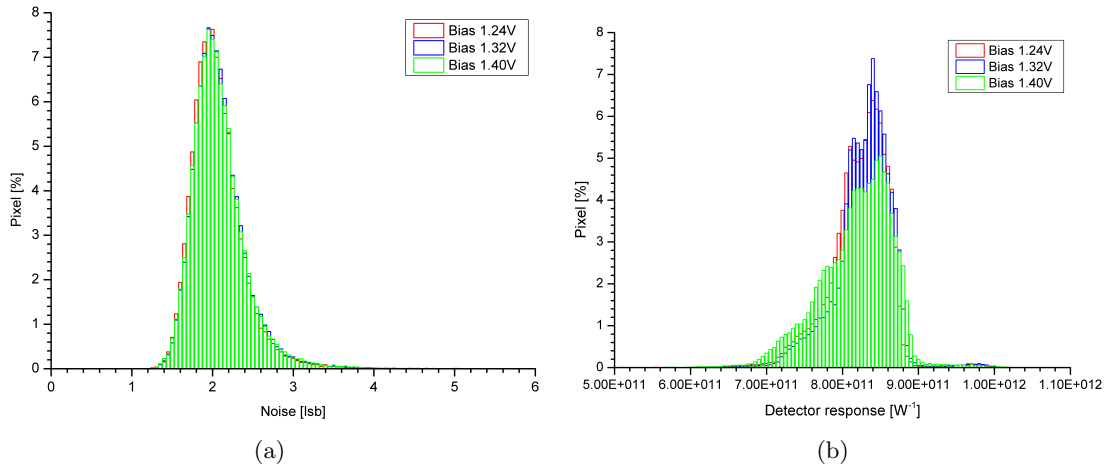


Figure 5.5.: Histogram plot showing the noise (a) and the response (b) distribution of  $256 \times 256$  pixel array of detector II/1 for detector bias voltages of 1.24 V (red), 1.32 V (blue) and 1.40 V (green).

plotted as histograms (figure 5.5(a)). The plot shows that the noise distributions for the three bias voltages are practically identical. A change of the bias voltage has no effect on the noise. The integral response for the three cases of bias voltages was calculated using the blackbody measurements at 263 K and 218 K and plotted as histograms (figure 5.5(b)). The plot shows that the integral response distribution for the bias voltages of 1.24 V (red) and 1.32 V (blue) are practically identical, with the latter being slightly better. The integral response for the bias voltage of 1.40 V (green) has a broader distribution with the barycenter shifted towards smaller response values. Based on this findings, a detector bias voltage of 1.32 V is chosen as the best case among the three bias voltages analyzed. A further refined optimization of the bias voltage is not worth the effort since the effect on the detector is small.

### Detector temperature optimization

The measurements were done at a detector bias voltage of 1.32 V (best case) and at three detector temperatures of 50 K (lower most range), 55 K (middle range) and 62 K (upper most range) to find the optimum operating temperature.

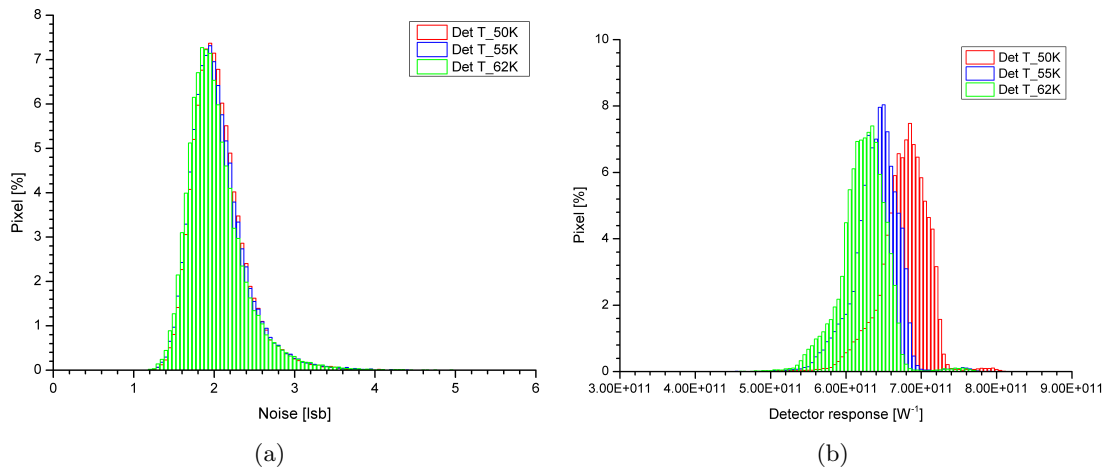


Figure 5.6.: Histogram plot showing the noise (a) and the response (b) distribution of  $256 \times 256$  pixels for detector temperatures of 50 K (red), 55 K (blue) and 62 K (green).

DC measurements with 1000 frames were analyzed. The noise values for the three cases for all pixels were calculated for blackbody measurements at a temperature of 221 K and plotted as histograms (figure 5.6(a)). The plot shows that the noise distribution for 62 K is a little smaller than 55 K, which is a little smaller than 50 K. A change of the detector temperature has very little effect on the noise. The integral response values for the three cases were calculated with blackbody measurements at 260 K and 221 K and plotted as histograms (figure 5.6(b)). The plot shows that a detector temperature of 50 K gives the highest value of the integral detector response distribution curves. A further analysis of the spectral response is necessary to make a final judgement about the selection of the optimum detector operating temperature.

### Spectrally resolved measurements

Interferometric measurements were performed at three different detector temperatures (50 K, 55 K and 62 K) looking at a blackbody at room temperature as source. An integration time of 36.7  $\mu\text{sec}$  was used for all three measurements.

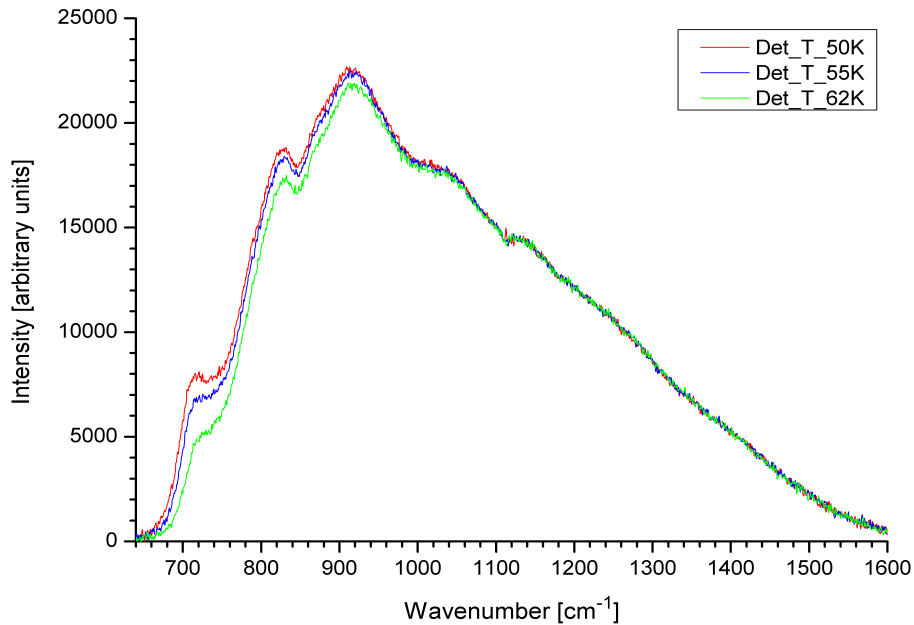


Figure 5.7.: Blackbody spectrum measured at detector temperatures of 50 K (red), 55 K (blue) and 62 K (green).

Three spectra for pixel (128,124) which is relatively in the center of the detector array is shown in figure 5.7. The plot shows that the signal of the detector in the range between 680  $\text{cm}^{-1}$  and 1000  $\text{cm}^{-1}$  is higher for 50 K than for the 55 K and 62 K measurements. The detector signal in the range between 1000  $\text{cm}^{-1}$  and 1400  $\text{cm}^{-1}$  does not show significant differences for all three cases.

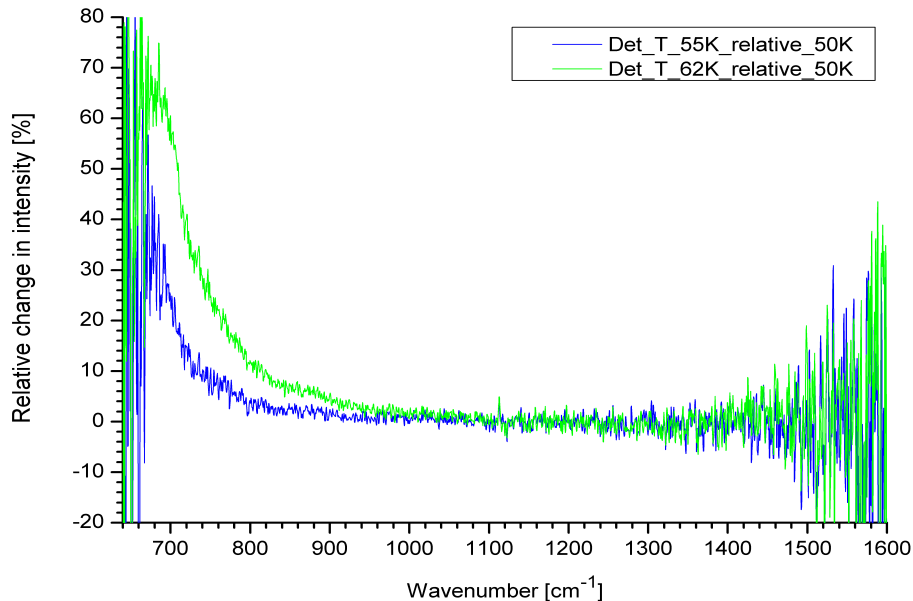


Figure 5.8.: The relative change of the spectra for detector temperatures of 55 K (blue) and 62 K (green) with respect to the measurement at 50 K.

The relative change of the blackbody spectrum measured with detector temperatures of 55 K (blue) and 62 K (green) with respect to the 50 K spectrum is shown in figure 5.8. It is found that, at the lower cutoff region ( $780\text{ cm}^{-1}$ ) of the detector, the spectral intensity for the case of a 55 K spectrum deviates up to 6 % and that for the case of a 62 K spectrum deviates up to 18 %. This is also the reason for the integral response value being higher at the lower detector temperature (figure 5.6(b)). The plot gives a temperature dependence of the detector signal as a function of wavenumber. At present the detector temperature is measured with a resolution of 1 K. A detector temperature change of e.g., 0.5 K will result in a spectrally dependent gain error during the measurement period. The estimated gain error at  $780\text{ cm}^{-1}$  will be roughly 0.6 %.

### Summary: Detector parameter optimization

Three detector bias voltages and three detector temperatures were analyzed spanning the entire available range. The conclusion can be drawn that the noise distribution is barely affected by the change of the bias voltage or the temperature. The bias voltages show no appreciable difference in the detector integral response distribution. The best result was found at 1.32 V whereas the results for 1.40 V shows a deteriorated response and hence should be avoided. The detector temperature of 50 K gives the highest spectral signal in the lower wavenumber region of the detector and thus the highest integral response. It is therefore best suited for these measurements.

#### 5.1.5. Detector comparison

##### Comparison of detector II/1 and detector II/1a

The detectors II/1 and II/1a were compared based on their individual radiometric properties. The measurement setup used is shown in figure 5.1. DC measurements were performed with blackbody temperatures of approximately 220 K and 262 K for detector II/1, and 230 K and 269 K for detector II/1a. The difference in the absolute value of the measurement temperature between the two detectors is not critical here, as only a relative comparison of the two detectors is analyzed. A detector pixel area of  $256 \times 256$  pixels with an integration time of  $17.1\ \mu\text{s}$  was used. The measurements were averaged over 1000 frames in order to improve the signal-to-noise ratio. The radiometric parameters like

noise, response and NEP were compared for the two detectors. The NEP comparison result is shown here for the measurements performed with a cold blackbody.

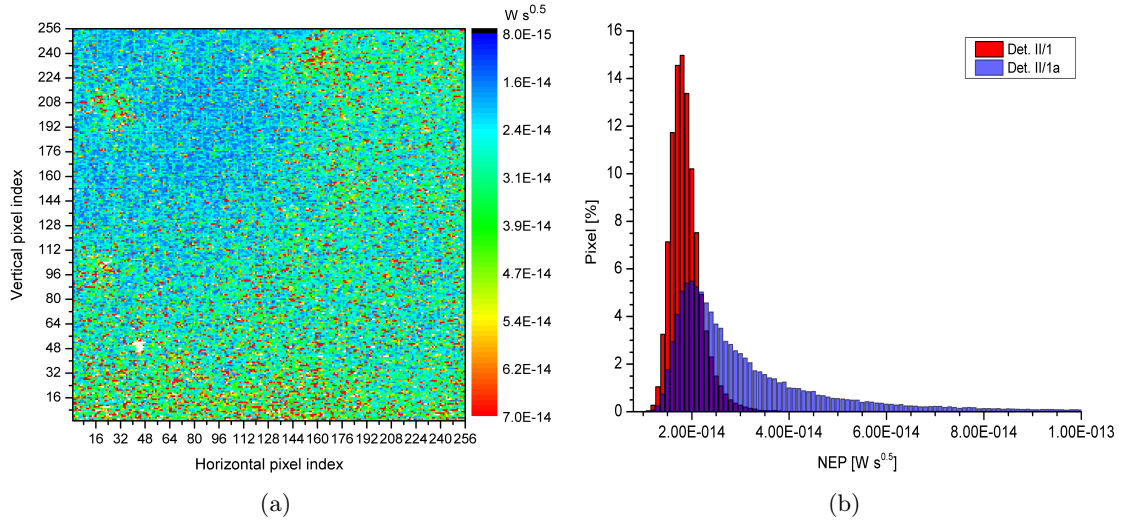


Figure 5.9.: NEP plot calculated using cold blackbody measured with  $256 \times 256$  detector array. (a) 2D NEP plot for detector II/1a. (b) Histogram plot showing the NEP distribution for detector II/1 (red) and II/1a (blue).

The 2D NEP distribution for detector II/1a and detector II/1 are shown in figure 5.9(a) and figure 5.4(a), respectively. Figure 5.9(b) shows the histogram plot of the NEP distribution for the two detectors. The plot shows that the NEP distribution for detector II/1a is broader than that of detector II/1 with the barycenter shifted towards higher NEP values. The median of the NEP value for detector II/1a is  $2.59 \times 10^{-14} W s^{0.5}$  which is higher as compared to the median for detector II/1 which is  $1.83 \times 10^{-14} W s^{0.5}$ . The distribution of the high NEP values for the detector II/1a is scattered over the detector array. This detector is not suitable for atmospheric measurements and therefore is rejected after performing the acceptance testing.

### Comparison of detector II/1 and detector II/2

The silicone oil bath cooler setup used for the comparison of detector II/1 and II/1a broke and was not available for measurements when detector II/2 was supplied by AIM. A new setup with the interferometer was used to make a relative comparison of the radiometric properties of the detectors II/1 and II/2. A blackbody plate mounted inside the interferometer just in front of the entrance window was used as the radiation source. Measurements with a fixed interferometric slide were performed at one OPD position and two instrument temperatures (around 221 K and 260 K). Since the blackbody was placed inside the instrument, its temperature was the same as that of the instrument. The measurements were averaged over 1000 frames in order to improve the signal-to-noise ratio. The measurements were performed with a full detector array (configuration 1) and a subset of the array (configuration 2). The second subset was chosen since it was planned to use only  $128 \times 128$  pixels for atmospheric measurements. The aim of this comparison is to check the detector quality, to make a pixel map of the good and the bad pixels and to find a region on the detector array with as few bad pixels as possible. The measurement settings and the detector parameters used are given in table 5.2.

The setup with the instrument at the same temperature as the blackbody is made with the intention to be similar to the setup as in figure 5.1. Although it has to be noted that it has a port problem associated with the interferometer. The center pixels of the detector array partly see themselves (at about 60 K) as back reflection mostly through

Table 5.2.: The parameters used for the comparison of the radiometric properties of detector II/1 and II/2

Detector II/1	Detector II/2
Detector temperature: 62 K	Detector temperature: 58 K
<b>configuration 1</b>	
$T_c = 222.5$ K, $T_h = 261.7$ K	$T_c = 221.5$ K, $T_h = 257.5$ K
Detector area: 256×256 pixels; Pixel offset: 0, 0; Integration time: 17.1 $\mu$ s	
<b>configuration 2</b>	
$T_c = 222.0$ K, $T_h = 260.9$ K	$T_c = 218.8$ K, $T_h = 258.3$ K
Detector area: 128×128 pixels; Pixel offset: 56, 56; Integration time: 47.1 $\mu$ s	

the beamsplitter unit as well as the other optics in the path of the beam. Whereas, the pixels further away from the center partly see the relatively warm instrument background (at about 220 K or 260 K). The total transmittance ( $\tau$ ) for this setup is pixel dependent because of the port problem and is not exactly known. As the measurements are used only for inter-comparison of detectors, it is assumed to be unity for the calculations.

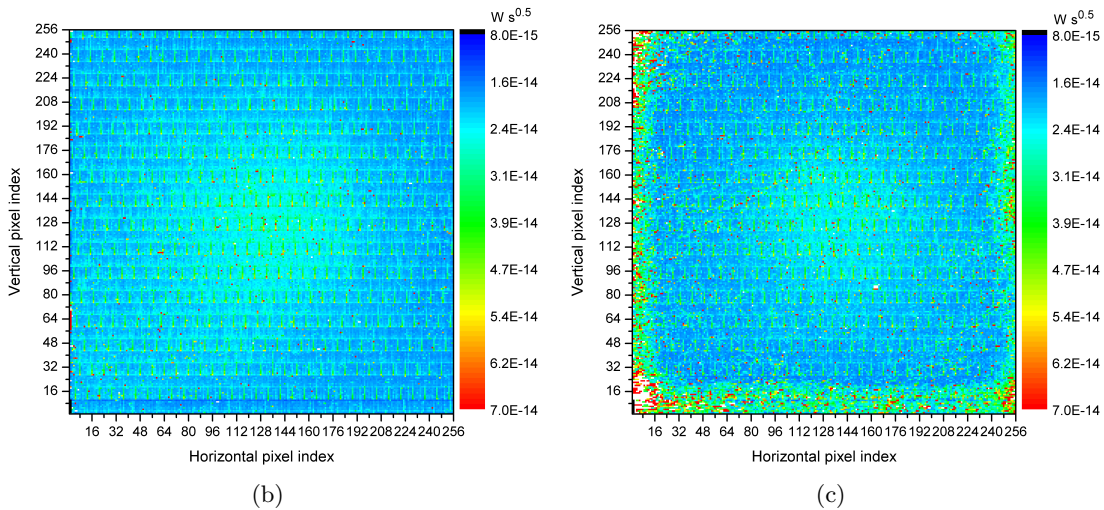
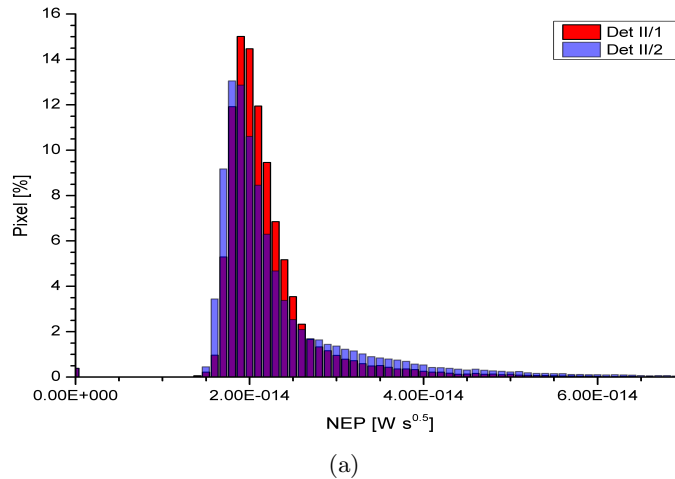


Figure 5.10.: NEP plot for cold blackbody measured with the 256×256 detector array setup. (a) Histogram plot showing the NEP distribution for the cold blackbody for detector II/1 (red) and detector II/2 (blue). (b) 2D NEP plot for detector II/1 (left). (c) 2D NEP plot for detector II/2 (right).

A histogram plot of the NEP for a cold blackbody for detector II/1 (red) and detector II/2 (blue) for the  $256 \times 256$  pixel array (configuration 1) is shown in figure 5.10(a). The plot shows that detector II/2 has more pixels with lower NEP values than detector II/1, as well as having some pixels which have higher values of NEP than detector II/1. Figures 5.10(b) and 5.10(c) show a 2D plot of the NEP for a cold blackbody for detector II/1 and detector II/2 over the  $256 \times 256$  pixel array, respectively. The central pixels in the array show a slightly higher NEP with gradually decreasing values in every direction of the pixel array for both detectors. This effect is not real (see figure 5.4(a)) and is a measurement artifact caused by the port problem. The integral response values for the central pixels are low resulting in the high NEP values. The differences in the additional background radiation sources seen by the detector pixels are the cause of this artifact. In spite of the port problem, these measurements can still be used to give a quantitative comparison between the detectors. The pixels around the border of detector II/2 have high NEP values coming from a comparably low response and a high noise. So, the corner areas of the detector II/2 are not suitable for atmospheric measurements. The central area of detector II/2 has a smaller number of bad pixels and is therefore investigated further as a possible configuration for atmospheric measurements. The stripe pattern in the vertical and horizontal directions due to noise can be seen for both detectors. In particular, the regular stripe pattern seems to be weaker for detector II/2. On the other hand there are more randomly distributed pixels with high noise. The median of the NEP values for detector II/1 and detector II/2 are  $2.065 \times 10^{-14} \text{ W s}^{0.5}$  and  $2.051 \times 10^{-14} \text{ W s}^{0.5}$ , respectively.

Measurements were made with the settings of configuration 2. This configuration was chosen as the detectors in this region have a smaller number of bad pixels and the optical axis position is relatively in the center of the selected array. This selection will have symmetric off-axis effects on the corner pixels of the detector array. This area was also chosen because it is the area that is used in practice. The radiometric parameters were evaluated from the DC measurements and the NEP values for the cold blackbody measurements which are shown here.

A histogram plot of the NEP for a cold blackbody for detector II/1 (red) and detector II/2 (blue) for the  $128 \times 128$  pixel array setup is shown in figure 5.11(a). The plot shows that detector II/2 has more pixels with lower NEP values than detector II/1 for this range. Although, it has to be noted that the temperature of the cold blackbody was 3 K warmer for detector II/1 as compared to detector II/2. This results in a slightly higher noise which leads to a slightly higher NEP value for detector II/1. The median of the NEP value for detector II/1 and detector II/2 are  $1.795 \times 10^{-14} \text{ W s}^{0.5}$  and  $1.752 \times 10^{-14} \text{ W s}^{0.5}$ , respectively. Figure 5.11(b) and 5.11(c) show a 2D plot of the NEP for the cold blackbody for detector II/1 and detector II/2 over a  $128 \times 128$  pixel array, respectively. The noise pattern (stripe pattern in the vertical and horizontal directions) can be seen for both detectors. The 2D plot for detector II/2 shows that the pixels with high NEP values are scattered over the detector array. In addition, a small region ( $\approx 5 \times 3$  pixels) around the pixel position (161,75) for detector II/2 shows very low response values. About 2.8 % and 5.6 % of the pixels of detector II/1 and II/2, respectively, are beyond a threshold of two times the median value of the NEP over the array. These pixels are considered as bad pixels. The selection of the threshold for the bad pixel determination is rather arbitrary. In addition, the last column of the cub files has a readout problem. These pixels are also considered as bad pixels. Figure 5.12(a) and figure 5.12(b) show the distribution of the bad pixels based on the NEP criterion for detector II/1 and II/2, respectively. The final bad pixel list for a detector consists of pixels which are determined based on their radiometric properties and nonlinearity correction criteria (see figure 5.21). Both detectors (II/1 and II/2) are found to have comparable radiometric properties and are accepted for performing atmospheric measurements. Detector II/2 was used to perform measurements during the

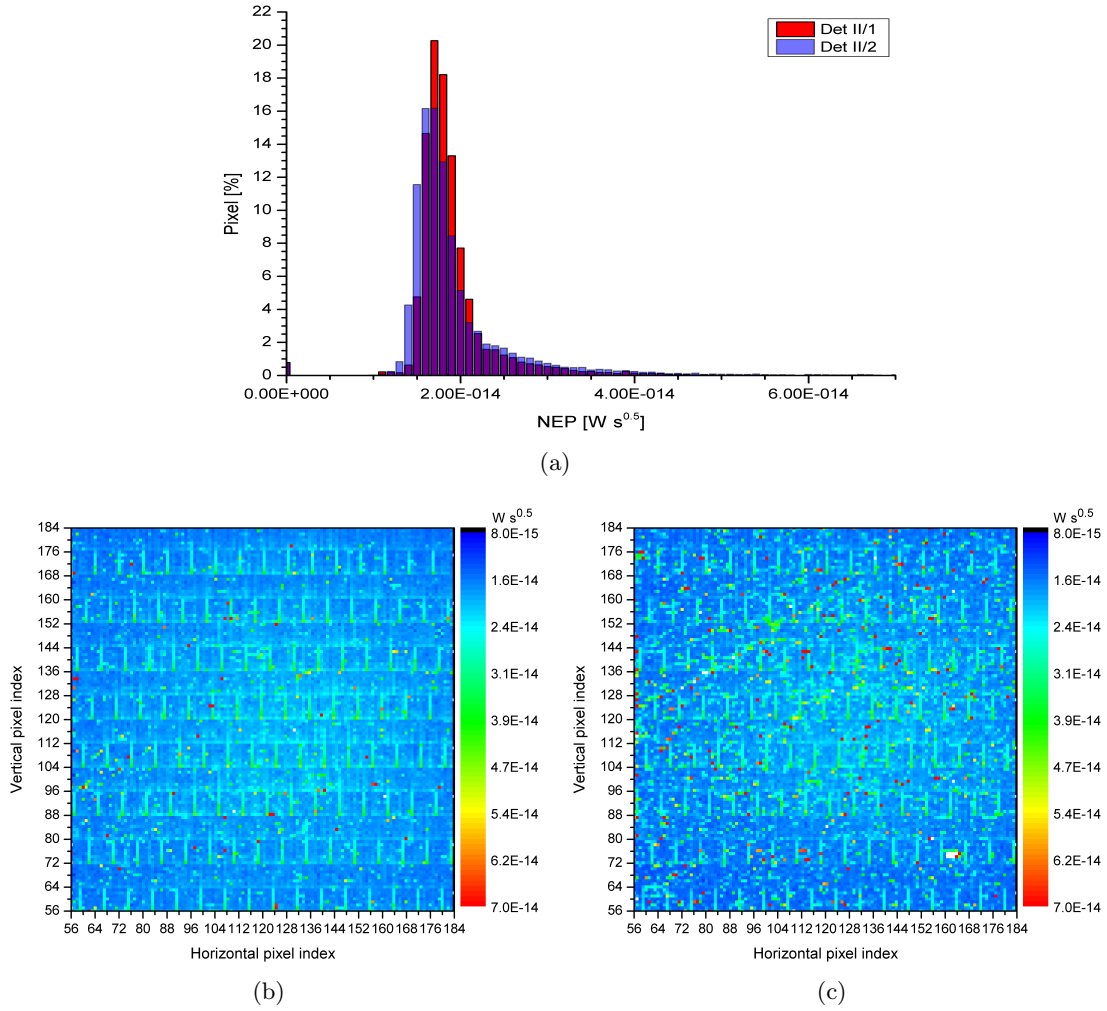


Figure 5.11.: NEP plot for cold blackbody measured with the  $128 \times 128$  detector array setup. (a) Histogram plot showing the NEP distribution for the cold blackbody for detector II/1 (red) and detector II/2 (blue). (b) 2D NEP plot for detector II/1 (left). (c) 2D NEP plot for detector II/2 (right).

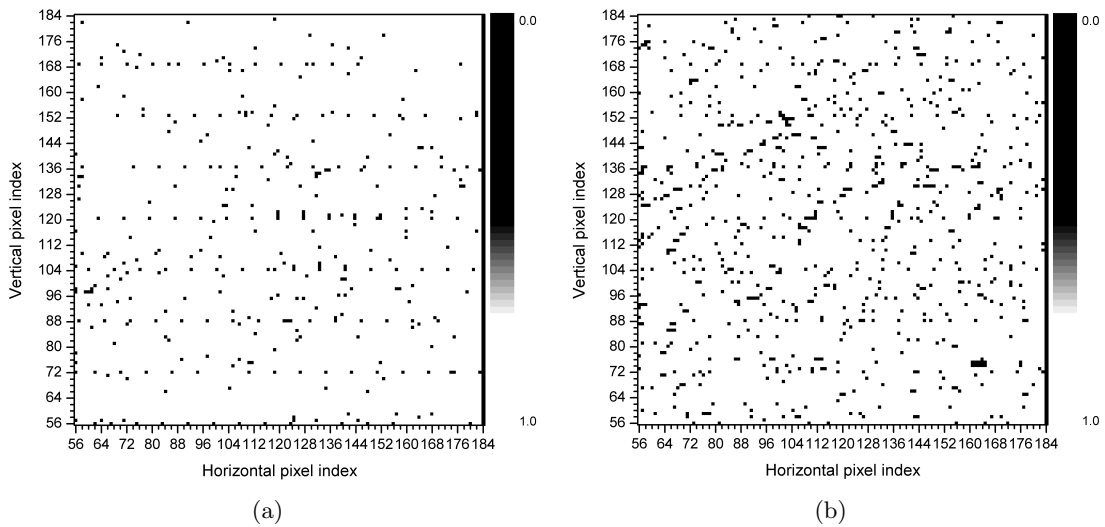


Figure 5.12.: Distribution of the bad pixels (black) based on the radiometric criterion for detector II/1 (a) and detector II/2 (b).

first scientific campaign flights (ESSenCe campaign). After the campaign detector II/2 had a technical problem such that it had to be sent to the manufacturer for repairing. As a result, detector II/1 was used to perform measurements during the second scientific campaign flights (TACTS and ESMVal campaigns).

### **Summary: Detector comparison**

The comparison between the detectors has been done by looking at the NEP. The results show that detector II/1a has pixels with high (poor) NEP values all over the array which makes it not suitable for atmospheric measurements. This detector was thus rejected and sent back to the manufacturer. Detector II/2 has pixels with a high NEP around the borders. These pixels have a higher noise and lower response as compared to the other inner pixels. The results of the analysis give a map of the good pixels over the detector array. The detector pixel area for the atmospheric measurements can be chosen freely from the central region. A further comparison considering the radiometric properties for the smaller area with  $128 \times 128$  pixels shows that the number of bad pixels in both detectors (II/1 and II/2) are about 2.8% and 5.6%, respectively. The stripe pattern in the vertical and horizontal directions due to noise are seen for both detectors but are weaker for detector II/2. Both detectors showed comparable NEP values (excluding the large number of bad pixels in the boundary area of detector II/2) and are accepted for performing atmospheric measurements.

## **5.2. Nonlinearity**

A photovoltaic Mercury-Cadmium-Telluride detector is used in GLORIA. The detector and its electronics is offered as integrated detector cooler assembly (IDCA, see section 3.4). Ideally, the output of a photovoltaic detector module should be a linear function of the incoming flux. However, in reality, this behavior can be nonlinear, based on either the detector itself or on the processing electronics like read-out circuit (ROIC), voltage amplifiers or analog-to-digital converters (ADCs). Nonlinearities in the available infrared detectors and in the electronics of the signal processing circuitry cause distortions in the measured interferogram, leading to artifacts in the spectrum. As a result the spectrum generated is inaccurate and corrections must be made in order to obtain a correct representation of the incident radiation distribution. Inappropriate correction of the nonlinearity effect would lead to a calibration error.

The detector system used in GLORIA exhibits a certain nonlinearity which is assumed to be caused by the electronic components of the detector. The measured IR signal is not directly proportional to the number of incident photons, especially at low and high signals. The nonlinear effect of the detector system leads to out-of-band artifacts in the spectrum falsely indicating the presence of energy in the wavenumber range where the detector is insensitive (figures 5.15, 5.16). A two point radiometric calibration approach which is being used in GLORIA is valid only if the measured interferograms are linear. The nonlinearity effect therefore has to be quantified and corrected prior to applying the two point radiometric calibration.

There are several methods of nonlinearity corrections proposed in literature [47–51]. The method used in this study (developed by Hilbert [50]) is found to be the best suited for GLORIA. The proposed method of the nonlinearity characterization requires DC measurements with different integration times (covering the dynamical range of the detector) while looking at a constant radiation source. The correction parameters are found from on-ground measurements and can be applied to any measurement performed on-ground or in-flight.

### Correction procedure

Fixed slide measurements have been performed on-ground looking at a constant radiation source (blackbody) which was placed inside the interferometer just in front of the entrance window. As a result, the blackbody has the same temperature as the interferometer when it is cooled. The measurements have been performed for a blackbody temperature of approximately 216 K and for several integration times covering the entire dynamical range of the detector. A low temperature was selected such that more data points can be selected within the dynamical range.

The idea of the nonlinearity correction method is to correct the measured nonlinear detector signal directly at each point of the interferogram using a correction factor appropriate to the intensity of a virtual linear detector at that precise point. The nonlinearity correction is applied to the raw interferogram. The detector response of the virtual detector is a linear function of the integration time. The linear detector scale is constructed for each individual pixel. Three measurement points are chosen from the middle region of the detector's dynamical range. A linear fit is performed to the selected measurement points. Equation 5.6 shows the expression of the linear scale.

$$DC_{lin} = a_0 + a_1 \times t_{int} \quad (5.6)$$

where  $a_0$  is the intercept,  $a_1$  is the slope and  $t_{int}$  is the detector integration time.

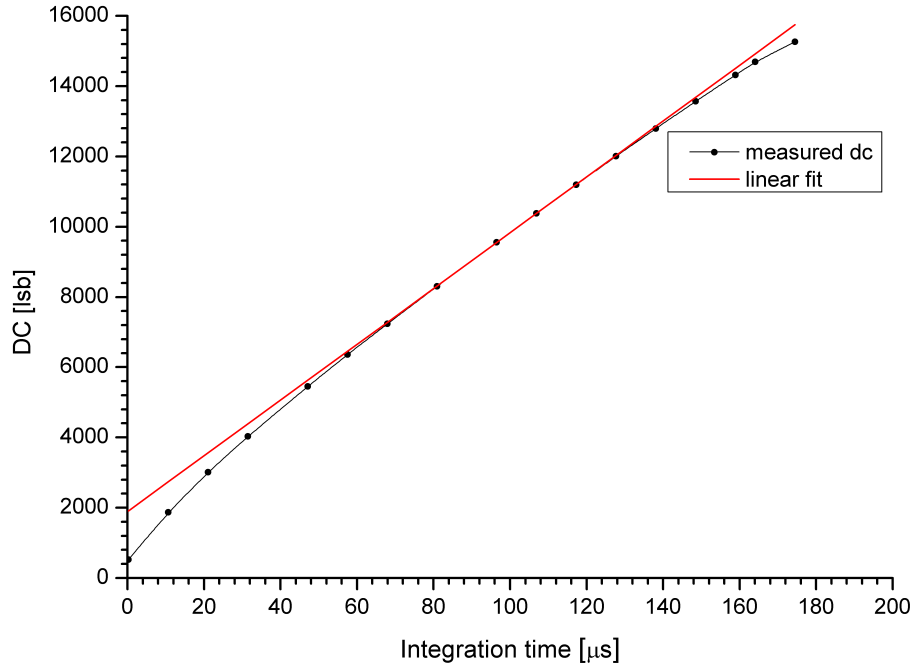


Figure 5.13.: Interferogram DC plot of a blackbody source measured at different integration times (black points) and a linear fit of the DC values over the range of the central three DC values (red line).

A linear DC scale is built as a function of the integration time using the coefficients of the linear fit  $a_0$  and  $a_1$ . Figure 5.13 shows a virtual linear DC curve (red line) based on the measurement DC values (black points) for a pixel (104,170) of detector II/2. The plot for the selected pixel is exemplary. The integration time of up to 180  $\mu\text{s}$  was selected because beyond this limit the corner pixels of the array reach the saturation level. The measured DC versus the linear DC for a given set of integration times is plotted in figure 5.14. A polynomial fit of 3rd, 4th, 5th, 6th and 7th order was fitted to the measurement points. The difference between the fit results of the 4th order and the 3rd order was higher as

compared to the difference of the 5th and 4th order fit results. A fourth order fit was sufficient as the difference between the fit results of the higher order fits did not differ significantly. The black points in figure 5.14 represent the data points and the black curve represents the fitted fourth order polynomial curve.

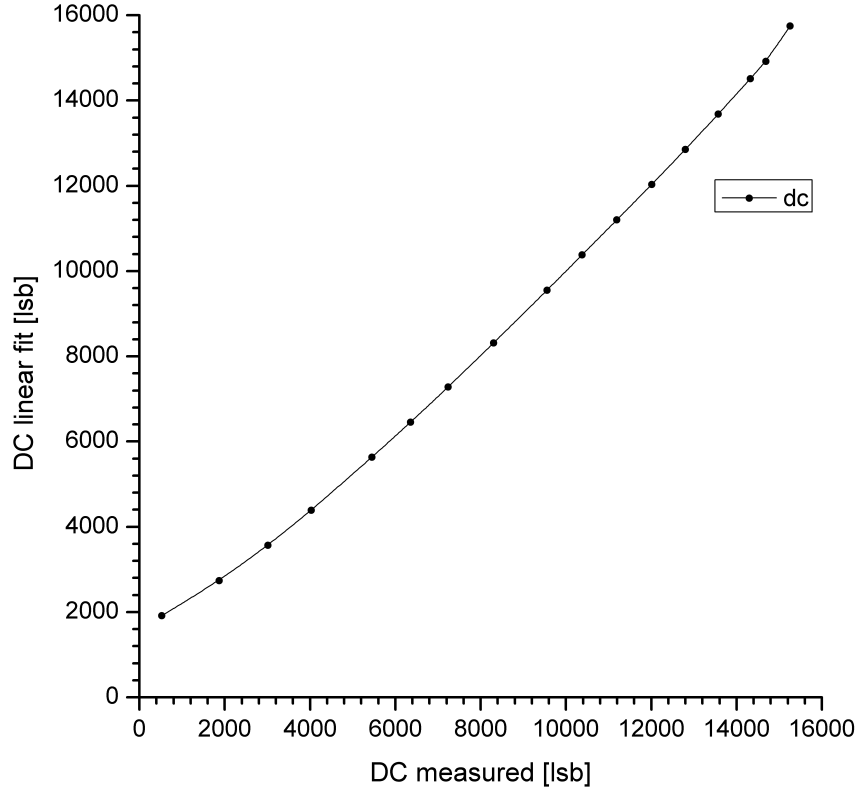


Figure 5.14.: DC linear plotted with respect to the measured DC for different integration times.

Each measurement point of an interferogram is mapped on the virtual linear detector, using the fourth order polynomial. The coefficients of the polynomial fit are represented as  $p_0, p_1, p_2, p_3$  and  $p_4$ . The corrected interferogram signal ( $I_{corr}$ ) is built up using the polynomial coefficients and the measured interferogram signal ( $I_m$ ) as follows

$$I_{corr} = p_0 + p_1 I_m + p_2 I_m^2 + p_3 I_m^3 + p_4 I_m^4 \quad (5.7)$$

The individual coefficients of each detector pixel are calculated from the laboratory measurements. In order to check the quality of the nonlinearity correction, at first the correction is applied to the in-flight blackbody measurements. These results are shown here. Later on, the correction was applied to all in-flight measurements. The detector integration time for the measurement was selected such that the DC value of the interferogram lies in the linear region of the curve in figure 5.13. This will result in a reduced nonlinearity effect as compared to the case when the interferogram was measured at the low or high end of the detector's dynamical range. In addition, it also reduces errors due to the inevitable imperfection of the nonlinearity correction method.

The nonlinearity correction is applied in two ways. First approach: The nonlinearity correction is applied to each pixel with the correction parameters calculated for this pixel. Second approach: The nonlinearity correction is applied to each individual pixel with the correction parameters of one exemplary pixel (a good pixel having a nonlinearity curve as the one shown in figure 5.17 - black curve). The nonlinearity correction coefficients following the second approach are calculated from the laboratory measurements for an

exemplary good pixel (102,170) of detector II/1 and pixel (104,170) of detector II/2. The coefficient values are listed in table 5.3. Using the coefficient values, a lookup table for the nonlinearity correction has been prepared which contains the scaling values for each possible measured interferogram value within the dynamical range. This correction table is used as an input while performing the level0 processing of the GLORIA data. A minimization of the artifacts is a good quality control for the nonlinearity correction.

Table 5.3.: Coefficients of the polynomial fit for performing a nonlinearity correction following the second approach.

Coefficient	Detector II/1	Detector II/2
P0	$1.4696225e^{+003}$	$1.678801498e^{+003}$
P1	$4.4685754e^{-001}$	$4.225276408e^{-001}$
P2	$7.6709233e^{-005}$	$8.238716565e^{-005}$
P3	$-4.8528599e^{-009}$	$-5.849532396e^{-009}$
P4	$1.2912459e^{-013}$	$1.687791339e^{-013}$

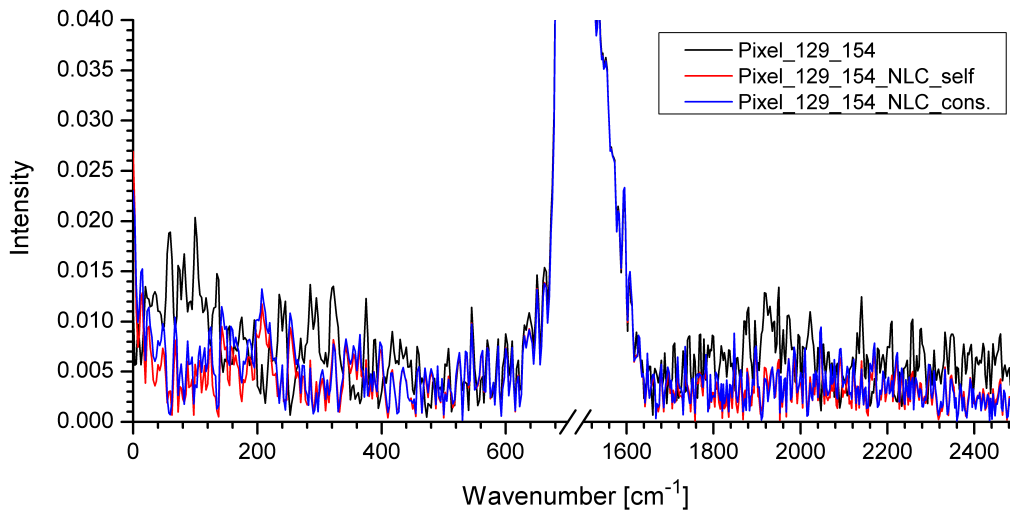


Figure 5.15.: Blackbody spectrum plot before (black) and after nonlinearity correction following the first (red) and the second (blue) ways for a single pixel (129,154) of detector II/1. The maximum of the spectrum is scaled to 1. The interferogram has a DC value of approximately 8520 lsb.

The magnitude spectrum for a single pixel (129,154) of detector II/1 before (black) and after the nonlinearity correction following the two approaches (red: First approach, blue: Second approach) is shown in figure 5.15. The maximum of the spectrum is scaled to one. The measurement data is from the TACTS campaign and was performed by looking at the GLORIA blackbody at about 245 K. The out-of-band artifacts below  $600 \text{ cm}^{-1}$  and above  $1600 \text{ cm}^{-1}$  are clearly seen in the uncorrected data (black curve). After the nonlinearity correction, the artifact signal in these spectral ranges is reduced and is dominated by noise only.

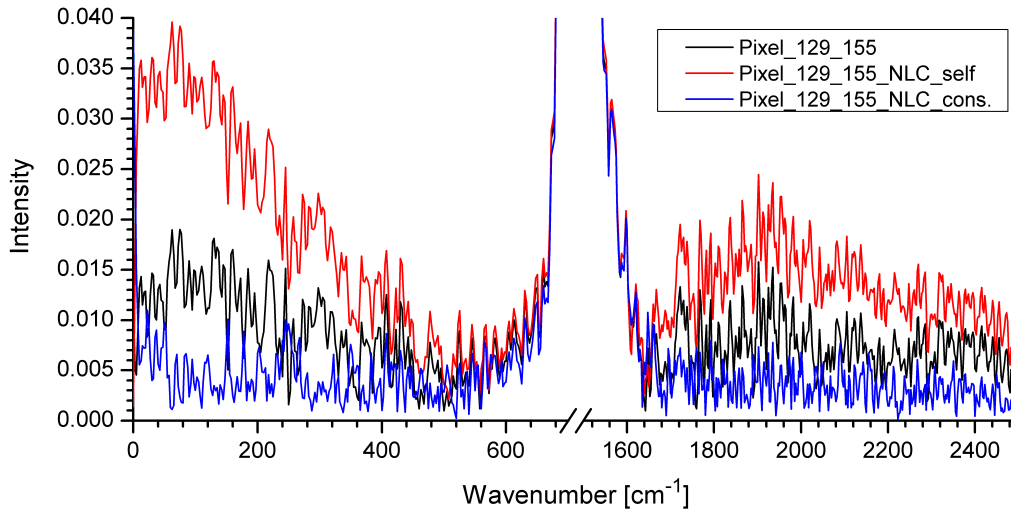


Figure 5.16.: Blackbody spectrum plot before (black) and after nonlinearity correction following the first (red) and the second (blue) ways for a single pixel (129,155) of detector II/1. The maximum of the spectrum is scaled to 1. The interferogram has a DC value of approximately 8355 lsb.

For some pixels, applying the correction using the coefficients of its own pixel (first approach) does not reduce their artifacts. Whereas, applying the correction factor of a good pixel manages to reduce the nonlinearity for those pixels. Figure 5.16 shows an example of such a pixel (129,155) of detector II/1. This pixel is the immediate neighbor of the pixel shown in figure 5.16. The nonlinearity correction following the first approach (red curve) shows an increase in the artifact in the out-of-band spectral regions, whereas the nonlinearity correction following the second approach (blue curve) shows a decrease in the artifact.

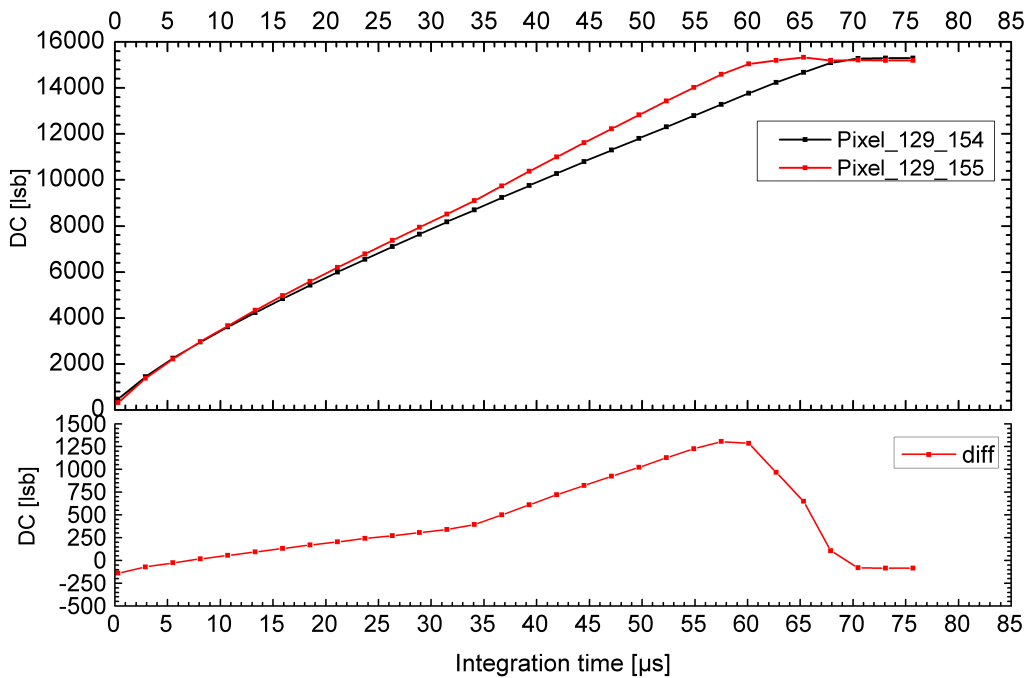


Figure 5.17.: Interferogram DC plots of a blackbody source measured at different integration times for two pixels (129,154) (black points) and (129,155) (red points) of detector II/1. The difference of the DC values for the two pixels are plotted below.

The interferogram DC plots with respect to the integration time for both pixels (129,154) (black) and (129,155) (red) of detector II/1 are shown in figure 5.17. The curve for the pixel (129,155) deviates from that of the pixel (129,154) as the integration time increases. The deviation is not constant or linearly increasing but shows a bump at higher DC values. The correction parameters found using the DC values for pixel (129,155) can therefore not reduce the nonlinearity whereas applying the correction parameters of the reference pixel can reduce the nonlinearity. The second approach is based on the assumption that the characteristic of the nonlinearity is pixel independent and the nonlinearity of all pixels can be corrected by using the parameters of a reference good pixel.

The nonlinearity correction following both approaches has been applied individually to all pixels of detector II/1 and II/2 ( $48 \times 128$  pixels) used for the measurement. The spectral intensity between  $20 \text{ cm}^{-1}$  and  $400 \text{ cm}^{-1}$  is taken for the quality control of the nonlinearity correction. The measurement data shown for detector II/1 and II/2 are from the TACTS and ESSenCe campaigns and were performed by looking at the GLORIA blackbody at about 245 K and 260 K, respectively.

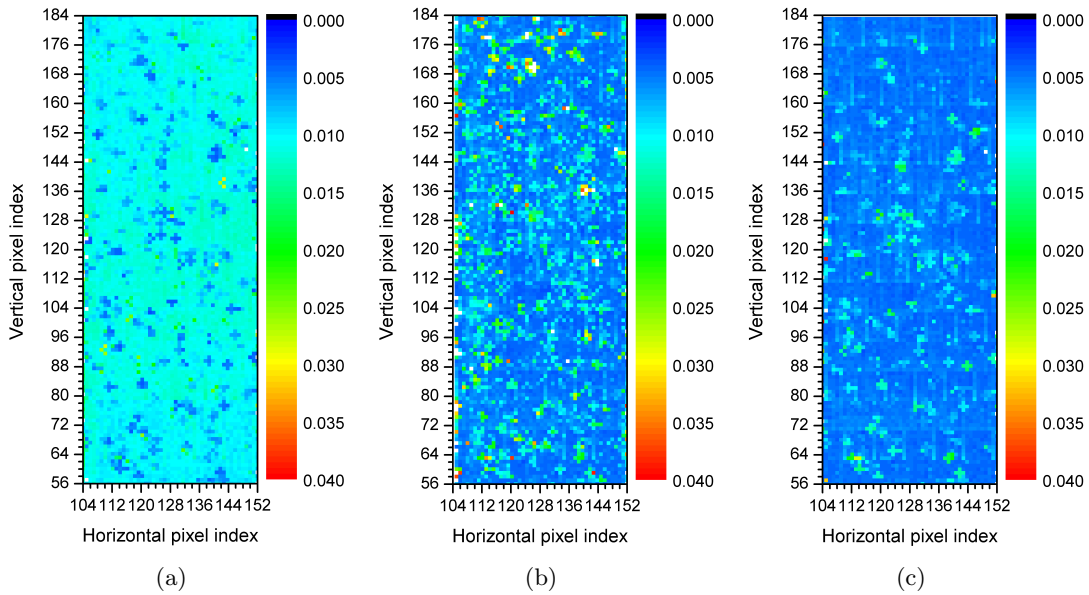


Figure 5.18.: Mean signal of a blackbody spectrum in the range between  $20 \text{ cm}^{-1}$  and  $400 \text{ cm}^{-1}$  without (a) and with a nonlinearity correction following the first approach (b) and the second approach (c) plotted for  $48 \times 128$  pixels of detector II/1. The maximum of the spectrum is scaled to one.

The mean of the blackbody spectrum in the range between  $20 \text{ cm}^{-1}$  and  $400 \text{ cm}^{-1}$  before (figure 5.18(a)) and after performing the nonlinearity correction following the first (figure 5.18(b)) and the second (figure 5.18(c)) approaches of applying the nonlinearity correction for  $48 \times 128$  pixels of detector II/1 are shown in figure 5.18.

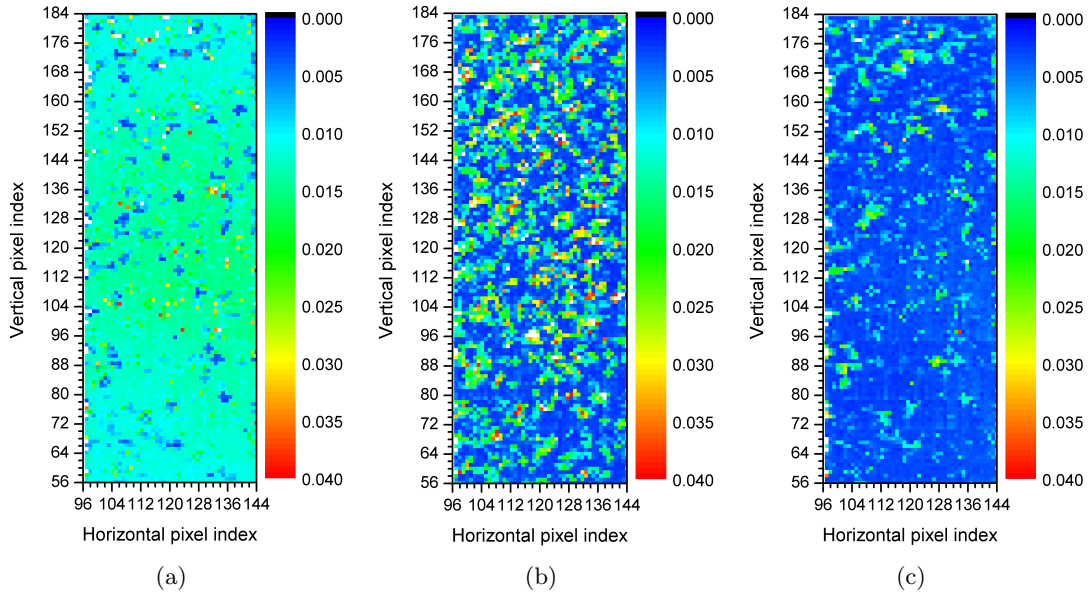


Figure 5.19.: Mean signal of a blackbody spectrum in the range between  $20\text{ cm}^{-1}$  and  $400\text{ cm}^{-1}$  without (a) and with a nonlinearity correction following the first approach (b) and the second approach (c) plotted for  $48 \times 128$  pixels of detector II/2. The maximum of the spectrum is scaled to one.

The mean of the blackbody spectrum in the range between  $20\text{ cm}^{-1}$  and  $400\text{ cm}^{-1}$  before (figure 5.19(a)) and after performing the nonlinearity correction following the first (figure 5.19(b)) and the second (figure 5.19(c)) approaches of applying the nonlinearity correction for  $48 \times 128$  pixels of detector II/2 are shown in figure 5.19.

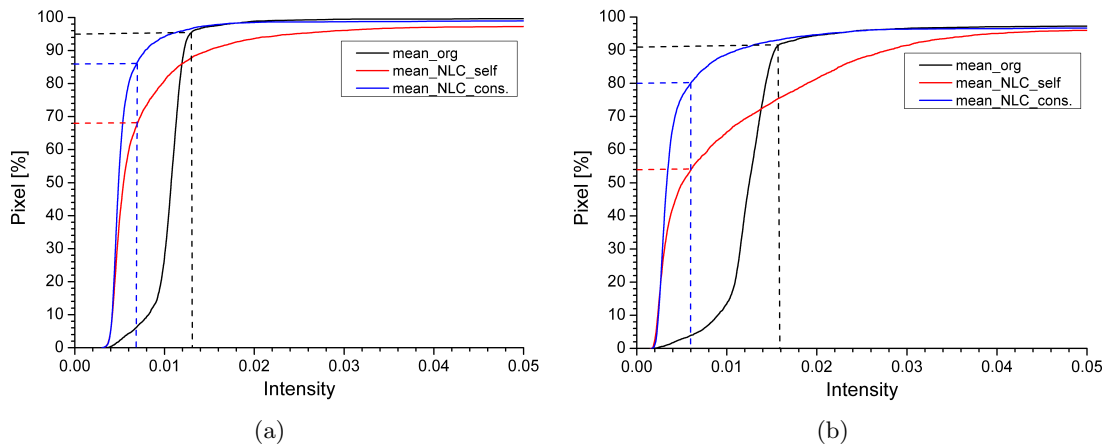


Figure 5.20.: Percentage of pixels plotted against the mean signal of the blackbody spectrum in the range between  $20\text{ cm}^{-1}$  and  $400\text{ cm}^{-1}$  before (black) and after performing the nonlinearity correction following the first approach (red) and the second approach (blue) for detector II/1 (a) and detector II/2 (b).

The pixels are arranged in the ascending order of their artifact intensity. Figure 5.20(a) and figure 5.20(b) show the plot of the artifact before (black) and after applying the nonlinearity correction following the first approach (red) and the second approach (blue). The threshold for the selection of the bad pixels is considered as the point where the curve bends and goes towards a plateau. The threshold selection is made by hand and is shown as dotted lines in figure 5.20. Selecting a threshold for the blue curve gives that

the correction did not work for about 14 % and about 20 % of the pixels for detector II/1 and II/2, respectively, following the second approach. These pixels show a very strange nonlinearity curve where even the application of this method fails and a different method of nonlinearity correction has to be applied. Considering the same intensity limit as set for the blue curve and by looking at the red curve (figure 5.20), it gives about 32 % and 46 % of the pixels which are beyond the selected limit. These pixels are having a higher value of artifact remaining after the nonlinearity correction following the first approach.

The comparison results of the nonlinearity correction following the two approaches for all pixels show that the correction is more precise following the second approach and the majority of the pixels can be corrected using this method. It is therefore chosen as the standard for the processing of the scientific data measured during the campaign flights and also for the laboratory measurements. The pixels for which the nonlinearity correction did not work have to be further investigated. Furthermore, during the analysis of the flight data it has been found that the nonlinearity has a coupling with the integration time and the photon flux. The stability and reproducibility of the nonlinearity behavior of the pixels over all flights is currently under investigation.

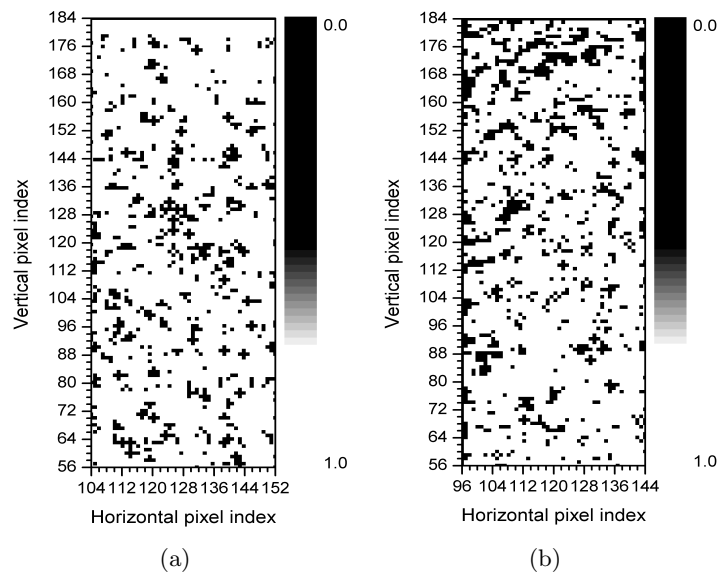


Figure 5.21.: Distribution of the bad pixels (black) based on the nonlinearity criterion following the second approach for detector II/1 (a) and detector II/2 (b).

The distribution of the bad pixels based on the nonlinearity criterion following the second approach for detector II/1 and detector II/2 is shown in figure 5.21(a) and figure 5.21(b), respectively.

### Summary: Nonlinearity

A nonlinearity correction method is presented, applied and tested with the in-flight measurements performed with the detectors II/1 and II/2. The correction parameters are derived from the DC measurements performed by looking at a constant radiation source for several integration times. The correction is applied to the flight data of the blackbody measurements with  $48 \times 128$  pixels. The nonlinearity corrected spectra are checked for the artifacts in the out-of-band spectral region. The mean signal of the artifacts is reduced after the nonlinearity correction with the residual of noise. About 14 % and 20 % of the pixels are identified for detector II/1 and II/2, respectively, where the nonlinearity correction did not work properly following the approach where the nonlinearity correction

of a good pixel is being used for performing the correction over the whole array and are considered as bad pixels. These pixels have to be revisited to better understand their nonlinearity behavior.

### 5.3. Noise analysis: Theoretical evaluation

Noise has a major impact on the output signal delivered by an infrared focal plane array (FPA). The noise may come from the FPA, the detector read out integrated circuit (ROIC), or from outside the detector unit. Some of the noise sources depend on the devices used, while some others are dependent on the operating conditions of the FPA and the ROIC. It is necessary to analyze the sources and their contribution to the total noise present in the measured infrared signal in order to control the noise contributions from the sources which are dependent on the operating conditions, thereby improving the output signal-to-noise ratio.

#### 5.3.1. Photon loads and dark current

In the process of the quantification of the noise it is necessary to inspect the different sources of electron loads on the detector. The detected signal is comprised of the electrons generated by the photons coming from the scene and the instrument background and the electrons generated by the dark current.

The photon flux ( $\phi_n$ ) from a blackbody source arriving on a given area ( $A_{pix}$ ) and a given solid angle ( $\Omega_{pix}$ ) is calculated as

$$\phi_n(\sigma, T) = \frac{L(\sigma, T)}{E_{ph}(\sigma)} A_{pix} \Omega_{pix} \quad (5.8)$$

where  $E_{ph}(\sigma) = h_p c \sigma$  is the photon energy and  $L$  is the Planck function.

The number of electrons per second ( $\dot{N}_{p,scene}$ ) generated by the photons arriving from the scene at a given temperature ( $T_s$ ) to the detector is calculated as the integral of the photon flux over the detectable spectral range.

$$\dot{N}_{p,scene} = \int_{\sigma_1}^{\sigma_2} \eta(\sigma) \tau(\sigma) \phi_n(\sigma, T_s) d\sigma \quad (5.9)$$

where  $\eta(\sigma)$  is the detector quantum efficiency (section 5.5.5) and  $\tau$  is the instrument transmission (section 5.5.2).

The number of electrons per second ( $\dot{N}_{p,bg}$ ) generated by the photons arriving from the instrument background at a given temperature ( $T_{bg}$ ) and the instrument emissivity ( $\epsilon_{bg}$ ) to the detector is calculated as the integral of the photon flux over the detectable spectral range.

$$\dot{N}_{p,bg} = \int_{\sigma_1}^{\sigma_2} \eta(\sigma) \epsilon_{bg} \phi_n(\sigma, T_{bg}) d\sigma \quad (5.10)$$

The total number of electrons recorded as a result of the photons arriving at the detector from the scene and the instrument background for a given integration time ( $t_{int}$ ) is calculated as

$$N_p(t_{int}) = (\dot{N}_{p,scene} + \dot{N}_{p,bg}) t_{int} \quad (5.11)$$

In addition to the electrons generated from the photons, a dark current ( $I_D$ ) is generated by the electrons detected over time which is independent of the radiance falling on the detector. The dark current arises from the thermal energy causing an excitation of the energy level of the electrons, such as to cross the barrier potential and enter into the conduction band. The dark current for the second generation AIM detectors used for

GLORIA was measured by AIM. The median of the dark current measured could be represented as a function of  $1/(\lambda_c T_d)$ , where  $\lambda_c$  is the detector cutoff wavelength expressed in  $\mu\text{m}$  and  $T_d$  is the detector temperature expressed in K. The dark current measured can be approximated by an exponential fit expressed as [28]

$$I_D = C_{det} e^{\frac{-C_E}{k_B T_d \lambda_c}} \quad (5.12)$$

where the factor  $C_{det} = 30000 \text{ A cm}^{-2}$  is specific to this detector type,  $C_E = 1.24 \text{ eV } \mu\text{m}$ ,  $k_B = 8.62 \times 10^{-5} \text{ eV K}^{-1}$  is the Boltzmann constant. The numerator of the exponential of the equation 5.12 is equivalent to the product of  $h_p$  and  $c$  and is represented as the ground energy of the electron at the cutoff wavelength. The dark current can be written as

$$I_D = C_{det} e^{\frac{-E_g}{k_B T_d}} \quad (5.13)$$

where  $E_g = h_p c / \lambda_c = h_p c \sigma_c$ . A typical value of the detector dark current for a pixel area of  $40 \mu\text{m}^2$  at a temperature of 59 K and at a cutoff wavenumber of  $780 \text{ cm}^{-1}$  is 2 nA.

The number of electrons recorded as a result of the dark current ( $I_D$ ) is given by

$$N_D(t_{int}) = \frac{I_D t_{int}}{q} \quad (5.14)$$

where  $q = 1.602 \times 10^{-19} \text{ C}$  is the charge of the electron.

The total signal recorded by the detector as a function of the detector integration time for a given measurement is calculated as

$$DC(t_{int}) = (N_p(t_{int}) + N_D(t_{int})) \frac{2^{Nb}}{Q_{fw}} \quad (5.15)$$

where  $2^{Nb}/Q_{fw}$  is the scaling factor to convert DC values to lsb units,  $Nb = 14$  is the detector quantization level,  $2^{Nb}$  is the dynamic range of the analog to digital converter and  $Q_{fw} = 2.326 \times 10^7$  is the detector full well capacity.

### 5.3.2. Noise sources

The major noise sources in the combination of a photovoltaic detector and the associated electronics are the photon noise, the detector dark current noise, the Johnson noise, the kTC noise, the preamp noise and the quantization noise. These noise sources are discussed here. All these noise contributions are independent. The resulting total noise is given by the square root of the sum of the individual noise squares.

The block diagram of a single detector pixel and a simplified detector readout electronics used in GLORIA are shown in figure 5.22. The output of every detector pixel (indicated as OUT1, OUT2, ...) has to pass through a series of electronic components (e.g. preamp, ADC converter, multiplexer) as shown in the figure 5.22(b). The detector is operating in stare while scan mode (SWS). The principle of operation in this mode is such that the capacitor C1 is used for the integration of the signal charge, while the capacitor C2 is used as an in-pixel sampling capacitor. The sampling of the signal is controlled by the clock pss1. The integration period is identical for all pixels in the array. A group of eight pixels is read at once in the vertical direction of the detector array. In this operational mode the signal of a pixel is read out from the capacitor C2, while the signal for the next frame is integrated in the capacitor C1.

The **photon noise** arises from the fundamental statistical nature of the arrival of the photons coming from the source and the background at the detector surface. The photon noise is calculated as

$$\nu_p(t_{int}) = \sqrt{N_p(t_{int})} \frac{2^{Nb}}{Q_{fw}}. \quad (5.16)$$

The photon noise is dependent on the signal, the background and the integration time.

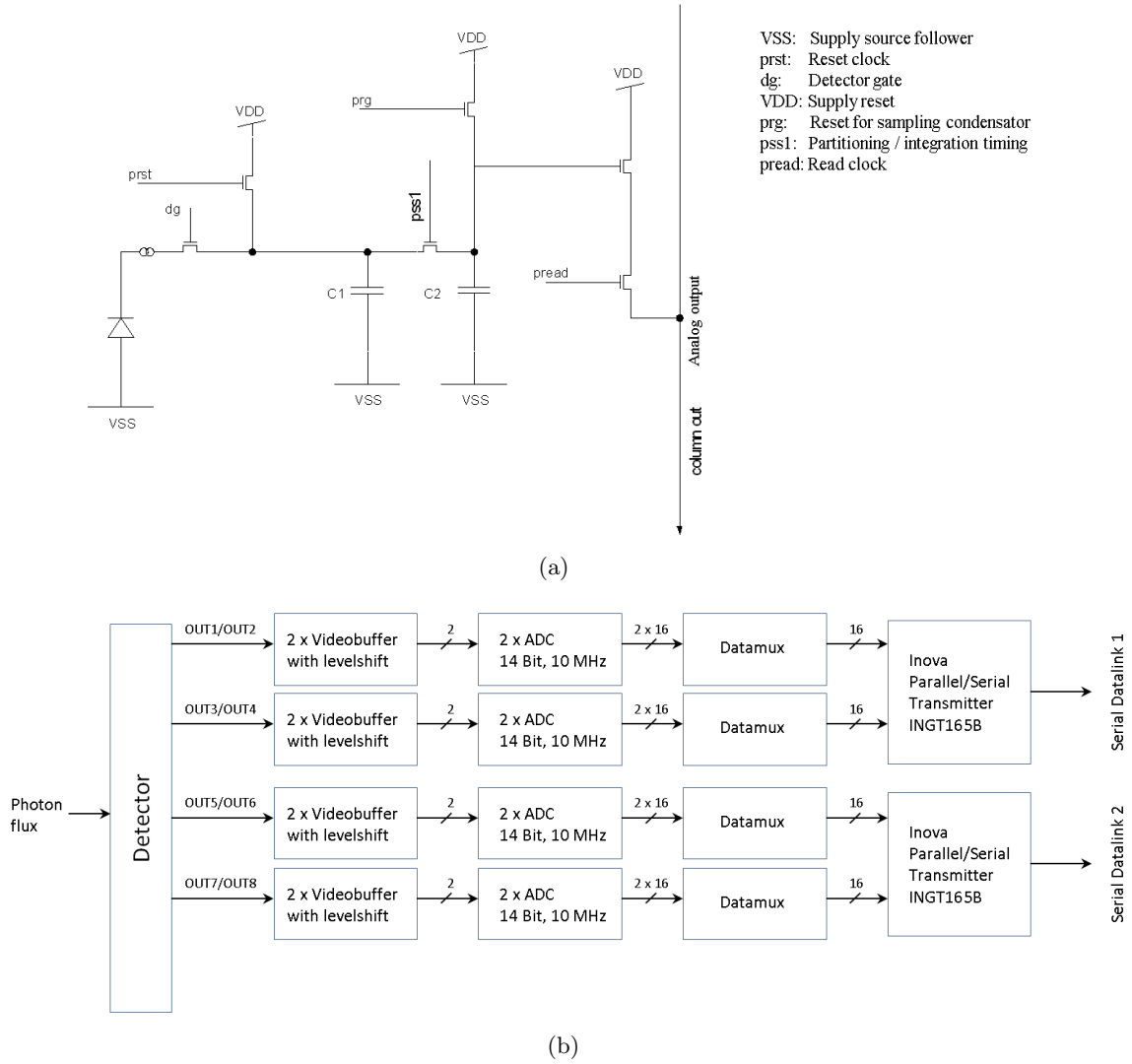


Figure 5.22.: (a) Block diagram of a detector pixel and (b) a simplified detector readout electronics [52, 53].

The **dark current noise** is associated with the dark current flow in the detector across the potential barrier. The current flow across the junction is not smooth but random. This random distribution of the charge carriers due to the dark current flow is the source of the dark current noise. The current flowing through the resistors does not have this noise. The dark current noise is a function of the integration time and is calculated as

$$\nu_D(t_{int}) = \sqrt{N_D(t_{int})} \frac{2^{Nb}}{Q_{fw}}. \quad (5.17)$$

The **Johnson noise** is referred to the fluctuation caused by the thermal motion of the charge carriers in a resistive element. The Johnson noise voltage is defined as [54]

$$V_J = \sqrt{4k_B T_d R \Delta f}. \quad (5.18)$$

where  $\Delta f$  is the bandwidth (Hz) and  $R$  is the circuit resistance.

The Johnson noise voltage is directly proportional to the square-root of the circuit resistance. The noise contribution due to the Johnson noise is much smaller than the photon noise. The detector zero biased resistance ( $r_{det} = 6.17 \times 10^7$  ohm) characterizes the resistance of the detector pixel. The noise contribution is calculated for the  $r_{det}$ . Noise

contributions from the other resistance elements are smaller in the circuit and they cannot be calculated exactly due to lack of knowledge about the resistors. The Johnson noise across the detector in terms of the electron fluctuation for a given time interval  $t_{int}$  is calculated as

$$\nu_J(t_{int}) = \frac{\sqrt{4k_B T_d(t_{int}/r_{det})}}{q} \frac{2^{Nb}}{Q_{fw}}. \quad (5.19)$$

The **kTC noise** is referred to the fluctuation caused by the thermal motion of the charge carriers via a capacitor. The capacitors must be reset after the data is read out from the buffer. The kTC noise is introduced during this reset process. The noise term is called kTC because of its dependence on the three terms  $k_B$ ,  $T$  and  $C_s$  (is the specific detector element capacity having a value of  $2.3 \times 10^{-15}$  F  $\mu\text{m}^{-2}$ ). The kTC noise can be calculated as [55]

$$\nu_{kTC} = \frac{\sqrt{k_B T_d C_s A_{pix}}}{q} \frac{2^{Nb}}{Q_{fw}} \quad (5.20)$$

The kTC noise is a one time value occurring during the signal readout and is therefore independent of the integration time.

The **preamp noise** is generated by the preamplifier which is used to provide an amplification to the signal being read from the detector.

The **quantization noise** is present in the quantization of the signal amplitude and occurs while performing the analog-to-digital conversion of the signal. The noise is independent of the signal. The quantization noise is given as [56]

$$\nu_q = \frac{1}{\sqrt{12}} \quad (5.21)$$

The detector electronics is a network of different resistors and capacitors. The noise coming from the random thermal motion of the charge carriers through this network cannot be sensibly estimated without a deep knowledge of the properties of the ROIC. The detailed information about the ROIC is not disclosed by the supplier. The noise contributions which are independent of the integration time (kTC noise, preamp noise and quantization noise) are estimated empirically from the noise determined from the measurement (see section 5.4.2). The combined noise which is independent of the integration time is named as the constant noise ( $\nu_{constant}$ ).

The **total noise** is calculated as

$$\nu_{tot}(t_{int}) = \sqrt{\nu_p(t_{int})^2 + \nu_D(t_{int})^2 + \nu_J(t_{int})^2 + \nu_{constant}^2}. \quad (5.22)$$

## 5.4. Noise analysis: Measurement evaluation

In this section, laboratory measurement data is analyzed and both the DC and noise are evaluated. The noise model is tuned to the measurement values. The instrument emissivity and the constant noise term are estimated from the fit result.

### Measurement setup for DC and noise

DC measurements were performed with the full interferometer with a fixed slide looking at a blackbody placed inside the interferometer in front of the entrance window. The measurements were performed at two instrument temperatures of 219 K and 258.5 K, such that the noise model can be validated at both low and high temperatures. The blackbody being placed inside the interferometer has approximately the same temperature as the interferometer. The detector II/2 was configured to a  $128 \times 128$  pixel array with an offset

of (56,56 (pixels in horizontal, vertical direction)) (configuration 2 of table 5.2). The data was recorded for several detector integration times. Measurements with five integration times covering the dynamical range of the detector, for both hot and cold instrument temperatures, were used for the DC and noise analysis.

#### 5.4.1. DC analysis from fixed slide measurements

The DC of a pixel is represented by the mean of the values of the measured frames of the pixel in a cub file. If  $x_i$  represents the individual signal value for the  $i^{th}$  frame, where  $i$  is ranging from 1 to  $N$ , the DC is calculated as follows

$$DC = \frac{1}{N} \sum_{i=1}^N x_i \quad (5.23)$$

The DC has the unit of lsb. The mean and the standard deviation of the DC values are calculated over the  $128 \times 128$  detector pixel array. The detector signal shows a nonlinear behavior with the integration time (section 5.2). The measurement values are therefore corrected for nonlinearity and are compared with the theoretically expected values. The expected DC to be recorded by the detector for the same source temperature, instrument temperature and integration time is calculated using equation 5.15 and tuning the parameters like integral detector quantum efficiency and instrument emissivity.

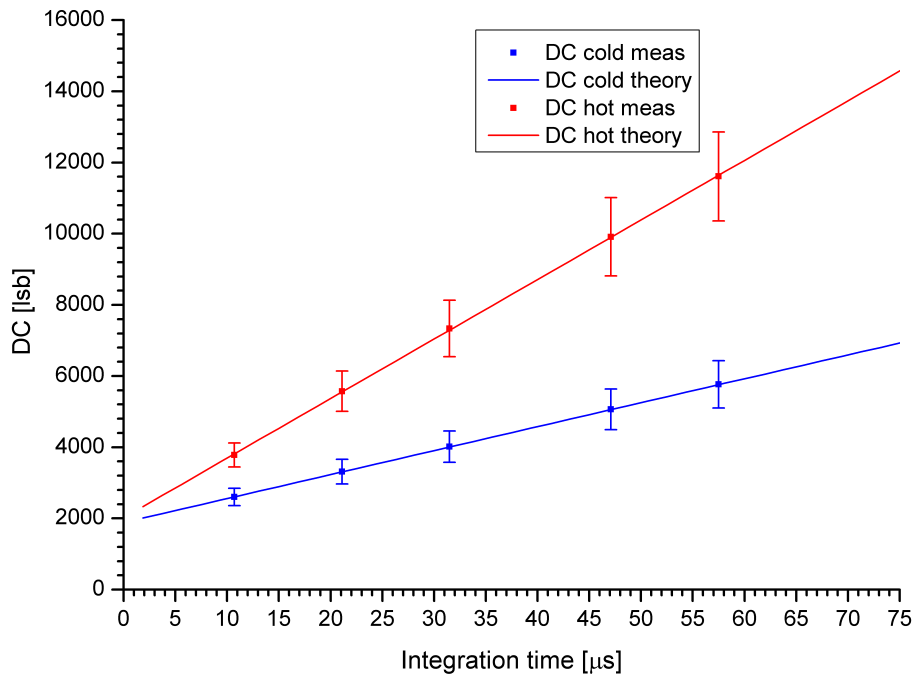


Figure 5.23.: The mean DC plot showing measurement (filled squares) and theoretically calculated (lines) values for detector II/2 using a  $128 \times 128$  pixel array for a cold (blue) and a hot (red) blackbody at 219 K and 258.5 K, respectively. The vertical bars corresponding to each mean DC value represent the variability of the measured DC values over the pixel array.

The mean DC plot as filled squares and the variability of the DC values over the  $128 \times 128$  pixels as vertical bars for cold (blue) and hot (red) blackbody temperatures, respectively, are shown in figure 5.23. The lines (figure 5.23) represent the theoretically calculated DC values at different integration times for both blackbodies. The theoretically expected DC values calculated using equation 5.15 are adjusted to the measurements values. The fit

parameters found are an integral detector quantum efficiency ( $\eta$ ) of 0.76 and an instrument emissivity of 0.55 ( $1 - \text{mean}(\tau(\sigma))$ ). The theoretically calculated curve matches the measurement values well for both temperatures.

#### 5.4.2. Noise analysis from fixed slide measurements

The noise from the measurement data is determined by calculating the standard deviation of 1000 frames of a cub file.

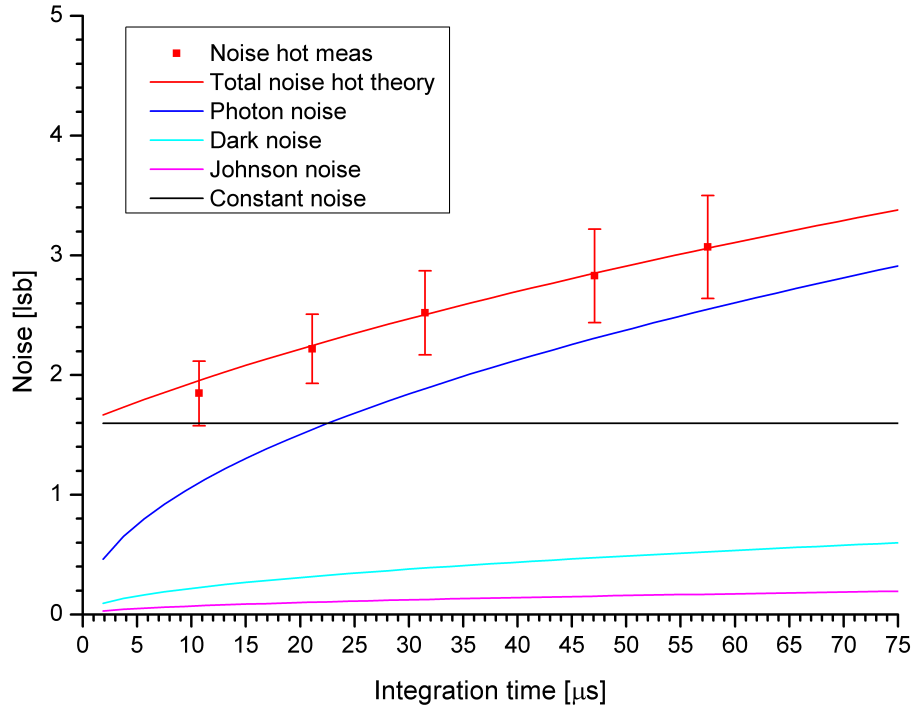


Figure 5.24.: The noise plot shows measured (filled squares) and theoretically calculated (lines) values for detector II/2 using a 128x128 pixel array for a hot blackbody at 258.5 K. The vertical bars corresponding to each mean noise value represent the variability of the measured noise values over the detector array. The theoretical predictions for the individual noise components are shown as lines.

The mean of the measured noise (filled red squares) and its variability (vertical bars) over the  $128 \times 128$  pixels calculated at five different integration times from the blackbody measurements at 258.5 K are shown in figure 5.24. The noise distribution over the detector array is supposed to be statistical in nature and follow a gaussian distribution, neglecting some of the pixels affected by the electromagnetic compatibility (EMC) problem (see figure 5.2(b)). The variability of the measured noise values is due to the presence of the EMC problem of the individual ADCs and the high noise for some of the ADCs and the preamps. This will lead to the presence of a correlated noise over the detector array (see figure 5.2(a)). The pixels which have noise values greater than a threshold of twice the median were rejected for the mean calculation. About 6 % of pixels were rejected for each measurement case. The measurement noise values are to be compared to the theoretical estimate of the noise contributions from different sources calculated using equation 5.22 and for the same measurement conditions. As the theoretical estimate of the noise is a representation for the average of the detector pixels, removing of the extreme bad pixels from the measurement data set is therefore justified. The theoretical estimate of the noise contributions from the photon noise, the dark current noise, the Johnson noise are calculated and plotted in figure 5.24. The constant noise term (a combination of the kTC noise, the preamp noise and the quantization noise) is estimated empirically from the

measurement such that the theoretical value of the total noise (red curve) matches with the measurement noise values. The constant noise term is shown as black curve. The plot shows that the photon noise and the constant noise (major contribution from the preamp noise) are the primary dominant noise sources for GLORIA. The photon noise is strongly dependent on the detector integration time. It equals the constant noise after a certain integration time (21.5  $\mu$ s in this case), thereafter the photon noise overpasses the constant noise term.

## 5.5. Spectral features of the detector and instrument parameters

In this section the spectral dependence of the detector and the instrument parameters are investigated. Interferometric measurements were performed by looking at the GLORIA blackbodies. The results shown in this section are from the characterization measurements performed on-ground just before the maiden flight of GLORIA and also from the measurements performed during flight.

The spectrum recorded by a Michelson interferometer is represented as [18] (adapted)

$$S(\sigma, T) = \frac{1}{2} A_{pix} \Omega_{pix} M \tau(\sigma) R_D(\sigma) L(\sigma, T) \quad (5.24)$$

where

- $S$  is the spectrum,
- $A_{pix}$  is the pixel area,
- $\Omega_{pix}$  is the pixel solid angle,
- $M$  is the Modulation efficiency,
- $\tau$  is the instrument transmittance,
- $R_D$  is the detector response,
- $L$  is the spectral radiance,
- $T$  is the temperature of the blackbody.

### 5.5.1. Instrument response

The instrument response is defined as the ratio of the change in output signal to the change in input signal. It is determined from the blackbody measurements performed at two different temperatures and calculated as

$$R_{inst}(\sigma) = \frac{S_{bbh}(\sigma) - S_{bbc}(\sigma)}{L_{bbh}(\sigma) - L_{bbc}(\sigma)} \quad (5.25)$$

where

$S_{bbh}(\sigma)$ ,  $S_{bbc}(\sigma)$  are the magnitudes of the spectral intensity of the hot and cold blackbodies,

$L_{bbh}(\sigma)$ ,  $L_{bbc}(\sigma)$  are the spectral radiances corresponding to the hot and cold blackbodies.

The instrument response ( $R_{inst}$ ) can be expressed in terms of the detector response as (calculated from equation 5.24)

$$R_{inst}(\sigma) = \frac{\Delta S(\sigma, T)}{\Delta L(\sigma, T)} = \frac{1}{2} A_{pix} \Omega_{pix} M \tau(\sigma) R_D(\sigma). \quad (5.26)$$

The spectral dependency of the detector response can be calculated from the spectral dependency of the instrument response, knowing the modulation efficiency, instrument transmittance, pixel area and pixel solid angle. These parameters are calculated in the following sections.

The instrument response is calculated from on-ground measurements, performed just before the first flight, by looking at the two GLORIA blackbodies at hot (300.1 K) and cold (275.3 K) temperatures using detector II/2. The cold blackbody could only be cooled to  $-30\text{ }^{\circ}\text{C}$  below the ambient temperature and the hot blackbody could only be heated to 300.1 K in relation to the cold blackbody. The calculation is done with a spectral resolution of  $2.5\text{ cm}^{-1}$  and a detector integration time of  $34.1\text{ }\mu\text{sec}$ .

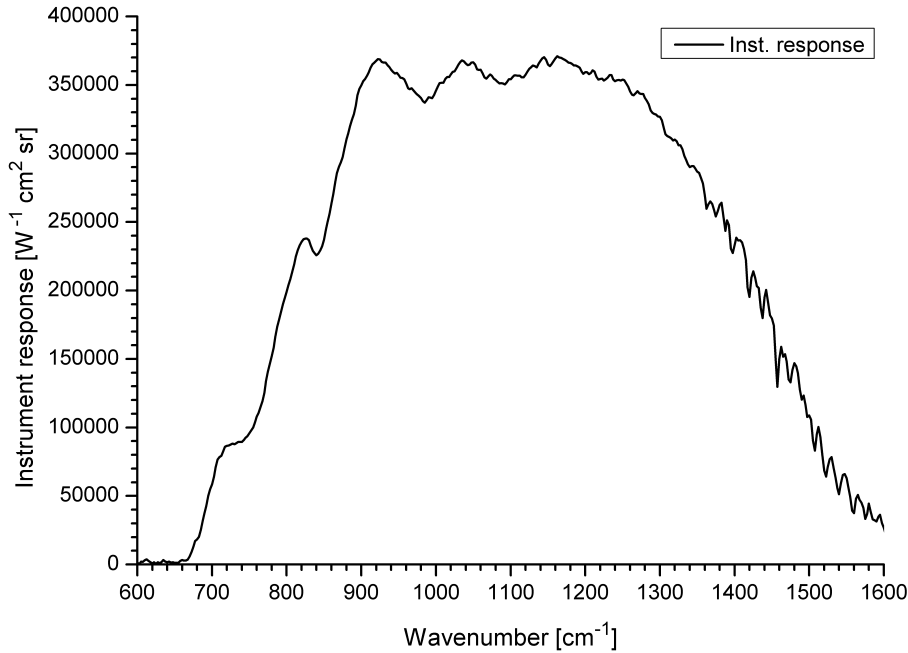


Figure 5.25.: The instrument response curve for pixel (119,121) from on-ground measurements looking at the GLORIA blackbodies at hot (300.1 K) and cold (275.3 K) temperatures using detector II/2.

The calculated instrument response for a single pixel (119,121) as a function of wavenumber is shown in figure 5.25. The pixel selected is an exemplary pixel which represents the median value of the distribution. The response value is almost constant in the spectral range around  $900\text{ cm}^{-1}$  to  $1300\text{ cm}^{-1}$  but falls rapidly outside this range. For example, the response value falls by 50 % of the maximum value at  $800\text{ cm}^{-1}$ . The wiggles seen in the response curve occurring at a period of approximately  $110\text{ cm}^{-1}$  are giving evidence of a Fabry-Perot effect due to multiple reflections inside the detector substrate. All other optical components are wedged to avoid channeling. The response curve above  $1400\text{ cm}^{-1}$  falls rapidly because of the fact that the instrument transmittance also falls rapidly in this wavenumber region (see figure 5.26). The soft increase in the instrument response curve in the lower wavenumber range is due to the detector response particular to the detector material and will be addressed in section 5.5.4.

The 2D distribution of the mean of the instrument response calculated over the spectral range from  $780\text{ cm}^{-1}$  to  $1400\text{ cm}^{-1}$  is shown in figure 5.27(b). The plot shows that the response distribution is roughly constant over the detector array with the exception of having low response values for the lower most detector rows. This feature is particular to this measurement setup where the detector might have been looking at the edge of the blackbody. In general the response calculated from the flight data does not show low values in the lower most detector rows. In addition, figure 5.27(b) shows some pixels which are outliers (black and yellow points). These pixels are to be handled carefully during the scientific data processing and checked for rejection as bad pixels.

### 5.5.2. Instrument transmission

The transmittance curves for the optical components of GLORIA such as entrance window, the detector window, the beamsplitter, lens1 and lens2 are shown in appendix A. The coatings of some of the components (e.g., beamsplitter surfaces) are not disclosed by the provider. The transmittance of these surfaces are assumed. The instrument transmittance is calculated by considering the radiation passing through the individual optical surfaces, starting at the entrance window until finally arriving at the FPA. An estimate of the total transmittance of the GLORIA interferometer is plotted in figure 5.26. The transmittance is a function of wavenumber, the dips in the lower wavenumber region is due to the absorption at the entrance window and the quick fall beyond  $1400\text{ cm}^{-1}$  is due to the transmittance curves of the lenses. The derivation of the total transmittance is shown in appendix A.

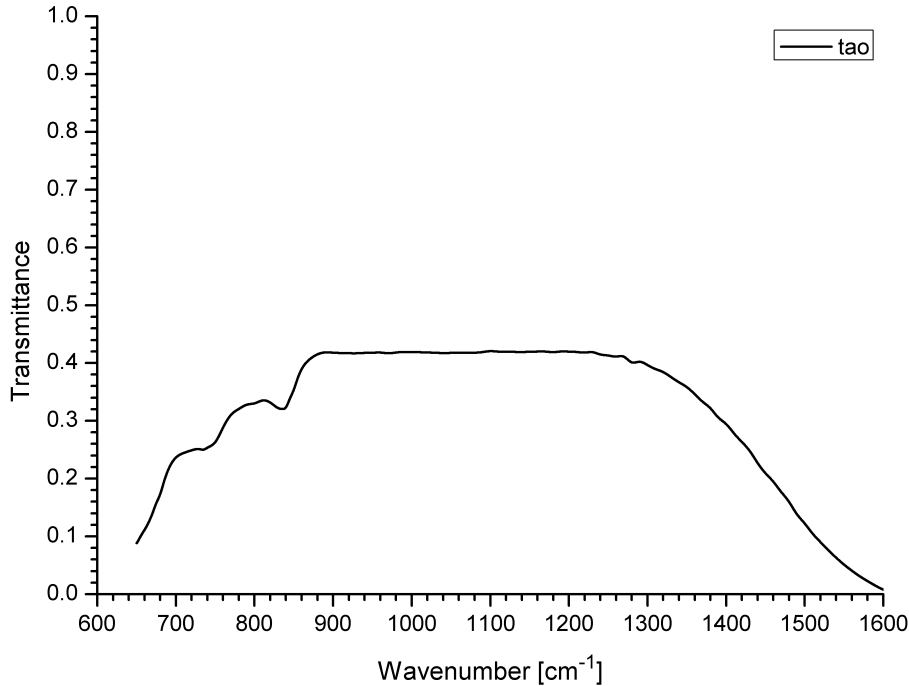


Figure 5.26.: Transmittance curve for GLORIA.

### 5.5.3. Modulation efficiency

Modulation efficiency ( $M$ ) is the figure of merit for the optical quality of the introduced parameters. It is a quantity with unit one. A high modulation is desired because the measured signal is directly proportional to it. Several physical parameters like the quality of the optical components, the quality of the interferometer drive and the degree of misalignment of the components in the interferometer play a role for the modulation efficiency. It is a wavenumber dependent quantity, with its value decreasing with increasing wavenumber. The modulation value at a higher wavenumber (or short wavelength) is very sensitive to the quality of the optical components (such as surface roughness). With the measurement setup used, only a mean modulation over the spectral range can be determined. When measuring a hot and a cold blackbody as source, the modulation efficiency can be calculated as

$$M = \frac{\max(I_{bbhac}) - \max(I_{bbcac})}{\text{mean}(I_{bbh}) - \text{mean}(I_{bbc})} \quad (5.27)$$

where

$M$  is the modulation efficiency,

$I_{bbhac}$  is the ac coupled interferogram of the hot blackbody,

$I_{bbac}$  is the ac coupled interferogram of the cold blackbody,  
 $I_{bbh}$  is the dc coupled interferogram of the hot blackbody,  
 $I_{bbc}$  is the dc coupled interferogram of the cold blackbody.

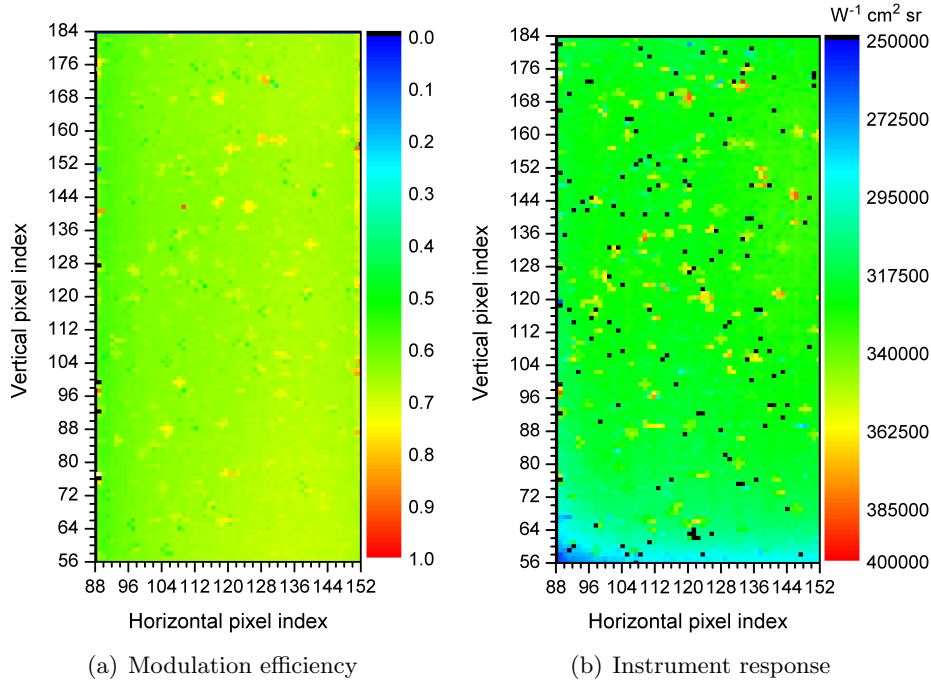


Figure 5.27.: (a) The modulation efficiency and (b) the mean instrument response in the range of  $780\text{ cm}^{-1}$  to  $1400\text{ cm}^{-1}$  are plotted over the  $64\times 128$  detector pixel array for detector II/2. The calculation is done using blackbody measurements performed at hot and cold temperatures. The instrument response has the units of  $\text{W}^{-1}\text{cm}^2\text{sr}$ .

The modulation efficiency is calculated from an ac and a dc coupled interferograms of two blackbody measurements at hot (300.1 K) and cold (275.3 K) temperatures and is plotted over the detector array (figure 5.27(a)). The measured interferogram is dc coupled (see figure 2.2(a)). A linear fit is calculated and subtracted from the interferogram to get the ac coupled interferogram. The linear fit eliminates the slowly varying drifts in the interferogram over OPD. The plot shows that the modulation efficiency distribution is roughly constant over the detector array. The right side of the array shows a slightly higher value than the left side. Modulation is an interferometer property and cannot change fast from pixel to pixel. If at all, a rather smooth change is expected over the detector array. The outlier pixels showing individual high and low values of modulation efficiency are a reflection of the individual pixel response of the detector. The mean modulation efficiency over the detector array is 0.7.

#### 5.5.4. Detector response

The detector response is a measure of the sensitivity of the detector. It can be calculated using equation 5.26 and with the knowledge of the instrument response, modulation efficiency and instrument transmission derived earlier.

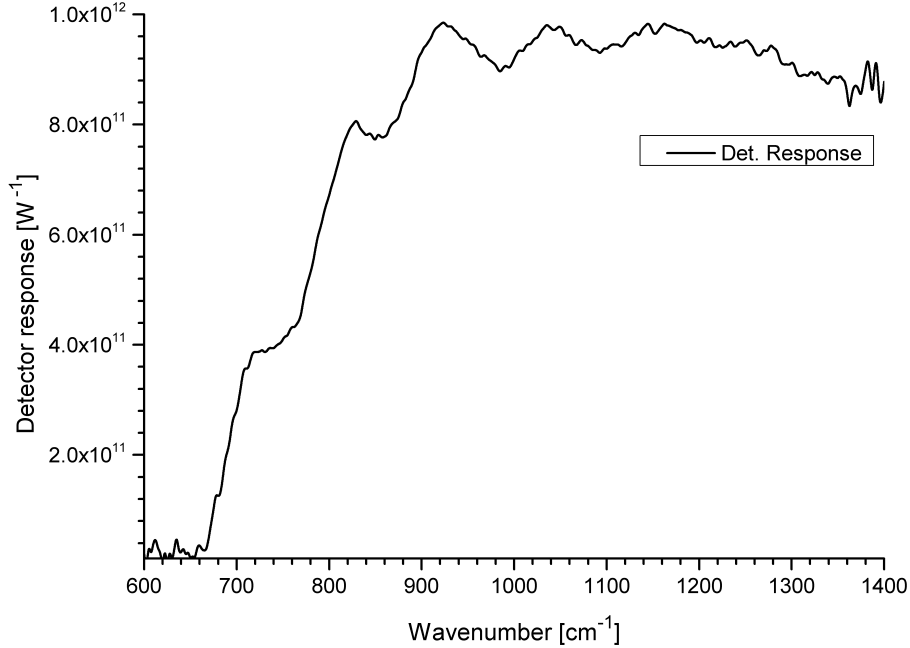


Figure 5.28.: Detector response for pixel (119,121) of detector II/2. The measurement was done for a detector integration time of 34.1  $\mu\text{s}$ .

The detector response for pixel (119,121) of detector II/2 plotted as a function of wavenumber is shown in figure 5.28. The same data set as used for the calculation of the instrument response is also used here. The detector response value beyond the cutoff wavenumber shows a soft increase until about 900  $\text{cm}^{-1}$ . This effect is a property of the alloy of the detector material and this curve is specific to the pixel of this detector. The detector response values above 1400  $\text{cm}^{-1}$  are not shown because the total transmittance curve (figure 5.26) above 1400  $\text{cm}^{-1}$  falls rapidly and is going close to zero. The wiggles seen in the plot are a combination of the multiple reflections occurring at the detector substrate and small amount of absorption which may be present in the optical components whose exact transmittance curve is not known. The modulation efficiency is assumed to be constant over the wavenumber range for the calculation.

The detector response can also be expressed as a function of the detector parameters. The detector response represented in terms of the quantum efficiency (section 5.5.5) and scaled to lsb units is defined as (equation is adapted from [54])

$$R_D(\sigma, t_{int}) = t_{int} \frac{\eta(\sigma)}{E_{ph}(\sigma)} \frac{2^{Nb}}{Q_{fw}} \quad (5.28)$$

where

$E_{ph}(\sigma) = h_p c \sigma$	is the photon energy,
$\eta(\sigma)$	is the detector quantum efficiency,
$t_{int}$	is the detector integration time,
$Nb = 14$	is the detector quantization level,
$2^{Nb}$	is the dynamic range of the analog to digital converter,
$Q_{fw}$	is the detector full well capacity.

The photon energy at the cutoff wavenumber ( $\sigma_1 = 780 \text{ cm}^{-1}$ ) is given as

$$E_g = h_p c \sigma_1 = 1.55 \times 10^{-20} \text{ J}. \quad (5.29)$$

### 5.5.5. Detector quantum efficiency

The detector quantum efficiency ( $\eta$ ) reflects the effectiveness of the detector producing an electronic charge from the incident photons. The detector quantum efficiency is a quantity with unit one and has the values in the range of 0 to 1.

Modifying equations 5.28 gives the detector quantum efficiency expressed as

$$\eta(\sigma) = \frac{R_D(\sigma, t_{int}) E_{ph}(\sigma) Q_{fw}}{t_{int} 2^{Nb}} \quad (5.30)$$



Figure 5.29.: Detector quantum efficiency for pixel (119,121) of detector II/2. The measurement was done for a detector integration time of  $34.1 \mu\text{s}$ .

The quantum efficiency curve for pixel (119,121) of detector II/2 is shown in figure 5.29. The same data set as used for the calculation of the detector response is also used here. The quantum efficiency value beyond the cutoff wavenumber shows a soft increase until about  $900 \text{ cm}^{-1}$ . This effect is a property of the alloy of the detector material. The quantum efficiency above  $1400 \text{ cm}^{-1}$  is not shown due to a large uncertainty in its determination. The occurrence of the wiggles is explained in the previous section.

### 5.5.6. Detector cutoff

The cutoff wavenumber for the detector is calculated as the wavenumber at which the detector response drops to 50 % of its mean value calculated in the range between  $900 \text{ cm}^{-1}$  and  $1300 \text{ cm}^{-1}$ .

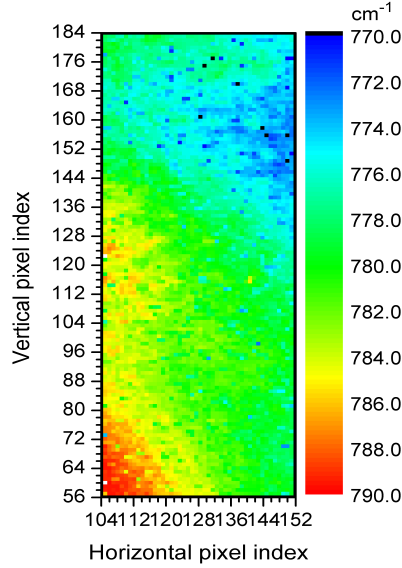


Figure 5.30.: 2D distribution of the cutoff wavenumber plotted over the  $48 \times 128$  pixel array.

The distribution of the cutoff wavenumber over the detector array is shown in figure 5.30. The plot shows that the distribution of the cutoff wavenumber for the pixels varies by about  $20 \text{ cm}^{-1}$  over the pixel array. A possible source for this variation is associated with the detector material which is made up of an alloy of CdTe and HgTe. It is assumed that the plot gives a picture of the inhomogeneity in the alloy distribution over the pixel array. The average cutoff wavenumber is about  $780 \text{ cm}^{-1}$ . The lower left corner of the detector array shows a higher cutoff wavenumber and the upper right corner shows a lower cutoff wavenumber. The cutoff variation over the detector array has an impact on the line strength of the spectral lines around the cutoff region and will affect the quality of the trace gas retrieval around the cutoff wavenumber region over the detector array.

### 5.5.7. Noise equivalent spectral radiance

#### NESR: Theoretical evaluation

The noise equivalent spectral radiance (NESR) is a measure of the amount of spectral radiance required to yield a signal-to-noise ratio of one. It has the units of  $\text{nW}/(\text{cm}^2 \text{ sr cm}^{-1})$  or SRU (spectral radiance units). The theoretical value of the NESR is calculated as [46]

$$NESR(\sigma, t_{int}) = \frac{\nu_{tot}(t_{int})}{R_D(\sigma, t_{int}) A_{pix} \Omega_{pix} M \tau(\sigma) \delta \sigma A_{po} \sqrt{(t_{int} F_f C_{bins})/2}} \quad (5.31)$$

where

- $\delta \sigma$  is the spectral sampling,
- $F_f$  is the frame frequency,
- $A_{po}$  is a scaling factor depending on apodization,
- $C_{bins}$  is the number of pixels co-added.

The apodization factor corresponds to 1.2, 1.4 and 1.6 for a weak, medium and strong apodization, respectively [22, 23]. The rest of the parameters has been already explained previously.

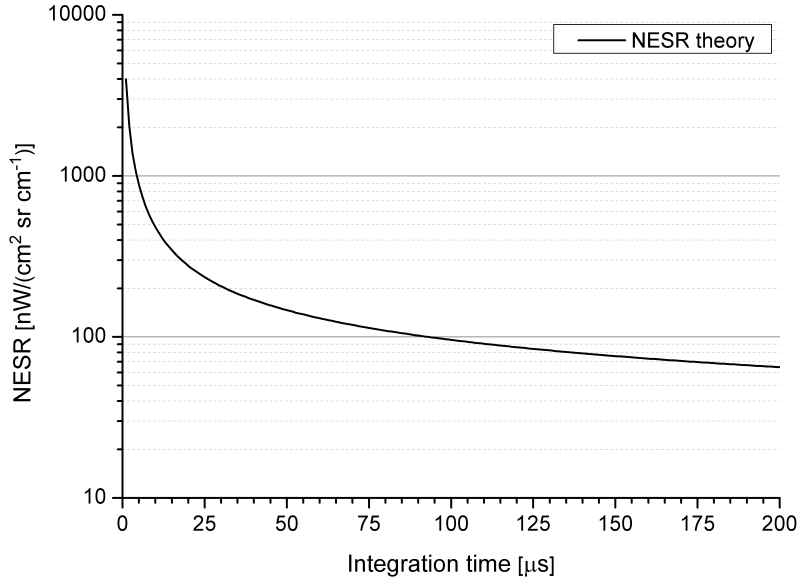


Figure 5.31.: The theoretical values of the NESR plotted (logarithmic scale) as a function of detector integration time at  $1000 \text{ cm}^{-1}$  and instrument parameters mentioned in the text.

The theoretical NESR values plotted as a function of the detector integration time for a given measurement condition is shown in figure 5.31. The NESR values are calculated for a spectral position at  $1000 \text{ cm}^{-1}$  and a spectral sampling of  $0.0625 \text{ cm}^{-1}$  (CM resolution). The detector response value used is from on-ground measurement for pixel (119,121) of detector II/2. The interferometer temperature is set to 222 K and the blackbody temperature is set to 287 K (these values represent the measurement values shown in table 5.4). The total noise is calculated using equation 5.22. A mean modulation efficiency ( $M$ ) value of 0.74 and the total transmittance curve (section 5.5.2) are used. The bins is set to unity as the calculation is done for a single pixel, a frame frequency of 4940.7 Hz and the detector temperature of 59 K are used for this calculation. The resulting curve gives an estimate of the NESR value to be expected for a given detector integration time.

### NESR: measurement evaluation

The NESR from the measurement data is calculated as the standard deviation of the imaginary part of the calibrated spectra of different subsequent measurements and expressed as

$$NESR(\sigma) = \sqrt{\frac{\left( n \sum_{i=1}^n S_{ci}(\sigma)^2 - \left( \sum_{i=1}^n S_{ci}(\sigma) \right)^2 \right)}{n(n-1)}} \quad (5.32)$$

where

$S_{ci}$  is the imaginary part of the calibrated spectrum of individual measurements,

$n$  is the number of measurements.

The measured NESR is compared with the modeled NESR value for the same condition.

### Measurement setup

The NESR is calculated from on-ground (pre flight) and in-flight (K01\_F02, K03\_F20) measurements looking at the blackbody and the atmosphere as scene, respectively. The on-ground and flight K01\_F02 measurements were performed with detector II/2 while the measurements during flight K03\_F20 were performed with detector II/1. The GLORIA interferometer was operated cold (at temperatures of  $T_{bg}$  shown in table 5.4). A summary of the parameters corresponding to the measurements and those used for the theoretical calculations are given in table 5.4.

Table 5.4.: Parameters for the NESR evaluation from spectrally resolved measurement

Parameter	Ground	Fl. K01_F02	Fl. K03_F20
Detector used	II/2	II/2	II/1
Pixel range used (array)	64×128	48×128	48×128
Frame frequency ( $F_f$ )	4940.7 Hz	6281.407 Hz	6281.407 Hz
Detector integration time ( $t_{int}$ )	34.1 $\mu$ s	65.3 $\mu$ s	99.1 $\mu$ s
Interferogram recording time ( $t_{iint}$ )	16.2 s	12.56 s	10.92 s
Detector temperature ( $T_D$ )	59 K	59 K	51 K
Scene temperature ( $T_s$ )	287 K	not known	not known
Background temperature ( $T_{bg}$ )	222 K	216 K	214 K
spectral sampling ( $\delta\sigma$ )	0.0625 $\text{cm}^{-1}$	0.0625 $\text{cm}^{-1}$	0.071429 $\text{cm}^{-1}$
Background emissivity ( $\epsilon_{bg}$ )	0.55	0.55	0.55
Modulation efficiency (M)	0.74	0.74	0.74
number of bins	1	1	1

### NESR calculation for ground measurements

The NESR has been evaluated from the measurements performed on-ground before the flight with the GLORIA blackbody as scene using equation 5.32. Figure 5.32 shows the measured NESR plot (red dots) for a single pixel (119,121) of detector II/2 measured with an integration time of 34.1  $\mu$ s.

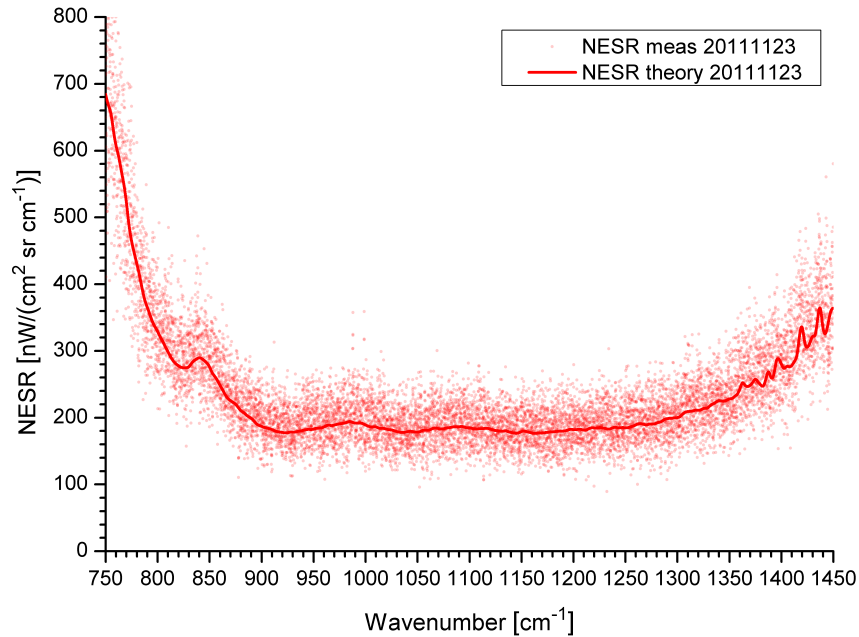


Figure 5.32.: NESR plot from on-ground measurements (red dots) looking at a blackbody at 287 K for a single pixel (119,121) of detector II/2 measured with an integration time of 34.1  $\mu$ s and a spectral sampling of 0.0625  $\text{cm}^{-1}$ . The modeled value of the NESR (red line) is calculated for a similar scenario.

The modeled NESR has been calculated using equation 5.31 and plotted as red line in figure 5.32. For the theoretical calculations, the detector response is taken for pixel (119,121)

from the laboratory measurements (section 5.5.4). The electrons generated due to the photon load on the detector are estimated from the photon flux on the detector calculated using equation 5.9 and 5.10 with the knowledge of the scene temperature and the background temperature. The total noise contribution is calculated for the integration time of the measurement using equation 5.22. The rest of the parameters are taken from table 5.4 and some parameter values which were defined earlier (e.g., the pixel area, the solid angle and the instrument transmittance). The theoretically calculated values fit quite well with the measured values. The pixel is chosen such that it represents the median value of the mean NESR calculated for the spectral range of  $900\text{ cm}^{-1}$  to  $1300\text{ cm}^{-1}$ . This implies that the selected pixel represents the pixels in the array well.

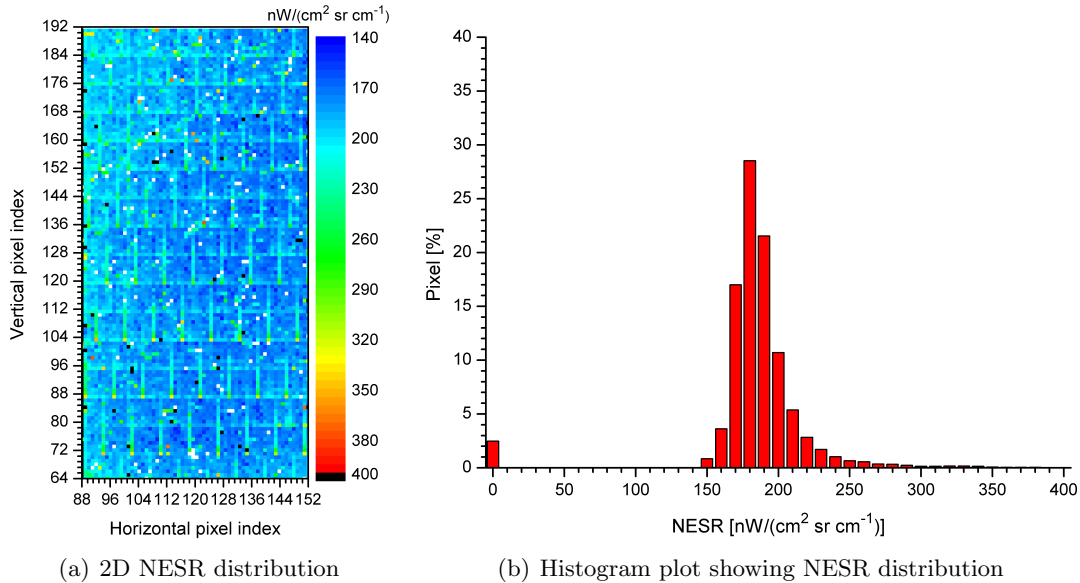


Figure 5.33.: Mean NESR in the range of  $900\text{ cm}^{-1}$  to  $1300\text{ cm}^{-1}$  plotted for  $64 \times 128$  pixels calculated with the measurements performed on-ground looking at the GLORIA blackbody at  $287\text{ K}$  as scene. (a) 2D distribution of the mean NESR. (b) Histogram distribution of the mean NESR. The median of the histogram is  $184.24\text{ nW}/(\text{cm}^2\text{ sr cm}^{-1})$ .

2D distribution and the corresponding histogram plot of the mean NESR calculated for the spectral range of  $900\text{ cm}^{-1}$  to  $1300\text{ cm}^{-1}$  are shown in figure 5.33(a) and figure 5.33(b), respectively. The NESR distribution shows the presence of correlated noise structures as seen earlier in the noise plot. The plot shows stripe patterns of eight pixels in the vertical direction which are caused by an EMC problem and horizontal stripes over the full line occurring at every eighth pixel which reflect the individual noise properties of the ADCs and the preamps. The correlated noise degrades the SNR gain achieved by pixel binning. A bad pixel mask was applied to the data, these pixels were not processed and are shown as black points on the 2D plot.

### NESR calculation from ESSenCe flight K01\_F02 measurements

The NESR has been evaluated from in-flight measurements performed during the ESSenCe campaign (flight K01\_F02) with atmosphere as scene. The NESR from the measurement has been evaluated in the same way as discussed in the previous section. The scene temperature is variable and not known for the theoretical calculation of the expected NESR. The electrons generated due to the photon load coming from the scene is calculated by integrating the radiance signal of the real part of the calibrated signal. The electrons generated due to the photon load arriving from the instrument background are calculated for the instrument temperature. The photon noise is calculated from the measured signal rather than being estimated from the source temperature. The total noise is calculated

using equation 5.22 and is taken for the theoretical NESR calculation.

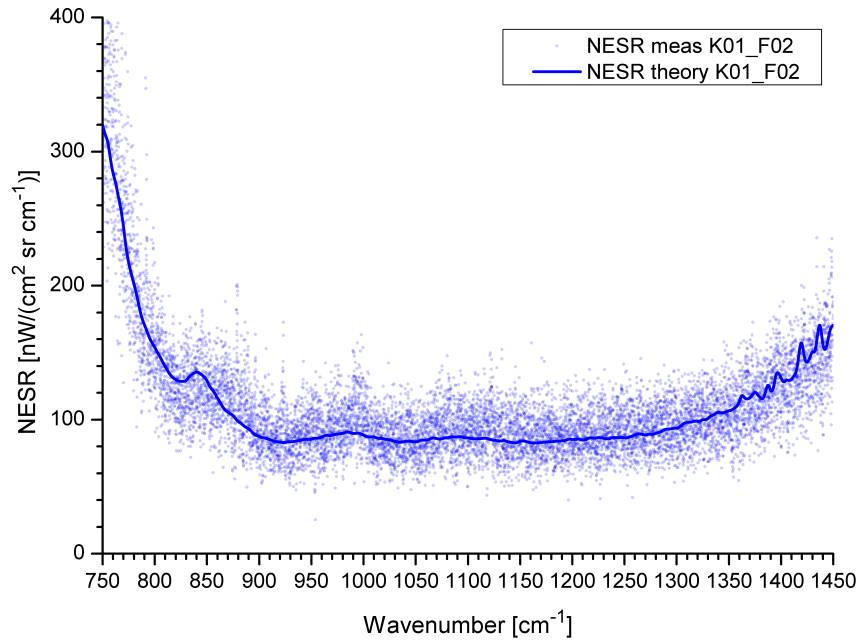


Figure 5.34.: NESR plot from measurements performed in-flight K01\_F02 (blue points) looking at the atmosphere as scene for a single pixel (119,121) of detector II/2 measured with an integration time of  $65.3 \mu s$  and a spectral sampling of  $0.0625 \text{ cm}^{-1}$ . The theoretical value of the NESR (blue line) is calculated for a similar scenario.

The theoretically expected (blue line) and the measured (blue dots) NESR for a single pixel (119,121) of detector II/2 for an integration time of  $65.3 \mu s$  is shown in figure 5.34. The theoretical values fit well with the measured trend in data. The pixel selected is the same as for the on-ground measurement analysis.

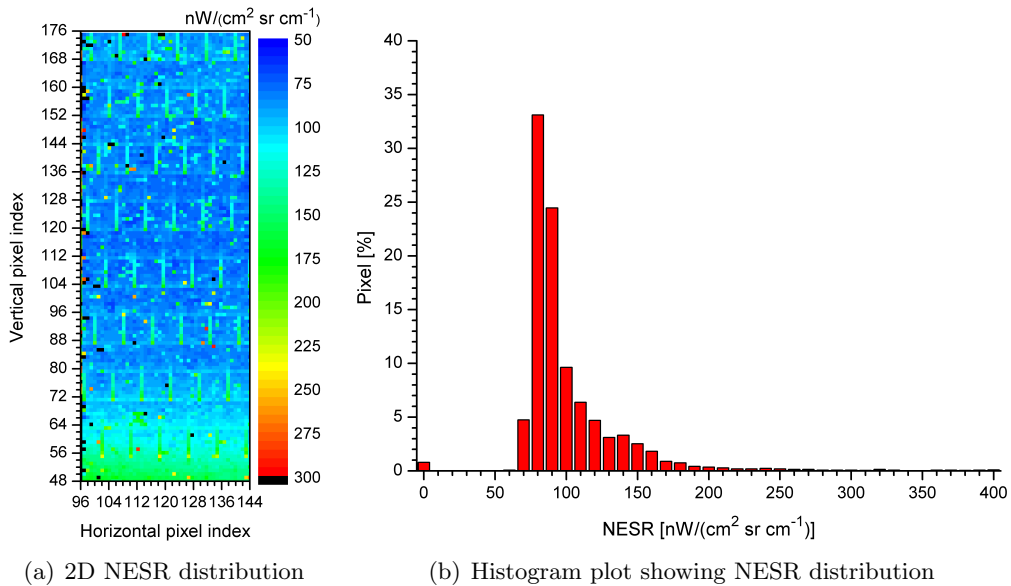


Figure 5.35.: Mean NESR in the range of  $900 \text{ cm}^{-1}$  to  $1300 \text{ cm}^{-1}$  plotted for  $48 \times 128$  pixels calculated with the measurements performed in-flight K01\_F02 looking at the atmosphere as scene. (a) 2D distribution of the mean NESR. (b) Histogram distribution of the mean NESR. The median value of the histogram is  $88.71 \text{ nW}/(\text{cm}^2 \text{ sr cm}^{-1})$ .

2D distribution and the corresponding histogram plot of the mean NESR calculated for the spectral range of  $900\text{ cm}^{-1}$  to  $1300\text{ cm}^{-1}$  are shown in figure 5.35(a) and figure 5.35(b), respectively. The correlated noise pattern is the same as discussed in the previous section. A bad pixel mask was applied during data processing and are shown as black points in the 2D plot. A cloud layer is seen in the lower pixel rows. Depending on the temperature of the cloud, it will influence the photon load and therefore the photon noise of the pixels. The high NESR values seen in the lower pixel rows cannot be explained by the presence of clouds only. An other possible reason can be the presence of a line-of-sight jitter problem, which is prominent in the region of signal gradients such as presence of clouds. A combination of these two effects gives a higher NESR value for the pixels in the lower row (below vertical pixel index 58). The jitter problem is not seen in figure 5.33(a) where the measurement has been performed by looking at a homogeneous blackbody source.

### NESR calculation from TACTS flight K03\_F20 measurements

The NESR has been evaluated from in-flight measurements performed during the TACTS campaign (flight K03\_F20) with the atmosphere as scene. The NESR from the measurement and theoretically expected values were evaluated in the same way as discussed for flight K01\_F02.

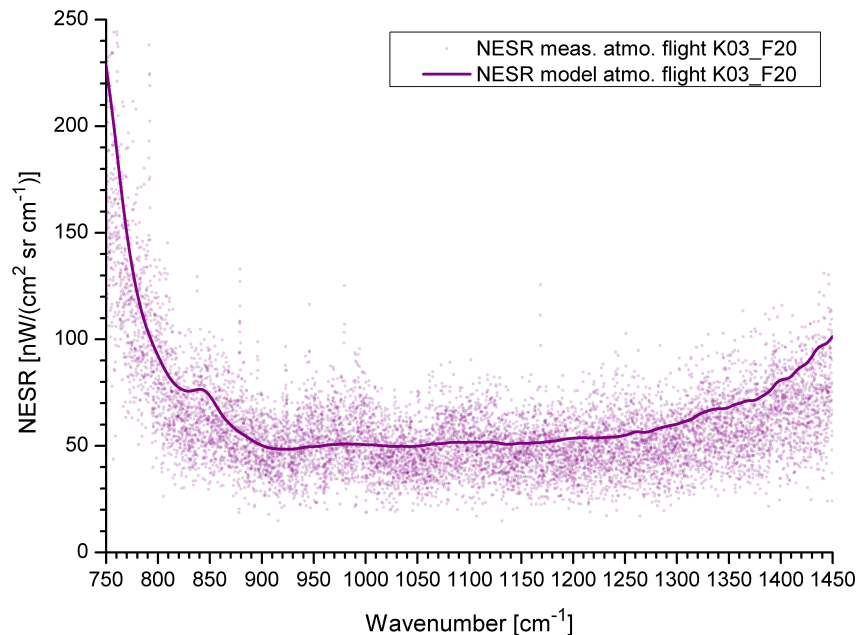


Figure 5.36.: NESR values from measurements performed in-flight K03\_F20 (violet points) looking at the atmosphere as scene for a single pixel (128,118) of detector II/1 measured with an integration time of  $99.1\ \mu\text{s}$  and a spectral sampling of  $0.071429\text{ cm}^{-1}$ . The theoretical value of the NESR (violet line) is calculated for a similar scenario.

The modeled (violet line) and the measured (violet dots) NESR values for a single pixel (128,118) of detector II/1 measured with an integration time of  $99.1\ \mu\text{s}$  and a spectral sampling of  $0.071429\text{ cm}^{-1}$  is shown in figure 5.36. The pixel selected represents the median value of the mean NESR calculated for the spectral range of  $900\text{ cm}^{-1}$  to  $1300\text{ cm}^{-1}$ . The radiometric calibration of the data of this flight is not perfect, leaving with a residual offset in the spectra after performing the radiometric calibration. This might be the cause for the deviation of the theoretical curve around the  $1400\text{ cm}^{-1}$  region.

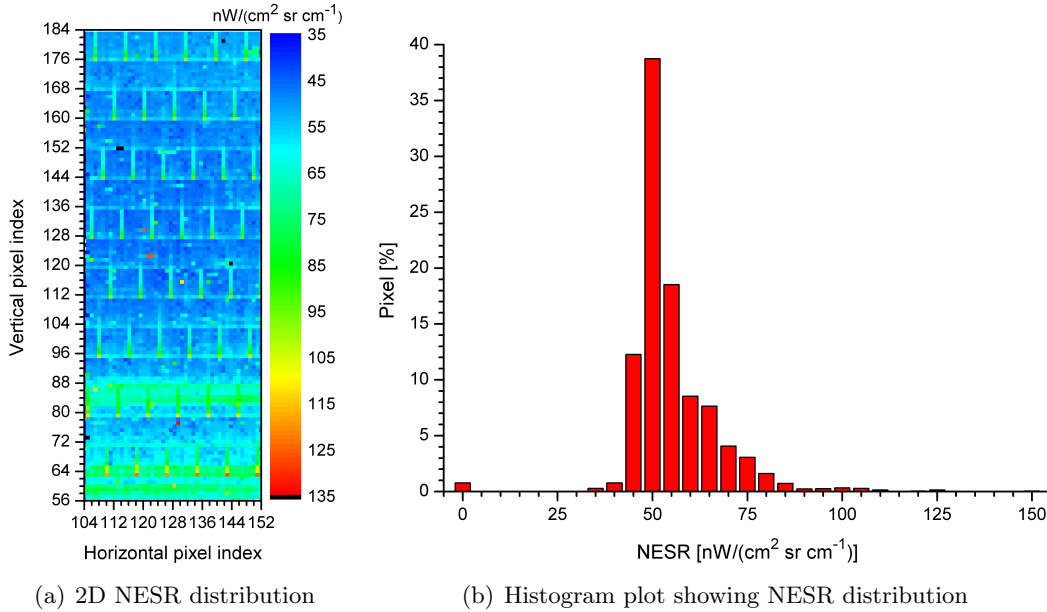


Figure 5.37.: Mean NESR in the range of  $900\text{ cm}^{-1}$  to  $1300\text{ cm}^{-1}$  plotted for  $48 \times 128$  pixels calculated with the measurements performed in-flight K03\_F20 looking at the atmosphere as scene. (a) shows the 2D distribution of the mean NESR. (b) shows the histogram distribution of the mean NESR. The median value of the histogram is  $51.94\text{ nW}/(\text{cm}^2\text{ sr cm}^{-1})$ .

2D distribution and the corresponding histogram plot of the mean NESR calculated for the spectral range of  $900\text{ cm}^{-1}$  to  $1300\text{ cm}^{-1}$ . The correlated noise pattern is seen here as well. The high NESR seen in two layers of the lower rows, once around vertical pixel indices 80 to 88 and second time around vertical pixel indices 56 to 68, are due to the presence of an additional signal depending on the cloud temperature and a line-of-sight jitter problem which is prominent at steep radiance gradients.

### Summary: Spectral features of the detector and instrument parameters

The spectral features of the detector and the instrument parameters were addressed in this section. These parameters are calculated from measurements performed both on-ground and in-flight. The theoretically expected NESR is calculated using the noise model of GLORIA. The noise model gives an estimate of the noise contribution coming from different sources. The measured and theoretical values for NESR are found to be in good agreement. This confirms that the noise performance of the instrument was nominal during both the on-ground and in-flight measurements. This proves that the noise sources for the good pixels have been accounted for in the model and that there are no hidden sources. The distribution of the NESR over the pixel array is found to be quite homogeneous with the exception of the stripes due to excess correlated noise among the pixels. The difference in the NESR values for the three data sets are due to the difference in the operating conditions (e.g., integration time, frame frequency, spectral sampling etc.). The model concluded to be sufficient for predicting the instrument performance under various circumstances and hence can be used for further scientific work.

## 5.6. Imaging quality over the FPA

The imaging quality of the GLORIA optics over the focal plane array (FPA) is presented in this section. Laboratory measurements were performed to check the imaging quality. The measurement results are compared with a theoretical estimation to find the focus position for the infrared objective at a given temperature.

### Measurement setup and characterization results

Four infrared blackbody sources are placed at the focal plane of an off-axis parabolic mirror (focal length of 1000 mm). The setup with the infrared light sources and the off-axis parabolic mirror is fixed on a supporting bench and placed in front of the interferometer. DC measurements were performed with the full interferometer with a fixed slide looking at the infrared blackbody sources. The emitting surface area of the IR source is  $1.7 \times 1.7 \text{ mm}^2 = 2.89 \text{ mm}^2$ . The spot size on the detector is roughly  $4 \times 4$  pixels. The infrared objective is placed at the focus position for the warm instrument. The focus position is verified by checking the visual sharpness of the four infrared light sources on the FPA with an auto-collimation telescope. The focus point is estimated with an accuracy of  $\pm 5$  IRO counts. The IRO is then set to the estimated focus position (provided by the lens manufacturer) for the cold instrument at  $-55 \text{ }^\circ\text{C}$ . DC measurements with the above mentioned setup are made at three instrument temperatures:  $-47.8 \text{ }^\circ\text{C}$ ,  $-55.6 \text{ }^\circ\text{C}$  and  $-64.7 \text{ }^\circ\text{C}$ . These temperatures were selected as they cover the range of the possible operational temperature of the GLORIA interferometer during flight.

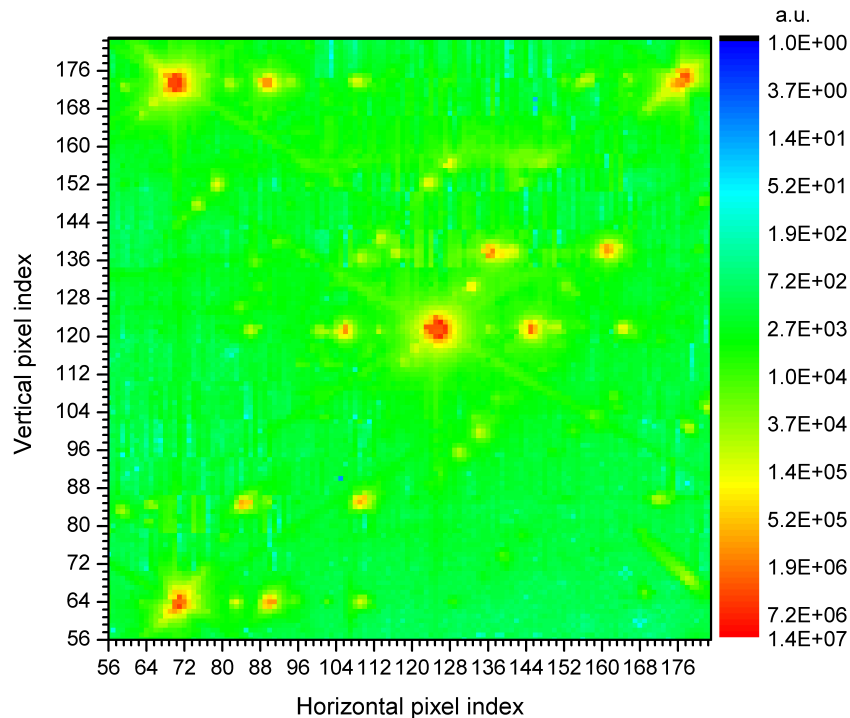


Figure 5.38.: The image of the four IR blackbody sources on the GLORIA detector array of  $128 \times 128$  pixels for an instrument temperature of  $-55.6 \text{ }^\circ\text{C}$ .

The image of four infrared blackbody point sources on the detector array of  $128 \times 128$  pixels for an instrument temperature of  $-55.6 \text{ }^\circ\text{C}$  is shown in figure 5.38. In addition to the four main images, several other images are also found on the detector array. These images are called parasitic images which will be discussed in detail in section 5.7.

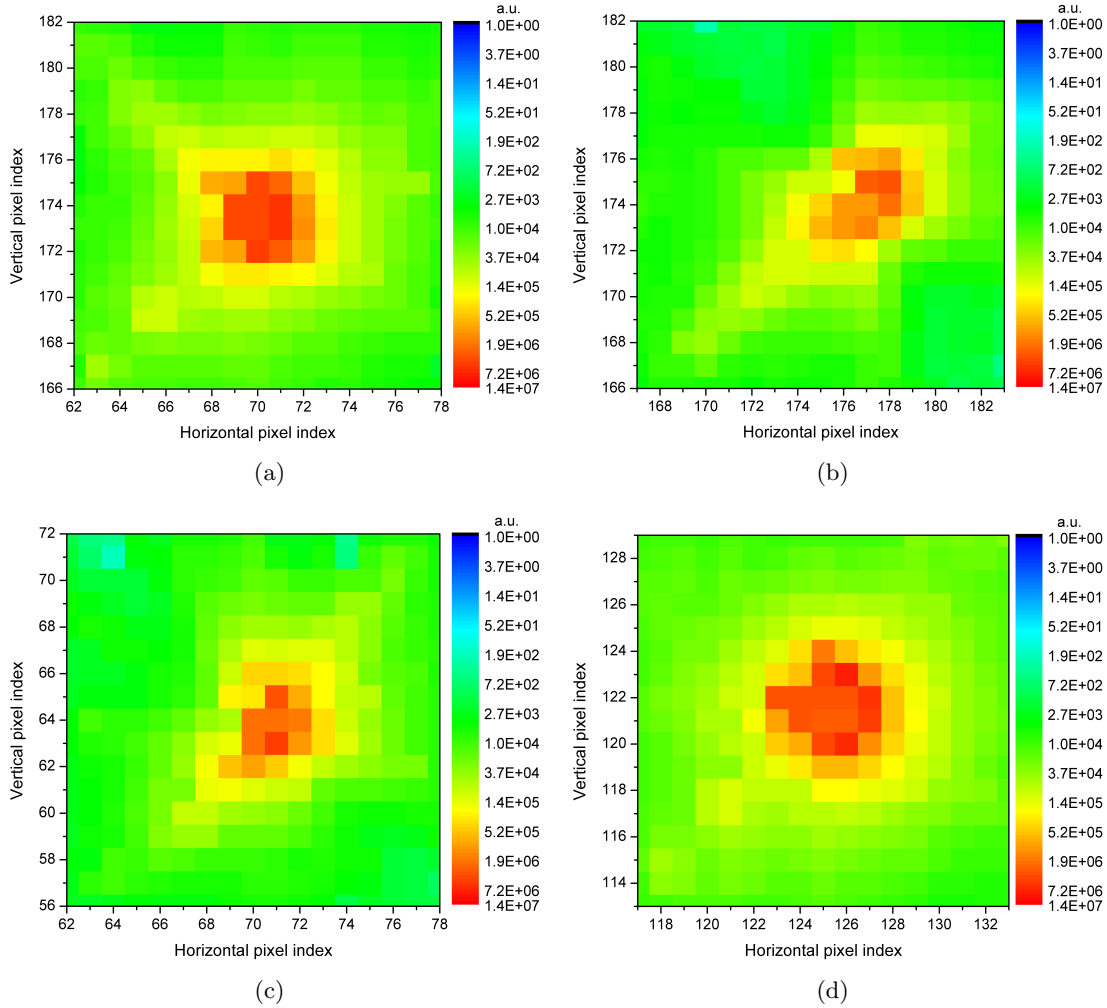


Figure 5.39.: Zoom plots of the four main images of the infrared blackbody source on the GLORIA detector for an instrument temperature of  $-55.6$  °C. (a) shows the image on the top left side, (b) shows the image on the top right side, (c) shows the image on the bottom left side and (d) shows the image on the center of the detector array.

Zoom plots of the four main images are shown in figure 5.39. The top left image (figure 5.39(a)) shows a diagonal deformation of the image in the upper left side. The top right image (figure 5.39(b)) and the bottom left image (figure 5.39(c)) show the deformation in the diagonal direction from the lower left to the upper right side. This effect for the corner images can be caused from the presence of coma, spherical aberration or distortion. The central image (figure 5.39(d)) is quite circular and may have spherical aberration, it does not show as strong distortion effects as for the corner images. The image of the infrared blackbody is dispersed over several pixels due to the diffraction effect of the off-axis parabolic mirror giving a broader shape of the image. These images show a qualitative overview of the imaging quality over the focal plane array (FPA). They themselves do not give an indication if the measurement performed at the IRO is the focus position for the given temperature. It is necessary to check the image quality with measurements performed at the other two temperatures ( $-47.8$  °C and  $-64.7$  °C). Those measurements are analyzed to find the focus position and hence know the quality of the images with the IRO being placed at the focus position.

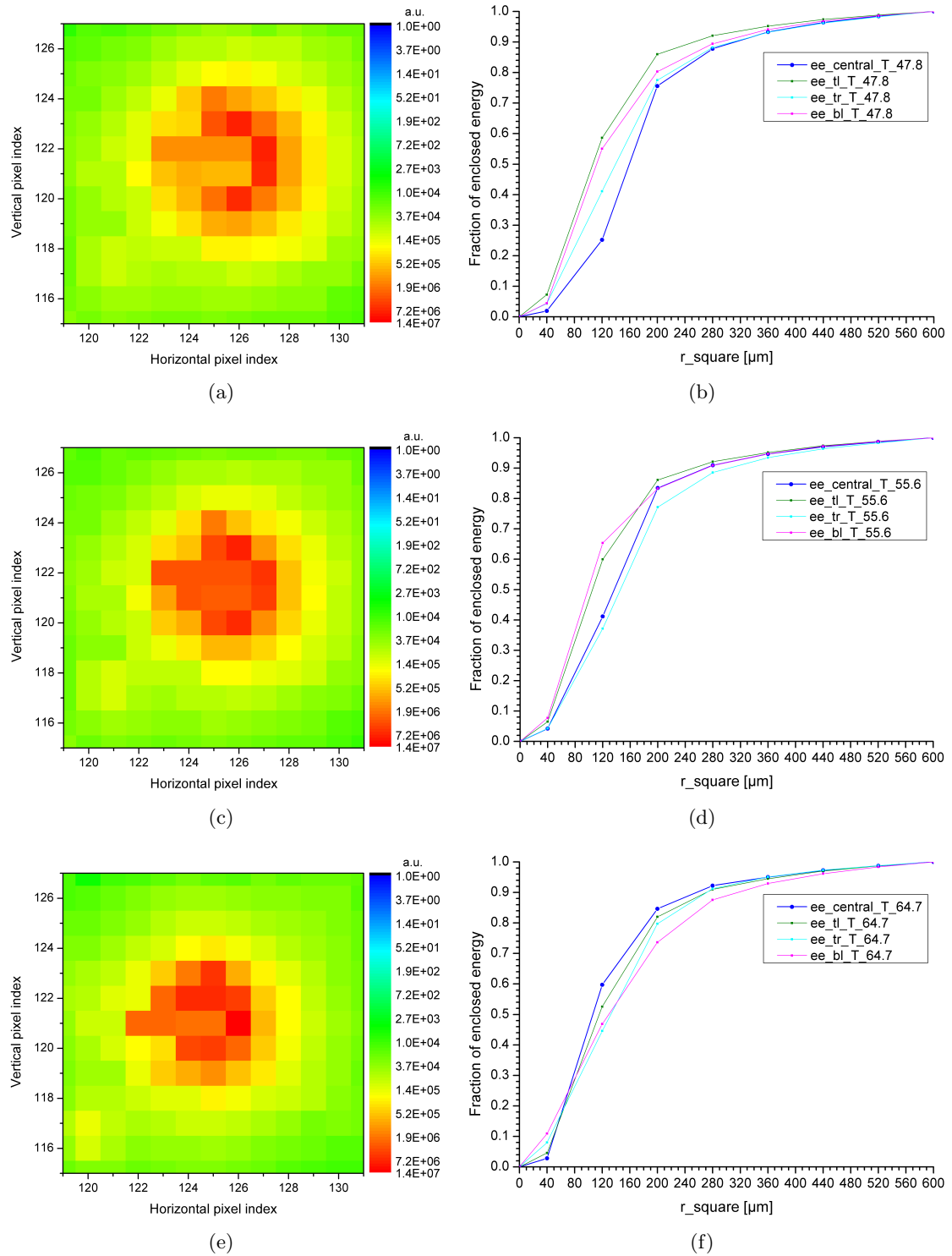


Figure 5.40.: Zoom of the image of the central infrared blackbody on the GLORIA detector for  $-47.8\text{ }^{\circ}\text{C}$ ,  $-55.6\text{ }^{\circ}\text{C}$  and  $-64.7\text{ }^{\circ}\text{C}$  are plotted in (a), (c) and (e), respectively. Ensquared energy diagram for the squared area of all four images corresponding to the temperature of  $-47.8\text{ }^{\circ}\text{C}$ ,  $-55.6\text{ }^{\circ}\text{C}$  and  $-64.7\text{ }^{\circ}\text{C}$  are plotted in (b), (d) and (f), respectively.

Zoom plots of the central infrared blackbody and the ensquared energy diagram<sup>2</sup> for the squared area of all four images corresponding to the instrument temperatures of  $-47.8\text{ }^{\circ}\text{C}$ ,

<sup>2</sup>The ensquared energy diagram is a method to quantify the fraction of optical energy present in an image on the detector for an optics system. It is generated by starting at the center of the spot diagram and counting the fraction of incident rays that are within any squared radius.

-55.6 °C and -64.7 °C are shown in figure 5.40. The image of figure 5.40(a) shows a dispersed semicircular shape. The shape becomes more circular for images of figure 5.40(c) and figure 5.40(e). The ensquared energy diagram for the three cases shows that the curve for the central image for -47.8 °C is below that of the other curves and goes higher as the temperature decreases. This effect is compared with the theoretically expected curves.

A Zemax model comprising the optical components of the GLORIA interferometer has been used for the theoretical calculations and comparison with the measurement results.

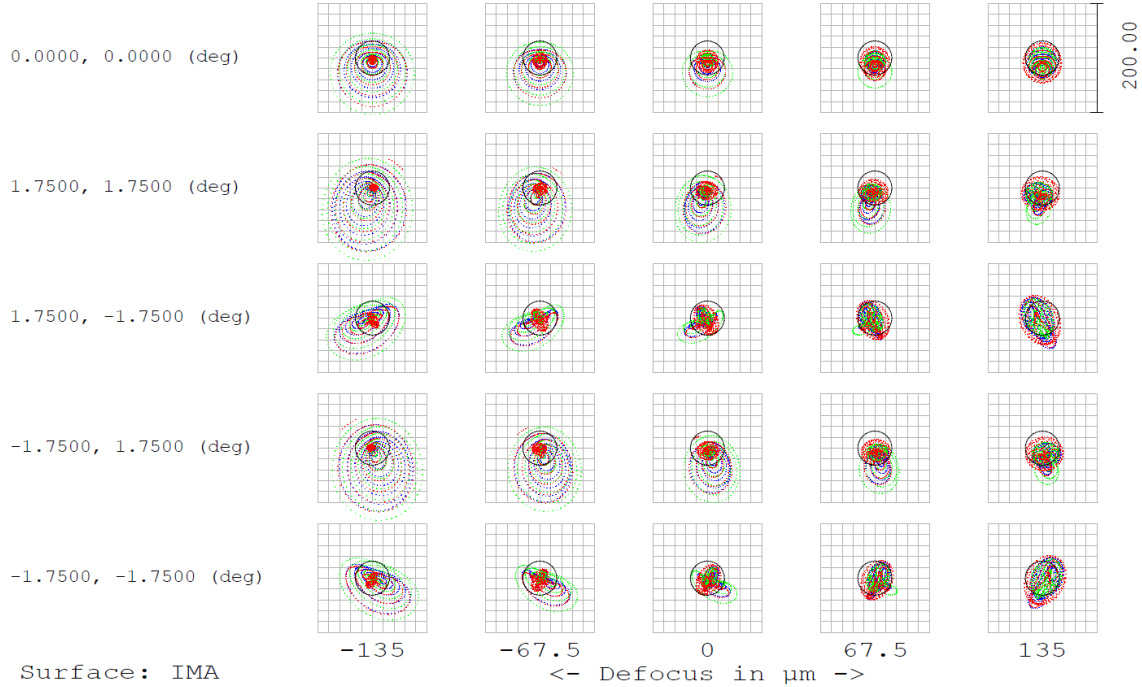
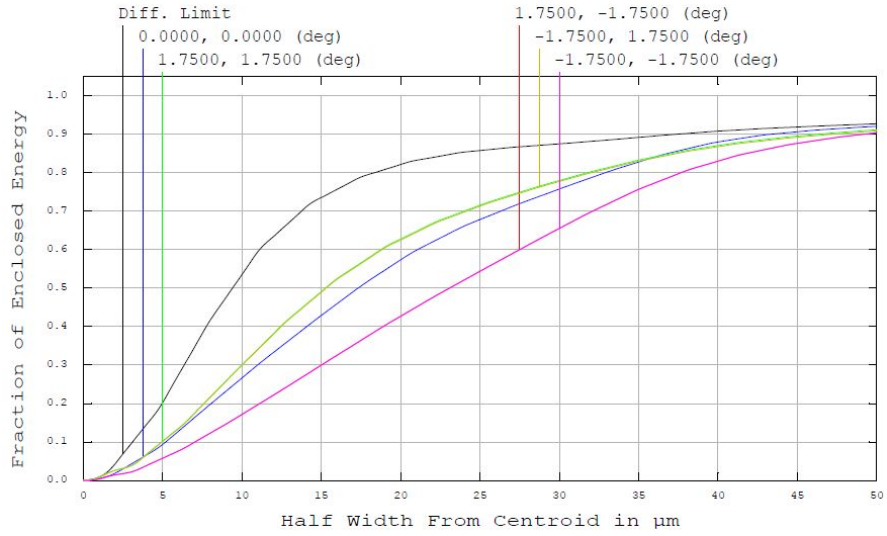
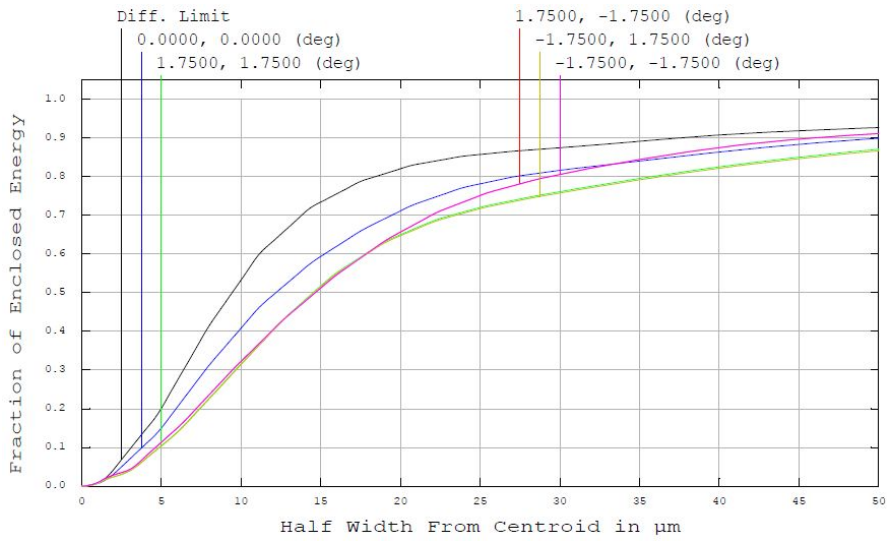


Figure 5.41.: Through focus spot diagrams for the IRO being placed at the focus position and four other defocused positions in steps of  $\pm 67.5 \mu\text{m}$  away from the focus [57].

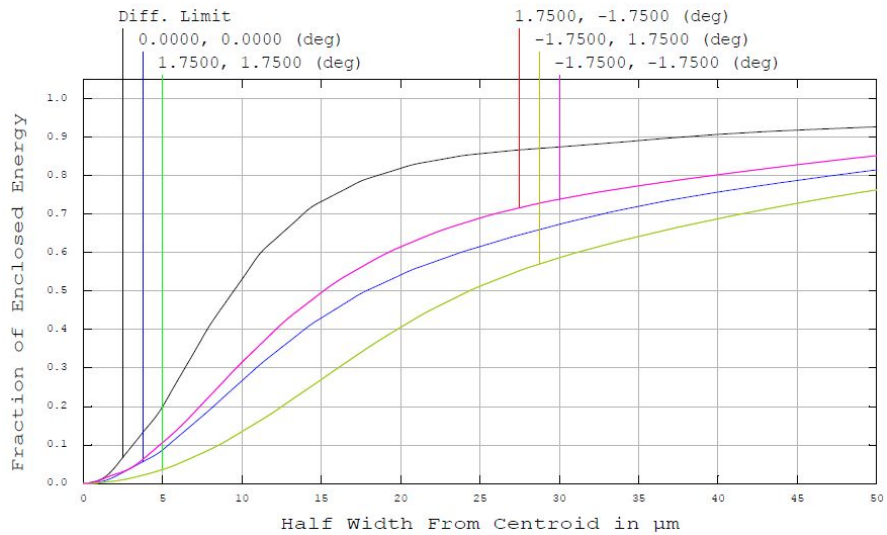
A through-focus spot diagram of a point source imaged on the central and the four corner positions on the detector array is shown in figure 5.41. The spot diagrams show the characteristic of aberrations and suggest the size of the image blur. The middle column is for the IRO placed at the focus position. The four other columns are for the defocused position with the IRO being placed in steps of  $\pm 67.5 \mu\text{m}$  away from the focus in both directions of the focus plane (either towards the detector or towards the beamsplitter). The negative and the positive defocused directions are equivalent to the IRO moving towards the beamsplitter and towards the detector, respectively. The spot diagrams for the central pixel (0,0) show the image broadening for the negative defocused direction and a more concentrated image for the positive defocused direction. Comparing this effect to the spot diagrams of the central image of the measurement (figure 5.40), it is seen that the image is getting less divergent at a lower instrument temperature. The decreasing area of the measured spot diagrams in the order from measurements at -47.8 °C and going towards measurements at -64.7 °C could be compared to the pattern of the theoretical defocused spot diagrams in the order from -135  $\mu\text{m}$  and going towards 135  $\mu\text{m}$  case.



(a) Ensqared energy diagram for the instrument temperature of -47.8 °C



(b) Ensqared energy diagram for the instrument temperature of -55.6 °C



(c) Ensqared energy diagram for the instrument temperature of -64.7 °C

Figure 5.42.: Ensqared energy diagram plotted for a squared area with a spot simulated for three instrument temperatures [57].

The ensquared energy diagrams calculated for a squared area with a spot at the central and the four corner positions on the detector array simulated for three defocused positions corresponding to the temperatures of  $-47.8\text{ }^{\circ}\text{C}$ ,  $-55.6\text{ }^{\circ}\text{C}$  and  $-64.7\text{ }^{\circ}\text{C}$  are shown in figure 5.42. The simulation has been done considering the focus position for the temperature of  $-55.6\text{ }^{\circ}\text{C}$ . The plots show that the curve for the central pixel area (blue line) is above the corner positions (green, dark yellow, pink and magenta lines) for the on-focus case, whereas it is below the curves for the two corner positions pink and magenta for one defocused position (at  $-47.8\text{ }^{\circ}\text{C}$ ) and green and dark yellow for the other defocused position (at  $-64.7\text{ }^{\circ}\text{C}$ ). A similar pattern is found in the measurement ensquared energy diagram. It is found that the curve for the central position is below all other curves corresponding to the corner positions (figure 5.40(b)) for measurement performed at the temperature of  $-47.8\text{ }^{\circ}\text{C}$  and the central curve gradually goes above the curves of the corner positions (one curve for  $-55.6\text{ }^{\circ}\text{C}$ , see figure 5.40(d) and three curves for  $-64.7\text{ }^{\circ}\text{C}$ , see figure 5.40(f)) for the measurements performed at the other two temperatures. As a general trend, as the focus position is approached, the curve for the central position raises above the other curves corresponding to the corner positions. This confirms that the focus position is being approached. The spot diagram comparison (figure 5.40) between the cases for temperatures of  $-55.6\text{ }^{\circ}\text{C}$  and  $-64.7\text{ }^{\circ}\text{C}$  shows that the image is getting concentrated for measurements performed at a colder temperature. This gives the evidence that the actual focus is somewhere between the two temperatures of  $-55.6\text{ }^{\circ}\text{C}$  and  $-64.7\text{ }^{\circ}\text{C}$ . Hence, it is evident that the predetermined position of the focus provided by the supplier is not the real focus. This leads to the necessity to find a table or a mapping which gives the focus position for the corresponding instrument temperature. There is a known thermal drift of the interferometer during long duration measurement flights. However, it may become necessary to have a mapping to adjust the IRO to the focus position with the change of interferometer temperature during flight. This topic will be addressed in chapter 6.8. The present setup used for the characterization measurement gave a qualitative estimate of the imaging quality. The setup is limited due to the diffraction of the optics. A new measurement set has to be developed for a more precise determination of the imaging quality over the detector array. In addition, the focus position has been determined from the spectral line width which be discussed in chapter 6.8.

## 5.7. Parasitic images

Parasitic images appear on the detector array along with the main image (figure 5.38, 5.43). The occurrence of a parasitic image on a given pixel adds an additional signal along with the radiation signal from the source and background falling on that given pixel. Therefore, it is necessary to identify the cause and to quantify the positions and the intensities of these parasitic images. The measurement setup used is the same as discussed in section 5.6. DC measurements were done with a fixed slide. The blackbody source signal was modulated with 10 Hz, such that frequency analysis of the signal can be done to improve the signal-to-noise ratio.

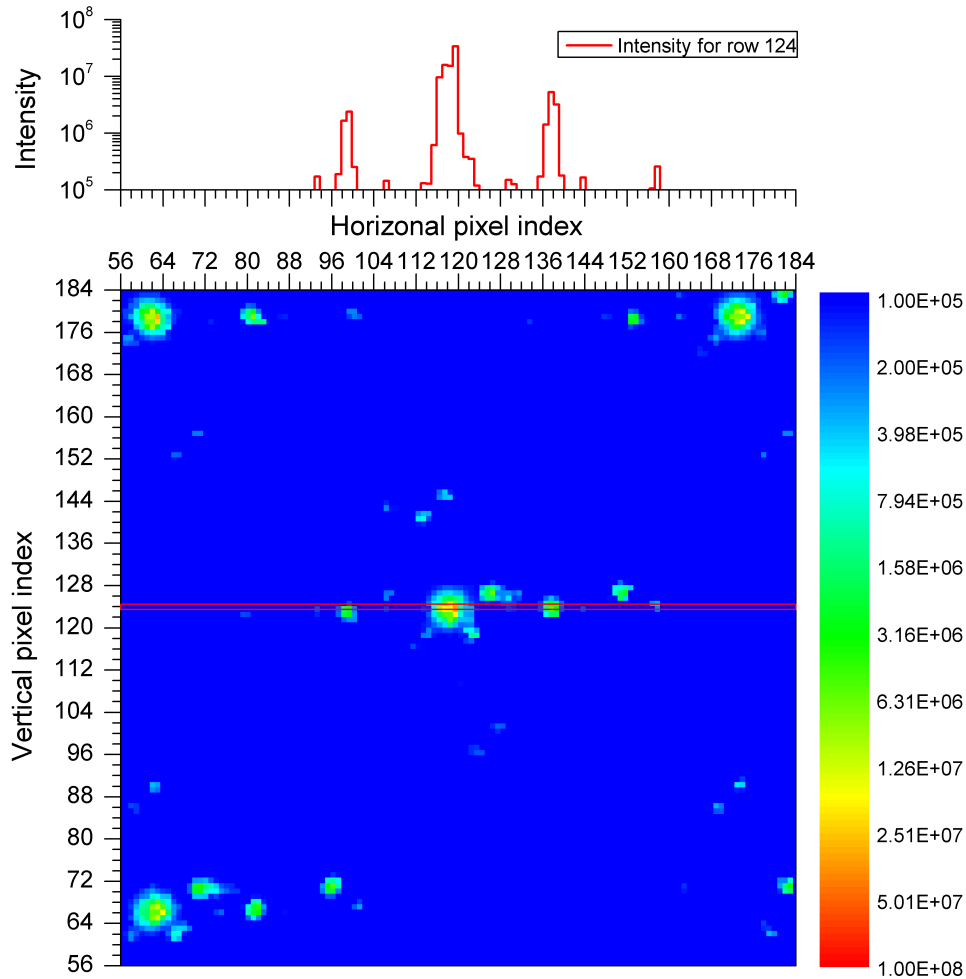


Figure 5.43.: Intensity plot (logarithmic scale) showing the main image and the parasitic images of the four point sources over the detector array. Top: Intensity plot of a horizontal cut through the detector at the vertical pixel index of 124.

The image of the detector array at the modulation frequency of the source is shown in figure 5.43. The plot shows the four main images and several other parasitic images. The central image and the corresponding parasitic images associated to it are all lying on the selected detector area. Pixels in row number 124 with the central spot image has been analyzed in detail. It has two strong parasitic images formed to the right (first parasitic image) and to the left (second parasitic image) of the main image. The centers of these images are located approximately 17 and 21 pixels away from the main image. These parasitic images are assumed to be formed due to the multiple reflections occurring at the beamsplitter surfaces. These reflections are present in both interferometer arms and add to the interferogram AC signal. Figure 5.43 also shows a set of three other parasitic images

formed approximately four rows above. These parasitic images disappear when the signal of the compensator arm is blocked, indicating that these parasitic images are formed by multiple reflections at the compensator surfaces. The multiple reflections being present in only one interferometer arm are not modulated by the interferometer and add to the interferogram DC signal only. As the interferogram DC is subtracted before calculating the spectra, the parasitic images formed from the reflections at the compensator plate are not included further in this study and therefore are rejected.

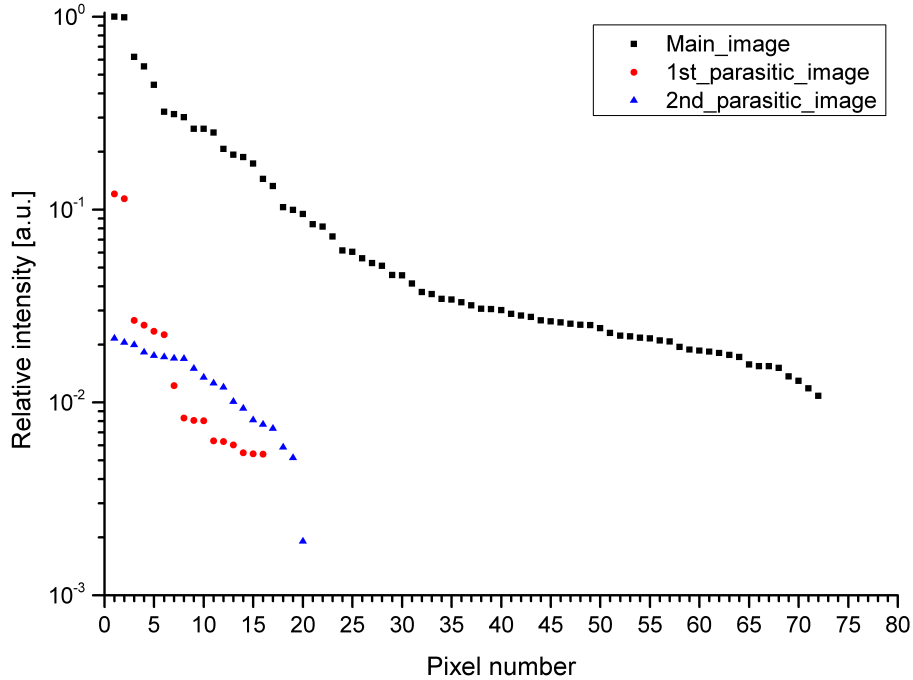


Figure 5.44.: The intensity distribution of the main image and two parasitic images over the detector pixel array. The pixel numbers are arranged in the order of their relative intensity.

Intensity distribution of the main image (black squares), the first parasitic image (red dots) and the second parasitic image (blue triangles) in the horizontal direction over the detector pixels for the central infrared blackbody source is shown in figure 5.44. The pixels are arranged in the decreasing order of their relative intensity. The intensity of the area of the first parasitic image is 4.88 % of the area of the main image. The intensity of the area of the second parasitic image is 3.11 % of the area of the main image. The intensities of the other multiple parasitic images in the horizontal direction are three orders of magnitude smaller than the main image (see figure 5.43 - top) and are neglected.

### Parasitic images: Theoretical analysis

A theoretical calculation of the above mentioned observation has been performed to verify the findings of the measurements. The parasitic images are assumed to be formed due to secondary reflections from the wedged beamsplitter substrate. It is made of KCl (Potassium Chloride) substrate, coated with a beam splitting layer (material not known - this information is not provided by the supplier). The path of the light propagation through the beamsplitter is shown in figure 5.45. The reflection and the transmission at the optical surfaces are shown explicitly. The reflectance and the transmittance coefficients are calculated with some assumptions which are theoretical entities. These values are used to calculate position and intensity of the parasitic images. A detailed calculation is presented in appendix B. The comparison will show if the assumed values are close to the real

ones and if the position and intensity of the parasitic images can be well represented by theoretical knowledge.

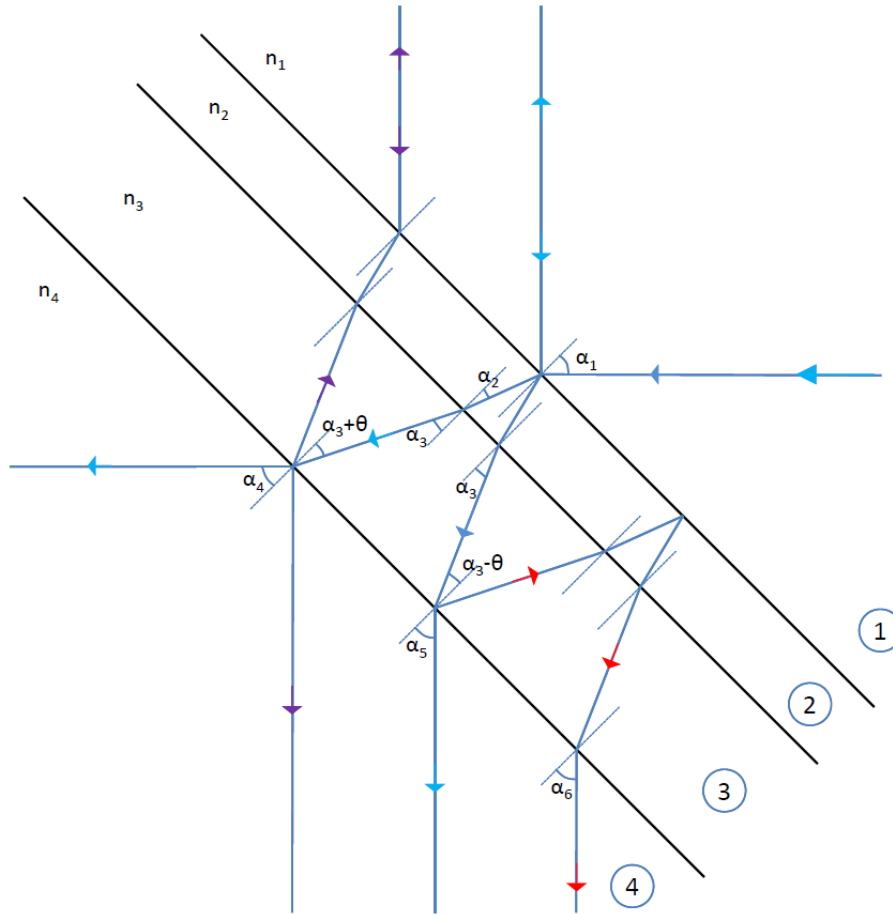


Figure 5.45.: Ray propagation through the beamsplitter showing multiple reflections and transmission at its surface. The refractive indices of the surfaces are marked with numbers. The wedge angle is represented by  $\theta$ .

The theoretical calculation shows that the parasitic images due to multiple reflections at the beam splitter surfaces are formed at -19.407 pixel and 19.266 pixel away in the horizontal direction from the main image. This is of the same order as the values derived from the measurements. The discrepancy with the measurement results may be due to the approximation of the parameters used, such as the wedge angle ( $\theta$ ), the refractive index and the angle of incidence of the radiation beam with respect to the beamsplitter ( $\alpha_1$ ). Varying some of these parameters, the parasitic image distances are calculated and are shown in annex B.

The intensities of the DC part of the main image, the first parasitic image and the second parasitic image are 0.8688, 0.0336 and 0.0243, respectively. The ratio of the intensity of the first parasitic image to the intensity of the main image is 3.867 %. The ratio of the intensity of the second parasitic image to the intensity of the main image is 2.797 %. The intensity of the DC part of the theoretical calculation does not match exactly with the measurement values. The area of the first parasitic image has a higher intensity value as compared to the area of the second parasitic image. This can also be seen in the measurement values. The theoretical estimate of the intensities of the images has been done by considering a single layer of dielectric surface. However, the beamsplitter coating is made up of multi layer dielectric surfaces which is not disclosed by the supplier. Thus, although good estimates are possible, numerically exact values cannot be achieved.

The intensities of the AC part of the main image, the first parasitic image and the second parasitic image are 0.434, 0.0136 and 0.0122, respectively. The ratio of the intensity of the first parasitic image to the intensity of the main image is 3.13 %. The ratio of the intensity of the second parasitic image to the intensity of the main image is 2.81 %. The intensity of the AC part of the parasitic image (incident on a given pixel) gives an additional contribution of the signal for the corresponding spectrum of the pixel. This additional signal is not a problem for a homogeneous scene in the horizontal direction, as the effect is the same for the calibration sources and is removed during radiometric calibration. The parasitic images from the beamsplitter surface being present in the horizontal direction does not affect the retrieval results as the pixel binning is performed in the horizontal direction. If the parasitic images (modulated part) were formed in the vertical direction, it would have caused problem to have signal contribution from one tangent altitude to the other tangent altitude. In case of horizontally inhomogeneous scenes, the effect of the parasitic images has to be taken into account if retrieval results are analyzed for each individual pixels. The additional signal, although small, will lead to an error in the retrieval of the trace gas concentration over the detector array.

### **Summary: Parasitic images**

The DC measurement looking at the four infrared blackbody sources shows a main image plus several parasitic images. Two parasitic images at a distance of 17 and 21 pixels away (horizontally) from the main image and the three parasitic images at four pixels away (vertically) from the main image are investigated. The intensities of the other multiple reflections are three orders of magnitude smaller than the main image and are thus neglected. The three parasitic images formed at four pixels away (vertically) from the main image are found to be forming due to multiple reflections at the compensator plate, which are unmodulated signal contributing only to the DC of the interferogram. The parasitic images in the horizontal direction on both side of the main image are found to be due to multiple reflections at the beamsplitter surface. The measured intensities of the parasitic images (horizontal) are 4.9 % and 3.1 % of the main image. Theoretical calculations show that the multiple reflections at the beamsplitter surface give two main parasitic images (horizontal), formed at approximately 19 pixels (one to the left and the other to the right) from the main image. The calculated intensities of the DC part of these two main parasitic images are 3.9 % and 2.8 % of the main image. The exact values of the position and the intensity of the parasitic images cannot be calculated theoretically with the present information of the beamsplitter coating. However, the estimates found are sufficient for a qualitative comparison. The calculated intensities of the AC part of the two main parasitic images are estimated to be 3.1 % and 2.8 % of the main image. From the measurement analysis it can be concluded that, during the atmospheric measurements with the present beamsplitter used in GLORIA interferometer, any given pixel receives the radiation falling on it plus a contribution of the paraxial images. The additional signal due to the parasitic image is not a problem for a homogeneous (horizontal direction) scene, but the effect has to be taken into account for cases of horizontally inhomogeneous scenes. The radiation contribution of the parasitic images is small but will lead to an error in the retrieval of the trace gas concentration over the detector array during scientific data processing.



## 6. Spectrometric characterization

This chapter begins with a description of the methods used to determine and characterize the spectral properties of the GLORIA instrument. In particular, the physical and the mathematical background for the spectral calibration is presented first and the choice of the calibration sources is discussed thereafter. The methods used for the line position determination and optimization of a selected method is presented in the next section. A selection criterion for the lines used for the spectral calibration is discussed in the subsequent section. In the next section, the noise effect on the determination of the spectral calibration method is investigated. The effect of varying the position of the infrared objective on the optical axis position is discussed next. The spectral calibration of the flight data is performed and the results are presented in the following section. An estimation of the accuracy of the spectral calibration is given thereafter. In the next section, the relationship between the line width of the spectral lines and the image distance is evaluated. The line width of the atmospheric lines is used as an indicator for finding the focus position at a given instrument temperature. The chapter concludes with a detailed analysis of the cube corner misalignment producing shear in the interferometer and an analysis and quantification of the shear vibration is presented.

### 6.1. Spectral calibration - Introduction

The modulated part of the interferogram of a monochromatic source is expressed as

$$I(x) = \cos(2\pi\sigma_H x), \quad (6.1)$$

where  $\sigma_H$  is the wavenumber of the monochromatic source and  $x$  is the OPD. The collimated rays passing through the focusing lens travel towards the detector at different angles (figure 2.3). The OPD for the pixel  $(i,j)$  on the detector array is expressed as [18]

$$x_{i,j} = x_0 \cos(\alpha_{i,j}), \quad (6.2)$$

where

- $x_{i,j}$  is the OPD of the pixel  $(i, j)$ ,
- $x_0$  is the OPD of the on-axis pixel,
- $\alpha_{i,j}$  is the off-axis angle of the pixel  $(i, j)$ .

If the OPD of the interferogram is assumed to be pixel independent, then the change in length of the abscissa by  $\cos\alpha_{i,j}$  can be associated with the wavenumber. The wavenumber  $\sigma_{i,j}$  for the off-axis pixels then becomes [18]

$$\sigma_{i,j} = \sigma_0 \cos(\alpha_{i,j}), \quad (6.3)$$

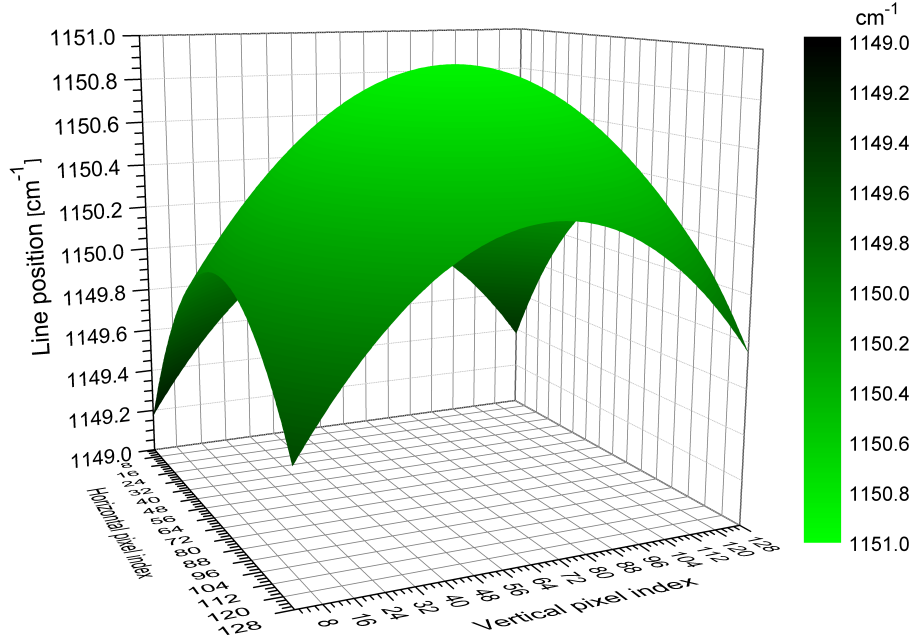


Figure 6.1.: The line position distribution of the  $\text{N}_2\text{O}$  line at  $1150.9099 \text{ cm}^{-1}$  over the detector array showing a three-dimensional bell shape which represents the cosine distribution for the off-axis pixels.

where

$\sigma_0$  is the wavenumber of the on-axis pixel,

$$\cos(\alpha_{i,j}) = b / \sqrt{(b^2 + r_{i,j}^2)},$$

$b$  is the image distance,

$r_{i,j}$  is the distance between the center of the pixel  $(i, j)$  to the optical axis.

Figure 6.1 shows the line position of the  $\text{N}_2\text{O}$  line at  $1150.9099 \text{ cm}^{-1}$  over the detector array for an optical axis position of  $(72, 68)$ . The three-dimensional bell shape represents a cosine distribution.

The off-axis angle is a function of the distance of the pixel center to the optical axis and the image distance. It is represented as follows

$$\alpha_{i,j} = \tan^{-1}\left(\frac{r_{i,j}}{b}\right). \quad (6.4)$$

Substituting the value of  $\cos(\alpha_{i,j})$  in equation 6.3, the equation can be written as

$$\sigma_{i,j} = \sigma_0 \left( \frac{b}{\sqrt{(b^2 + r_{i,j}^2)}} \right). \quad (6.5)$$

The wavelength of the reference laser diode is used to find the x axis scale for the interferogram. The processing is started with an a-priori assumption of the laser wavelength. If the a-priori laser wavelength information is not the true laser wavelength, an additional scaling factor ( $f_{corr}$ ) of the spectral axis has to be applied. The scaling factor has to be adapted corresponding to the temperature drift of the laser diode during the measurement duration. The reference laser diode used in GLORIA has a wavelength drift depending on the temperature change of its surrounding. The scaling factor for the spectral axis is pixel independent. The wavenumber for an individual pixel is written as

$$\sigma_{i,j} = f_{corr} \cdot \sigma_0 \left( \frac{b}{\sqrt{(b^2 + r_{i,j}^2)}} \right). \quad (6.6)$$

Four parameters are needed to calculate the spectral calibration factors for each pixel. It is necessary to determine the image distance, the horizontal (h) and vertical (v) position of the optical axis on the detector array and the scaling factor of the spectral axis for the on-axis position. A minimum of four pixels has to be used in order to calculate all four parameters. Due to the presence of noise in the measurement, an increase in the number of pixels will improve the quality of the parameters retrieved. The line selection criteria for the pixels will be discussed in section 6.3. All available pixels with emission lines satisfying these selection criteria are used for finding the spectral calibration parameters. The calculation of the spectral calibration parameters using the above model is a simplified approach where optical effects like distortion and chromatism are not taken into account. The spectral calibration error for measurement data neglecting these effects is within the error budget, therefore using the simplified model is justified.

### 6.1.1. Determination of the spectral calibration parameters

The spectral position values ( $\sigma_{i,j}$ ) of the selected line for each pixel are determined following a line position determination method (section 6.4). The spectral position values follow a 2D cosine curve (equation 6.3). The values are fitted with a second order 2D polynomial fit routine, which is a good approximation to the cosine dependency of the values. The fit gives the value and the position of the maximum point on the pixel array. The value at the maximum is expressed as  $\sigma_0$ , its position represents the optical axis position ( $h_0, v_0$ ) on the detector array. The optical axis position is determined in a sub pixel resolution. The distance of the center of each pixel from the optical axis is expressed as

$$r_{i,j} = \sqrt{(h_i + 0.5 - h_0)^2 + (v_j + 0.5 - v_0)^2} \quad (6.7)$$

where h and v represent the horizontal and vertical pixel indices.

The  $r_{i,j}$  and the corresponding  $\sigma_{i,j}$  values are sorted in ascending order of  $r_{i,j}$ , thereby transferring the 2D problem into an 1D problem. A curve fit is performed with an a-priori information about the selected line position and the image distance. The function used for the curve fit is given by

$$y = \frac{a_0 a_1}{a_0 + x} \quad (6.8)$$

where  $x = r_{i,j}^2$ ,  $y = \sigma_{i,j}^2$ ,  $a_0 = b^2$ ,  $a_1 = \sigma_0^2$ .

In content, equation 6.8 is the same as equation 6.5. The fitted value of the square root of  $a_0$  and  $a_1$  gives the best estimate of the image distance and the line position. The scaling factor ( $f_{corr}$ ) of the spectral axis is given by the ratio between the determined value of  $\sigma_0$  and the theoretical value  $\sigma_H$  for the used line.

$$f_{corr} = \frac{\sigma_H}{\sigma_0} \quad (6.9)$$

where

$\sigma_0$  is the fitted line position,

$\sigma_H$  is the line position value from HITRAN database [58].

This process is now applied to several selected spectral lines (see section 6.3). The mean of the parameters derived from the selected lines is taken as the final value. If noise is the leading source of error, then the mean parameter value will improve the precision of the determination of the spectral calibration parameters.

The spectral calibration parameters determined are used to calculate the correction factor for each pixel based on the off-axis angle ( $\alpha_{i,j}$ ). The scaling factor for performing the correction is implemented during the interpolation process in level0 by scaling the reference laser wavelength with the appropriate factor for each pixel, therefore the spectra generated are on the same output grid.

### 6.1.2. Spectral calibration sources

The calibration source should have the following properties: Its spectral properties should be well known with lines lying within the spectral range of the instrument. It should fill the full field-of-view (FOV) and full aperture of the instrument to avoid differences between the calibration and scene measurements.

Spectral calibration can be performed by using the following three kinds of sources:

- A laser source with a single line,
- A gas cell containing a gas with one or more lines,
- The atmosphere having spectral lines from different gases.

#### **Laser as a calibration source**

A quantum cascade laser (QCL) can be used as a spectral calibration source. It has the advantage of having a strong and stable spectral line with a good signal-to-noise ratio. However there are several drawbacks for a laser being used as a spectral calibration source. The alignment and operation of the source is complex as both the temperature and operating current have to be kept stable during the whole operation. The QCL sources are highly coherent, they can produce laser speckles which generate an amplitude modulation on the detected signal. The amplitude modulation degrades the spectrum. During atmospheric measurements the QCL has further drawbacks, the whole system is bulky and a dedicated measurement mode with its own time allocation is needed. In case of GLORIA, the QCL is not used for the purpose of spectral calibration but for the characterization and adjustment of the interferometer shear.

#### **Gas cell as a calibration source**

A gas cell with a known mixture of gases within the spectral range of the instrument is a good calibration source. It has the advantage that any gas species or known mixtures of gases for the gas cell can be used. Several spectral lines of the gas can be used at once to improve the precision of the parameters determined. However, there are certain drawbacks when using a gas cell as a spectral calibration source for atmospheric measurements. The precise monitoring of the temperature, pressure and gas composition of the cell is extremely difficult on flight. The gas cell has to be big enough to fill the full instrument aperture and the FOV. An alternative would be to use a smaller gas cell with collimation optics. Moreover, a dedicated measurement mode with an own time allocation is needed. Laboratory characterization measurements have been performed with a gas cell containing N<sub>2</sub>O gas. N<sub>2</sub>O gas has been chosen because it has well isolated lines which are within the spectral coverage of GLORIA.

#### **Atmosphere as a calibration source**

The spectral lines of different known gases in the atmosphere serve as a good source for performing the spectral calibration. The selected lines need to be sufficiently isolated, have a good signal-to-noise ratio and should be well characterized spectroscopically. Selecting lines from the atmosphere has the advantage that the source fills the aperture and the FOV. The measurement object is essentially self-calibrated using its already well known properties. No dedicated measurements for spectral calibration are needed.

## 6.2. Gas cell measurements

$\text{N}_2\text{O}$  gas cell measurements have been performed in the laboratory for determining the spectral calibration parameters. The measurements are used to gain knowledge of the line selection criteria and to establish a method for the determination of the line positions.

### 6.2.1. Laboratory measurement setup

Gas cell measurements were done in the laboratory with GLORIA being placed inside a thermal-vacuum chamber. The chamber was cooled and temperature controlled by liquid nitrogen ( $\text{LN}_2$ ) passing through the tubes inside the chamber. Gaseous nitrogen is flushed inside the chamber in order to avoid interfering species during the measurement. The pressure in the vacuum chamber was kept at about 120 mbar and the temperature at about 210 K, in order to simulate the atmospheric pressure and temperature at the flight altitude of the HALO aircraft. The line parameters are evaluated from the  $\text{N}_2\text{O}$  emission lines measured from the gas cell setup. The chamber setup and the gas cell were developed by Erik Kretschmer for the purpose of instrumental line shape (ILS) characterization [59].

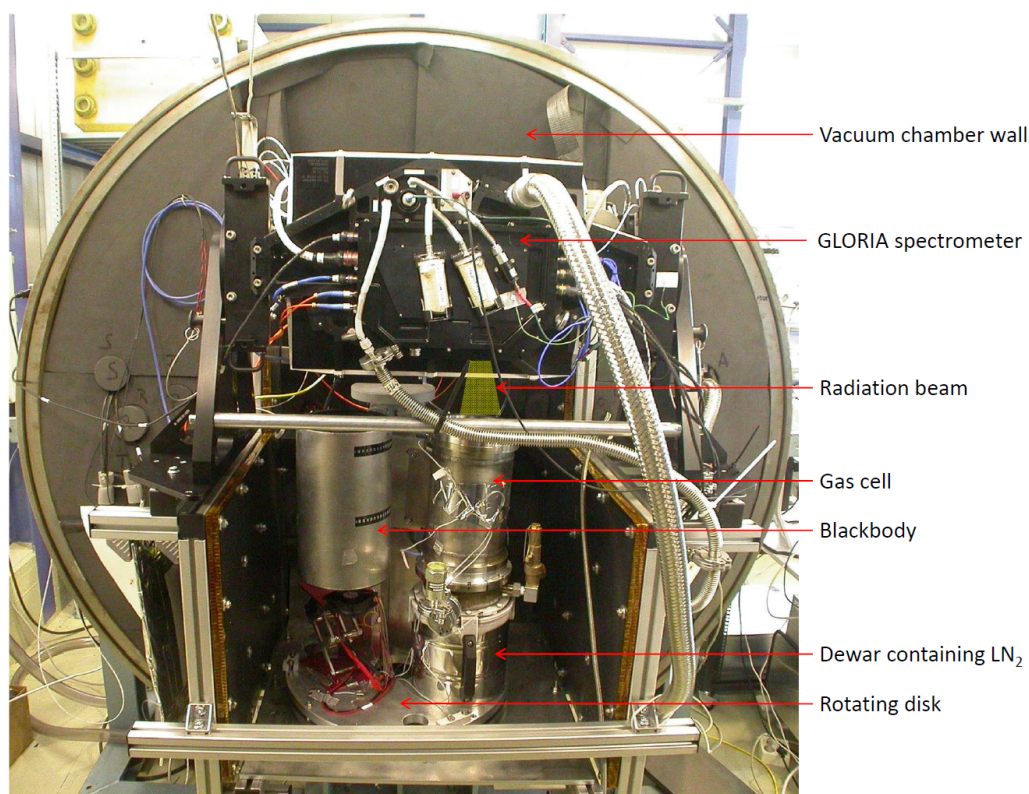


Figure 6.2.: Measurement setup with GLORIA being placed inside the thermal-vacuum chamber.

The setup of the GLORIA spectrometer fixed inside on the wall of the thermal-vacuum chamber is shown in figure 6.2. The spectrometer is looking downwards in this configuration. The gas cell with the liquid nitrogen holder (as background) is placed below GLORIA on a rotating disk along with a blackbody. The rotating disk gives the possibility to look at both sources while the instrument is fixed at one position. The dark yellow beam shows the path of the radiation beam entering from the dewar to the interferometer.

Some of the important settings used for the measurements are

- (i) the gas cell filling: 10 mbar of  $\text{N}_2\text{O}$  and about 150 mbar of total pressure,
- (ii) the gas temperature: 233 K to 266 K with a background temperature of 80 K,
- (iii) the blackbody temperature:  $\approx 258$  K,

- (iv) the spectral band selected containing N<sub>2</sub>O lines: 1120 cm<sup>-1</sup> to 1220 cm<sup>-1</sup>,
- (v) an interferogram length: 8.192 cm,
- (vi) a measurement time for one *cube*: 24.6 sec.

### 6.2.2. Simulations

The first step in the spectral calibration process is the selection of the single isolated lines with a good signal-to-noise ratio. The selection criteria for the spectral lines are determined by using a simulated spectrum. A band of the N<sub>2</sub>O spectrum in the range between 1120 cm<sup>-1</sup> and 1220 cm<sup>-1</sup> is simulated using the KOPRA (Karlsruhe Optimized and Precise Radiative transfer Algorithm) [60] forward model, where the GLORIA instrument parameters and gas cell parameters are given as input for the simulation. The simulated spectrum is generated without noise.

Some of the principle parameters used for the simulation are

- (i) a homogeneous path in the gas cell,
- (ii) a spectral sampling of 0.0625 cm<sup>-1</sup> (corresponds to a MOPD of 8 cm),
- (iii) a Norton-Beer strong apodization.

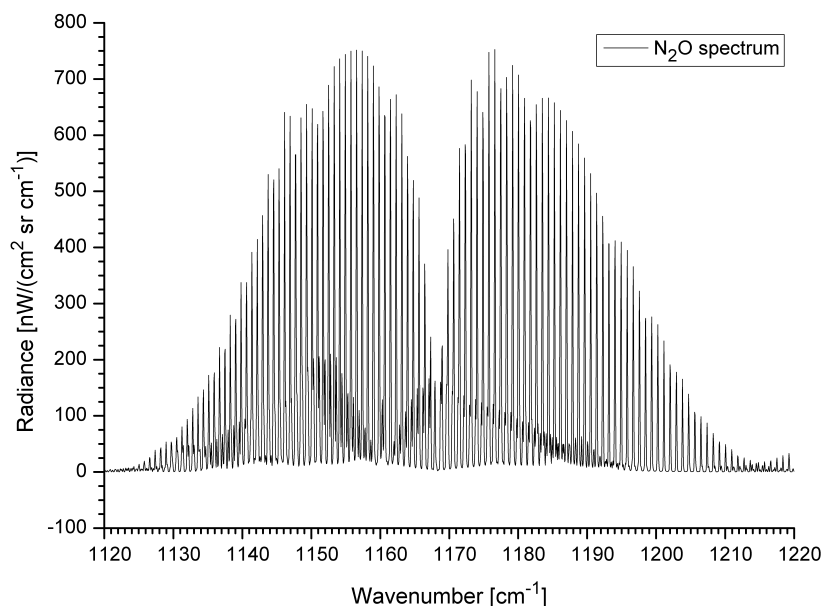


Figure 6.3.: Simulated N<sub>2</sub>O spectrum without noise generated using KOPRA and realistic parameters for the GLORIA instrument.

A noise free simulated N<sub>2</sub>O spectrum is shown in figure 6.3. The simulated spectrum is re-sampled on a finer grid by zero filling. All N<sub>2</sub>O lines which are selected have an intensity greater than  $1 \times 10^{-21} \text{cm}^{-1}/(\text{molecule cm}^{-2})$  according to the HITRAN database and lie within the above selected spectral range. The line position at 1167.87832 cm<sup>-1</sup> is labeled as 0 line index for reference. All selected lines which are to the right of line 0, i.e., increasing wavenumber side are given positive number indices, and all selected lines which are to the left of line 0 are given negative number indices, for eg., line +2: 1169.8138 cm<sup>-1</sup> and line -2: 1166.45808 cm<sup>-1</sup>.

### 6.3. Line selection criteria

The simulated spectrum (figure 6.3) has been used to determine which lines are to be used for the spectral calibration. The line positions and intensities of all selected indexed N<sub>2</sub>O lines are determined using the zero filling method (see section 6.4) of the line position determination.

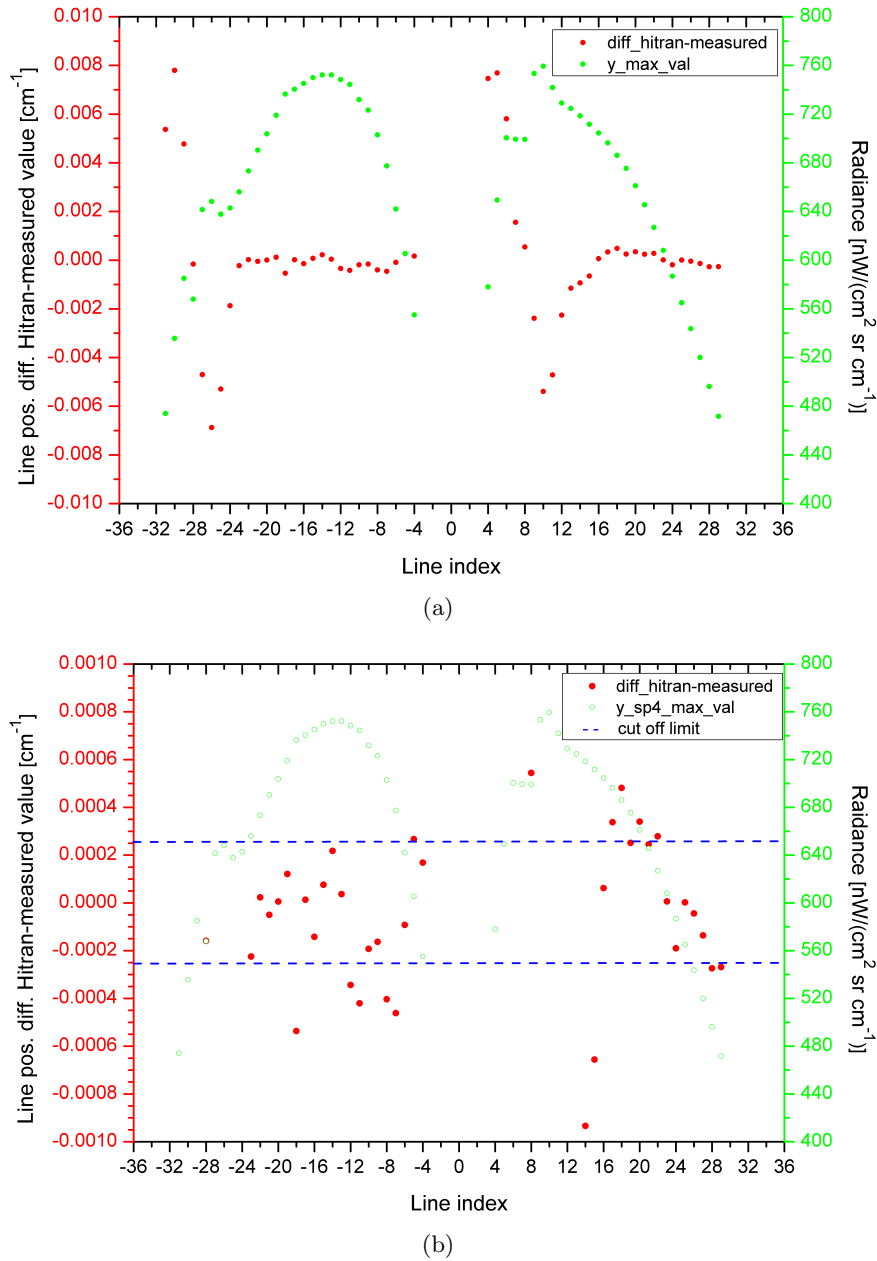


Figure 6.4.: The line intensity and line position differences between the HITRAN values and the  $\text{N}_2\text{O}$  lines simulated by using KOPRA considering realistic instrument parameters are plotted against the  $\text{N}_2\text{O}$  line indices. (a) plot with all lines and (b) zoom of the central part in the ordinate axis range  $\pm 0.001 \text{ cm}^{-1}$ . The blue dotted lines represent the limit for the selection of  $\text{N}_2\text{O}$  lines for further analysis.

The difference in the line position between the simulated spectrum and the HITRAN values plotted against the line indices is shown in figure 6.4(a). The difference in the line position is higher for the lines at the beginning of the P and R branch of the  $\text{N}_2\text{O}$  band. The lines which are in the middle or at the end of the P and R branch have less overlapping between the weak and the strong  $\text{N}_2\text{O}$  lines. Some lines with small intensities have an influence on the neighboring lines. These lines are not fully resolved and an overlapping neighboring line leads to an error in the determination of the peak position of the line. A limit of  $\pm 0.00025 \text{ cm}^{-1}$  (blue dotted lines, figure 6.4(b)) is chosen arbitrarily. The line position error of the selected lines is less than 0.22 ppm. All lines with differences within the selected limit are selected and lines outside this limit are avoided for further analysis.

The selected lines are sufficiently isolated from their neighboring lines.

The N<sub>2</sub>O lines selected by using the above criteria are listed below. The line position values are taken from the HITRAN database:

Line index	Position [cm <sup>-1</sup> ]	Line index	Position [cm <sup>-1</sup> ]	Line index	Position [cm <sup>-1</sup> ]
-28	1145.33057	-15	1155.75224	+16	1181.77992
-23	1149.30847	-14	1156.5651	+19	1184.38527
-22	1150.1084	-13	1157.37975	+21	1186.12933
-21	1150.90987	-10	1159.83409	+22	1187.00339
-20	1151.71288	-9	1160.65575	+23	1187.87875
-19	1152.51749	-6	1163.13155	+24	1188.75539
-17	1154.13154	-5	1163.96045	+25	1189.63324
-16	1154.94105	-4	1164.79117	+26	1190.51228
				+27	1191.39245

The effect of noise in the determination of the line position for the selected lines is shown in section 6.5.

## 6.4. Line position determination methods

Three different methods have been considered for determining the spectral position of the selected line. The advantages and disadvantages of these methods are discussed in this section. One of the methods will be chosen as a standard for further data processing. A N<sub>2</sub>O line with a good signal-to-noise ratio has been selected from the gas cell measurements for testing the line position determination methods. The spectral shift is the difference between the detected line position and the theoretical value from the HITRAN database.

### Line fitting method

The line fitting method implies that a theoretical line shape is fitted to the selected line from the measurement. The maximum position of the fitted line gives the line position of the selected line. The line fitting program used for this analysis was previously developed for the MIPAS-balloon (Michelson Interferometer for Passive Atmospheric Sounding) instrument [61]. It has several parametrization options, such that it can be used for data measured with any kind of instrument. The measured spectra are apodized. A Gauss profile is fitted to each line and the best fit is then found by an iterative process. This method has certain drawbacks. It needs a-priori knowledge of the line position and certain instrument parameters to simulate the Gaussian line profile. The processing is time consuming as several iteration steps might be needed for fitting two spectra (measured and simulated) for each line detected in the spectral window.

### Zero filling method

The zero filling method does a zero filling of the interferogram before performing the Fourier transformation to get the spectrum on a finer grid. A spectral region containing the isolated line is selected. The maximum position of the line within this region gives the line position of the selected line. The accuracy of the line position determination based on the zero filling term is discussed later in this section. This method has the advantage of being quite straight forward. The calculation time for the zero filling method depends on the zero filling term used, which is dependent on the spectral accuracy requirements.

The measured spectrum from the gas cell measurement is cut around the region of 1120 cm<sup>-1</sup> to 1220 cm<sup>-1</sup> containing the N<sub>2</sub>O lines. The cut spectrum is Fourier transformed to get an interferogram. The interferogram is zero filled such that the number of points after the

zero filling is  $2^n$ , where  $n$  is the zero filling term. The zero filled interferogram is Fourier transformed in order to get a spectrum on a much finer grid. Increasing  $n$  results in an increase in the calculation time. Therefore a trade off between the zero filling term and the calculation time has to be made. The minimum value of the zero filling term that will give sufficiently accurate results in determining the spectral calibration parameters is to be determined (see section 6.4.1).

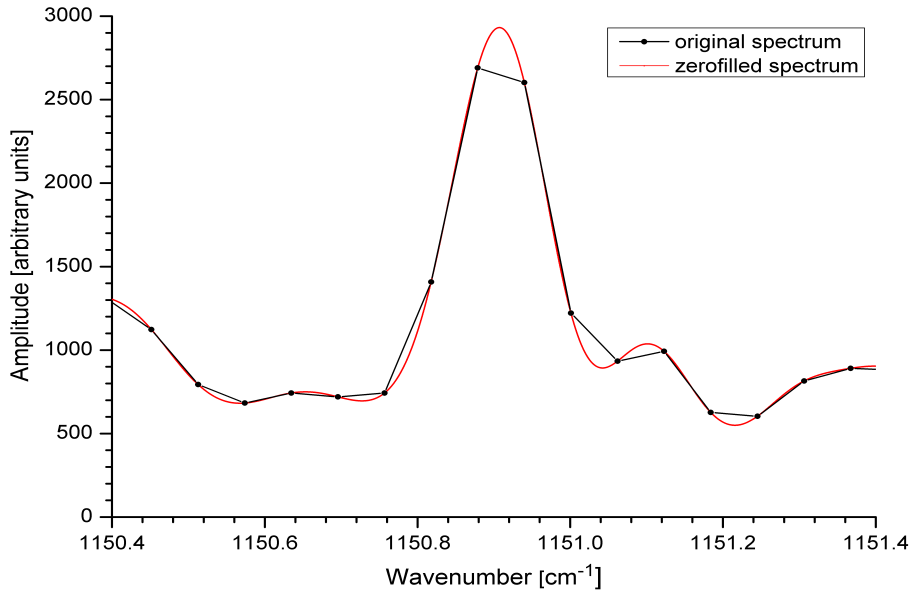


Figure 6.5.: A measured  $\text{N}_2\text{O}$  line spectrum plotted as a function of wavenumber. Black: Original spectrum, red: Zero filled spectrum.

A measured spectral line (black curve) and the spectrum (red curve) of the zero filled interferogram calculated with a zero filling term of 20 are shown in figure 6.5. The original grid is  $\approx 0.061035 \text{ cm}^{-1}$  and the interpolated grid after the zero filling becomes  $\approx 0.000153 \text{ cm}^{-1}$ . The line position information of the selected  $\text{N}_2\text{O}$  lines are used as a-priori knowledge. An expected line position is calculated dependent on the pixel position on the FPA by using equation 6.6 with the knowledge of the a-priori information of the line position from the HITRAN database, the optical axis position and the image distance. A spectral window of  $\pm 0.3 \text{ cm}^{-1}$  has been chosen around the expected line position. The abscissa and the ordinate values of the maximum point of the interpolated spectrum within this range give the line position and line amplitude, respectively.

### Line derivative method

The line derivative method uses the zero crossing point of the derivative of a spectral line as the maximum position of the selected line. The spectrum is generated by performing the Fourier transform of a moderately zero filled interferogram. The derivative of the spectral line is calculated. The zero crossing point of the line derivative is found by performing a linear interpolation between the two points which are closest to zero. The abscissa value of the zero crossing point represents the line position of the selected line. The error in the line position determination is dependent on the discrete nature of the spectrum. Performing a moderate zero filling reduces the sensitivity to noise. The greater the number of data points in the zero filled spectrum across the line, the smaller is the difference between the measured line profile and the actual profile. The derivative calculation amplifies the noise. The derivative method has the advantage that only a moderate amount of zero filling is needed. On the other hand it requires an additional mathematical step of finding the line

derivative. This method is faster than the two methods described above as here only a coarse zero filling is needed.

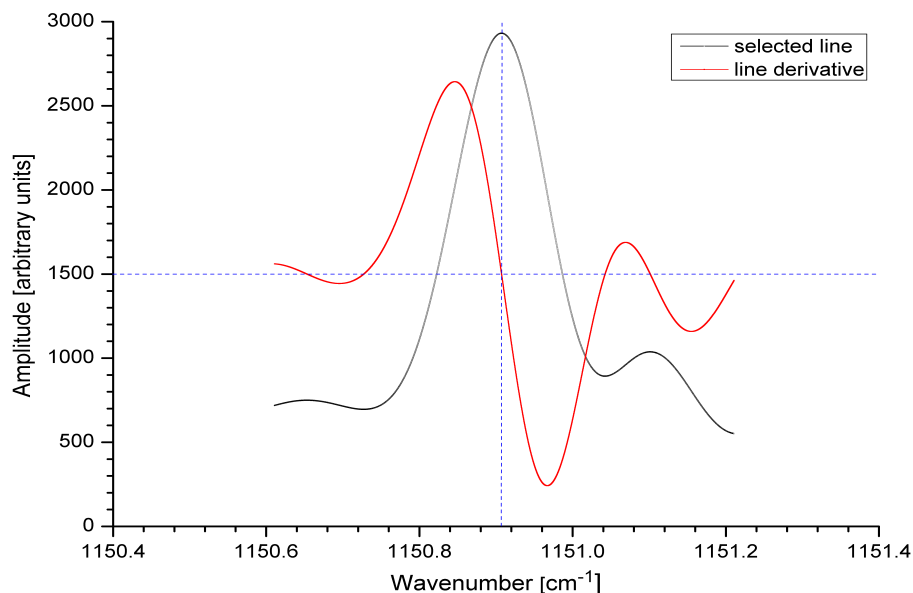


Figure 6.6.: A measured  $\text{N}_2\text{O}$  line spectrum and its first order derivative plotted as a function of wavenumber. Black: Zero filled spectrum, red: First order derivative of the zero filled spectrum, horizontal and vertical blue dotted lines passing through the zero crossing point and maximum point of the curves, respectively.

The same measured spectrum as mentioned above has been taken for verifying this method. A spectral window of  $\pm 0.3 \text{ cm}^{-1}$  has been chosen around the expected line position. A first order derivative of the moderately zero filled spectrum in the selected spectral window is calculated. Figure 6.6 shows the selected spectral line after zero filling and its first order derivative.

### Summary: Line position determination methods

The line fitting method, the zero filling method and the line derivative method gave comparable results for the spectral calibration parameters. The line fitting method is very time consuming compared to the other two processes because of its iterative process of fitting the line. The line derivative method requires less zero filling but needs an extra calculation step of finding the line derivative. The zero filling method is chosen for further data analysis for finding the spectral calibration parameters because of its straightforward approach.

#### 6.4.1. Optimization of the zero filling method for the line position determination

The line positions of the selected  $\text{N}_2\text{O}$  lines (section 6.3) for one *cub* file are determined using the zero filling method with several zero filling terms. This method is optimized for speed at the cost of precision.

The zero filling method has been tested with different cases of zero filling performed to the interferogram with zero filling terms of  $n = 12, 13, 14, 16, 18$  and  $20$ . The measurement data set has a spectral sampling of  $0.061035 \text{ cm}^{-1}$ , which corresponds to having 1310 points in the spectral range of  $1120 \text{ cm}^{-1}$  to  $1220 \text{ cm}^{-1}$ . A time analysis and comparison of the calibration parameters derived has been done for all zero filling terms.

A-priori information about the approximate values of the spectral calibration parameters is known and used to calculate the expected line position for each pixel. The distance between the  $\text{N}_2\text{O}$  lines (as indexed in figure 6.4(a)) is in the range of  $0.78 \text{ cm}^{-1}$  to  $0.89 \text{ cm}^{-1}$ . A window of  $\pm 0.3 \text{ cm}^{-1}$  is chosen around the selected line position values. The line position of the selected line is determined as the position of the maximum value within this window. A further test is made to check if the determined line position lies in the center 50 % (i.e.,  $\pm 0.15 \text{ cm}^{-1}$  of the expected line position) range of the selected spectral window. This way, a false detection of the peak can be avoided in case of the presence of high values in the region away from the peak. The high values can be due to the presence of noise and neighboring lines of low intensity. The lines of those pixels which pass the selection criteria are taken for the calculation of the spectral calibration parameters. The same selection criterion is applied for the on-axis and all off-axis pixels taking the off-axis effects into account.

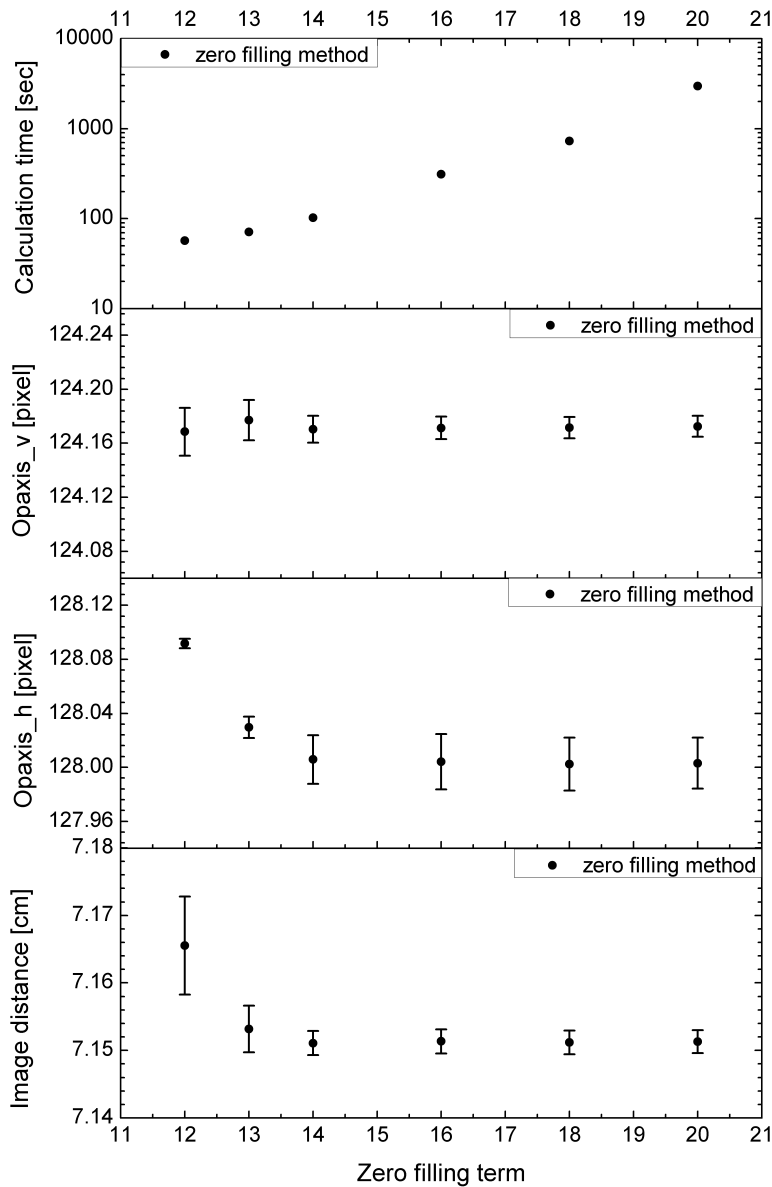


Figure 6.7.: The spectral calibration parameters plotted for different zero filling terms using the zero filling method of line finding. (1st - top) the calculation time plotted on logarithmic scale, (2nd) the optical axis v, (3rd) the optical axis h and (4th - bottom) the image distance, all plots are corresponding to the zero filling terms of 12, 13, 14, 16, 18 and 20.

Table 6.1.: Line position difference for the zero filling method using several zero filling terms.

zero filling term	spectral sampling ( $\text{cm}^{-1}$ )	zero filling method error (ppm)
20	0.000153	reference
18	0.000610	0.02
16	0.002440	-0.02
14	0.009760	0.11
13	0.019521	-0.10
12	0.039041	-4.12

The calculation time (plotted on logarithmic scale) needed for processing with different zero filling terms using the zero filling method is shown in figure 6.7 (top). The number of points in the spectrum increases with the increase in the zero filling term, which in turn increases the computational time for the data processing. The calculation time is almost the same for the zero filling terms of 12, 13 and 14. It starts to increase at 16 and shows a significant increase for the zero filling terms of 18 and 20.

The mean (circular points) and the standard deviation (vertical bar) of the spectral calibration parameters of the selected  $\text{N}_2\text{O}$  lines are shown in figure 6.7 (plot 2 - 4). The parameter values calculated for zero filling terms of 20, 18, 16 and 14 are almost the same. The values calculated for the zero filling term of 13 show a small difference and the values differ largely for the zero filling term of 12.

The line position for the corner pixel (56,56) of the selected array has been calculated from the spectral calibration parameters for all cases of zero filling. Since the actual position of the optical axis parameters are not known, the real position of the line position for the corner pixel cannot be determined. Therefore, the line position calculated for the zero filling method with the zero filling term of 20 has been taken as reference. An estimation of the error made for all other cases has been calculated and is shown in table 6.1. The best possible scenario is to use the highest zero filling term provided calculation time is not an issue. However, for cases where calculation time is critical, a zero filling term of 16 is a reasonable compromise between the calculation time and accuracy.

## 6.5. Noise effect on the determination of the spectral calibration parameters

The simulated  $\text{N}_2\text{O}$  spectrum as described in section 6.2.2 has been used for the analysis of the noise effect on the determination of the spectral calibration parameters. The simulated spectrum has been used for each pixel by scaling the spectral axis of the spectrum with  $\cos(\alpha_{i,j})$ , where  $\alpha_{i,j}$  is the off-axis angle corresponding to pixel (i,j). The settings used for performing the scaling of the spectral axis are

- (i) the detector offset (h,v) as (56,56) pixel,
- (ii) the detector pixel area as  $128 \times 128$  pixels,
- (iii) the optical axis position (h,v) as (128,124) pixel,
- (iv) the image distance (b) as 7.2 cm.

After performing the spectral scaling with the off-axis angle, the spectrum for each pixel is interpolated on an equidistant grid of  $0.05 \text{ cm}^{-1}$  using a sinc interpolation. The line positions of the selected  $\text{N}_2\text{O}$  lines are determined using the zero filling method with a zero filling term of 16.

The simulated spectrum has been combined with white noise of different levels. The spectral calibration parameters are calculated from the without-noise and with-noise spectra for several signal-to-noise ratios. The signal-to-noise ratios shown in table 6.2 correspond to the line with the maximum intensity (line at  $1156.565186 \text{ cm}^{-1}$ ) in the band. Laboratory gas cell measurements had a signal-to-noise ratio of three. Atmospheric measurements during the ESSenCe measurements had a signal-to-noise ratio between fifteen and slightly below three depending on the measurement tangent altitude. The mean and standard deviation of the calculated parameters from the selected 25  $\text{N}_2\text{O}$  lines (section 6.3) are given in table 6.2. The error column in the table represents the line position difference for the corner pixel (56,56) between the expected value from the simulation parameters and the value calculated using the determined spectral calibration parameters.

Table 6.2.: Spectral parameters from simulated spectrum without and with noise.

SNR	optical_axis_h (pixel)		optical_axis_v (pixel)		b (cm)		error
value	mean,	sd	mean,	sd	mean,	sd	ppm
No noise	127.998,	$2.4e^{-5}$	123.999,	$2.1e^{-5}$	7.2,	$1.43e^{-5}$	-0.01
16	127.999,	$5.57e^{-3}$	123.999,	$3.23e^{-3}$	7.201,	$9.46e^{-4}$	-0.59
12	127.996,	$6.65e^{-3}$	123.999,	$7.33e^{-3}$	7.202,	$8.37e^{-4}$	-0.78
10	128.000,	$7.31e^{-3}$	123.999,	$7.31e^{-3}$	7.202,	$1.51e^{-3}$	-1.23
8	127.997,	$8.16e^{-3}$	123.99,	$1.03e^{-2}$	7.204,	$1.61e^{-3}$	-1.75
6	128.00,	$1.48e^{-2}$	123.99,	$1.37e^{-2}$	7.206,	$1.96e^{-3}$	-2.72
4	127.99,	$1.93e^{-2}$	123.99,	$1.67e^{-2}$	7.208,	$3.82e^{-3}$	-3.77
3	128.00,	$2.65e^{-2}$	123.99,	$2.10e^{-2}$	7.208,	$4.61e^{-3}$	-3.55

The parameters determined for the noise free spectrum are very close to the a-priori values. The difference between the result and the input value is due to interpolation and numerical rounding. The maximum error in the line position for the corner pixel due to noise is less than 4 ppm for a SNR of down to three. The standard deviation of the image distance value for the SNR of two is an order of magnitude higher (0.016 cm) than the standard deviation for the SNR of three (0.004 cm). The number of pixels which are rejected in the line selection criteria are high for the scenario with SNR of two. The high scatter and less number of usable pixels makes the determination of the spectral calibration parameters difficult for the scenario with SNR of two. The average SNR of the selected lines from the ESSenCe campaign measurement data is about nine. This implies that the line position error for the corner pixel due to noise will be less than 1.7 ppm. Experience with the instruments measuring the atmospheric emission has shown that for performing trace gas retrieval an error budget of 10 ppm is allowed for spectral calibration. The line position error value for the corner pixel is a factor of 6 smaller than the 10 ppm error budget.

The effect of noise for each individual line is investigated for the selected  $\text{N}_2\text{O}$  lines (section 6.3). The line position for each pixel is determined for the simulation performed without noise and with noise (SNR of twelve). The difference in the line position position of the two cases will give the noise effect on the error in the line position determination. The ratio of the line intensities of the strongest and the weakest line from those selected  $\text{N}_2\text{O}$  lines is 1.5.

The standard deviation of the  $\text{N}_2\text{O}$  line position values for each selected line for  $128 \times 128$  pixels are calculated and plotted against the corresponding line positions in the range between  $1140 \text{ cm}^{-1}$  and  $1200 \text{ cm}^{-1}$  are shown in figure 6.8. The line position determination

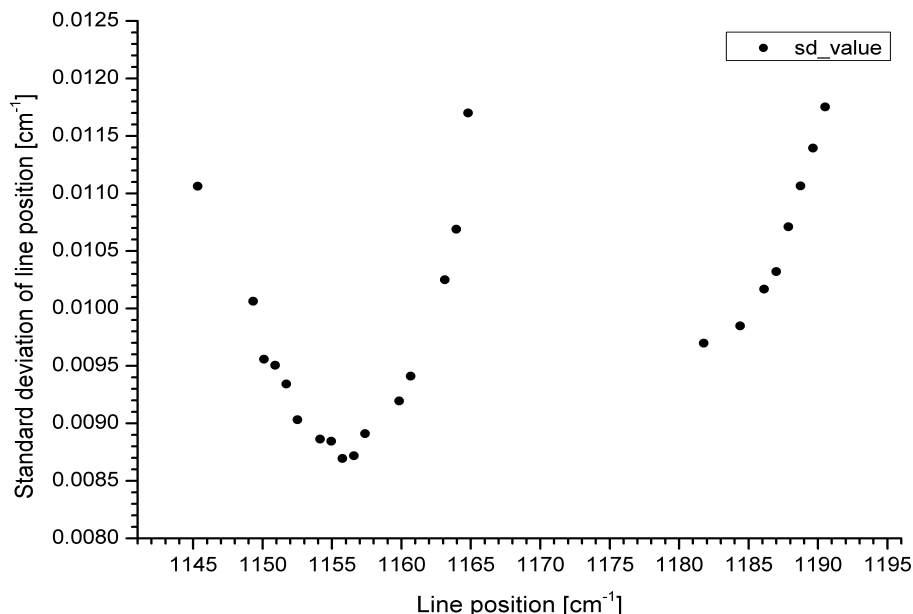


Figure 6.8.: The standard deviation of the line position values for  $128 \times 128$  pixels plotted for the  $\text{N}_2\text{O}$  lines with a SNR of 12 for the strongest line in the range between  $1140 \text{ cm}^{-1}$  and  $1200 \text{ cm}^{-1}$ .

works better for lines with a higher signal-to-noise ratio. The standard deviation of the line position variation is in the range of 7.4 ppm to 10 ppm depending on the selected lines. The standard deviation increases by less than 30 % while the line intensity changes by a factor of 1.5. Using other selected lines with a slightly reduced line strength increases the precision in the determination of the spectral calibration parameters.

The simulation results show the sensitivity of the method for the determination of the line position and the spectral calibration parameters with respect to white noise. The measurement data has other instrumental effects, namely varying SNR over the detector array depending on the source, pixel dependent noise amplitudes, defocusing and chromatic aberrations which may influence the line position determination. The line position and the spectral calibration parameters determined from the atmospheric measurement are discussed in section 6.7.

## 6.6. Optical axis variation with infrared objective movement

The infrared objective (IRO) has to be adjusted to the focus position, which varies with the operating temperature of the GLORIA interferometer. The IRO is placed in a mechanical holder and can be rotated on a thread to move in the forward and backward directions. The eccentricity of the thread determines the change in the position of the optical axis with the change of the position of the IRO upon movement. Laboratory measurements were performed at several infrared objective positions moving in steps of 25 counts (approximately 0.169 mm) and with a gas cell containing  $\text{N}_2\text{O}$  gas as source. The gas cell filling for the measurement was such that the  $\text{N}_2\text{O}$  lines in the band of  $1240 \text{ cm}^{-1}$  to  $1320 \text{ cm}^{-1}$  showed lines with good signal-to-noise ratio. Four lines with a good signal-to-noise ratio and sufficiently away from the neighboring lines are selected for determining the optical axis position. The gas cell had a cold background of a liquid nitrogen bath to improve the signal contrast. The measurements were performed at room temperature and pressure and with an interferometer temperature of approximately 223 K.

The optical axis (h,v) positions for four spectral lines for each position of the IRO are calculated and plotted in figure 6.9. The horizontal (solid points) and the vertical (empty

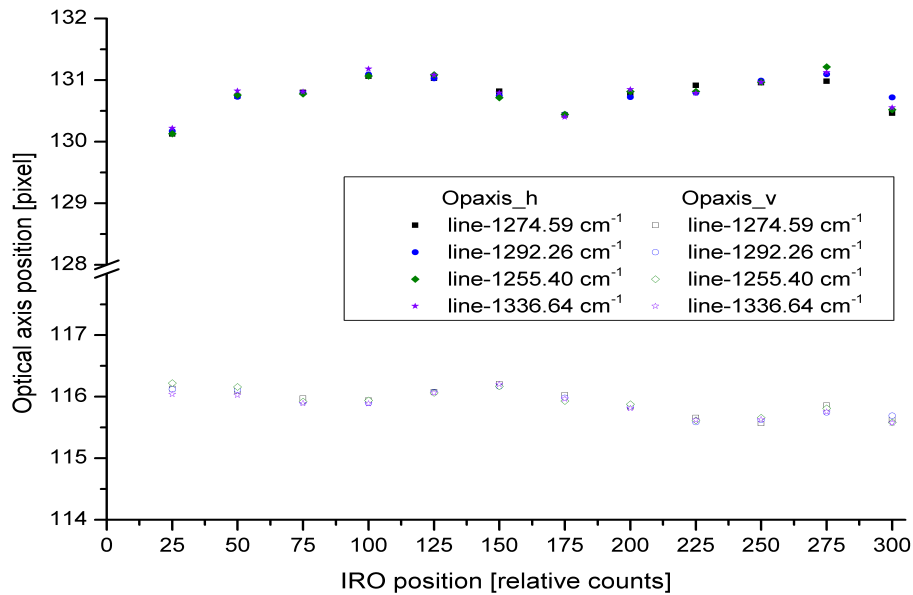


Figure 6.9.: The optical axis (h,v) position variation with the movement of the infrared objective on its axis. The periodic oscillation corresponds to one complete rotation of the IRO on its rotation axis.

points) components of the optical axis values show a periodic variation. The variation frequency is roughly 150 counts (approximately 1 mm) which corresponds to one complete rotation of the IRO around its axis. The plot shows the form of the movement of the IRO on its holder. This effect has to be taken care of while performing the spectral calibration of data for cases where the IRO has to be adjusted. In case the IRO is moved by 75 counts (approximately 0.5 mm) and the optical axis position of the first data set is used for performing spectral calibration of the second data set, then the line position error for the corner pixel (56,56) will be about 19 ppm. The adjustment of the IRO with the change of the interferometer temperature has to be preferably done in one direction only. Moving the IRO in the reverse direction makes a jump in the optical axis by approximately  $2 \times 2$  pixels.

## 6.7. Spectral calibration from in-flight measurements

The spectral calibration performed with the measurements recorded during the ESSenCe campaign flight K01\_F02 and the TACTS campaign flight K03\_F14 is discussed in this section.

### Spectral calibration of the ESSenCe flight K01\_F02 data

The spectral calibration parameters from the ESSenCe flight data are determined from atmospheric chemistry mode measurements<sup>1</sup> by co-adding 18 measurements in one interferometer drive direction (forward drive movement). The co-adding has been done to get a better signal-to-noise ratio. An approximate SNR value of 16 is achieved by the co-addition for the CO<sub>2</sub> line at  $951.192263 \text{ cm}^{-1}$  (strongest line in the range of  $940 \text{ cm}^{-1}$  to  $972 \text{ cm}^{-1}$ ) for the central pixel. The measurements were done with a detector array of  $48 \times 128$  pixels having an offset of 96,56. The detector offset was chosen such that the optical axis position lies relatively close to the center of the selected detector array for the measurement.

<sup>1</sup>Measurements are in the time range between 14:28:55 and 14:49:15

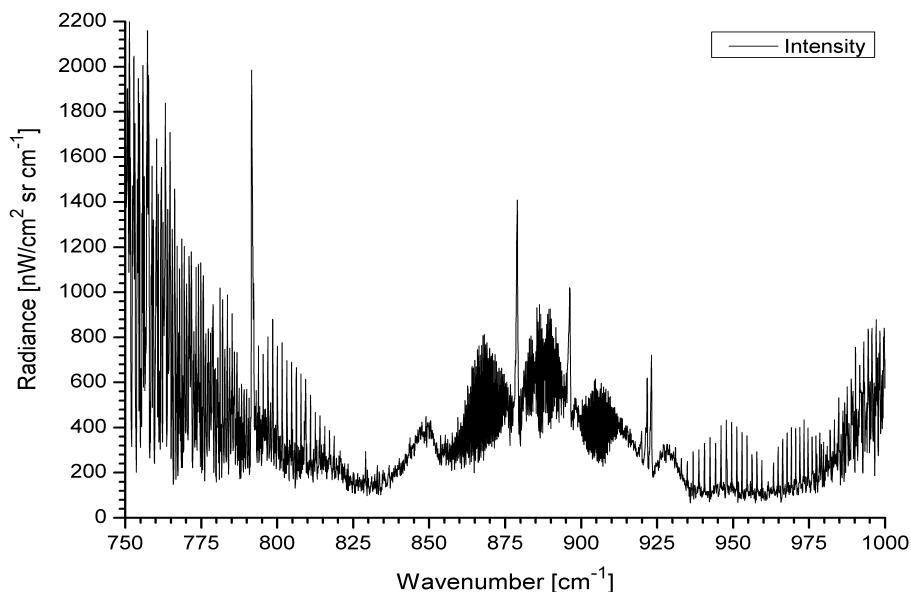


Figure 6.10.: Atmospheric spectrum plot for pixel (126,124) from flight K01\_F02 in the range between  $750\text{ cm}^{-1}$  and  $1000\text{ cm}^{-1}$ .

Table 6.3.: The line position and intensity of the selected  $\text{CO}_2$  lines from the HITRAN database used for the spectral calibration of the data measured during flight.

Line number	Line position [ $\text{cm}^{-1}$ ]	Line intensity [ $\text{cm}^{-1}/(\text{molecule}\cdot\text{cm}^{-2})$ ]
1	940.548098	$1.775e^{-23}$
2	942.383336	$1.946e^{-23}$
3	944.194029	$2.084e^{-23}$
4	945.980229	$2.176e^{-23}$
5	949.479313	$2.174e^{-23}$
6	951.192263	$2.064e^{-23}$
7	952.880849	$1.876e^{-23}$
8	954.545086	$1.612e^{-23}$
9	956.184982	$1.279e^{-23}$
10	957.800537	$8.884e^{-24}$
11	964.768981	$1.103e^{-23}$
12	966.250361	$1.478e^{-23}$
13	967.707233	$1.791e^{-23}$
14	969.139547	$2.032e^{-23}$
15	970.547244	$2.195e^{-23}$
16	971.930258	$2.28e^{-23}$

The most suitable region for finding isolated lines from atmospheric spectra recorded by GLORIA is between  $940\text{ cm}^{-1}$  and  $972\text{ cm}^{-1}$ . This region contains  $\text{CO}_2$  lines (figure 6.10) along with the presence of  $\text{O}_3$  lines towards the end of the R branch of the band. Single isolated  $\text{CO}_2$  lines with a good signal-to-noise ratio (according to HITRAN database)

are selected from this region. The CO<sub>2</sub> lines which are present due to isotopes or other vibrational levels in this spectral region have intensities which are two orders of magnitude smaller than the selected lines, so they have very little influence on the main lines. The spectral lines chosen are listed in table 6.3. The line position and intensity values shown in table 6.3 are taken from the HITRAN database. All other regions in the spectral range of GLORIA either have a contribution of lines from multiple gases or have gases with no single isolated line with good signal-to-noise ratio over the whole array.

### Determination of the spectral calibration parameters

The line positions for the selected spectral lines are determined using the zero filling method. The calculation time was not an issue for this analysis, so a zero filling term of 20 was used such as to have minimum error due to the determination method. The spectral sampling before and after the zero filling are  $0.0625 \text{ cm}^{-1}$  and  $0.00019085 \text{ cm}^{-1}$ , respectively.

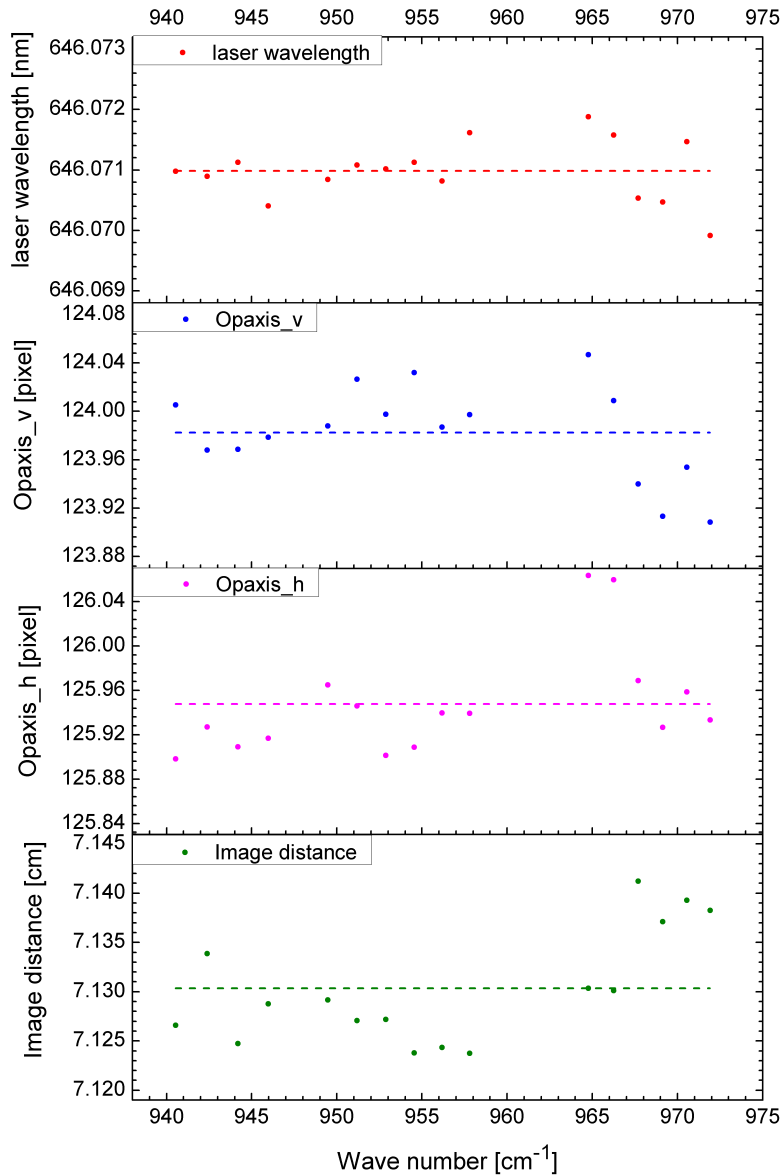


Figure 6.11.: The spectral calibration parameters calculated using the selected atmospheric lines of set 1 forward direction data from flight K01\_F02. (1st - top) the laser wavelength, (2nd) the vertical component of the optical axis, (3rd) the horizontal component of the optical axis, (4th - bottom) the image distance.

The reference laser wavelength, the position of the optical axis  $v$  and  $h$  and the image distance ( $b$ ) are calculated using the line position information for the selected lines (table 6.3) over the detector array. The values for individual lines are plotted in figure 6.11 from the top to the bottom in the order as mentioned above. The dashed lines in the plots represent the mean of the values. The mean and standard deviation of the parameters are given in table 6.4.

Table 6.4.: Mean and standard deviation of the spectral calibration parameters calculated using the selected atmospheric lines from flight K01\_F02.

Parameter	mean	sd
Optical axis $h$ [pixel]	125.94	0.0495
Optical axis $v$ [pixel]	123.98	0.0396
Image distance ( $b$ ) [cm]	7.130	0.00584
Laser wavelength [nm]	646.0709	0.000507

The pixel selection criterion applied for the measurement is the following: An estimated line position for the selected line for any given pixel is calculated from the a-priori information about the spectral calibration parameters taking the off-axis effect into consideration. The distance between the  $\text{CO}_2$  lines (in the range of  $940 \text{ cm}^{-1}$  to  $972 \text{ cm}^{-1}$ ) is in the range of  $1.86 \text{ cm}^{-1}$  to  $1.36 \text{ cm}^{-1}$ . A window of  $\pm 0.5 \text{ cm}^{-1}$  is chosen around the estimated line position of the selected line. The line position of the selected line is determined as the position of the maximum value within this window. A further test is made to check if the determined line position lies in the center 50 % (i.e.,  $\pm 0.25 \text{ cm}^{-1}$  of the expected line position) range of the selected spectral window. This additional limit helps to avoid a false detection of the peak in case of the presence of high values in the region away from the peak. The high values can be due to the presence of noise and/or neighboring lines of low intensity. The lines of those pixels which pass the selection criteria and have emission lines, are taken for the calculation of the spectral calibration parameters. The line positions of the selected pixels for one spectral line are shown in figure 6.12 (extreme left plot). The pixel range selected is quite representative for other lines as well. Pixels from the lower part of the array are rejected due to clouds. The spectra of these pixels contain absorption lines instead of emission lines.

### Performing the spectral calibration

The data set described above was spectrally calibrated using the parameters calculated and shown in table 6.4. The spectrally calibrated measurements are co-added and checked for the line position variation over the detector array.

The line positions for the  $\text{CO}_2$  line at  $967.707 \text{ cm}^{-1}$  over the detector array of  $48 \times 128$  pixels are determined before (figure 6.12, left) and after (figure 6.12, middle) performing the spectral calibration. The line position after performing the spectral calibration should be equal to the theoretical value if the calibration has worked properly. However, the line position distribution after performing the spectral calibration shows a constant value with some random high and low values (figure 6.12, middle). Approximately 56 % and 82 % of the pixels fall in the range with the line position error of  $\pm 5 \text{ ppm}$  and  $\pm 10 \text{ ppm}$ , respectively. The signal-to-noise ratio of the  $\text{CO}_2$  line at  $967.707 \text{ cm}^{-1}$  is determined for each pixel over the detector array and shown in figure 6.13 (right). The plot shows that the SNR is varying between 15 and slightly below 3 for the detector array with  $48 \times 128$  pixels. The SNR gets worse for the pixels in the upper rows which are looking above the flight altitude. The line position determination is affected by the low SNR. This

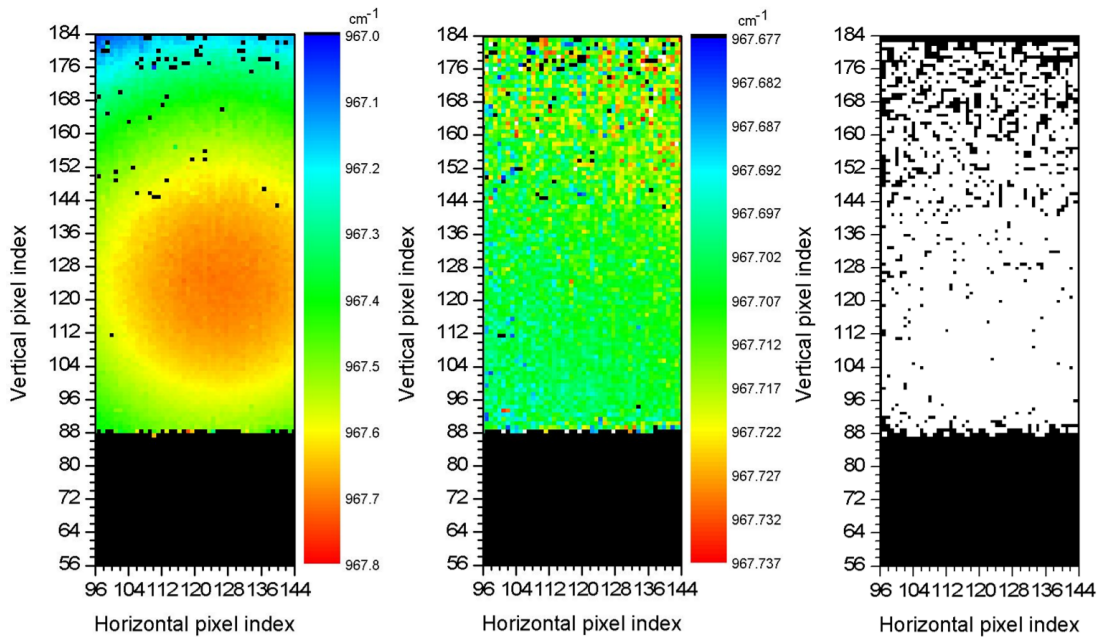


Figure 6.12.: Left: Line position plot for the  $\text{CO}_2$  line at  $967.707 \text{ cm}^{-1}$  over the detector array ( $48 \times 128$  pixels) before spectral calibration; middle: Line position after spectral calibration; right: Pixels used (black dots) for the calculation of the spectral calibration parameters.

accounts for the high variability of the determined line position values in the upper rows of the detector array (figure 6.12, middle). All pixels below pixel number 88 (vertical pixel index) are cloud contaminated and are therefore rejected. Due to the large scatter in the line position values, a further pixel selection criteria has been applied to the data used for finding the spectral calibration parameters. An estimated line position is calculated using a 2D surface fit to the determined line position of the selected line. The line position difference between the estimated surface fit and the measurement values is calculated. All pixels which have the line position difference within the threshold of  $\pm 0.01 \text{ cm}^{-1}$  are selected. This selection criteria helps in the removal of pixels with a large deviation in the line position values mostly due to a low SNR. The image distance is calculated for each pixel using the information of the optical axis position, the distance of the pixel from the optical axis position and the fitted line position value for the on-axis pixel. All pixels which have the image distance in the range between 6 cm and 8 cm are selected. This selection criteria helps in the removal of the spikes in the line position values close to the optical axis position. The black points in the figure 6.12 (right) represent those pixels which were discarded during the pixel filtering process for the determination of the spectral calibration parameter.

The standard deviation of the  $\text{CO}_2$  line position values for each selected line for  $48 \times 128$  pixels have been calculated and plotted (figure 6.13, left) against the corresponding line positions in the range between  $940 \text{ cm}^{-1}$  and  $975 \text{ cm}^{-1}$ . The variation is in the range of 8.7 ppm to 12.3 ppm depending on the selected lines. The standard deviation increases by about 34 % between the strongest and the weakest line, while the line intensity changes by a factor of 1.5. This again shows that the line position determination works better for lines with a higher signal-to-noise ratio. Using other selected lines with a slightly reduced line strength increases the precision in the determination of the spectral calibration parameters.

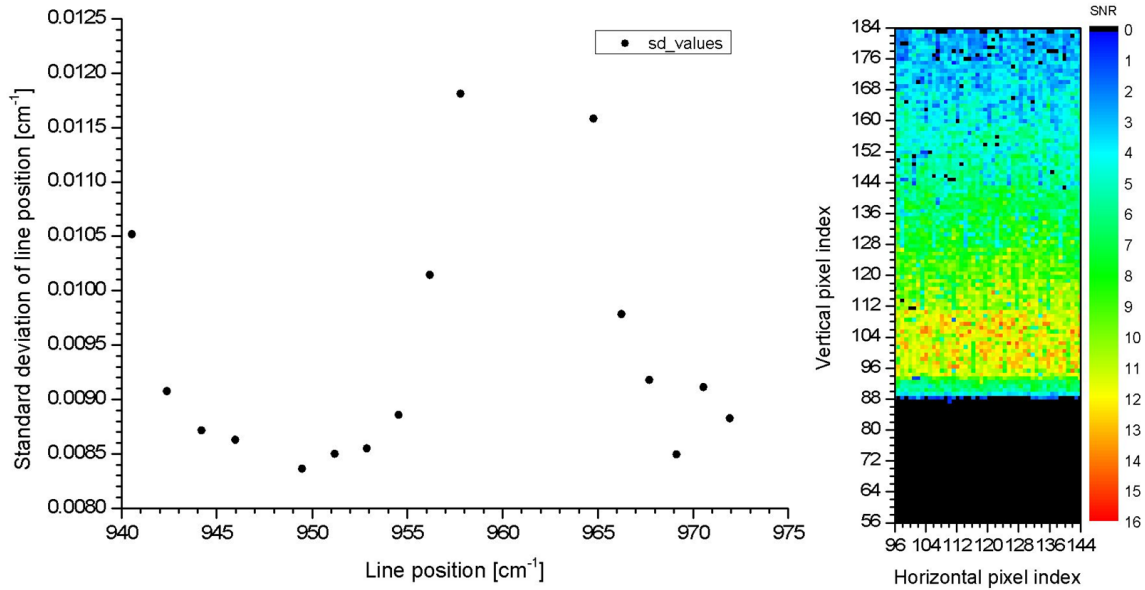


Figure 6.13.: Left: Standard deviation of the selected  $\text{CO}_2$  line position values for  $48 \times 128$  pixels from the measurement data and plotted against their respective line positions in the spectral range between  $940 \text{ cm}^{-1}$  and  $975 \text{ cm}^{-1}$ . Right: Signal-to-noise ratio distribution for the  $\text{CO}_2$  line at  $967.707 \text{ cm}^{-1}$  over the detector array ( $48 \times 128$  pixels). The black points represent the discarded pixels during line position determination from the spectrally calibrated data.

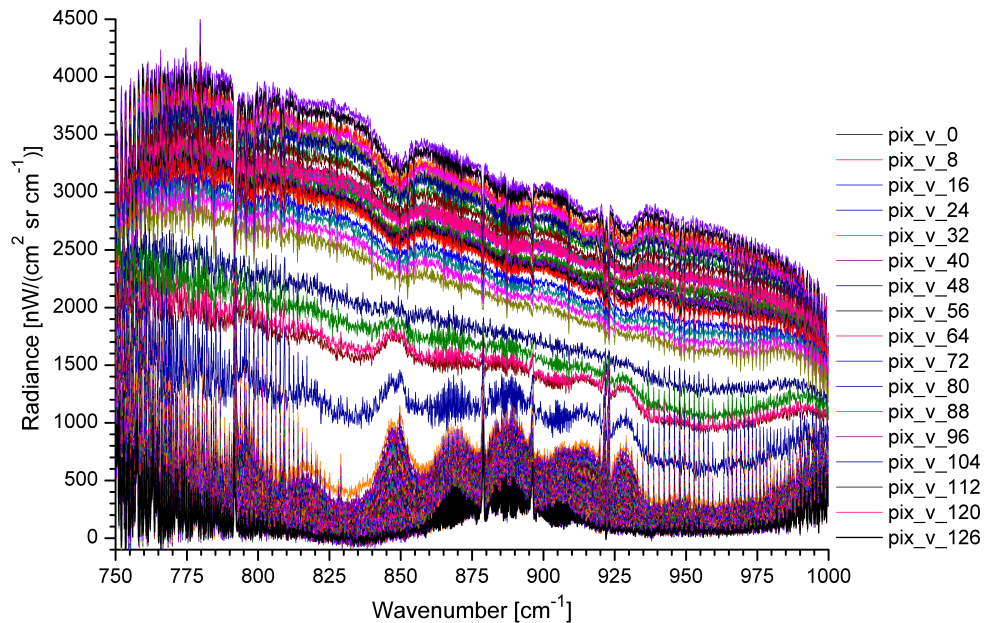


Figure 6.14.: Spectra (horizontal pixels binned) plot over the vertical pixel distribution after spectral calibration of flight (K01\_F02) data.

The spectrally calibrated spectra are binned for each row and used as an input for the level2 data processing. Figure 6.14 shows a plot of the binned pixels for a section of the spectral range between  $750 \text{ cm}^{-1}$  and  $1000 \text{ cm}^{-1}$ . The top layers of the plot show a high radiance signal (blackbody shape) with absorption lines due to the presence of clouds. The transition from the cloudy to the cloud free pixels is seen with the navy blue curve. The lower most curve (black) represents the top most row on the detector field. The upper rows of the detector look upwards.

### Stability of the spectral calibration parameters

The stability of the spectral calibration parameters was tested with another data set (set 2) of flight K01\_F02. Fourteen atmospheric chemistry mode measurements in the forward interferometer drive direction were co-added and taken for the analysis. The measurement data of set 2 are for the measurement sequence<sup>2</sup> performed about two hours ten minutes later than the sequence (set 1) for which the spectral calibration parameters were determined. The spectral calibration parameters of set 1 have been used to perform the spectral calibration of set 2. The results will show the time dependent drift effects of the instrument on the spectral line position.

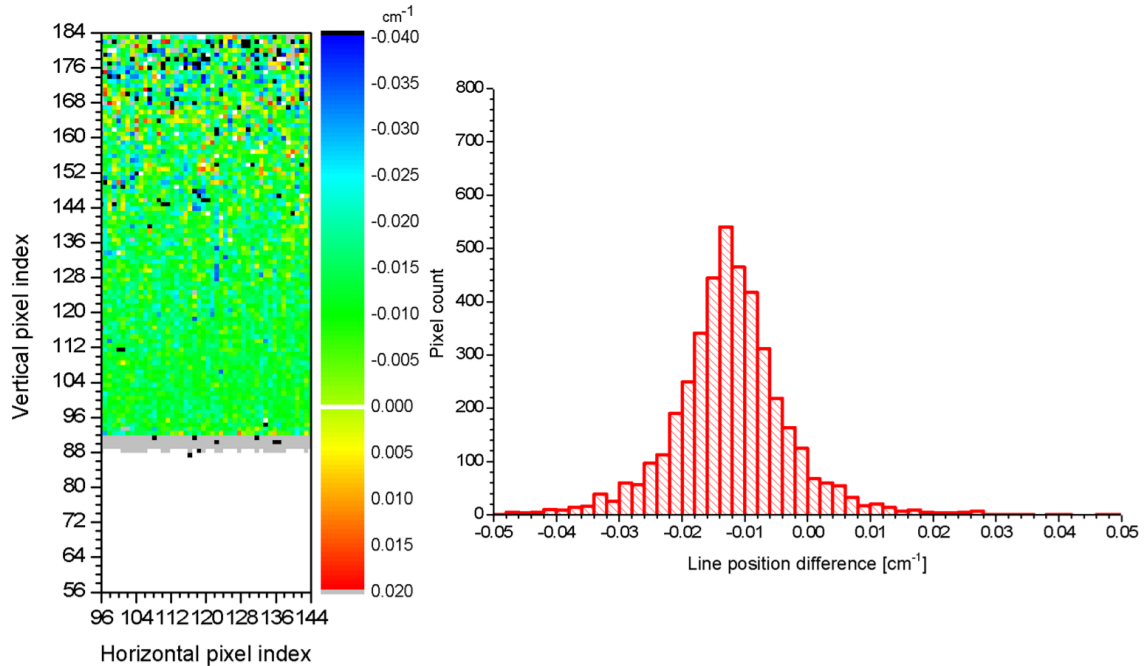


Figure 6.15.: Left: Line position difference between set 1 and set 2 for the CO<sub>2</sub> line at 967.707 cm<sup>-1</sup> over the detector array (48×128 pixels). The spectral calibration for set 1 was performed using the parameters determined from the same measurement set and the spectral calibration for set 2 was performed using the parameters determined from set 1. Right: Histogram plot of the 2D distribution of the line position difference as shown in the left figure. The median value is at -0.0124 cm<sup>-1</sup>.

The line positions for the CO<sub>2</sub> line at 967.707 cm<sup>-1</sup> are determined for the detector array of 48×128 pixels from both data sets (set 1 and set 2). The difference in the line position values between the two data sets is plotted in figure 6.15 as 2D and histogram plots. The pixels below the 88 vertical pixel index (white colored) are cloud contaminated in both cases. The gray color pixels around the vertical pixel index of 88 to 91 represent additional cloud layers present in the later measurements (set 2). The median of the line position difference is -0.0124 cm<sup>-1</sup> with the distribution of the pixels being in the range of the natural spectral sampling. The data of set 2 shows a line position shift of about 12 ppm with respect to the data of set 1. This indicates that the spectral calibration parameters have changed in between the two measurement sequences.

<sup>2</sup>Measurements are in the time range between 16:39:25 and 16:51:52.

The spectral calibration parameters for both directions of the interferometer drive movement are calculated independently for both data sets (set 1 and set 2). The results are presented here.

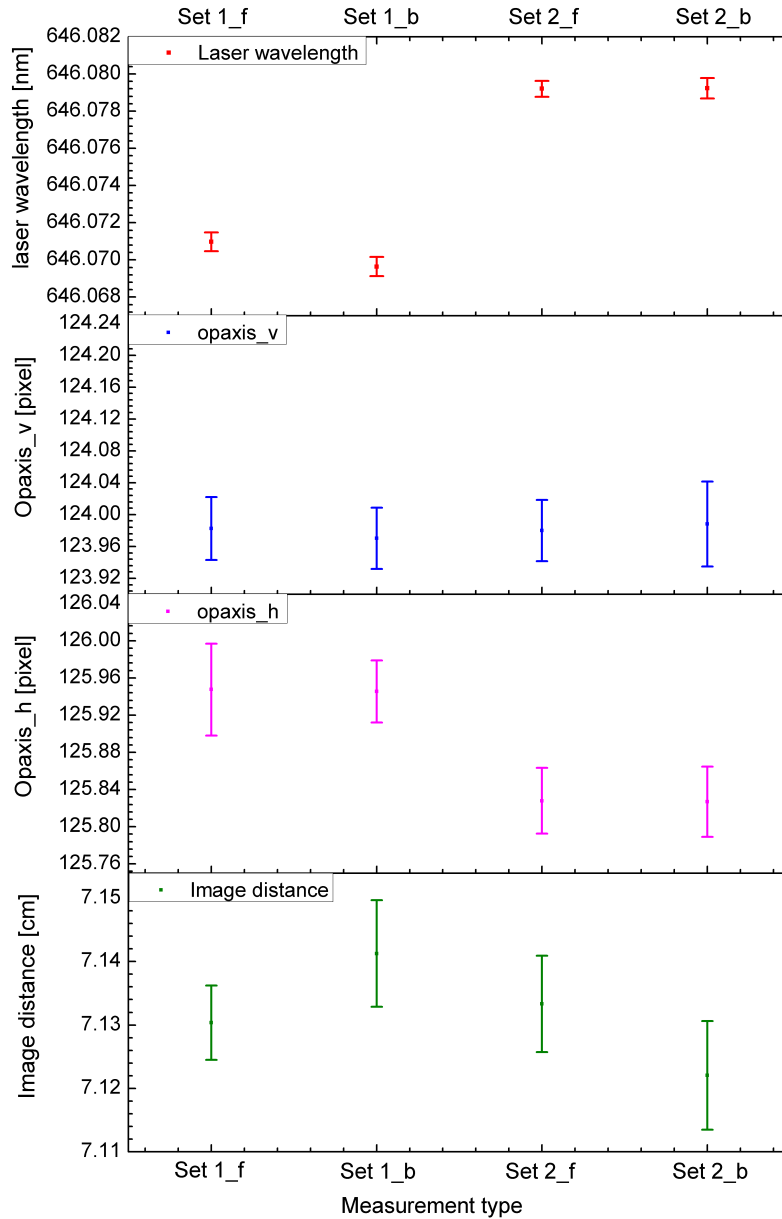


Figure 6.16.: The spectral calibration parameters calculated using the selected atmospheric lines of set 1 and 2 set for forward and backward direction data from flight K01\_F02. (1st - top) the laser wavelength, (2nd) the vertical component of the optical axis, (3rd) the horizontal component of the optical axis, (4th - bottom) the image distance.

The mean of the spectral calibration parameter values (circular points) and its standard deviation (vertical bars) for the selected CO<sub>2</sub> lines are calculated and plotted in figure 6.16. The plot shows that the laser wavelength for set 1 and set 2 differ by approximately 0.00822 nm, the later value being higher. The vertical optical axis position shows no such pattern. The horizontal optical axis position shows a difference of about 0.12 pixel. The image distance value has a higher variability for each direction and each measurement set, as a result, no pattern can be identified which could be related to the drift of interferometer temperature.

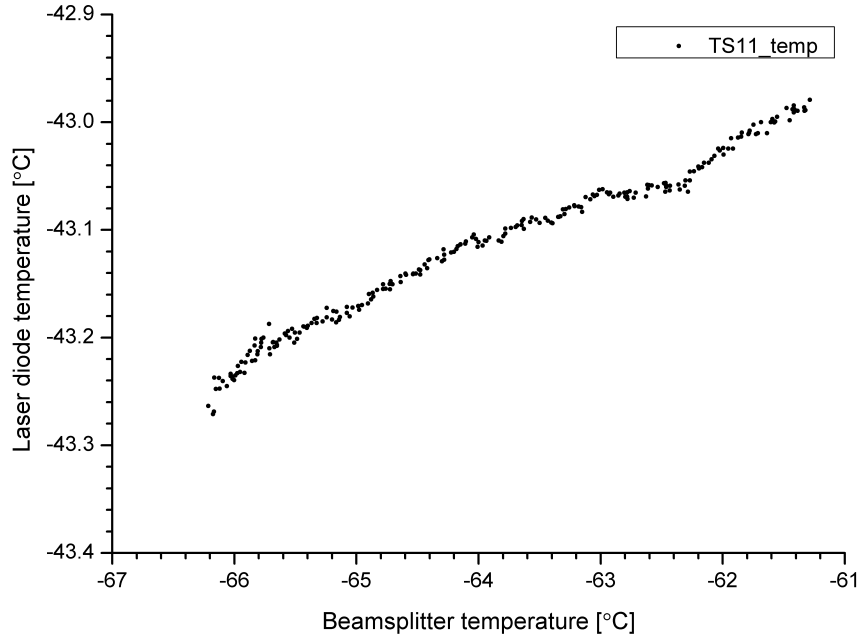


Figure 6.17.: The temperature drift of the reference laser due to the temperature drift of the GLORIA interferometer. The instrument temperature was measured at the beamsplitter. The laser diode was regulated with a Dawn element during the measurement.

The reference laser diode has a wavelength drift depending on the temperature drift of the GLORIA interferometer. The reference laser diode used during the ESSenCe campaign (flight K01\_F02) has a wavelength drift rate of approximately 0.03 nm/K [30]. The reference laser diode was heated with a Dawn element (DS1125 - properties similar to DN505 [62, 63]) in order to keep it at the desired operating temperature. This configuration was later replaced with the Peltier controlled laser diode operation for the next campaigns. A drift rate of approximately 0.06 K/K between the laser diode temperature with respect to the temperature of the GLORIA interferometer has been measured in the laboratory (figure 6.17) with the Dawn element [64]. The instrument temperature drifts at a rate of 1.5 - 2 K/hour when cooled with dry ice (ref.: Laboratory measurements). The interferometer was cooled with dry ice during flight K01\_F02. As a result, the laser wavelength drift is equal to  $0.06 \text{ K/K} \times 0.03 \text{ nm/K} = 0.0018 \text{ nm/K}$ . The laser wavelength drift per hour of flight measurements is equal to  $0.0018 \text{ nm/K} \times 2 \text{ K/hour} = 0.0036 \text{ nm/hour}$ . This corresponds to a wavelength drift of 0.00781 nm between the two measurement sequences at an interval of 2 hours 10 minutes. Thus, the expected line position shift for the  $\text{CO}_2$  line at  $967.707 \text{ cm}^{-1}$  due to the laser wavelength drift is approximately  $0.0123 \text{ cm}^{-1}$ . This value is close to the calculated value of the median ( $0.0124 \text{ cm}^{-1}$ ) of the line position shift (figure 6.15). This confirms that the shift in the line position is primarily due to the drift in the reference laser wavelength due to the temperature drift of the interferometer. The change in the optical axis position causes only a slight variation of the line position. The change for the corner pixel due to the shift of the optical axis h position by 0.12 pixel is approximately 0.9 ppm.

### Spectral calibration of flight K03\_F14 data

The variation of the spectral calibration parameters has been further investigated using the data of flight K03\_F14. Atmospheric "deep space" measurements of several calibration sequences performed during the flight were analyzed. The deep space measurement sequence contains five measurements per sweep direction which were co-added to improve the SNR of the individual lines. The SNR of the CO<sub>2</sub> line at 951.1875 cm<sup>-1</sup> for the central pixel after co-addition is about eleven. The deep space measurements were selected, since these measurements have a homogeneous scene measured over the detector array with low contributions from only some lines from more abundant trace gases. It also has the advantage of having a cloud free scene, as these measurements were performed by looking at an approximately +10° elevation angle, therefore none of the pixels have to be rejected due to cloud contamination. The measurements were performed with a pixel offset of (104,56) and an array size of 48×128 pixels. The optical axis position was determined prior to the flight and the offset was chosen such that the optical axis position lies on or close to the center of the selected detector array. The deep space measurements during the ESSenCe campaign had a low signal-to-noise ratio ( $\approx 3$  and less) and so the chemistry mode measurements with a better signal-to-noise ratio ( $\approx 16$  in the center) were better suited and used for performing spectral calibration.

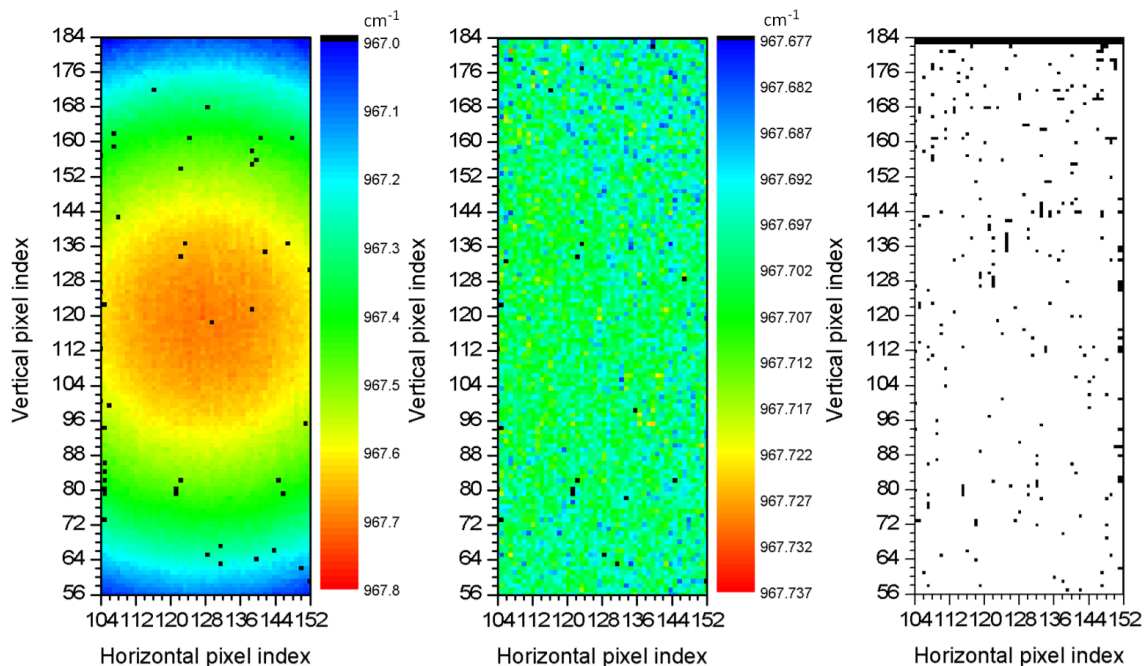


Figure 6.18.: Left: Line position plot for the CO<sub>2</sub> line at 967.707 cm<sup>-1</sup> over the detector array (48×128 pixels) before the spectral calibration; middle: Line position after the spectral calibration; right: Pixels used (black dots) for the calculation of the spectral calibration parameters.

The line positions for the CO<sub>2</sub> line at 967.707 cm<sup>-1</sup> over the detector array of 48×128 pixels are determined before (figure 6.18, left) and after (figure 6.18, middle) performing the spectral calibration for the measurements performed around 09:20 hours. The deep space measurement gave the opportunity to use pixels from the lower part of the detector array as well, due to the absence of clouds. This was not possible for the atmospheric measurements of the ESSenCe data as the pixels below the vertical pixel index of 88 had to be rejected due to the cloud contamination. The black points represent those pixels which are rejected during the line position determination following the criteria mentioned earlier in this section. The line position after performing the spectral calibration should

be equal to the theoretical value if the calibration has worked properly. The line position distribution after performing the spectral calibration shows a constant value with some random high and low values (figure 6.18, middle). Approximately 57 % and 86 % of the pixels fall in the range with the line position error of  $\pm 5$  ppm and  $\pm 10$  ppm, respectively. Figure 6.18 (right) shows the pixels which were rejected during the pixel filtering process (following the additional criterion as mentioned earlier) for finding the spectral calibration parameters.

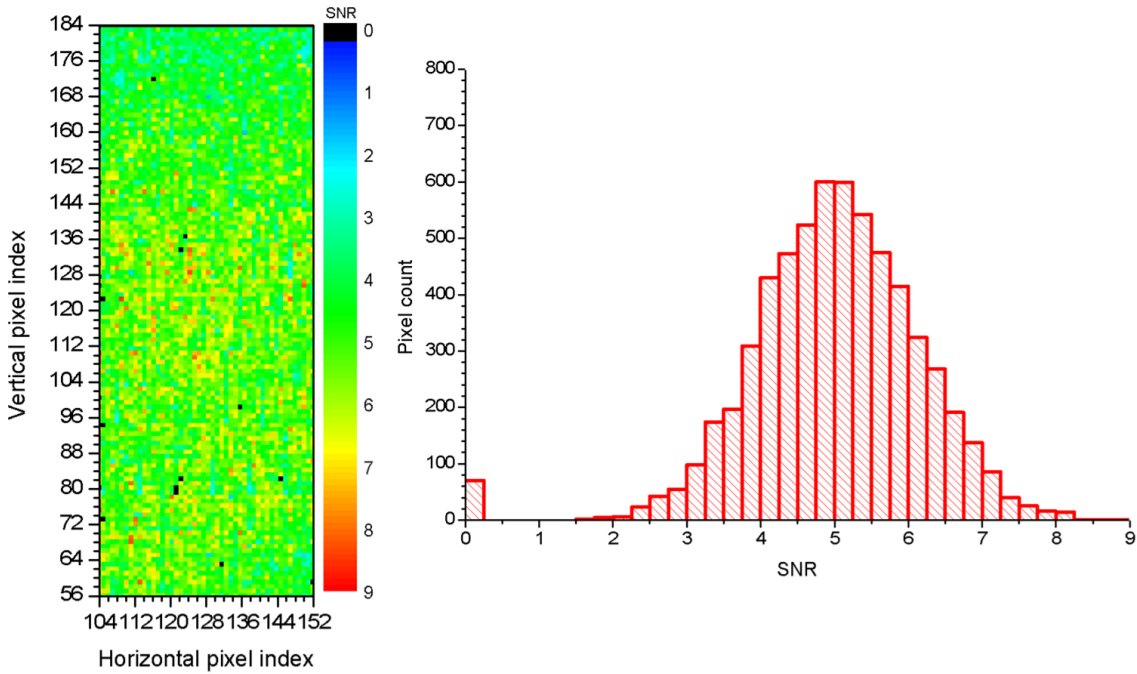


Figure 6.19.: Signal-to-noise ratio distribution for the  $\text{CO}_2$  line at  $967.707 \text{ cm}^{-1}$  over the detector array ( $48 \times 128$  pixels) for deep space measurements performed during flight K03\_F14. The black points represent the discarded pixels during line position determination of the selected line.

The signal-to-noise ratio distribution for the  $\text{CO}_2$  line at  $967.707 \text{ cm}^{-1}$  over the detector array ( $48 \times 128$  pixels) is shown in figure 6.19. The SNR is varying between nine and slightly below two with a median value of about five. The black points in the plot represent those pixels which were discarded during the pixel filtering process for the line position determination. Majority of the pixels have good SNR value over the detector array. The pixels in the lower and middle region is close to the air mass having higher concentration of  $\text{CO}_2$  as a result they show high SNR values as compared to the pixels in the upper part of the pixel array. The line position determination worked well for this measurement set (see figure 6.18, middle). The determined line position is fairly homogeneous and do not show high variability as seen in the ESSenCe data (figure 6.12, middle). The measurement was free from cloud contamination and as a result no pixel had to be rejected due to cloud contamination.

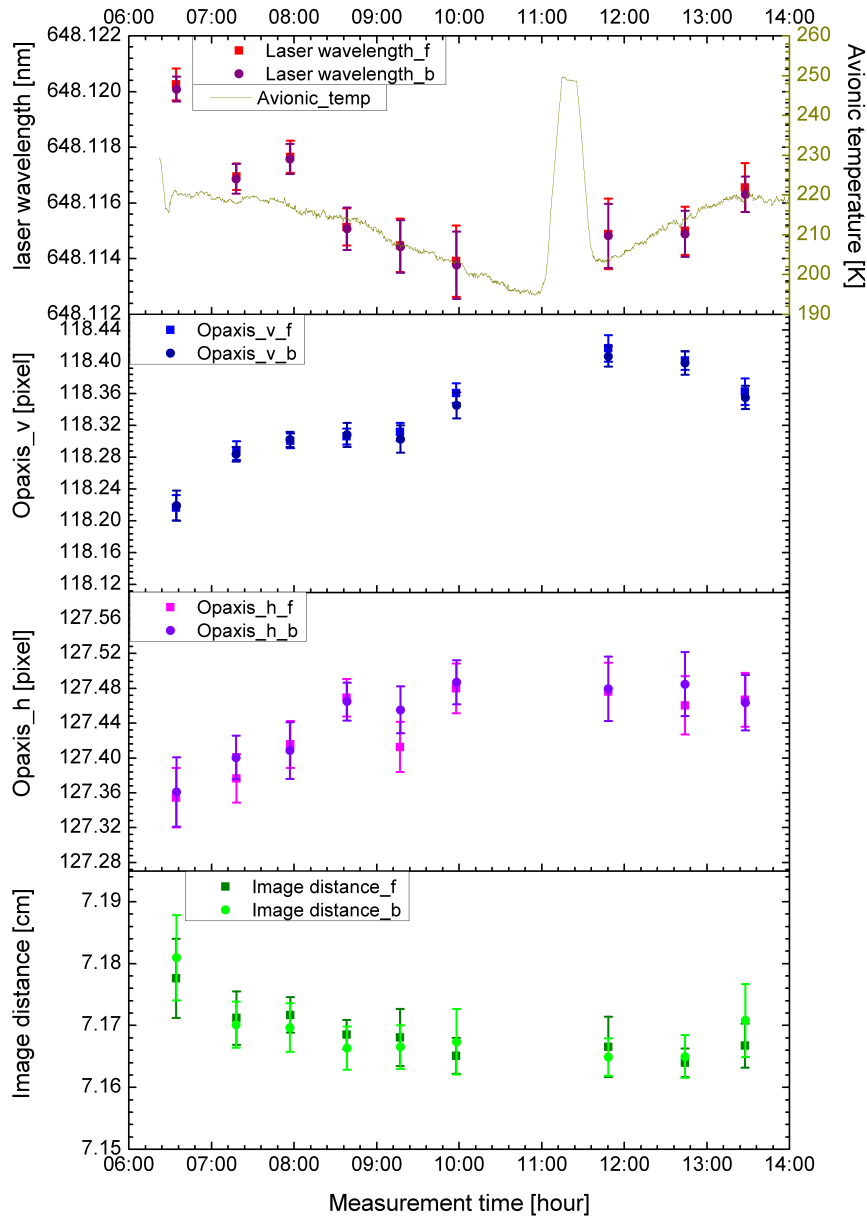


Figure 6.20.: The spectral calibration parameters calculated using the selected atmospheric lines for the forward and backward direction data from flight K03\_F14. (1st - top) the laser wavelength, (2nd) the vertical component of the optical axis, (3rd) the horizontal component of the optical axis, (4th - bottom) the image distance.

The spectral calibration parameters calculated from the measurements of several sequences and plotted against the measurement time are shown in figure 6.20. The values are plotted for both the forward (square) and backward (circle) direction of the interferometer drive motion. The values for both directions are within the standard deviation, showing once again no significant difference in the spectral calibration parameters for the two directions. The air temperature measured using the temperature sensor of the aircraft avionic is plotted along with the laser wavelength. As the temperature sensors inside the instrument did not work during the flight, the temperature from the avionics measured outside the instrument serves as a proxy for the temperature change in the instrument during the flight. The laser wavelength shows a correlation with respect to the temperature. The optical axes h and v positions show an increasing pattern over the measurement range with a maximum increase of about 0.2 pixel. The image distance values show a small correlation with respect to the temperature but it has a large scatter in the values.

In order to perform the spectral calibration of the atmospheric data of flight K03\_F14, two methods can be followed. One method would be to use the mean of the parameters from all measurement sequences for performing the spectral calibration of the data during the whole flight. This will make the calculations simpler but it will also give an error in the line position for the measurements which were performed at high and low temperature values of the instrument. The error in the line position for the corner pixel ((23,62) pixels away from the optical axis position) due to the laser wavelength difference will be about  $\pm 3$  ppm, while the error due to the optical axis h, v and image distance values for the first measurement sequence will be about  $\pm 2$  ppm. In order to avoid this error, an intelligent interpolation of the parameters has to be done. The spectral calibration of the atmospheric data has to be performed with the interpolated parameters, the same parameters should also be used for performing the spectral calibration of the respective calibration measurements. This will be in line with the basic criterion for the two point radiometric calibration approach used for performing the radiometric calibration of the GLORIA data.

### Accuracy of the spectral calibration

The quality of the spectral calibration is checked by comparing the line position of the corner pixel with a pixel close to the optical axis and by comparing the absolute position of the selected line with the HITRAN position. The first check gives an estimate about the correctness of the pixel dependent correction parameters (optical axis h,v and image distance) and the second check gives the correctness of the laser wavelength used for the spectral calibration. The correction for the off-axis effect is a scaling term for the OPD, its absolute effect is larger at the higher wavenumbers. The pixel dependent line position error is the critical error as it will lead to ILS distortion when several pixels of one row are co-added. A single isolated line with a good signal-to-noise ratio over the detector array cannot be found for a higher wavenumber region, as a result several pixels are co-added. A set of  $5 \times 5$  pixels is co-added for pixels around the optical axis (pixel range: 125-129 (h) and 116-120 (v)) and also pixels in the corner of the detector array (pixel range: 108-112 (h) and 60-64 (v)).

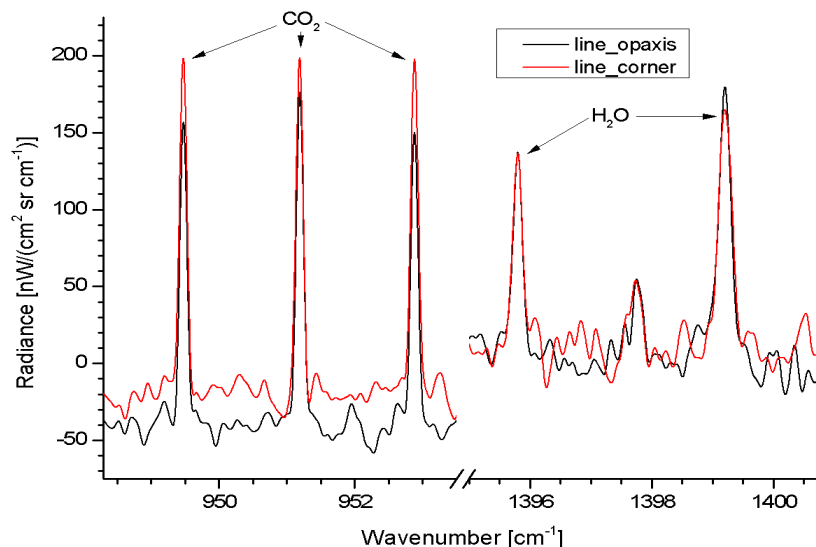


Figure 6.21.: Spectrally calibrated spectra from flight K03\_F14 plotted for co-added pixels (125-129,116-120) in black and pixels (108-112,60-64) in red for two spectral ranges showing CO<sub>2</sub> and H<sub>2</sub>O lines.

The CO<sub>2</sub> lines and H<sub>2</sub>O lines for the co-added pixels around the optical axis (black) and corner (red) of the detector array are shown in figure 6.21. The radiometric calibration

is not perfect which leaves with the negative radiances in the spectra, but this is not a problem for checking the quality of the spectral calibration. The selected corner pixels have a higher line strength because they are looking downwards into a scene with a higher trace gas concentration of CO<sub>2</sub> and H<sub>2</sub>O as compared to the pixels close to the optical axis. The mean difference in the line positions of the selected CO<sub>2</sub> lines (table 6.3) and H<sub>2</sub>O lines between the center and corner is 0.6 ppm and 1.35 ppm, respectively. The error made for the CO<sub>2</sub> lines is low which confirms that the off-axis correction has worked well. As this error is a scaling error its value increases for the H<sub>2</sub>O lines at higher wavenumbers. The mean difference in the line positions of the selected CO<sub>2</sub> lines and H<sub>2</sub>O lines with respect to the corresponding HITRAN positions for the central pixels is 3.5 ppm and 1.55 ppm, respectively. This error is a constant error which is the same for all pixels. The wavenumber dependence points towards the presence of chromatic aberration. The error made is well below the threshold of 10 ppm budget and is not an issue for the current data processing. In order to make further improvements, a second iteration with the scaled laser wavelength could be used.

### **Summary: Spectral calibration from in-flight measurements**

The spectral calibration parameters have been calculated from the atmospheric chemistry mode and deep space measurements. Single isolated CO<sub>2</sub> emission lines between 940 cm<sup>-1</sup> and 975 cm<sup>-1</sup> with a good signal-to-noise ratio have been selected for the analysis. The line position distribution (data of the ESSenCe flight K01\_F02) of the spectrally calibrated data shows a constant value in the middle and high variability in the upper rows due to the lower SNR for the lines in this region. The SNR of the pixels plays an important role in the selection of the pixels and the quality of the determined spectral calibration parameters. The calibration parameters calculated from the first data set (set 1) of the ESSenCe flight K01\_F02, were applied for performing the spectral calibration for measurements done at a later time (approximately two hours ten minutes later) (set 2). Data from set 2 shows a median line position shift of about 12 ppm over the detector array. Comparison of the spectral calibration parameters from the set 1 and set 2 shows that the shift in the line position is primarily due to the drift of the reference laser wavelength corresponding to the temperature drift of the GLORIA interferometer. The spectral calibration parameters calculated over a longer measurement period (flight K03\_F14) show that the laser wavelength changes along with the temperature drift of the instrument. Moreover, the optical axis position  $h$  and  $v$  and the image distance position also show a change over the measurement time. Using the mean value for performing the spectral calibration causes an error in the line position of about  $\pm 3$  ppm due to the laser wavelength drift and about  $\pm 2$  ppm due to the optical axis position  $h$  and  $v$  and the image distance changes for the corner pixel. In order to avoid this error, an intelligent interpolation of the parameters has to be done. The same calibration parameters have to be used for the atmospheric measurements and the calibration sequence measurements. In general, the spectral calibration parameters can be determined from any chemistry mode measurement or deep space measurement with emission lines having good signal-to-noise ratio. Deep space measurements have the added advantage of usually having a homogeneous scene with no cloud contamination over the whole array. The temperature drift of the reference laser diode, the temperature drift of the interferometer and the adjustment of the IRO will define the frequency at which the spectral calibration parameters have to be determined and applied to the corresponding data set measured during a flight. The mean difference in the line positions of the selected CO<sub>2</sub> lines and H<sub>2</sub>O lines between the center and corner is found to be 0.6 ppm and 1.35 ppm, respectively. The mean difference in the line positions of the selected CO<sub>2</sub> lines and H<sub>2</sub>O lines with respect to the corresponding HITRAN positions for the central pixels is found to be 3.5 ppm and 1.55 ppm, respectively. The error made is well below the threshold of 10 ppm. This implies that the spectral calibration has worked well.

## 6.8. Focal plane determination using spectral line width

The spectral line has the minimum line width when the imaging lens is placed at the focus position. The effective pixel size increases as the lens moves away from the focus. This results in the modulation getting worse with a higher OPD which gives a broader instrumental line shape (ILS) leading to an increase in the line width of the measured line for the de-focused cases. The modulation loss becomes more prominent for pixels which are further away from the optical axis position. A simulation of the through-focus spot diagram for the lens being placed at the focus and four other de-focused positions for the central and four corner pixels has been shown in figure 5.41. In this section a method is described which can determine the IRO defocusing depending on the temperature change of the interferometer. Moreover, a relationship between the interferometer temperature and the image distance has been established. This relation can be used to adjust the IRO during the measurement with the thermally drifting GLORIA interferometer. The focal plane is determined using the line width of the spectral lines.

The insulation box surrounding the GLORIA spectrometer helps to reduce the heat exchange with the ambience to a certain extent but not completely. This causes a temperature drift in the interferometer for the measurement duration. The interferometer had a temperature drift of approximately 2 K/hour during the ESSenCe campaign. Since then the spectrometer has undergone some thermal changes which have led to an improvement in reducing the heat intake. The interferometer has a drift rate of approximately 1 K/hour in the present setup. It is therefore to be investigated if it is necessary to adjust the IRO position with the present drift of temperature of the interferometer during a measurement flight.

### Measurement setup and results for varying interferometer temperatures at a fixed IRO position

Laboratory measurements with a gas cell (containing  $N_2O$  gas) placed in front of the GLORIA interferometer were performed to quantify the image distance variation with the change of the interferometer temperature.

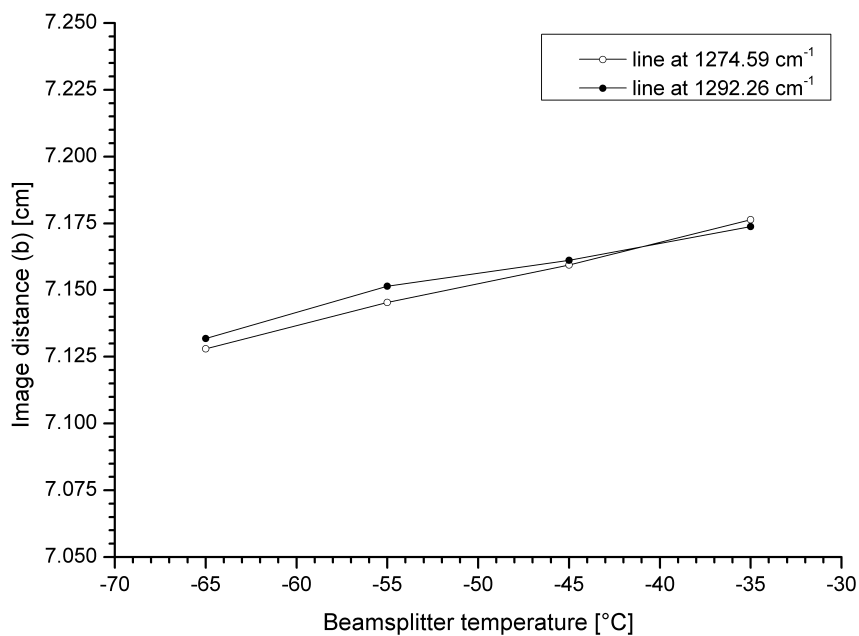


Figure 6.22.: Image distance plotted for two spectral lines with respect to the varying beamsplitter temperature for fixed IRO position.

The measurements were performed at room temperature and pressure. The gas cell had a cold background (liquid Nitrogen) to provide a better contrast for the lines. The measurements have been performed by placing the IRO at one position and varying the interferometer temperature from  $-35\text{ }^{\circ}\text{C}$  to  $-65\text{ }^{\circ}\text{C}$  in steps of approximately  $10\text{ }^{\circ}\text{C}$ . The change of the interferometer temperature causes a shift of the image distance. The image distance is calculated (as in section 6.1.1) for two selected  $\text{N}_2\text{O}$  lines with a good signal-to-noise ratio for the different interferometer temperatures. The selected lines in the  $\text{N}_2\text{O}$  band lie in the range between  $1240\text{ cm}^{-1}$  and  $1320\text{ cm}^{-1}$ . The  $\text{N}_2\text{O}$  band in the range between  $1140\text{ cm}^{-1}$  and  $1200\text{ cm}^{-1}$  has lines with a poor intensity for these measurements. This was due to the filling of the  $\text{N}_2\text{O}$  gas in the gas cell. Figure 6.22 shows a variation of the image distance values at a rate  $1.6163 \times 10^{-3}\text{ cm/K}$  along with the change of the interferometer temperature.

### Results of varying IRO positions at a fixed interferometer temperature

Measurements with the same setup as described above have been performed by placing the IRO at five different positions around the focus and with the interferometer temperature stabilized at  $-51\text{ }^{\circ}\text{C}$ . The focus position checked by visual methods gave the focus point to be roughly at around 280 IRO counts with a variation of  $\pm 5$  counts. The IRO position was varied in steps of 25 counts (equivalent to  $168.9\text{ }\mu\text{m}$ ). The IRO positions chosen for the measurements are at 230, 255, 280, 305 and 330 counts. The gas cell filling with  $\text{N}_2\text{O}$  gas was such that the band in the spectral range between  $1140\text{ cm}^{-1}$  and  $1200\text{ cm}^{-1}$  had a good signal-to-noise ratio. The  $\text{N}_2\text{O}$  lines from this spectral range were selected for the analysis. The full width at half maximum of the line increases and the line intensity decreases (reduction of the SNR for the line) with the increase of the lens de-focusing.

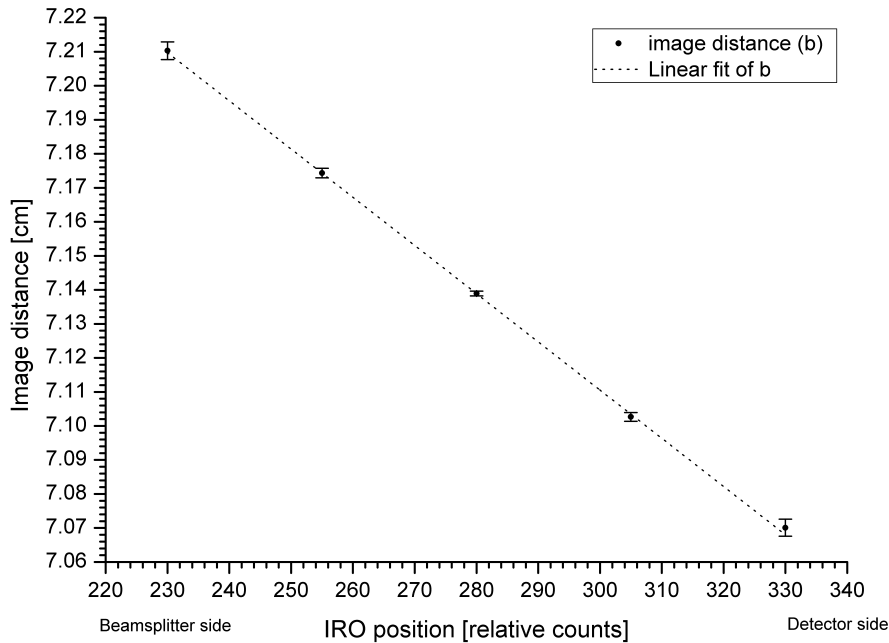


Figure 6.23.: Image distance plotted with respect to the IRO positions corresponding to the interferometer temperature of  $-51\text{ }^{\circ}\text{C}$ . The solid points represent the mean value and the vertical bars represent the standard deviation of the image distance calculated from the selected  $\text{N}_2\text{O}$  lines.

The image distance for the five IRO positions has been calculated as shown in section 6.1.1 for the 25 selected  $\text{N}_2\text{O}$  lines (section 6.3). Figure 6.23 shows a plot of the mean (black dots) and the standard deviation (vertical bars) of the image distance calculated from the 25 selected  $\text{N}_2\text{O}$  lines. The slope of a linear fit of the image distance values is

$1.4019 \times 10^{-3}$  cm/count. The image distance value at 280 IRO count has the smallest standard deviation for the selected  $\text{N}_2\text{O}$  lines. The standard deviation increases for the IRO positions of 255 and 305 counts and even more for the IRO positions of 230 and 330 counts. The higher variations of the image distance values for the de-focused cases may be due to chromatic aberrations. The chromatic aberration is a wavenumber dependent quantity. Increasing the defocusing of the lens results in a higher variation of the image distance of the lines selected over a wavenumber region. The variation for the outer most de-focused cases calculated is still small and therefore is not a problem for the measurements.

The variation of the IRO counts with respect to the interferometer temperature can be calculated from the slopes of the two curves shown in figures 6.22 and 6.23 and is found to be 1.1529 counts/K. With variations in the interferometer temperature, the IRO has to be moved at this rate in order to stay at the focus position. The GLORIA interferometer has a temperature drift rate of 1 K/hour in the present setup. A continuous measurement of 10 hours (HALO flight) will result in a temperature drift of 10 K in the interferometer. This implies that the IRO has to be moved by approximately 11.5 counts at the end of the flight in order to be placed at the focus position again. If the IRO is not moved with the temperature drift of the interferometer, the lens will not be placed at the focus which leads to a line shape distortion. One solution to avoid this is to fix the lens at the focus corresponding to the middle value of the measurement temperature range. If the absolute deviation in the temperature of the interferometer is within 10 K, the resulting line shift error (both defocusing directions) for a corner pixel located (64,24) pixels away from the on-axis pixel will be approximately  $\pm 0.8$  ppm. The error contribution is quite small in this case. Therefore it is recommended not to change the IRO position during the measurements performed at the given temperature range of 10 K. Certain aspects have to be kept in mind while moving the IRO during a measurement sequence. Moving the IRO in one direction only gives a slight change in the optical axis h and v positions as shown in figure 6.9. Changing the direction of motion of the IRO results in a jump of the optical axis position by  $2 \times 2$  pixels. As a result for each new position of the IRO, we need to make new calibration measurements which is quite time consuming. This result shows that if the IRO is moved, the spectral calibration parameters have to be determined and applied to the data more often for long duration flights.

### **Determination of the focus position**

The above mentioned analysis shows the relation between the image distance, the IRO position and the beamsplitter temperature. The standard deviation variation for the image distance values for the selected lines give a hint about the focus position. In this section, a novel method is described which can determine the focus position by analyzing the line width of the spectral lines. The effect of de-focusing is seen mostly for the corner pixels.

The measurement data for the five IRO positions has been analyzed to find the focus position. The measurement data contains  $128 \times 128$  pixels with an offset of (56,56). A sample spectrum for pixel (64,62) for the IRO placed at 280 count position is shown in figure 6.24. The selected pixel is (64,62) pixels away from the on-axis pixel (128,124). The spectrum is cut around the region where the  $\text{N}_2\text{O}$  lines are present. The region between  $1140 \text{ cm}^{-1}$  and  $1205 \text{ cm}^{-1}$  is named as band 1 and the region between  $1240 \text{ cm}^{-1}$  and  $1320 \text{ cm}^{-1}$  is named as band 2. These two regions are analyzed separately. Individual lines with a good signal-to-noise ratio having no overlapping from neighboring lines for all cases of IRO positions are selected from each band. The lines selected as in section 6.3 were also included in the selection criterion. The line width of each selected  $\text{N}_2\text{O}$  lines is calculated and used as an indicator for finding the focal plane.

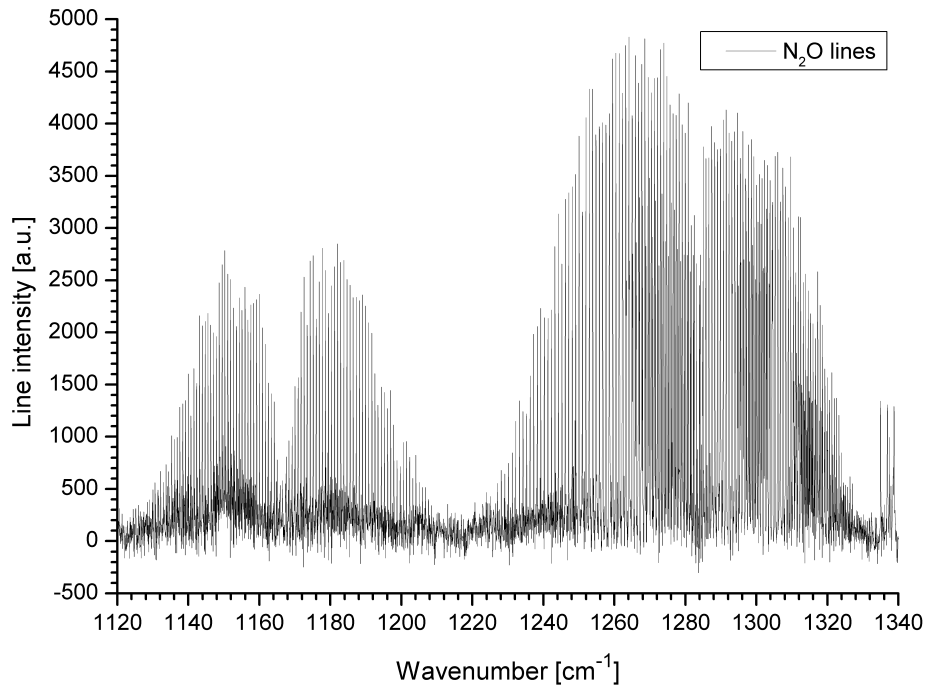


Figure 6.24.: A  $\text{N}_2\text{O}$  spectrum for pixel (64,62) for the IRO placed at 280 count position.

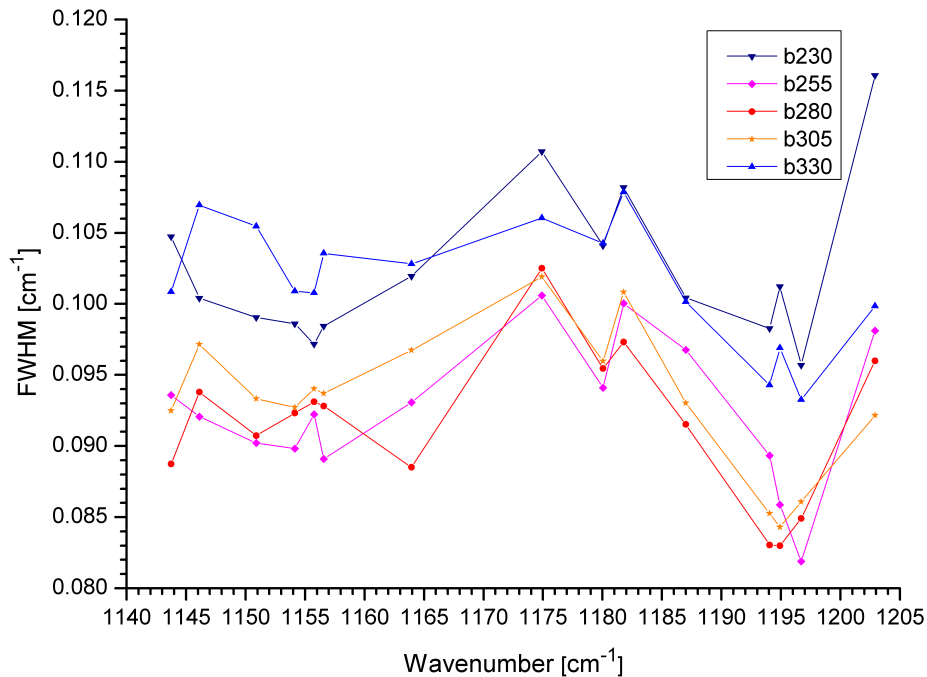


Figure 6.25.: The FWHM of the  $\text{N}_2\text{O}$  lines in the spectral range between  $1140\text{ cm}^{-1}$  and  $1205\text{ cm}^{-1}$  calculated for pixel (64,62) from measurement data and plotted for five different IRO positions separated by 25 counts.

The FWHM plots for the selected lines in band 1 and band 2 are shown in figure 6.25 and figure 6.26, respectively. The plots show that the IRO position at 280 count (red curve) has the minimum value for most of the lines. The curves for the IRO at 305 count (orange) and 255 count (magenta) show slightly higher values as compared to the curve for the IRO at 280 count. The magenta curve is closer to the red curve as compared to the orange curve. The curves for the IRO at 330 count (blue) and 230 count (navy) show values which

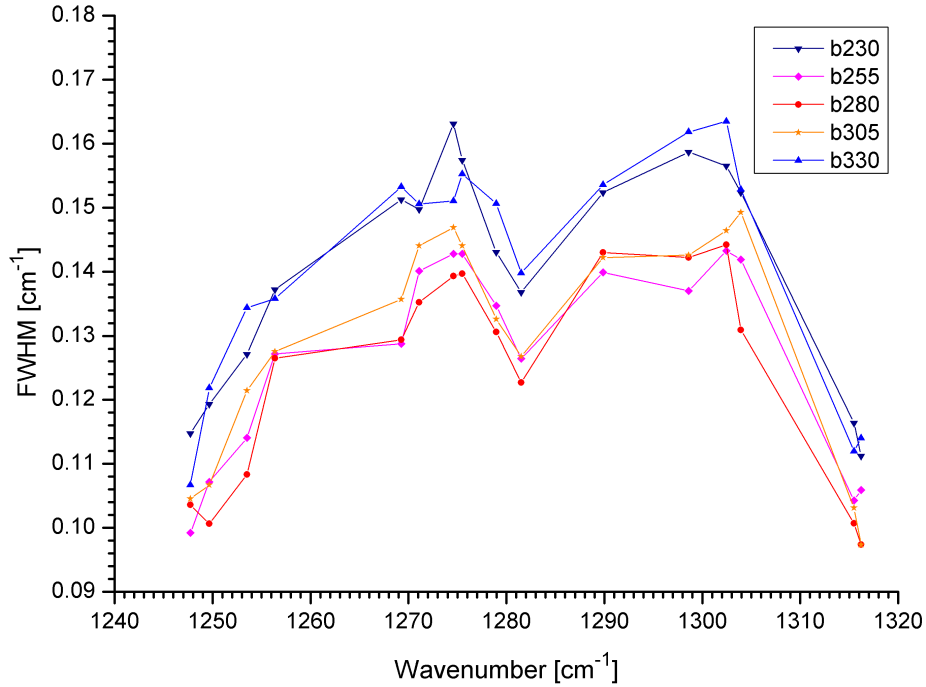


Figure 6.26.: The FWHM of the  $\text{N}_2\text{O}$  lines in the spectral range between  $1240\text{ cm}^{-1}$  and  $1320\text{ cm}^{-1}$  calculated for pixel (64,62) from measurement data and plotted for five different IRO positions separated by 25 counts.

are higher than the curve for the IRO at 280 count. The navy curve has values which are closer to the red curve as compared to the blue curve. Therefore, the focus position has to be in between the red (IRO at 280) and the magenta (IRO at 255) curve but closer to the red curve. The curves show that the method is sensitive enough to determine the focus position for up to 25 IRO counts (2.4 % of the focal length). The calculated FWHM values are affected by the noise in the spectrum. This may be the reason for the values crossing other curves for some of the spectral positions. The noise in the spectrum limits the focal position determination.

### Summary: Focal plane determination using spectral line width

The variation of the image distance values with the change of the interferometer temperature has been shown. The rate of change of the image distance values with respect to the interferometer temperature is  $1.6163 \times 10^{-3}\text{ cm/K}$ . The relationship between the image distance and the IRO position has been determined. The slope of the linear fit of the image distance values with respect to the IRO position is  $1.4019 \times 10^{-3}\text{ cm/count}$ . These two relations give the variation of the IRO counts with respect to the interferometer temperature as 1.1529 counts/K. The IRO has to be moved at this rate in order to stay at the focus position with the change of the interferometer temperature. Considering the situation, that the IRO is fixed at the center of the measurement temperature range of 10 K and not adjusted while the measurement is being performed, the line shift error for a corner pixel located (64,24) pixels away from the on-axis pixel, will be approximately  $\pm 0.8\text{ ppm}$ . Since the error contribution is small, it is suggested not to move the IRO. Moving the IRO will cause a change in the optical axis position. As a result new calibration measurements have to be performed with the changed IRO position, which is time consuming and therefore not adequate. The position of the lens which is closest to the focal plane is found by using the line width. The method is sensitive enough to determine the focus position for up to 25 IRO counts (2.4 % of the focal length).

## 6.9. Shear analysis

In this section a method is presented which determines the lateral shift (shear) in an interferometer from the center of the Haidinger fringe pattern for each frame (or OPD). Finding the shear will give the possibility to account for the effects and perform necessary shear corrections prior to the scientific measurements.

### Lateral shift: Cause and effect

In an ideal case, the interferogram ( $I_0$ ) for a monochromatic plane wave propagating at a defined angle is given as [18]

$$I_0(x) = S_0 [1 + \cos(2\pi\sigma_0 x \cos\alpha)] \quad (6.10)$$

where

$S_0$  is the unmodulated part,

$x$  is the OPD,

$\sigma_0$  is the wavenumber of the monochromatic source,

$\alpha$  is the off-axis angle of the ray.

The radiation beam traveling at an angle  $\alpha$  through the interferometer comes to focus at a distance  $r$  from the optical axis (see figure 2.3). The angles in the interferometer are projected as radii on the detector surface. The path difference variation is approximated by

$$x \cos\alpha \approx x\left(1 - \frac{\alpha^2}{2}\right) \approx x\left(1 - \frac{r^2}{2f^2}\right) \quad (6.11)$$

where  $r = f \sin\alpha \approx f \alpha$  and  $f$  is the focal length.

Equation 6.11 shows that the effective path difference for a point on the detector surface varies as  $r^2$ . This gives the circular fringes around the optical axis position. The spacing of the fringes is given by

$$\frac{xr^2}{2f^2} = m\lambda, \quad (6.12)$$

where  $m$  is an integer.

$$r^2 = \left(\frac{2f^2}{x\sigma}\right) m. \quad (6.13)$$

At a smaller path difference close to the ZPD, the fringes have a large radius and the 2D-detector array accepts a small part of a single fringe. As the path difference increases, it leads to the fringe width getting smaller and the detector array accepts a larger fraction of the fringe. As the path difference increases further more, the detector array accepts an entire ring. For an OPD larger than this point more than one ring is accepted. Figure 2.4 shows the Haidinger fringe pattern with several fringes over the FPA for an OPD of 5.5 cm away from the ZPD.

In case of a real-life interferometer, the radiation beams from the two arms may not be perfectly superimposed spatially, depending on the position of the cube corners and the beamsplitter. In such a situation they are said to be laterally sheared. The shear results in a shift of the Haidinger fringe center position on the detector array. The shear present in the interferometer is a field effect. It corresponds to an added OPD which is a function of the angle of propagation ( $\alpha$ ) in the interferogram. This results in a shift of the ZPD position, which leads to a complex ILS with a part of the signal in the imaginary part of the spectrum. The shear effect in an instrument can be tolerated as long as the contribution of the signal in the imaginary part is less than the noise level.

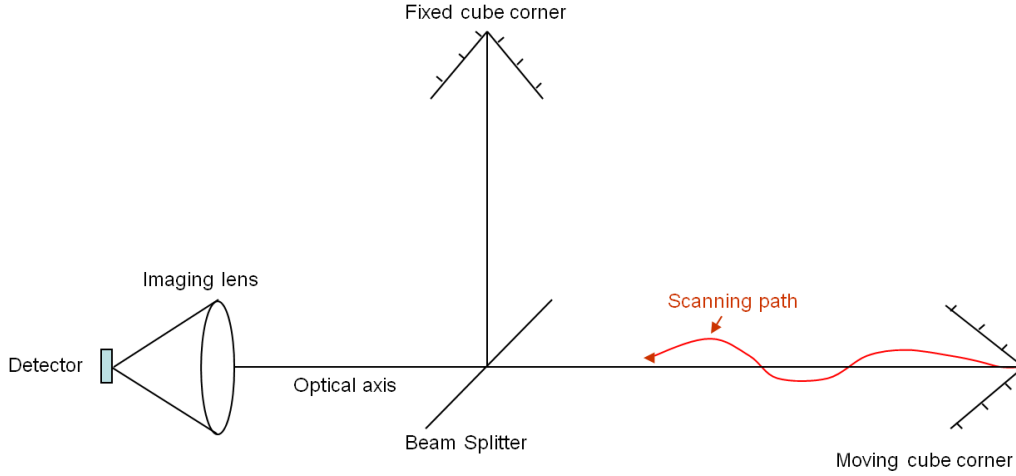


Figure 6.27.: A schematic diagram showing a possible path of the interferometer drive with the moving cube corner in GLORIA.

A possible path (red curve) of the moving cube corner in an interferometer is shown in figure 6.27. The moving cube corner may have a constant, a linear or a higher order (periodic or oscillatory) OPD dependent lateral shift. This misalignment may result from either the cube corner and the beamsplitter alignment error, thermo-elastic effects, gravity effects, shock, periodic or oscillatory vibrations of the cube corners caused by either the compressor or a vibration of the instrument on the aircraft. As a result, an additional term ( $\Delta_x(u, v)$ ) is introduced in the path difference of the interferogram. This additional term is dependent on the cube corner displacement and on the incident field angle. Hénault et al. [65] have studied the misalignment effect caused by the cube corner lateral shift and misalignment of the exit optics in the interferometer. The interferogram representation with this additional term for the cube corner lateral shift is given as

$$I_0(x) = S_0 [1 + \cos\{2\pi\sigma_0(x\cos u \cos v + \underbrace{2dy(x)\sin u \cos v + 2dz(x)\sin v}_{\Delta_x(u,v)})\}] \quad (6.14)$$

where  $dy$  and  $dz$  are the apparent lateral shifts of one cube corner apex along  $y$  and  $z$  axes<sup>3</sup>, respectively, with respect to the other cube corner apex.  $u$  and  $v$  represent the Cartesian field angles of the chief optical ray.

The lateral shift may be decomposed into three components: A constant, a linear and a higher order OPD dependent shear. The constant shear ( $y_0$  and  $z_0$ ) is caused by the misalignment between the cube corners and the beamsplitter. This might be due to shock or thermo-elastic effects. The effect of a constant lateral shift on the modulation and phases has been studied theoretically [66,67]. In an IFTS, the constant shear can be seen easily at the ZPD, with the occurrence of fringes. This shift is easy to be removed by aligning the fixed cube corner perfectly at the ZPD. The second possibility is the OPD dependent linear shift. It gives the information about the apparent trajectory of the moving cube corner along its mechanical path in the interferometer. A study of an OPD dependent linear shift based on the interferogram information has been described in literature [65,68]. The interferometer drive axis can be used to define the optical axis in an IFTS. In such a case no linear shift can be present. This approach is used in GLORIA. In addition, a higher order shift ( $H_y(x)$  and  $H_z(x)$ ) dependent on the OPD may occur. Considering both the constant and the higher order shift terms, the shear components in the  $y$  and  $z$  directions

<sup>3</sup>The  $x$  axis is in the direction of the slide movement, the  $y$  axis is perpendicular to the paper and the  $z$  axis is perpendicular to the  $x$  and  $y$  axes following the right hand rule.

for GLORIA are represented as

$$dy(x) = y_0 + H_y(x) \quad (6.15)$$

$$dz(x) = z_0 + H_z(x) \quad (6.16)$$

### Measurement method and characterization results

A QCL source filling the full field-of-view of GLORIA is used as the monochromatic source for the determination of the shear. These measurements were performed with a  $128 \times 128$  pixel array setup. The raw data for each pixel is recorded in a *cub* file measured on an equidistant temporal grid over the OPD. The monochromatic source forms a Haidinger fringe pattern over the FPA. The fringe pattern for an OPD of 5.5 cm away from the ZPD is shown in figure 2.4. The envisaged characterization method is a specific data processing of the fringe pattern for each frame of an interferogram such as to find the fringe center in the y and z components. The Haidinger fringe center of a frame is determined by performing an autocorrelation between the selected frame and the same frame rotated by  $90^\circ$ . The maximum position of the auto-correlation matrix gives the pixel position of the center of the fringes. A 2D Gauss fit is applied around the  $10 \times 10$  pixels of the maximum position. The maximum position of the fitted Gauss profile is taken as the precise center position in sub-pixel level. The shear in the y and z directions for each frame can be extracted from the center position using the following equations

$$sh_y(fr) = \frac{(cm_y - c_y) d x_{fr}}{2b} \quad (6.17)$$

$$sh_z(fr) = \frac{(cm_z - c_z) d x_{fr}}{2b} \quad (6.18)$$

where

- $sh_y$  and  $sh_z$  are the y and z components of the shear,
- $cm_y$  and  $cm_z$  are the y and z components of the measured fringe center,
- $c_y$  and  $c_z$  are the y and z components of the optical axis position,
- $fr$  is the index of the frame,
- $d$  is the pitch of a single pixel,
- $x_{fr}$  is the OPD value corresponding to the frame,
- $b$  is the image distance.

The spectral calibration parameters for the setup are derived from separate gas cell measurements.

The shear value is calculated for each frame as a function of the measurement time. The approximate OPD (x direction) is calculated by multiplying the time axis with the mean velocity of the interferometer drive. A Fourier transform of the shear curve versus the time in the directions of y and z gives the shear frequencies present in both directions. The vibration frequencies in the x direction (direction of the moving slide) can be evaluated separately by calculating a Fourier transform of the velocity signal. Therefore, the vibration effects of the slide in all three directions (x,y,z) over the interferogram length can be quantified.

Laboratory measurements were performed at interferometer temperatures of  $-14^\circ\text{C}$ ,  $-55^\circ\text{C}$  and  $-65^\circ\text{C}$ . The temperatures were selected such as to quantify the shear contribution with the change of temperature. A *cub* file is selected from measurements performed at  $-14^\circ\text{C}$ . In order to get an overview of the fringe center variation over the OPD, the fringe center is determined from every 100th frame (approximately 0.2 mm).

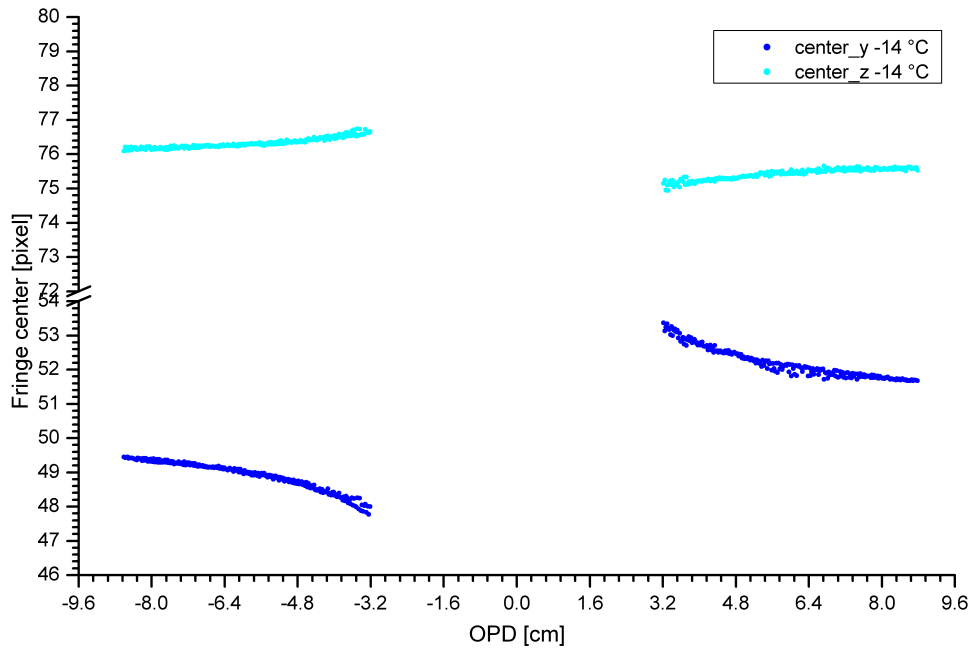


Figure 6.28.: The center of the Haidinger fringe variation in y (blue) and z (cyan) directions over OPD calculated for every 100th frame of an interferogram measured at the interferometer temperature of  $-14\text{ }^{\circ}\text{C}$ .

The variation of the Haidinger fringe center with respect to the OPD is shown in figure 6.28. As the ZPD is approached, the number of fringes in the Haidinger fringe figure on the detector array decreases and the fringes are not full anymore (equation 6.13). Determining the fringe center using this method therefore fails for frames which are close to the ZPD. The validity of the algorithm has been checked with synthetic data. The simulation results show that the fringe center determination fails for the OPD regions in the range of  $\pm 3.2\text{ cm}$  of the ZPD. As a result, all frames which are within  $\pm 3.2\text{ cm}$  around the ZPD are not analyzed.

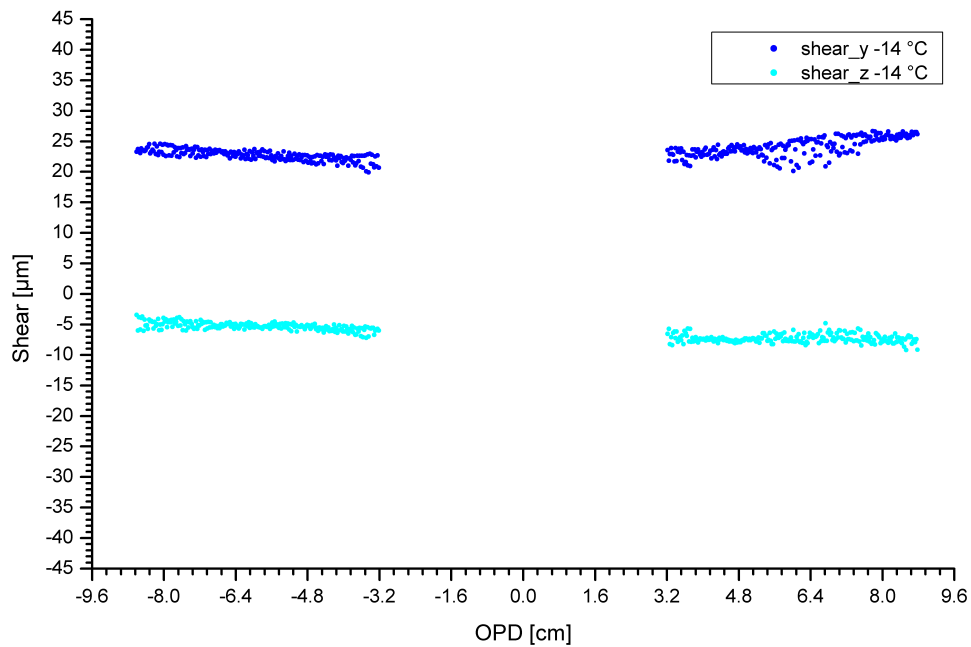


Figure 6.29.: Shear variation in y (blue) and z (cyan) directions over the OPD calculated for every 100th frame of an interferogram measured for an interferometer temperature of  $-14\text{ }^{\circ}\text{C}$ .

The shear values in the directions of y and z are calculated from the fringe center information using equations 6.17 and 6.18. Figure 6.29 shows the shear variation over the OPD. The plot shows a constant shear of approximately  $22 \mu\text{m}$  in the y (blue) and  $5 \mu\text{m}$  in the z (cyan) direction, respectively. The shear in the y direction shows a slightly bend shape going up at both ends. The z direction shows a slight negative slope for the negative OPD positions. This form represents the shape of the scan axis of the interferometer over the OPD in the y and z directions. The scatter in the fringe center and the shear plot for the OPD values around 6.4 cm are due to the presence of laser speckles close to the center of the Haidinger fringe pattern appearing only in this OPD region. The presence of speckles causes an error in the determination of the fringe center. The laser speckle, which occurred for this measurement, was due to a source alignment problem which was avoided for some of the measurements performed at other temperatures.

### Shear variation with interferometer temperature

The shear values over the OPD are calculated for measurements performed at instrument temperatures of  $-14 \text{ }^\circ\text{C}$ ,  $-55 \text{ }^\circ\text{C}$  and  $-65 \text{ }^\circ\text{C}$ .

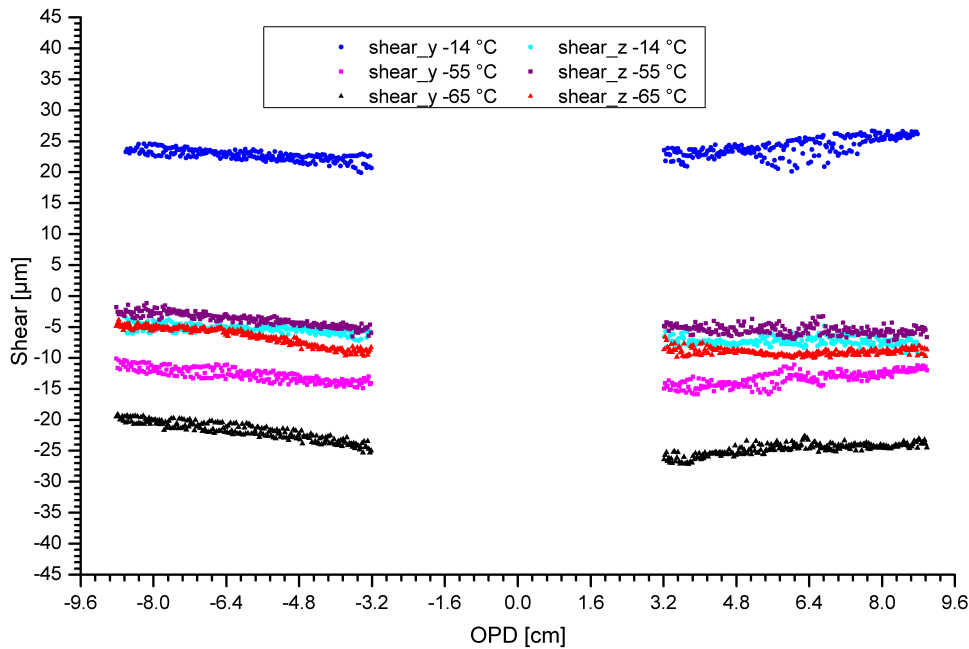


Figure 6.30.: Shear variation over the OPD calculated for every 100th frame of an interferogram measured for the interferometer temperatures of  $-14 \text{ }^\circ\text{C}$  (y component - blue, z component - cyan),  $-55 \text{ }^\circ\text{C}$  (y component - magenta, z component - violet) and  $-65 \text{ }^\circ\text{C}$  (y component - black, z component - red).

The plot of the y and z components of the shear for the measurements performed at the three temperatures are shown in figure 6.30. The y components of the shear (blue, magenta and black) show a change of the constant shear at a rate of  $1 \mu\text{m}$  per  $1 \text{ }^\circ\text{C}$ . The z components of the shear (cyan, violet and red) show only a very small change ( $< 5 \mu\text{m}$ ) with the change of the instrument temperature. During these three measurements no optical or mechanical adjustments were done for correcting the shear introduced due to the temperature change in the interferometer.

A second set of measurements was performed at  $-65 \text{ }^\circ\text{C}$  by adjusting the fixed cube corner in order to compensate for the constant shear. The adjustment was done visually by checking the frame picture at the ZPD position. The fixed cube corner had a mechanical mount with the possibility to be moved in the y and z directions. The fixed cube corner

was moved such that the shear fringe at the ZPD disappeared. A *cube* file was recorded with the shear-adjusted interferometer. The shear values in the y and z directions were calculated over the OPD range. Figure 6.31 shows the shear values before (y component - black, z component - red) and after (y component - olive, z component - green) making the shear adjustment. After the adjustment, the shear was reduced to  $\pm 5 \mu\text{m}$ . This amount of constant shear gives a relatively small shift (by about 1/10th of the natural sampling ( $\approx 0.00025 \text{ cm}$ )) of the ZPD, which is not a problem at all. The constant shear shows up as a constant phase which can be corrected during the phase correction of the data.

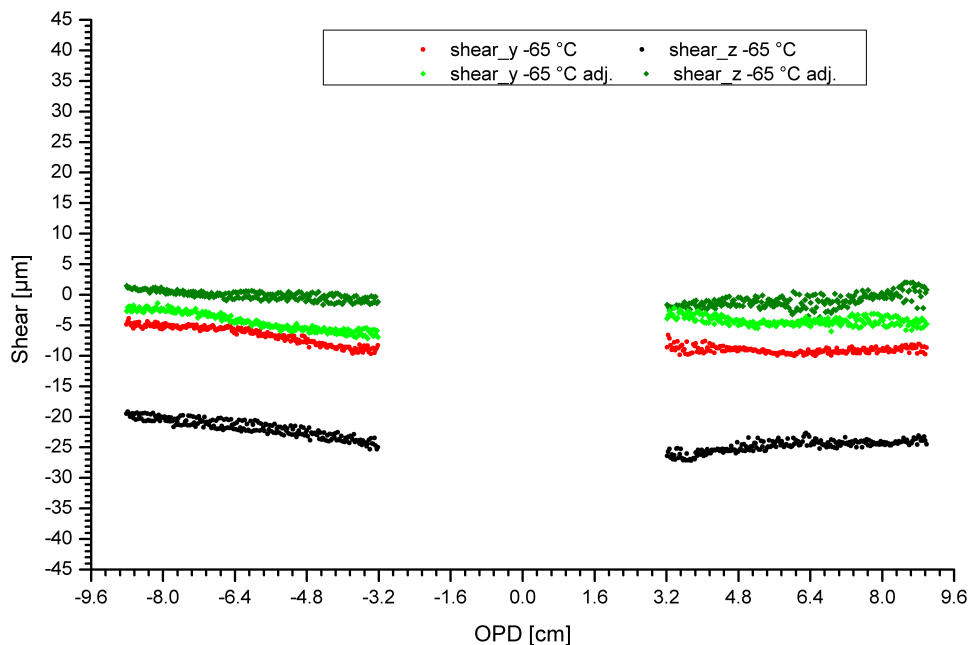


Figure 6.31.: Shear variation over the OPD before (y component - black, z component - red) and after (y component - olive, z component - green) making the shear adjustment, calculated for every 100th frame of an interferogram measured for the interferometer temperature of  $-65 \text{ }^\circ\text{C}$ .

The characteristics of the constant shear with the change of temperature are quantified and their reproducibility has been verified in the laboratory. This allowed to simplify the instrument by replacing the previously adjustable cube corner mount with the present fixed mount configuration in the GLORIA interferometer. In the present configuration, the cube corner has to be pre-adjusted to not have a constant shear for the interferometer's mean operating temperature. During a 10 hour measurement flight with HALO, with a current interferometer temperature drift rate of  $1 \text{ K/hour}$ , the maximum possible shear variation in the y direction is  $\pm 5 \mu\text{m}$ , which has a negligible effect on the ILS.

### Higher order shear variations over the OPD

A *cube* file from the measurements performed at an interferometer temperature of  $-65\text{ }^{\circ}\text{C}$  is taken for the analysis of the higher order shear variations over the OPD. The fringe center and the shear values are calculated for every frame for a limited OPD range and plotted in figure 6.32 and figure 6.33, respectively. The plots show oscillations at certain frequencies. The oscillations of the shear plot are analyzed in the following section. In addition, the small slowly changing shear variations over the selected OPD region can be seen well.

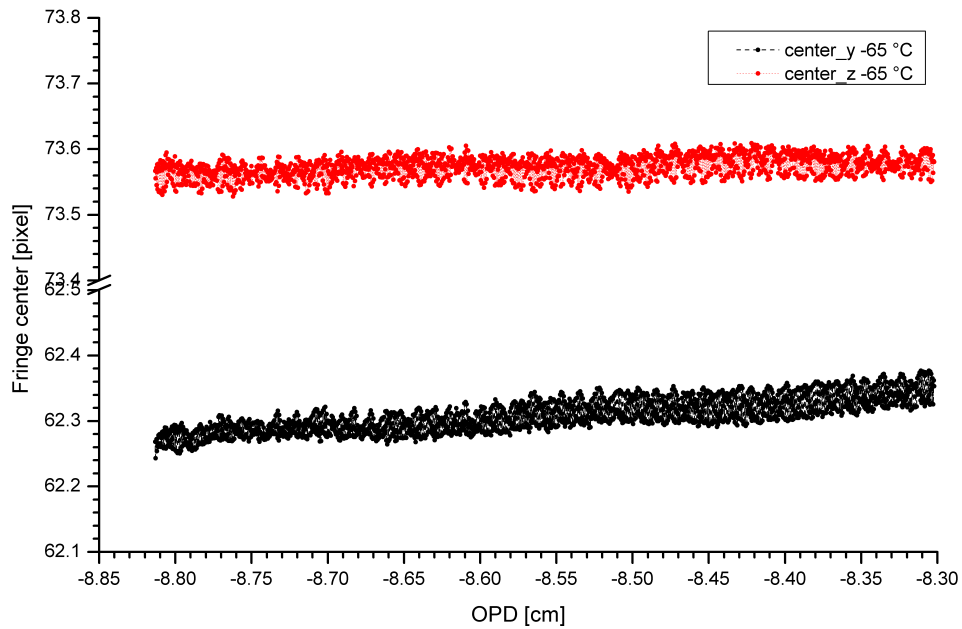


Figure 6.32.: The center of the Haidinger fringe variation in y (black) and z (red) directions over the OPD calculated for every frame of an interferogram measured for an interferometer temperature of  $-65\text{ }^{\circ}\text{C}$ .

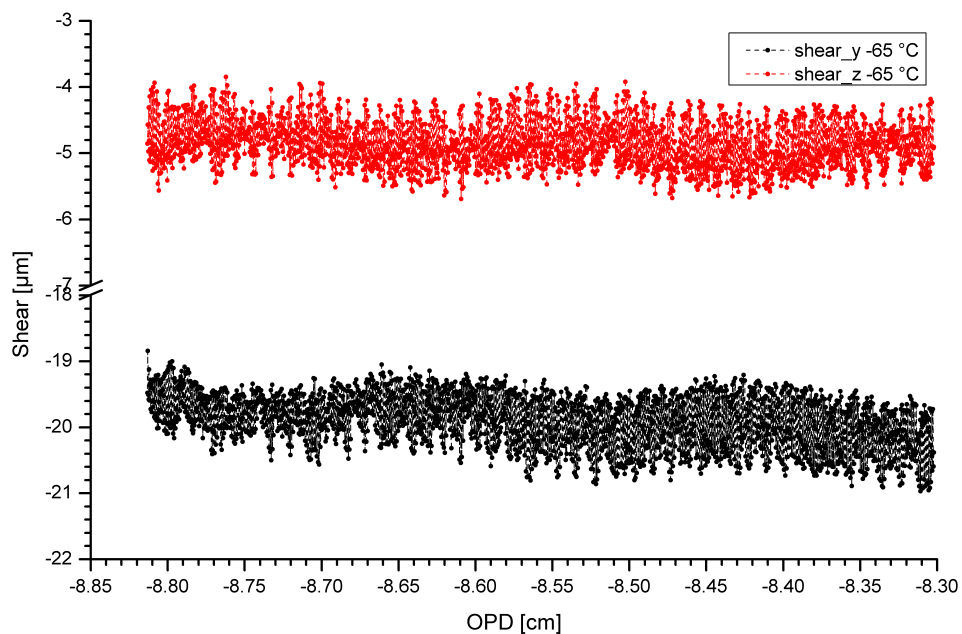


Figure 6.33.: Shear variation in y (black) and z (red) directions over the OPD calculated for every frame of an interferogram measured for an interferometer temperature of  $-65\text{ }^{\circ}\text{C}$ .

## Vibration analysis

The high resolution shear values allow a Fourier analysis of the vibrational shear components.

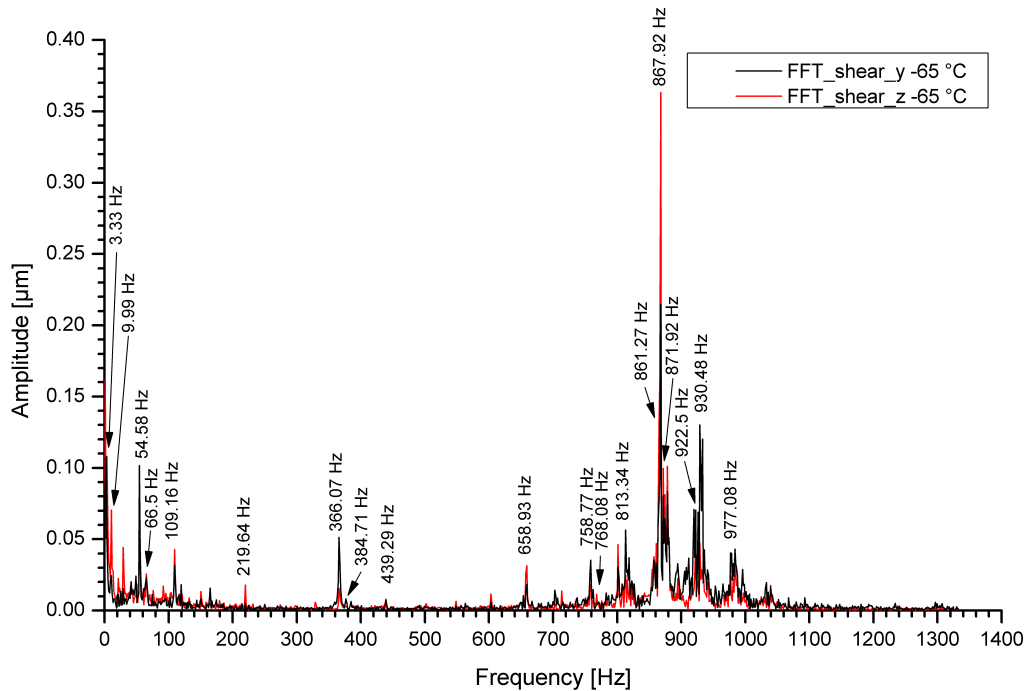


Figure 6.34.: The shear frequencies in y (black) and z (red) directions for measurements performed at an interferometer temperature of  $-65\text{ }^{\circ}\text{C}$ .

The shear frequencies in the y and z directions for measurements performed at an interferometer temperature of  $-65\text{ }^{\circ}\text{C}$  is shown in figure 6.34. They have been calculated by performing the Fourier transform of the shear values shown in figure 6.33. The vibrational frequencies are seen at 3.33 Hz and its overtones and at  $\approx 55$  Hz and its overtones. The spindle of the interferometer drive used during this measurement has a pitch of 1 mm. The calculated mean optical velocity of the interferometer drive during the measurement was 0.666 cm/sec which corresponds to a mean mechanical velocity of 0.333 cm/sec. This gives a frequency of 3.33 Hz vibration plus its overtones for every rotation of the spindle. The overtone frequencies which are picked up by the interferometer are found at about 9.99 Hz, 66.5 Hz, 366.07 Hz. These vibration frequencies caused by the spindle motion are dependent on the velocity at which the drive is moving. The vibration of the compressor gives 55 Hz and its overtone frequencies. The overtone frequencies which are picked up by the interferometer are found at about 109.16 Hz, 219.64 Hz, 384.71 Hz, 439.29, 658.93 Hz, 768.08 Hz. These vibration frequencies are independent of the interferometer's drive velocity.

The frequency seen at 867.9 Hz corresponds to  $1300\text{ cm}^{-1}$  and is the frequency of the monochromatic source (QCL) used for the measurements. This frequency is an artifact of the fringe center determination method which uses the 2D-detector array (square array) while calculating the auto-correlation. In addition, the ground frequencies and their overtone frequencies are seen to be repeated centering 867.9 Hz frequency line. The frequencies at about 758.77 Hz, 813.34 Hz, 922.5 Hz, 977.08 Hz are the overtones of 55 Hz frequency which are repeated centering the 867.9 Hz line. The overtones frequencies of 3.33 Hz are found to be repeating centering 867.9 Hz (e.g. 861.27 Hz and 871.92 Hz) and other 55 Hz repeated frequencies. These apparent ghost frequencies have no physical meaning.

A method to differentiate between the real vibration frequencies and the artifacts will be discussed later.

The maximum intensity of the vibration frequencies in both the  $y$  and  $z$  direction is  $0.1 \mu\text{m}$ . The effect can be seen as a phase modulation of the velocity signal by an amplitude variation of less than 5 %. The vibration frequency will cause a phase modulation of the interferograms leading to phase ghosts in the spectrum. A detailed analysis of the effect of the phase modulation with varying modulation amplitudes has been studied by Kimmig [69]. He showed that a phase modulation by an amplitude of 5 %, will cause a maximum relative amplitude of the phase ghosts of the order of  $1 \times 10^{-5}$ . This magnitude of the ghost will be hidden in the noise, therefore the higher order vibrational shear present in the measurement is not an issue for GLORIA.

The Fourier transform of the velocity signal corresponding to the *cube* file analyzed above gives the vibration frequencies in the direction of the movement of the spindle ( $x$  direction).

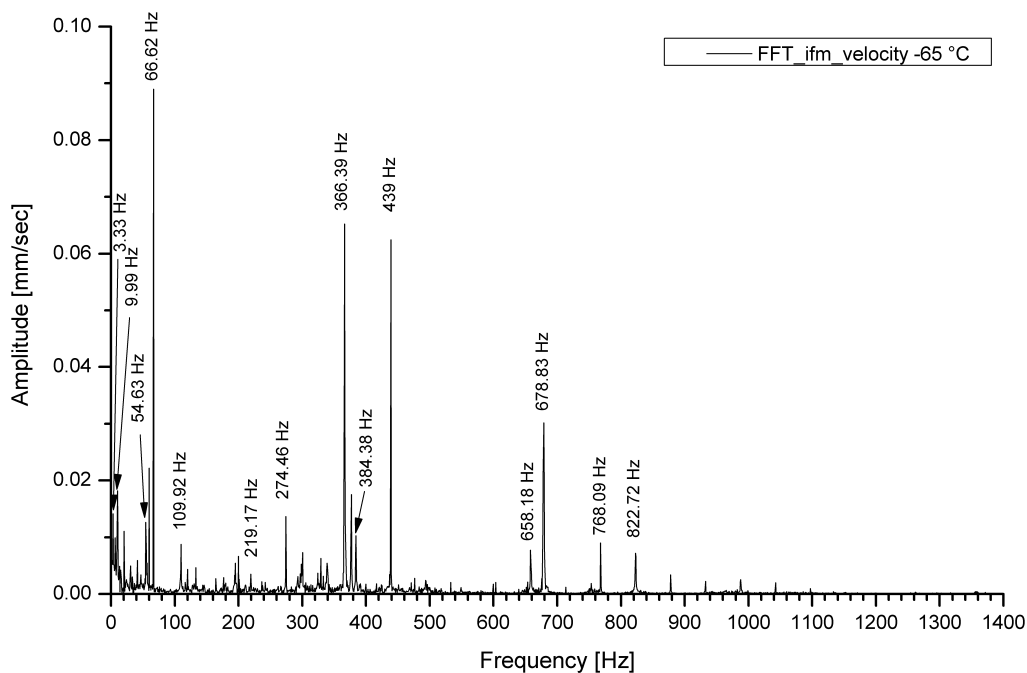
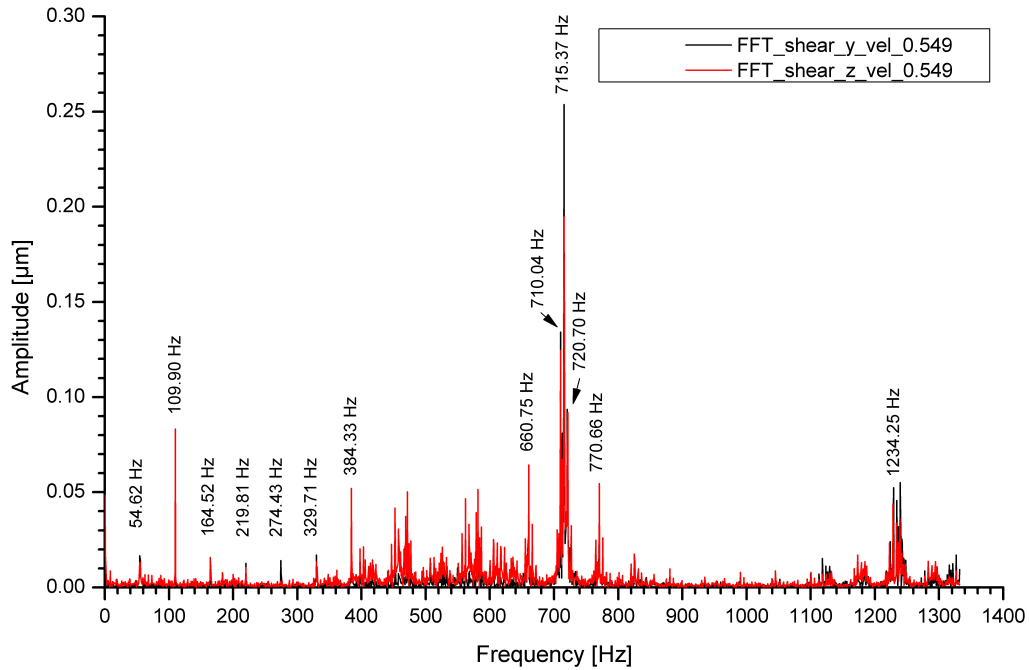


Figure 6.35.: Frequency plot in the direction of interferometer drive movement ( $x$  direction) for an interferometer temperature of  $-65 \text{ }^\circ\text{C}$ .

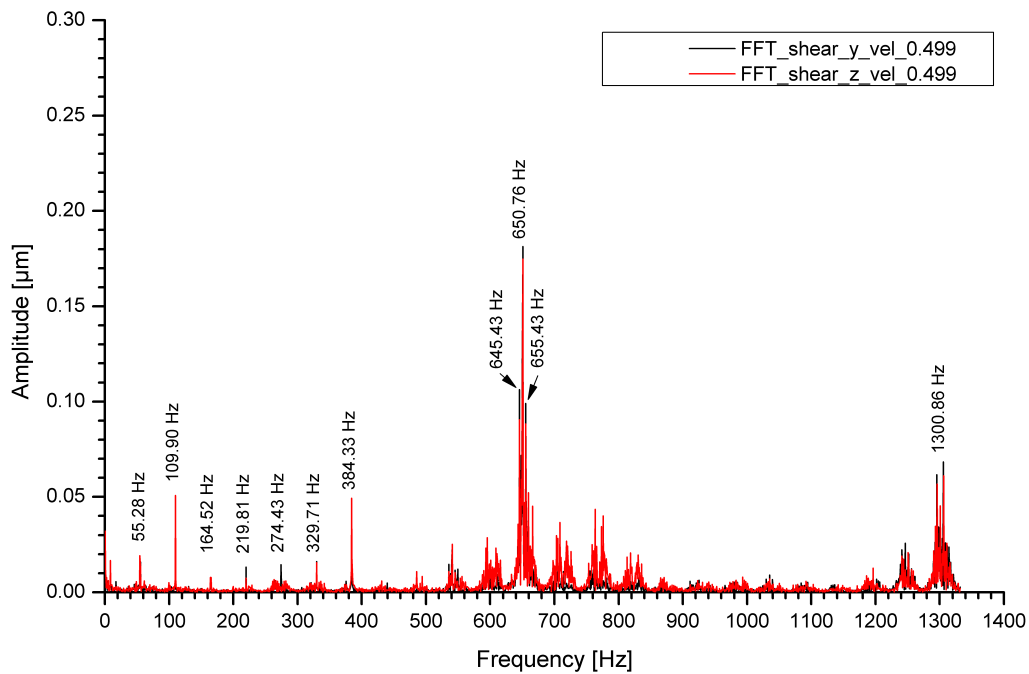
The vibration frequencies in the  $x$  direction are shown in figure 6.35. While most of these frequencies are seen in the  $y$  and  $z$  directions, some of them (e.g., 66.6 Hz, 274.46 Hz, 439 Hz, 678.83 Hz) are seen with reduced amplitudes. The vibrational frequencies extracted from the velocity signal is free from the artifacts coming from the laser frequency, while the analysis of the Haidinger fringes gives the shear vibration, as a combination of real frequencies and artifact frequencies, in the  $y$  and  $z$  directions. Therefore from the combination of the two analysis, the real vibration frequencies and their amplitudes can be determined in all three axes along the OPD from a single measurement.

The position of the artifact and the apparent ghost frequencies coming from the determination method are dependent on the velocity of the interferometer drive and the detector readout frequency. Laboratory measurements were done in order to identify this effect. Driving the interferometer with a different velocity shifts the position of the artifact and the apparent ghost frequencies. As a result the frequency regions which are of interest can be made free of apparent ghost frequencies by performing measurements at a selected velocity. Measurements were performed with a warm instrument looking at the QCL source

at four different interferometer velocities (0.666 cm/sec, 0.599 cm/sec, 0.549 cm/sec and 0.499 cm/sec). The shear frequencies were calculated for each case.



(a)



(b)

Figure 6.36.: Shear frequencies in y (black) and z (red) directions for measurements performed at interferometer velocities of 0.549 cm/sec (a) and 0.499 cm/sec (b) with the interferometer at room temperature.

The results for the interferometer velocity of 0.549 cm/sec and 0.499 cm/sec are shown in figure 6.36(a) and figure 6.36(b), respectively. The spindle of the interferometer drive used during the measurement has a pitch of 1 mm. The vibration frequencies due to the spindle are about 2.75 Hz and 2.5 Hz and their overtones for the interferometer velocities of

0.549 cm/sec and 0.499 cm/sec, respectively. Moreover, the plots also show the vibration frequency and its overtones due to the compressor. The detector sampling frequency for this measurement is approximately 2665 Hz for  $128 \times 128$  pixel array. The expected position of the artifact and the apparent ghost frequencies due to the laser are calculated from the knowledge of the interferometer velocity.

A detailed analysis of the artifact and the ghost frequencies for the measurements performed with a velocity of 0.549 cm/sec is shown here. The artifact frequency corresponding to the monochromatic source is at approximately 715 Hz and is named as the first artifact frequency. The frequency at 1234.25 Hz corresponds to twice the artifact frequency which is then folded at the detector Nyquist frequency of 1332.5 Hz. The expected position is at approximately  $2 \times 715 \text{ Hz} = 1430 \text{ Hz}$ , which is folded at 1332.5 Hz, giving the position as 1235 Hz. This is named as the second artifact frequency, its amplitude is reduced significantly with respect to the first artifact frequency. The third artifact frequency is expected to be formed at approximately  $3 \times 715 \text{ Hz} = 2145 \text{ Hz}$ , which is folded at 1332.5 Hz, giving the position as approximately at 520 Hz. The amplitude of this frequency is further reduced significantly. The fourth artifact frequency is expected at 195 Hz. The intensity of this frequency is further reduced as compared to the third artifact frequency. Higher order artifact frequencies are not seen as noticeable frequencies in figure 6.36(a). The amplitude of the artifact frequencies is observed to be decreasing with the increasing order of artifact frequencies. The apparent ghost frequencies of the compressor and the spindle are repeated centering the first and the higher order artifact frequencies. The amplitude of these apparent ghost frequencies decreases after each repetition. These frequencies can be seen up to the fourth order of repetition on both sides of the line of each artifact frequency. The structure of the first lobe (artifact frequency and spindle frequencies) and the neighboring three side lobes (compressor frequency and spindle frequencies) are found also for the apparent frequencies at 1234 Hz, 520 Hz and 195 Hz and are named as ghost frequencies. The second right side lobe of the artifact frequency at 1234 Hz is mirrored at the Nyquist frequency. The side lobes corresponding to the third artifact frequency at 520 Hz overlaps with the left side lobes of the first artifact frequency at 715 Hz.

The first artifact frequency for the measurements performed with a velocity of 0.499 cm/sec is at approximately 650 Hz. The estimated higher order artifact frequencies are at approximately at 1300 Hz, 715 Hz and 65 Hz. The two right lobes of the second artifact frequency at 1300 Hz are seen overlapping with the second artifact frequency and its first left lobe. The third artifact frequency at 715 Hz and its corresponding side lobes are also overlapping with the first artifact frequency at 650 Hz and its side lobes. The amplitude of these apparent ghost frequencies decreases after each repetition.

The real frequencies which are independent of the slide velocities (e.g., compressor vibrations) are found to be at the same position, whereas the velocity dependent real frequencies (e.g., vibrations due to the spindle movement) are found to be varying with respect to the velocity for all cases. The position of the artifact and ghost frequencies can be exactly calculated and are found to be at the previously estimated positions as shown in figure 6.36(a) and figure 6.36(b). The position and the intensity of the real frequencies are not affected by the determination method. If the vibrational frequencies are expected in a certain frequency regions, the measurements can be performed at a specified velocity such that the region of interest can be made free from any artifact or ghost frequencies (e.g. artifact free frequency regions around 400 Hz, 1100 Hz, etc. for figure 6.36(b)). Figure 6.36 also shows that the amplitude of the real frequencies varies slightly with the variation of the interferometer velocity because the components have different operating conditions, e.g., different driving currents for the interferometer slide corresponding to the interferometer velocity.

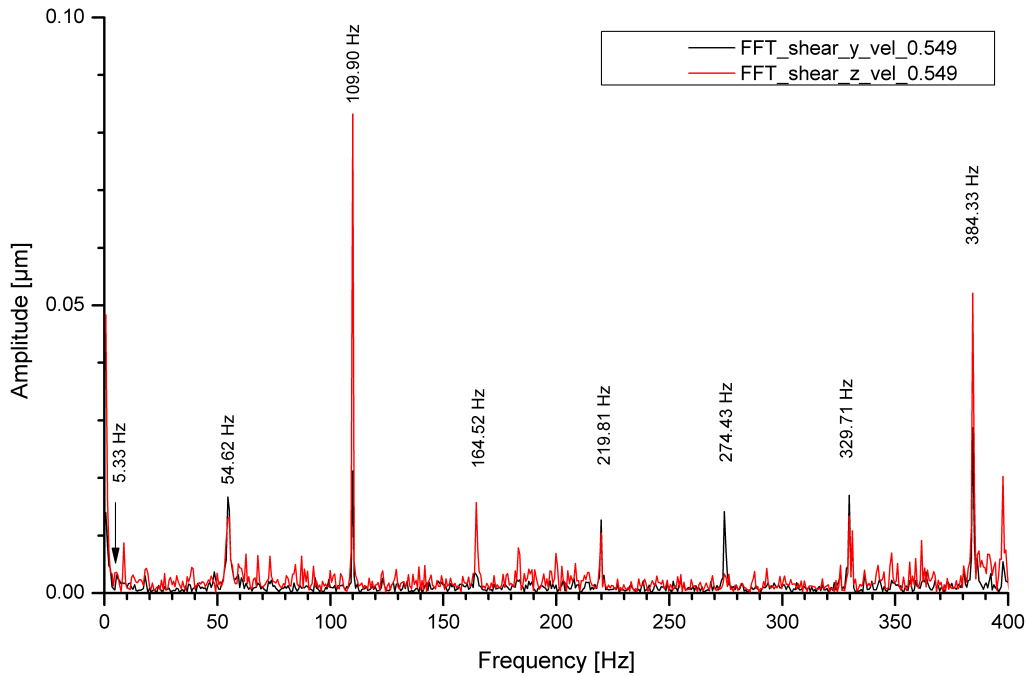


Figure 6.37.: A zoom of the shear frequencies (lower frequency range) in y (black) and z (red) directions for measurements performed at an interferometer velocity of 0.549 cm/sec with the interferometer at room temperature.

A zoom of the vibration frequencies in the y and z directions for the low frequency region of figure 6.36(a) is shown in figure 6.37. The plot shows that the ground vibrational frequency of 2.75 Hz due to the spindle is not recognizable but its overtone frequency can be seen with a very small amplitude at approximately 5.33 Hz. This is an improvement coming from a better spindle quality. The new spindle used for this measurement has a better finishing quality of the thread. In addition, a low temperature lubricant was used for the spindle. These two changes have resulted in the reduction of the intensity of the vibrational frequency due to the spindle.

### Summary: Shear analysis

A novel method for the determination of the shear in the interferometer from the Haidinger fringe pattern has been developed. A constant shear change at a rate of  $1 \mu\text{m}$  per  $1^\circ\text{C}$  in the y direction due to the change of the interferometer temperature has been identified with the adjustable cube corner mount setup and found to be reproducible. The shear in the z direction does not change much with the change of temperature. As a result of these observations, the dynamic adjustment possibility of the fixed cube corner setup was replaced with a static mount setup. With the present setup we have to preadjust the cube corner for the expected shear corresponding to the mean instrument operating temperature range. The shear plot over the OPD gives the manufacturing quality of the body of the slide. The analysis shows a small bend of roughly  $5 \mu\text{m}$  over its length in the y direction. The Fourier transform of the velocity signal gives the vibration frequencies in the x direction (direction of the slide movement). The Haidinger fringe analysis gives the position and the amplitude of the shear frequencies in the y and z directions. These frequencies are present due to the relative motion of the instrument optics caused by the instrument vibration. All frequencies found in the x direction are also found in the y and z directions but with different amplitudes. In addition, the vibration frequencies in the y and z directions show a signal corresponding to the laser frequency and some other frequency signals of the ground vibrations which are repeated up to three orders to the left and right of the laser frequency. This signal of the laser frequency and the

ghost frequencies (side lobes) are repeated up to four times the laser frequency. These disturbances are not found at all in the x direction (because of the the other method used) and are not real frequencies. The real frequencies are those which are found in all three (x,y,z) directions. The real vibration frequencies and amplitudes in all three directions over the OPD are quantified. The magnitude of the real vibrational shear frequencies present are small and are not an issue for GLORIA. The use of a better quality spindle and low temperature lubricant for the interferometer drive have reduced the magnitude of the vibration frequencies resulting from the rotation of the spindle.

## 7. Conclusions and outlook

The work presented in this thesis focuses on the radiometric and spectrometric characterization and optimization of the imaging Fourier transform spectrometer GLORIA. The most important results presented in this thesis are summarized in this chapter.

A characterization method for the judgment on the detector quality has been developed. Three second generation AIM's photovoltaic Mercury-Cadmium-Telluride (MCT) large focal plane arrays have been characterized, compared in terms of their noise equivalent power (NEP); and their operating conditions were optimized. One of the detectors (detector II/1a) has been found not to be suitable for atmospheric measurements based on its poor radiometric properties and has been discarded. The other two detectors (II/1 and II/2) have similar radiometric properties. Based on an NEP criterion, a small number of bad pixels of about 2.8% and 5.6% over the central  $128 \times 128$  pixel array were found for detector II/1 and detector II/2, respectively.

The detector system has shown to produce a nonlinear response. As a result the measured infrared signal shows nonlinearity features with the presence of artifacts in the out-of-band spectral regions. A proper nonlinearity correction is necessary such as to obtain a correct representation of the incident radiation. The two point radiometric calibration used in GLORIA is valid only if the interferograms are linear. A nonlinearity correction method based on Hilbert [50] has been applied in two ways to the measurement data. One approach was that the nonlinearity correction has been applied to each individual pixel with the correction parameters calculated for this pixel; the other approach was that the correction parameters of a good pixel was used for each individual pixel. In the comparison study made between the two ways of approaches, the latter has been found to be better suitable for reducing the nonlinearity. Hence, this correction method has been used as the standard for the data processing of all data measured in the laboratory and in-flight. The nonlinearity correction did not work properly for about 14% and 20% of the pixels (over the central  $48 \times 128$  pixel array) for detector II/1 and detector II/2, respectively. The prior assumption that the nonlinearity is dependent only on the carrier number has been disproved after analysis of the flight data. It seems that different nonlinearity correction parameters have to be used for different flux situations which needs to be further investigated.

A theoretical noise model for GLORIA has been presented which quantifies the sources contributing to the total signal and identifies the contribution of the different noise sources to the measured signal in GLORIA. The integral detector quantum efficiency, the instrument

emissivity and the constant noise term have been estimated by adjusting the parameters of the noise model to the radiometric measurements. The theoretical noise equivalent spectral radiance (NESR) values calculated using the noise model represent correctly the NESR values derived from the measurements performed both on-ground and in-flight. The good agreement verified the nominal performance of the instrument in both situations. The model predicts the performance of the instrument under various circumstances and hence can be used for further scientific work.

A characterization method for checking the imaging quality over the detector array for the GLORIA optics has been developed. With this method, the image of an extended infrared point source on the central and corner positions of the detector array has been characterized. It has been found that the central image does not show strong distortion effects whereas the corner images show image deformation which may be due to the presence of coma, spherical aberration or distortion, which has to be taken into account for further analysis. The present setup used for the characterization measurements gave a qualitative estimate of the imaging quality. A new measurement setup along with an improved ray tracing model has to be developed for a more precise determination of the imaging quality of the GLORIA optics over the detector array.

The current method of checking the imaging quality enables to characterize parasitic images formed on the detector surface due to multiple reflections at the beamsplitter unit. The theoretically expected values of the position and intensity of the parasitic images are of the same order as the observational results. The parasitic images (intensity of AC part is about 3% of the main image) are added to the radiance signal for any given pixel. This additional signal is not a problem for a homogeneous (horizontal direction) scene, but the effect has to be taken into account when single pixels in a horizontally inhomogeneous scene are analyzed, in order to avoid errors in the retrieved trace gas concentration. Knowing the position and intensity of the parasitic images will improve the estimation of the error.

A method for the determination of the spectral calibration parameters for an imaging Fourier transform spectrometer (IFTS) has been developed and applied to measurements performed with GLORIA both on-ground and in-flight. Among the three line position determination methods tested, the zero filling method, which is simple in its application and fast in the execution, has been selected and optimized. The line position determination is sensitive to the SNR of the lines. It is found that atmospheric and deep space measurements performed in the chemistry mode having a good SNR are both suitable for finding the spectral calibration parameters. In general, deep space measurements are found to be better suited due to the presence of a homogeneous scene measured over the detector array with low contributions from only some lines from more abundant trace gases. It also has a cloud free scene and therefore none of the pixels have to be rejected due to cloud contamination. However, for cases where the SNR of deep space measurements is low, we need to use atmospheric measurements which have a relatively higher SNR. The spectral calibration parameters are found to be slowly changing with the thermal drift of the interferometer. The rate at which the infrared objective (IRO) has to be moved in order to stay in focus with the changing temperature has been determined. It has been proposed to not move the IRO for the present HALO flights because that would have necessitated extra calibration measurements for each change of the IRO positions. This would have been time consuming and was not necessary since the estimated spectral calibration error made by not moving the IRO has been found to be  $\pm 2$  ppm which is well acceptable. The accuracy of the spectral calibration has been found to be well within the threshold specification of 10 ppm. The spectral calibration has worked well over the whole spectral range leaving only a small residual line position error which is acceptable.

---

A novel method for the determination of the focus position in an IFTS based on the line width has been developed. The method is sensitive enough to identify a de-focusing of approximately 2.4 ‰ of the focal length. This method can be used to verify the focus position from the in-flight measurements.

A novel method for the determination of the interferometer shear using the Haidinger fringe pattern has been developed. Using this method a constant, a linear and a higher order shear value over the OPD have been characterized. A constant shear change depending on the interferometer temperature has been identified and found to be reproducible. With the results of this observation the design concept of the fixed cube corner could be simplified from a dynamic adjustment possibility to a static mount. The shear determination method allows to qualify the mechanical quality of the slide in a very precise manner. The method also allows to identify and quantify the vibration frequencies in two perpendicular directions perpendicular to the direction of the slide movement. The vibrational frequencies are present due to the relative motion of the instrument optics caused by instrument vibration. In addition, with the determination method used, some unwanted artifact and ghost frequencies are found along with the real vibration frequencies determined from the Haidinger fringe pattern. It has been found that the magnitude of real vibrational shear frequencies present during the laboratory measurements are small and are not an issue for GLORIA.

As shown above, the interferometer and detector parameters of GLORIA have been characterized and optimized, which helped to better understand the important features of an IFTS instrument. An elaborate method to properly adjust and align the interferometer optics has been developed.

Potential research topics that should be further pursued are:

- A revisit of the nonlinearity behavior of the detector pixels to better understand the residual nonlinearity for those pixels where the correction has not worked properly is needed. The nonlinearity dependence on the detector integration time and photon flux has to be quantified from all in-flight data and by performing characterization measurements. The stability and reproducibility of the nonlinearity behavior of the pixels have to be investigated. An analysis of the usable dynamical range of the detector with good nonlinearity correction possibility has to be done. In addition, the quality of the nonlinearity correction has to be verified based on the level2 retrieval results.
- A new measurement setup for the precise determination of the imaging quality of the GLORIA optics over the detector array has to be developed. In addition, with the help of an improved ray tracing model, the imaging quality for on-focused and de-focused lens positions has to be investigated in detail and compared with measurements in future studies.
- The spectral calibration parameters for all in-flight measurements performed during the TACTS and ESMVal campaigns have to be evaluated and checked.
- A new method for the determination of the Haidinger fringe center has to be developed in order to characterize the vibrational frequencies free from the artifact and ghost frequencies.

Undertaking these tasks will provide further valuable information to improve the performance of the instrument.

The achievements of this work are that the radiometric and the spectrometric properties of GLORIA are better understood. The characterization work has made it possible to perform

scientific measurements with optimized instrument parameters. Furthermore, it helped in the analysis and better understanding of the measured scientific data. Measurements performed with a well characterized GLORIA enhance the knowledge of the processes occurring in the upper troposphere and lower stratosphere (UTLS) region which can give a significant contribution to the understanding of the global climate change processes.

# Bibliography

- [1] J. C. Farman, B. G. Gardiner, and J. D. Shanklin. Large Losses of Total Ozone in Antarctica Reveal Seasonal ClO<sub>x</sub>/NO<sub>x</sub> Interaction. *Nature*, 315:207–210, 16 May 1985.
- [2] Gloria L. Manney, Michelle L. Santee, Markus Rex, Nathaniel J. Livesey, Michael C. Pitts, Pepijn Veefkind, Eric R. Nash, Ingo Wohltmann, Ralph Lehmann, Lucien Froidevaux, Lamont R. Poole, Mark R. Schoeberl, David P. Haffner, Jonathan Davies, Valery Dorokhov, Hartwig Gernandt, Bryan Johnson, Rigel Kivi, Esko Kyrö, Niels Larsen, Pieternel F. Levelt, Alexander Makshtas, C. Thomas McElroy, Hideaki Nakajima, Maria Concepción Parrondo, David W. Tarasick, Peter von der Gathen, Kaley A. Walker, and Nikita S. Zinoviev. Unprecedented Arctic ozone loss in 2011. *Nature*, 478:469–475, 27 October 2011.
- [3] S. Solomon, D. Qin, M. Manning, R.B. Alley, T. Berntsen, N.L. Bindoff, Z. Chen, A. Chidthaisong, J.M. Gregory, G.C. Hegerl, M. Heimann, B. Hewitson, B.J. Hoskins, F. Joos, J. Jouzel, V. Kattsov, U. Lohmann, T. Matsuno, M. Molina, N. Nicholls, J. Overpeck, G. Raga, V. Ramaswamy, J. Ren, M. Rusticucci, R. Somerville, T.F. Stocker, P. Whetton, R.A. Wood, and D. Wratt. Technical Summary. In *In: Climate Change 2007: The Physical Science Basis. Contribution of Working Group I to the Fourth Assessment Report of the Intergovernmental Panel on Climate Change [Solomon, S., D. Qin, M. Manning, Z. Chen, M. Marquis, K.B. Averyt, M. Tignor and H.L. Miller (eds.)]*. Cambridge University Press, Cambridge, United Kingdom and New York, NY, USA, 2007.
- [4] G.C. Hegerl, F. W. Zwiers, P. Braconnot, N.P. Gillett, Y. Luo, J.A. Marengo Orsini, N. Nicholls, J.E. Penner, and P.A. Stott. Understanding and Attributing Climate Change. In *In: Climate Change 2007: The Physical Science Basis. Contribution of Working Group I to the Fourth Assessment Report of the Intergovernmental Panel on Climate Change*. Cambridge University Press, Cambridge, United Kingdom and New York, NY, USA., 2007.
- [5] Brian Kerridge, Michaela Hegglin, Jack McConnell, Donal Murtagh, Johannes Orphal, Vincent-Henri Peuch, Martin Riese, and Michiel van Weele. Report for Mission Selection, An Earth Explorer to observe atmospheric composition. Technical report, Report for Mission Selection: PREMIER (ESA SP-1324/3), 2012.
- [6] A. Gettelman, P. Hoor, L. L. Pan, W. J. Randel, M. I. Hegglin, and T. Birner. The extratropical upper troposphere and lower stratosphere. *Reviews of Geophysics*, 49:RG3003, doi:10.1029/2011RG000355, 2011.
- [7] Jean-Marie Flaud and Johannes Orphal. *Handbook of High-resolution Spectroscopy*. John Wiley and Sons, Inc., 15 Sep 2011.
- [8] H. Fischer. Remote Sensing of Atmospheric Trace Constituents Using Fourier Transform Spectrometry. *Berichte der Bunsengesellschaft für physikalische Chemie*, 96, Issue 3:229–524, March 1992.

- 
- [9] H. Fischer and H. Oelhaf. Remote sensing of vertical profiles of atmospheric trace constituents with MIPAS limb-emission spectrometers. *Applied Optics*, 35(16):2787–2796, 1 June 1996.
- [10] H. Fischer, M. Birk, C. Blom, B. Carli, M. Carlotti, T. von Clarmann, L. Delbouille, A. Dudhia, D. Ehhalt, M. Endemann, J. M. Flaud, R. Gessner, A. Kleinert, R. Koopman, J. Langen, M. López-Puertas, P. Mosner, H. Nett, H. Oelhaf, G. Perron, J. Remedios, M. Ridolfi, G. Stiller, and R. Zander. MIPAS: an instrument for atmospheric and climate research. *Atmospheric Chemistry and Physics*, 8, Number 8:2151–2188, 16 April 2008.
- [11] W. Woiwode, H. Oelhaf, T. Gulde, C. Piesch, G. Maucher, A. Ebersoldt, C. Keim, M. Hopfner, S. Khaykin, F. Ravagnani, A. E. Ulanovsky, C. M. Volk, E. Hosen, A. Dornbrack, J. Ungermann, C. Kalicinsky, and J. Orphal. MIPAS-STR measurements in the Arctic UTLS in winter/spring 2010: instrument characterization, retrieval and validation. *Atmospheric Measurement Techniques*, 5:1205–1228, 2012.
- [12] F. Friedl-Vallon, M. Riese, G. Maucher, A. Lengel, F. Hase, P. Preusse, and R. Spang. Instrument concept and preliminary performance analysis of GLORIA. *Advances in Space Research*, 37, Issue: 12:2287–2291, 2006.
- [13] F. Friedl-Vallon for the GLORIA team. Progress with GLORIA. In *Optical Society of America - Imaging and Applied Optics Congress proceedings, Toronto, Canada*, 10-14 July 2011.
- [14] F. Friedl-Vallon, P. Preusse, and H. Oelhaf. GLORIA: a new instrument for atmospheric research. In *Proceedings of the 39th COSPAR Scientific Assembly, Mysore, India*, 14–22 July 2012.
- [15] M. K. Sha for the GLORIA team. GLORIA - An Airborne Imaging FTS. In *Proceedings of the ICSO (International Conference on Space Optics), Ajaccio, Corse, France*, 9-12 October 2012.
- [16] T. Guggenmoser for the GLORIA team. Dynamic Trace Retrieval from GLORIA Data I. In *Proceedings of the 39th COSPAR Scientific Assembly, Mysore, India*, 14–22 July 2012.
- [17] J. Blank for the GLORIA team. Dynamic Trace Retrieval from GLORIA Data II. In *Proceedings of the 39th COSPAR Scientific Assembly, Mysore, India*, 14–22 July 2012.
- [18] Sumner P. Davis, Mark C. Abrams, and James W. Brault. *Fourier Transform Spectrometry*. Academic Press, 2001.
- [19] J. Kauppiner and J. Partanen. *Fourier Transform in Spectroscopy*. WILEY-VCH verlag Berlin GmbH, 2001.
- [20] Peter R. Griffiths and James A. de Haseth. *Fourier Transform Infrared Spectrometry*. Wiley-Interscience, 2007.
- [21] H. Nyquist. Certain topics in telegraph transmission theory. *Transactions of the AIEE*, 47:617–644, 1928.
- [22] Robert H. Norton and Reinhard Beer. New apodizing functions for Fourier spectrometry. *Journal of the Optical Society of America*, 66(3):259–264, March 1976.
- [23] Robert H. Norton and Reinhard Beer. New apodizing functions for Fourier spectrometry: Errata. *Journal of the Optical Society of America*, 67(3):419, March 1977.
- [24] A. Rogalski. HgCdTe infrared detector material: history, status and outlook. *Reports on Progress in Physics*, 68, Number: 10:2267–2336, 2005.

- [25] M. Arnold. Manufacture data sheet, 2007. Opto System Technik.
- [26] M. Haiml, M. Bruder, D. Eich, M. Finck, H. Lutz, Th. Simon, J. Wendler, R. Wollrab, and J. Ziegler. IR-detectors from 0.9  $\mu\text{m}$  to 13  $\mu\text{m}$  spectra range at AIM. In *Infrared Technology and Applications XXXII, Proc. of SPIE Vol. 6542, 65420F*, 2007.
- [27] E. L. Dereniak and G. D. Boreman. *Infrared Detectors and Systems*. John Wiley & Sons, INC., 1996.
- [28] R. Wollrab, A. Bauer, H. Bitterlich, M. Bruder, S. Hanna, H. Lutz, K.-M. Mahlein, T. Schallenberg, and J. Ziegler. Planar n-on-p HgCdTe FPAs for LWIR and VLWIR Applications. *Journal of Electronic Materials*, Vol. 40, No. 8:1618 – 1623, 2011.
- [29] G. J. Steckman, W. Liu, R. Platz, D. Schroeder, C. Moser, and F. Havermeier. Volume Holographic Grating Wavelength Stabilized Laser Diodes. *IEEE Journal of Selected Topics in Quantum Electronics*, 13, No. 3:672 – 678, May/June 2007.
- [30] ONDAX. Final Test Report - Product ID X5181. Data sheet, 2011. ONDAX Inc.
- [31] J. Lohrengel and R. Todtenhaupt. Wärmeleitfähigkeit, Gesamtemissionsgrade und spektrale Emissionsgrade der Beschichtung Nextel-Velvet-Coating 811-21 (RAL90015 tiefschwarz matt). *PTB-Mitteilungen*, 106:259–265, 1996.
- [32] F. Olschewski, A. Ebersoldt, F. Friedl-Vallon, B. Gutswager, J. Hollandt, A. Kleinert, C. Monte, C. Piesch, P. Preusse, C. Rolf, P. Steffens, and R. Koppmann. The in-flight blackbody calibration system for the GLORIA interferometer on board an airborne research platform. *Atmospheric Measurement Techniques Discussions*, 6:5529–5575, 2013.
- [33] T. Neubert, H. Rongen, K. Ziemons, F. Friedl-Vallon, T. Gulde, G. Maucher, and A. Kleinert. A Read-Out Electronic System for Imaging FTS. In *Optical Society of America - Imaging and Applied Optics Congress proceedings, Vancouver BC, Canada, 26-30 April 2009*.
- [34] iMAR Navigation. <http://www.imar.de/>.
- [35] C. E. Blom, T. Gulde, C. Keim, W. Kimmig, C. Piesch, C. Sartorius, and H. Fischer. MIPAS-STR: Entwicklung eines Instrumentes für Stratosphärenflugzeuge. In *Statusseminar des Ozonforschungsprogramms*, number 143, page 21, 1998.
- [36] ESSenCe - The ESA Sounder Campaign 2011. <https://www.essence11.org/>.
- [37] TACTS scientific goals. <http://www2.uni-frankfurt.de/46649808/Tacts>.
- [38] ESMVal project. <http://www.pa.op.dlr.de/ESMVal/>.
- [39] Myasishchev Design Bureau, Russia. *High-altitude M55 Geophysica aircraft, Investigators Handbook*, third edition edition, 2002.
- [40] HALO. <http://www.halo.dlr.de/>.
- [41] James W. Brault. New approach to high-precision Fourier transform spectrometer design. *Optical Society of America*, 35, No. 16:2891 – 2896, 1 June 1996.
- [42] A. Kleinert, F. Friedl-Vallon, and A. Lengel. Interferogram Resampling for GLORIA-AB. In *Optical Society of America - Imaging and Applied Optics Congress proceedings, Vancouver BC, Canada, 26-30 April 2009*.
- [43] Henry E. Revercomb, H. Buijs, Hugh B. Howell, D. D. LaPorte, William L. Smith, and L. A. Sromovsky. Radiometric calibration of IR Fourier transform spectrometers: solution to a problem with the High-Resolution Interferometer Sounder. *Applied Optics*, 27, No. 15:3210 – 3218, 1 August 1988.

- 
- [44] O. Trieschmann. Level 0 to 1b Data Processing of the MIPAS-B2 balloon borne Fourier Transform Spectrometer. Technical report, Technical Note PO-TN-IMK-GS-0003, Revision 1.2, 17.05.2000.
- [45] *personal communication, Tom Neubert, 2013.*
- [46] A. Villemaire and J. Giroux. FTS Sensitivity Calculation: the definite formula. In *ASSFTS, 7th International Workshop on Atmospheric Science from Space Using Fourier Transform Spectrometry, Oberpfaffenhofen*, May 12-14, 1997.
- [47] D. B. Chase. Nonlinear Detector Response in FT-IR. *Applied Spectroscopy*, 38, No. 4:491–494, 4 November 1984.
- [48] R. L. Lachance and L. Rochette. Non-linearity correction of FTIR instruments. In *Fifth Workshop of Infrared Emission Measurements by FTIR, Quebec City, Canada*, 9-11 February 2000.
- [49] R. O. Knuteson, H. E. Revercomb, F. A. Best, N. C. Ciganovich, R. G. Dedecker, T. P. Dirkx, S. C. Ellington, W. F. Feltz, R. K. Garcia, H. B. Howell, W. L. Smith, J. F. Short, and D. C. Tobin. Atmospheric Emitted Radiance Interferometer. Part II: Instrument Performance. *Journal of Atmospheric and Oceanic Technology*, 21:1777–1789, 8 December 2004.
- [50] B. Hilbert. Non-Linearity Correction Algorithm for the WFC3 IR Channel. Instrument Science Report WFC3 ISR WFC3-2004-06., Space Telescope Science Institute, May 13, 2004.
- [51] Anne Kleinert. Correction of detector nonlinearity for the balloonborne Michelson Interferometer for Passive Atmospheric Sounding. *Applied Optics*, 45, No. 3:425–431, 20 January 2006.
- [52] AIM Infrarot-Module GmbH. T-LW-HSAE PROXIMITY ELECTRONICS for the 256×256 LWIR MCT IDCA. Technical report, 2004.
- [53] AIM Infrarot-Module GmbH. Stare-While-Scan Betrieb. Technical report, 2007.
- [54] Robert H. Kingston. *Detection of Optical and Infrared Radiation*. Springer-Verlag Berlin Heidelberg New York, 1979.
- [55] Dennis D. Buss, Robert J. Kansy, and J. Brock Barton. KTC Noise on Direct Injection from IR Diodes. *IEEE Transactions On Electron Devices*, VOL. ED-27, NO. 5:998 – 1000, MAY 1980.
- [56] Ken C. Pohlmann. *Principles of Digital Audio*. McGraw-Hill, September 16, 2010.
- [57] *personal communication, Felix Friedl-Vallon, 2012.*
- [58] L. S. Rothman, I. E. Gordon, A. Barbe, D. Chris Benner, P. F. Bernath, M. Birk, V. Boudon, L.R. Brown, A. Campargue, J. P. Champion, K. Chance, L. H. Coudert, V. Dana, V. M. Devi, S. Fally, J. M. Flaud, R. R. Gamache, A. Glodman, D. Jacquemart, I. Kleiner, N. Lacome, W. J. Lafferty, J. Y. Mandin, S. T. Massie, S. N. Mikhailenko, C. E. Miller, N. Moazzen-Ahmadi, O. V. Naumenko, A. V. Nikitin, J. Orphal, V. I. Perevalov, A. Perrin, A. Predoi-Cross, C. P. Rinsland, M. Rotger, M. Simeckova, M. A. H. Smith, K. Sung, S. A. Tashkun, J. Tennyson, R. A. Toth, A. C. Vandaele, and J. Vander Auwera. The HITRAN 2008 molecular spectroscopic database. *Journal of Quantitative Spectroscopy & Radiative Transfer*, 110:533–572, 2009.
- [59] Erik Kretschmer. *Modelling of the Instrument Spectral Response of Conventional and Imaging Fourier Transform Spectrometers*. PhD thesis, Université Laval, 2013.

- [60] G. P. Stiller (Editor) with contributions from T. v. Clarmann, A. Dudhia, G. Echle, B. Funke, N. Glatthor, F. Hase, M. Höpfner, S. Kellmann, H. Kemnitzner, M. Kuntz, Linden, G. P. Stiller, A., M. Linder, and S. Zorn. The Karlsruhe Optimized and Precise Radiative transfer Algorithm (KOPRA). Wissenschaftliche Berichte des Forschungszentrums Karlsruhe, FZKA 6487, 2000, <http://www.imk-asf.kit.edu/english/312.php>.
- [61] A. Lengel. *Bestimmung der Apparatefunktion des Fourierspektrometers MIPAS-B2 aus Stratosphärischen Spektren*. PhD thesis, genehmigt von der Fakultät für Physik der Universität Karlsruhe (TH), Wissenschaftliche Berichte FZKA 7016, 2000.
- [62] DN505-data sheet. <http://thermooptics.com/wp-content/uploads/2011/03/DN505-1210.pdf>.
- [63] DS1125 Data sheet. DAWN Electronic, Inc.
- [64] *personal communication, Thomas Gulde, 2011*.
- [65] François Hénault, Philippe-Jean Hébert, Christophe Lucchini, and Didier Miras. Geometrical misalignment retrieval of the IASI interferometer. In *SPIE Proceedings, Volume 3870*, 20 September 1999.
- [66] M. V. R. K. Murty. Some More Aspects of the Michelson Interferometer with Cube Corners. *Journal of the Optical Society of America*, 50, No. 1:7–10, January 1960.
- [67] D. K. Lambert and P. L. Richards. Martin-Puplett interferometer: an analysis. *Applied Optics*, 17, No. 10:1595 – 1602, 15 May 1978.
- [68] Jyrki Kauppinen and Pekka Saarinen. Line-shape distortions in misaligned cube corner interferometers. *Applied Optics*, 31, No. 1:69–74, 1 January 1992.
- [69] W. Kimmig. *Das Abtastverfahren der InInterferogram des flugzeuggetragenen Fourierspektrometers MIPAS-STR*. PhD thesis, genehmigt von der Fakultät für Physik der Universität Karlsruhe (TH), Wissenschaftliche Berichte FZKA 6665, 2001.
- [70] Eugene Hecht and A. R. Ganesan. *OPTICS*. Dorling Kindersley (India) Pvt. Ltd., 2009.



# Publications of the author

- [1] M. K. Sha for the GLORIA team. GLORIA - Status and results from first aircraft mission. In *16th International Workshop on Atmospheric Science from Space using Fourier Transform Spectroscopy (ASSFTS 16)*, SSEC - University of Wisconsin-Madison, Wisconsin, USA, 22–24 May 2012.
- [2] M. K. Sha for the GLORIA team. GLORIA - An Airborne Imaging FTS. In *proceedings of the ICSO (International Conference on Space Optics)*, Ajaccio, Corse, France, 9–12 October 2012.
- [3] T. Guggenmoser, J. Ungermann, J. Blank, Th. Latzko, O. Suminska-Ebersoldt, M. Kaufmann, J.-U. Grooss, B. Vogel, A. Kleinert, M. K. Sha, F. Friedl-Vallon, P. Preusse, and H. Oelhaf for the GLORIA Team. Examining the UTLS with the GLORIA limb imager: Technique and first results from the TACTS/ESMVal campaign in 2012. In *7th Atmospheric Limb Conference, Bremen, Germany*, 17–19 June 2013.
- [4] M. Kaufmann, J. Blank, F. Friedl-Vallon, D. Gerber, T. Guggenmoser, M. Höpfner, A. Kleinert, M. K. Sha, H. Oelhaf, M. Riese, O. Suminska-Ebersoldt, W. Woiwode, R. Siddans, B. Kerridge, B. Moyna, S. Rea, and M. Oldfield. Technical Assistance for the Deployment of Airborne Limbsounders during ESSenCe. Technical report, 05 Oct 2012.
- [5] E. Kretschmer, F. Friedl-Vallon, M. K. Sha, F. Hase, and A. Kleinert. Instrument Spectral Response Model and Measurements for the Imaging FTS GLORIA. In *15th International Workshop on Atmospheric Science from Space using Fourier Transform Spectroscopy (ASSFTS 15)*, Nara, Japan, 11–13 May 2010.
- [6] M. K. Sha, A. Kleinert, and F. Friedl-Vallon. Radiometric characterization of the GLORIA detectors. In *15th International Workshop on Atmospheric Science from Space using Fourier Transform Spectroscopy (ASSFTS 15)*, Nara, Japan, 11–13 May 2010.
- [7] M. K. Sha, A. Kleinert, E. Kretschmer, and F. Friedl-Vallon. A novel method for the determination of the focal plane in an imaging FTS. In *15th International Workshop on Atmospheric Science from Space using Fourier Transform Spectroscopy (ASSFTS 15)*, Nara, Japan, 11–13 May 2010.



## Publications of the author in preparation

- [1] F. Friedl-Vallon, T. Gulde, F. Hase, A. Kleinert, T. Kulesa, G. Maucher, T. Neubert, F. Olschewski, C. Piesch, P. Preusse, H. Rongen, C. Sartorius, H. Schneider, A. Schönfeld, V. Tan, N. Bayer, J. Blank, R. Dapp, A. Ebersoldt, H. Fischer, T. Guggenmoser, M. Höpfner, M. Kaufmann, E. Kretschmer, H. Nordmeyer, H. Oelhaf, J. Orphal, M. Riese, G. Schardt, J. Schillings, M. K. Sha, O. Suminska-Ebersoldt, and J. Ungermann. Instrument concept of the imaging Fourier transform spectrometer GLORIA. *Atmospheric Measurement Techniques*, 2013.
- [2] F. Friedl-Vallon, T. Gulde, F. Hase, and M. K. Sha. The optical design of the GLORIA Spectrometer. *Atmospheric Measurement Techniques*, 2014.
- [3] T. Guggenmoser, J. Ungermann, A. Kleinert, J. Blank, M. Höpfner, O. Suminska-Ebersoldt, T. Latzko, M. K. Sha, E. Kretschmer, F. Friedl-Vallon, P. Preusse, , H. Oelhaf, J. Orphal, and M. Riese. Calibration of atmospheric emission spectra recorded by the GLORIA limb imager during the TACTS and ESMVal campaigns in 2012. *Atmospheric Measurement Techniques*, 2013.
- [4] A. Kleinert, J. Blank, F. Friedl-Vallon, T. Guggenmoser, M. Höpfner, E. Kretschmer, T. Latzko, T. Neubert, R. Ribalda, M. K. Sha, and J. Ungermann. Level 0-1 processing of the imaging Fourier transform spectrometer GLORIA: Generation of radiometrically and spectrally calibrated spectra. *Atmospheric Measurement Techniques*, 2013.
- [5] M. K. Sha, F. Hase, and F. Friedl-Vallon. Shear characterization and vibration frequency analysis for an imaging FTS. *Applied Optics*, 2014.
- [6] M. K. Sha, A. Kleinert, and F. Friedl-Vallon. Spectral calibration methodology for the imaging Fourier transform spectrometer GLORIA. *Atmospheric Measurement Techniques*, 2014.
- [7] M. K. Sha, A. Kleinert, F. Friedl-Vallon, and E. Kretschmer. Focus determination using the spectral line property for an imaging FTS. *Applied Optics*, 2014.



## A. Transmission curves of different optics used in GLORIA

The optical components which are on the path of the infrared radiation falling on the detector surface are shown in figure A.1 and are described in chapter 3.3. The path followed by the radiation is the same as that of a Michelson interferometer and is explained in chapter 2.2. The transmittance<sup>1</sup> and the reflectance<sup>2</sup> at the surfaces are given in the table A.1.

Table A.1.: Properties of the optical components used in GLORIA.

Component name	material	transmittance	reflectance
		symbol	symbol
Entrance window	Germanium (Ge)	$T_{EW}$	
Beam splitter	Potassium chloride (KCL) with coating	$T_{BS45D}$	
Beam splitter (front)	Potassium chloride (KCL) with coating	$T_5$	$R_5$
Beam splitter (back)	Potassium chloride (KCL)	$T_6$	
Compensator	Potassium chloride (KCL)	$T_{sub}$	
Cube corner	Zerodur with gold coating		$R_{cc}$
Lens 1	Zinc selenide (ZnSe)	$T_{L1}$	
Lens 2	Germanium (Ge)	$T_{L2}$	
Detector window	Germanium (Ge)	$T_{DW}$	

Transmittance measurement for the entrance window is taken from laboratory measurements performed by Erik Kretschmer. Transmittance measurements for the beamsplitter placed at 45° is taken from laboratory measurements performed by Felix Friedl-Vallon. Transmittance measurements for the detector window is taken from laboratory measure-

<sup>1</sup>Transmittance ( $T$ ) of an optical component is a measure of its ability to transmit radiation. It is expressed as the ratio of the transmitted flux to the incident flux.

<sup>2</sup>Reflectance ( $R$ ) of the surface of an optical component is a measure of its ability to reflect radiation. It is expressed as the ratio of the reflected flux to the incident flux.

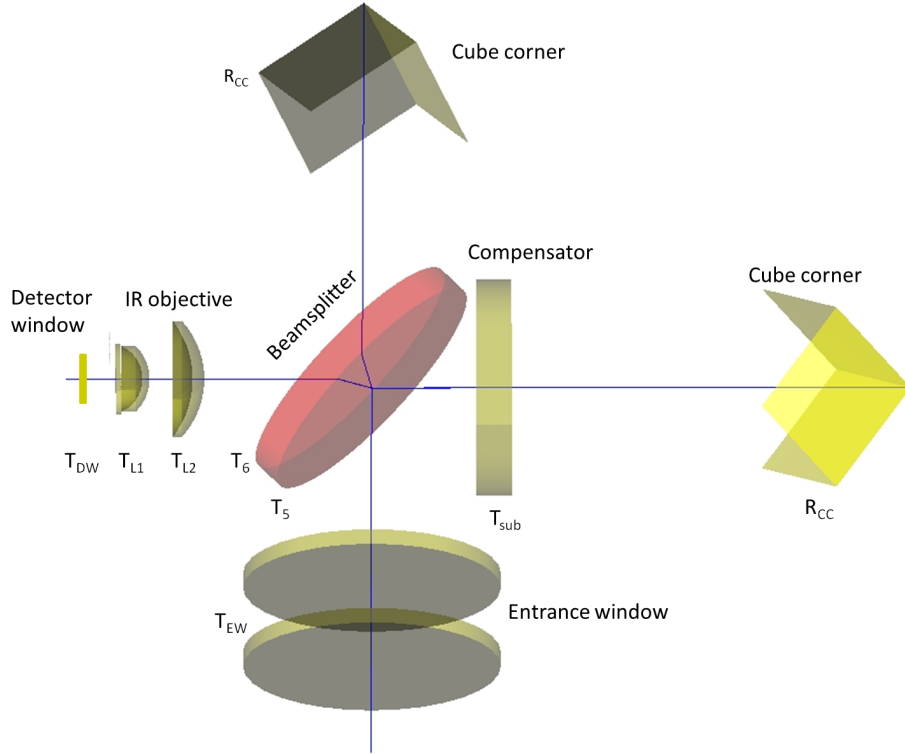


Figure A.1.: Schematic diagram of the optical components and its alignment in GLORIA interferometer. The blue line shows the central ray propagation through the optical components. (source: KIT)

ments performed by Thomas Gulde. Reflectance measurements for the lens 1 and lens 2 in the range of 5 - 15  $\mu\text{m}$  are taken from the data sheet provided by COHERENT IMAGING OPTICS LTD. The wavelength dependent transmittance values for the lenses are calculated using the relation  $R + T = 1$ , neglecting absorbance ( $< 1\%$ ). Transmittance curves for some surfaces are not provided. They are assumed to have a constant transmittance value over the wavenumber scale. The cube corners are assumed to be 100 % reflective.

The transmittance curves for the entrance window, the detector window, the beam splitter placed at  $45^\circ$ , the lens 1 and the lens 2 are plotted in figure A.2.

The surfaces for which constant transmittance and reflectance coefficient are assumed are

$$\begin{aligned} T_6 &= 0.98 \\ T_{sub} &= 0.98 \\ R_{cc} &= 1 \end{aligned}$$

Using the relation between reflectance and transmittance as mentioned before,  $R_5$  can be written as

$$R_5 = 1 - T_5 = 1 - \frac{T_{BS45D}}{T_6} \quad (\text{A.1})$$

where,  $T_5 \cdot T_6 = T_{BS45D}$

The total transmittance coefficient is estimated by taking the effect of the radiation passing through each optical surface. The secondary reflections at the beamsplitter surface are not considered here for the calculation. They do not contribute to the main image, as they are formed quite apart from the main image (see section 5.7.)

$$\tau = 2 \cdot T_{EW} \cdot R_5 \cdot T_5 \cdot T_6 \cdot T_6 \cdot T_{sub} \cdot R_{cc} \cdot R_{cc} \cdot T_{L1} \cdot T_{L2} \cdot T_{DW} \quad (\text{A.2})$$

Simplifying the components of equation A.2 it can be re-written as

$$\tau = 2 \cdot T_{EW} \cdot R_5 \cdot T_{BS45D} \cdot T_6 \cdot T_{sub} \cdot R_{cc}^2 \cdot T_{L1} \cdot T_{L2} \cdot T_{DW} \quad (\text{A.3})$$

The transmittance coefficient is a function of wavenumber, so re-writing equation A.3 and replacing  $R_5$  and  $R_{cc}$  with the corresponding values, the total transmittance can be expressed by the given equation

$$\tau(\sigma) = 2 \cdot T_{EW}(\sigma) \cdot (T_6 - T_{BS45D}(\sigma)) \cdot T_{BS45D}(\sigma) \cdot T_{sub} \cdot T_{L1}(\sigma) \cdot T_{L2}(\sigma) \cdot T_{DW}(\sigma) \quad (\text{A.4})$$

The plot of the total transmittance as a function of wavenumber is shown in figure 5.26.

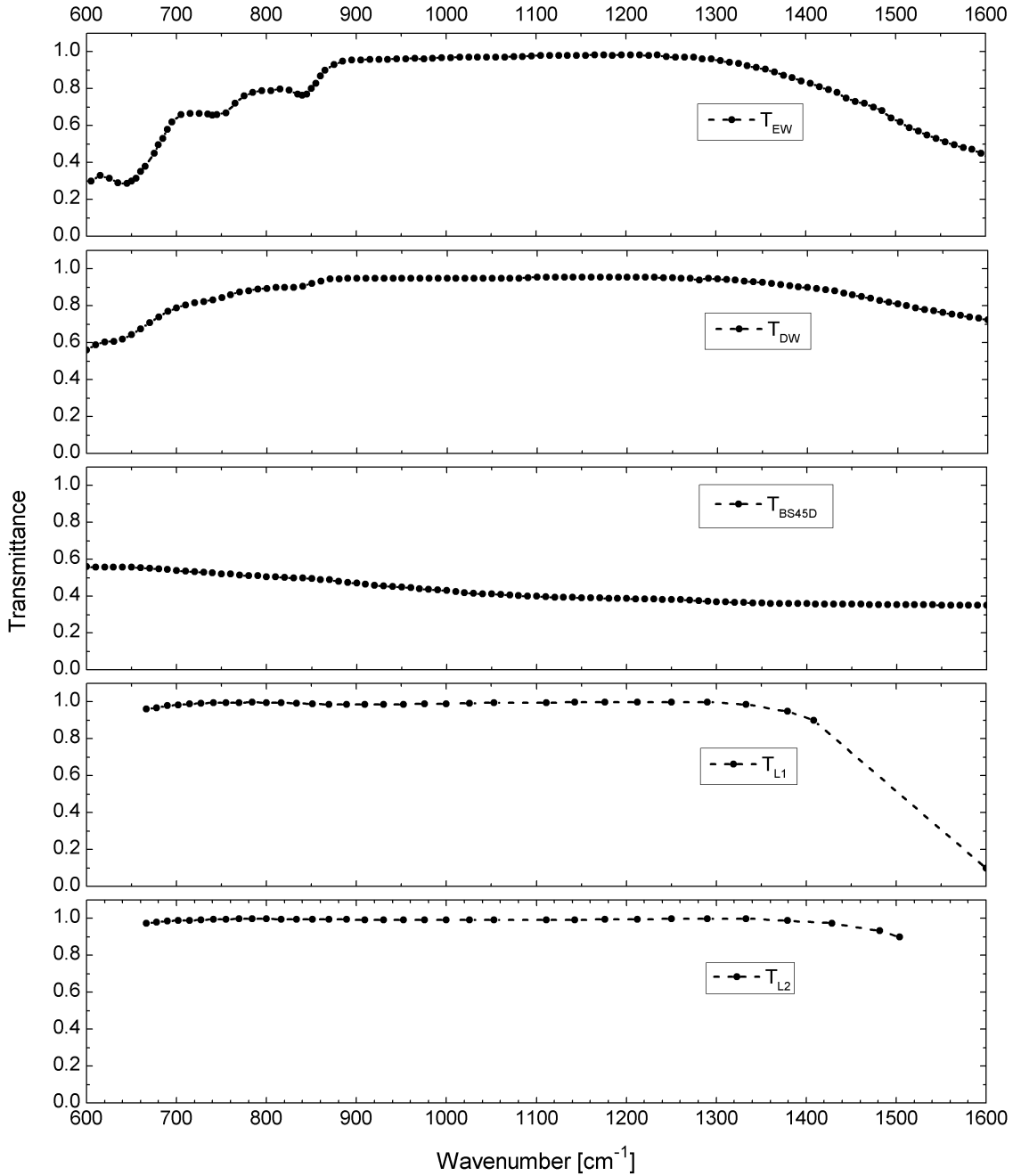


Figure A.2.: Transmission curve of the optical components used in GLORIA interferometer. Top to bottom are shown the transmission curves for the entrance window, the detector window, the beamsplitter at 45°angle, the lens 1 and the lens 2.



## B. Analysis of parasitic image

A theoretical analysis of the parasitic images is shown here. The parasitic images are assumed to be formed due to secondary reflections from the wedged beamsplitter substrate. The path of the light propagation through the beamsplitter is shown in figure B.1. The reflection and the transmission at the optical surfaces are shown explicitly.

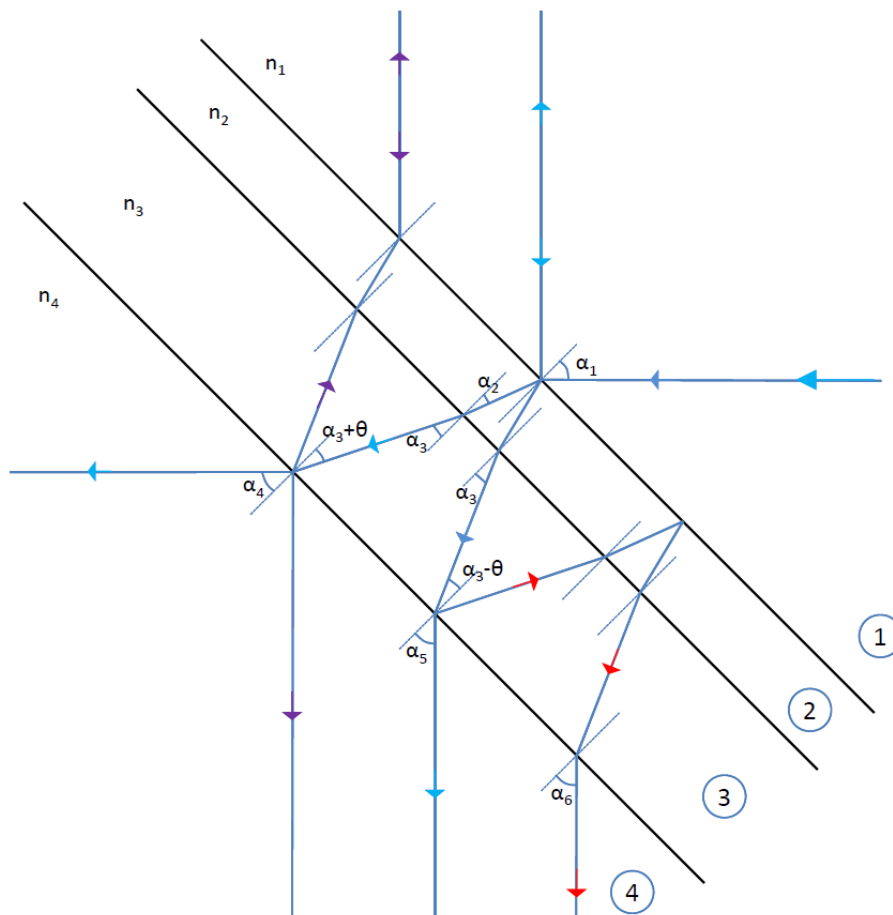


Figure B.1.: Ray propagation through the beamsplitter showing multiple reflections and transmission at its surface. The refractive indices of the surfaces are marked with numbers. The wedge angle is represented by  $\theta$ .

### Calculation of the reflectance and transmittance angles

The reflectance and transmittance coefficients are calculated with some assumptions about the values and are used to calculate the intensity and position of the parasitic images. The beamsplitter is made of KCl (Potassium Chloride) substrate, coated with a beam splitting layer (material not known - this information is not provided by the supplier). The light transmitted through the beamsplitter passes through four media with different refractive indices, while considering a single layer of the dielectric material on the KCl plate. The four media are the air, a beam splitting (BS) layer, a KCl layer and the air.

The refractive index of the corresponding layers are the following

$$n_1 = 1(\text{air}), n_2 = 3(\text{BS layer : educated guess}), n_3 = 1.468(\text{KCl}), n_4 = 1(\text{air}) \quad (\text{B.1})$$

The beamsplitter is wedged with an angle of  $\theta$  equal to  $10'$  or  $2.909 \times 10^{-3}$  radian. The angles made by the light upon incident, reflection and refraction at different surfaces are shown in figure B.1. The values of each angle can be calculated following Snell's law [70].

They are calculated as follows

$$\alpha_1 = \frac{\pi}{4}, \quad (\text{B.2})$$

$$\alpha_2 = \arcsin\left(\frac{n_1}{n_2} \cdot \sin(\alpha_1)\right) = 0.238, \quad (\text{B.3})$$

$$\alpha_3 = \arcsin\left(\frac{n_2}{n_3} \cdot \sin(\alpha_2)\right) = 0.503, \quad (\text{B.4})$$

$$\alpha_4 = \arcsin\left(\frac{n_3}{n_4} \cdot \sin(\alpha_3 + \theta)\right) = 0.7907, \quad (\text{B.5})$$

$$\alpha_5 = \arcsin\left(\frac{n_3}{n_4} \cdot \sin(\alpha_3 - \theta)\right) = 0.780116, \quad (\text{B.6})$$

$$\alpha_6 = \arcsin\left(\frac{n_3}{n_4} \cdot \sin(\alpha_3 - 3\theta)\right) = 0.76907. \quad (\text{B.7})$$

### Position determination of the parasitic images

The distance of the first two parasitic images from the main image is denoted by  $D_1$  and  $D_2$  in radian units,  $D_{11}$  and  $D_{21}$  in pixels

$$D_1 = (\alpha_5 - \alpha_4) = -0.010585 \text{ radian} \quad (\text{B.8})$$

$$D_2 = (\alpha_5 - \alpha_6) = 0.010508 \text{ radian} \quad (\text{B.9})$$

$$\text{pix} = \frac{4\pi}{128 \cdot 180} = 5.45415 \times 10^{-4} \text{ radian} \quad (\text{B.10})$$

$$D_{11} = \frac{D_1}{\text{pix}} = -19.407 \text{ pixel} \quad (\text{B.11})$$

$$D_{21} = \frac{D_2}{\text{pix}} = 19.266 \text{ pixel} \quad (\text{B.12})$$

### Calculation of the reflectance and transmittance coefficients

The reflectance and transmittance coefficients are calculated from the angles given above. They are calculated as [70]

$$R_{\perp 34} = \frac{(\sin(\alpha_3 + \theta - \alpha_4))^2}{(\sin(\alpha_3 + \theta + \alpha_4))^2} = 0.085 \quad (\text{B.13})$$

$$R_{\parallel 34} = \frac{(\tan(\alpha_3 + \theta - \alpha_4))^2}{(\tan(\alpha_3 + \theta + \alpha_4))^2} = 6.824 \times 10^{-3} \quad (\text{B.14})$$

$$T_{\perp 34} = \frac{\sin[2(\alpha_3 + \theta)] \cdot \sin(2\alpha_4)}{\sin(\alpha_3 + \theta + \alpha_4)^2} = 0.915 \quad (\text{B.15})$$

$$T_{\parallel 34} = \frac{\sin[2(\alpha_3 + \theta)] \cdot \sin(2\alpha_4)}{[\sin[(\alpha_3 + \theta) + \alpha_4]]^2 \cdot [\cos[(\alpha_3 + \theta) - \alpha_4]]^2} = 0.993 \quad (\text{B.16})$$

$$R_2 = \frac{R_{\perp 34} + R_{\parallel 34}}{2} = 0.046 \quad (\text{B.17})$$

$$T_2 = \frac{T_{\perp 34} + T_{\parallel 34}}{2} = 0.954 \quad (\text{B.18})$$

Since the reflectance and transmittance at the surfaces 1-2 and 2-3 are not known, they are assumed as one surface with the reflectance and transmittance coefficients as  $R_1$  and  $T_1$ , respectively.

$T_1 \times T_2 = 0.375$  (value extracted from the transmittance curve of the beamsplitter)

$$T_1 = \frac{0.375}{T_2} = 0.393 \quad (\text{B.19})$$

$$R_1 = 1 - T_1 = 0.607 \quad (\text{B.20})$$

### Intensity calculation of the parasitic images

Calculation of the interference coefficients for the main image:

The coefficient  $C_1$  for beam 1 is  $C_1 = r_1 t_1 t_2$

The coefficient  $C_2$  for beam 2 is  $C_2 = t_1 t_2^2 r_1 t_2 = r_1 t_1 t_2^3$

Calculation of the interference coefficients for the first parasitic image:

The coefficient  $C_1$  for beam 1 is  $C_1 = t_1 r_2 t_1^2 t_2 = r_2 t_1^3 t_2$

The coefficient  $C_2$  for beam 2 is  $C_2 = t_1 t_2 r_2 = r_2 t_1 t_2$

Calculation of the interference coefficients for the second parasitic image:

The coefficient  $C_1$  for beam 1 is  $C_1 = r_1 t_1 r_2 r_1 t_2 = r_1^2 r_2 t_1 t_2$

The coefficient  $C_2$  for beam 2 is  $C_2 = t_1 t_2^2 r_1 r_2 r_1 t_2 = r_1^2 r_2 t_1 t_2^3$

The intensity of the DC part of the main image ( $I_{mDC}$ ), the first parasitic image ( $I_{1mDC}$ ), and the second parasitic image ( $I_{2mDC}$ ) are as follows

$$\begin{aligned} I_{mDC} &= C_1^2 + C_2^2 + 2C_1 C_2 = r_1^2 t_1^2 t_2^2 + r_1^2 t_1^2 t_2^6 + 2r_1^2 t_1^2 t_2^4 \\ &= R_1 T_1 T_2 + R_1 T_1 T_2^3 + 2R_1 T_1 T_2^2 = 0.8688 \end{aligned} \quad (\text{B.21})$$

$$\begin{aligned} I_{1mDC} &= C_1^2 + C_2^2 + 2C_1 C_2 = r_2^2 t_1^6 t_2^2 + r_2^2 t_1^2 t_2^2 + 2r_2^2 t_1^4 t_2^2 \\ &= R_2 T_1 T_2 + R_2 T_1 T_2^2 + 2R_2 T_1^2 T_2 = 0.0336 \end{aligned} \quad (\text{B.22})$$

$$\begin{aligned} I_{2mDC} &= C_1^2 + C_2^2 + 2C_1 C_2 = r_1^4 r_2^2 t_1^2 t_2^2 + r_1^4 r_2^2 t_1^2 t_2^6 + 2r_1^4 r_2^2 t_1^2 t_2^4 \\ &= R_1^2 R_2 T_1 T_2 + R_1^2 R_2 T_1 T_2^3 + 2R_1^2 R_2 T_1 T_2^2 = 0.0243. \end{aligned} \quad (\text{B.23})$$

The ratio of the intensity of the first parasitic image to the intensity of the main image =  $0.0336/0.8688 \times 100 = 3.867\%$ .

The ratio of the intensity of the second parasitic image to the intensity of the main image =  $0.0243/0.8688 \times 100 = 2.797\%$ .

The intensity of the AC part of the main image ( $I_{mAC}$ ), the first parasitic image ( $I_{1mAC}$ ), and the second parasitic image ( $I_{2mAC}$ ) are given as follows

$$I_{mAC} = 2C_1 C_2 = 2r_1^2 t_1^2 t_2^4 = 2R_1 T_1 T_2^2 = 0.4341 \quad (\text{B.24})$$

$$I_{1mAC} = 2C_1 C_2 = 2r_2^2 t_1^4 t_2^2 = 2R_2 T_1^2 T_2 = 0.0136 \quad (\text{B.25})$$

$$I_{2mAC} = 2C_1 C_2 = 2r_1^4 r_2^2 t_1^2 t_2^4 = 2R_1^2 R_2 T_1 T_2^2 = 0.0122. \quad (\text{B.26})$$

The ratio of the intensity of the first parasitic image to the intensity of the main image =  $0.0136/0.4341 \times 100 = 3.133 \%$ .

The ratio of the intensity of the second parasitic image to the intensity of the main image =  $0.0122/0.4341 \times 100 = 2.81 \%$ .

### Parasitic image position calculation with variable parameter

The parasitic image position is calculated and shown in table B.1 for different cases, while changing the parameters like the wedge angle, the refractive index of the beamsplitter material, and the beamsplitter angle with respect to the incident beam. The results show that changing the parameters has an effect in the image position value.

Table B.1.: Position of the spurious images for variable parameter.

Parameter	Pixel distance positive	Pixel distance negative
<b>W (wedge angle)</b>		
8´	15.4352	-15.5251
<b>10´</b>	<b>19.2663</b>	<b>-19.4067</b>
10.5´	20.2225	-20.3770
20´	38.2646	-38.8150
<b>n (refractive index)</b>		
1.450	18.9624	-19.0962
1.455	19.0469	-19.1827
1.460	19.1314	-19.2689
<b>1.468</b>	<b>19.2663</b>	<b>-19.4067</b>
<b>alpha (in degrees)</b>		
33	17.0972	-17.1603
<b>45</b>	<b>19.2663</b>	<b>-19.4067</b>
50	20.3330	-20.5278
51.5	20.7990	-21.0182
53	21.3102	-21.5573

### Worst case calculation and the determination of the parasitic images

The above calculation was done considering beamsplitter surface made of single dielectric surface. In reality the dielectric surface is not a single layer but it is rather a multi layered surface. Considering different polarization direction of the light, the reflectance coefficient changes by 28 %.

**Positive worst case** situation is calculated by adding the change in reflectance coefficient. The coefficients gets a value as follows:

$$R_1 = 0.607 + 0.607 \times 28/100 = 0.77696 \quad (\text{B.27})$$

$$T_1 = 1 - R_1 = 0.22304 \quad (\text{B.28})$$

$$T_2 = 0.954 \quad (\text{B.29})$$

$$R_2 = 1 - T_2 = 0.046 \quad (\text{B.30})$$

The interference coefficients are calculated for the main image and its paraxial images as discussed earlier in this section.

---

### Intensity of the DC part

The ratio of the intensity of the first parasitic image to the intensity of the main image =  $0.0146/0.6312 \times 100 = 2.3195\%$

The ratio of the intensity of the second parasitic image to the intensity of the main image =  $0.02256/0.6312 \times 100 = 3.574\%$

### Intensity of the AC part

The ratio of the intensity of the first parasitic image to the intensity of the main image =  $0.0044/0.3154 \times 100 = 1.3842\%$

The ratio of the intensity of the second parasitic image to the intensity of the main image =  $0.01127/0.3154 \times 100 = 3.574\%$

**Negative worst case** situation is calculated by subtracting the change in reflectance coefficient. The coefficients gets a value as follows:

$$R_1 = 0.607 - 0.607 \times 28/100 = 0.43704 \quad (\text{B.31})$$

$$T_1 = 1 - R_1 = 0.22304 \quad (\text{B.32})$$

$$T_2 = 0.954 \quad (\text{B.33})$$

$$R_2 = 1 - T_2 = 0.046 \quad (\text{B.34})$$

### Intensity of the DC part

The ratio of the intensity of the first parasitic image to the intensity of the main image =  $0.0146/0.3551 \times 100 = 4.1235\%$

The ratio of the intensity of the second parasitic image to the intensity of the main image =  $0.00714/0.3551 \times 100 = 2.0104\%$

### Intensity of the AC part

The ratio of the intensity of the first parasitic image to the intensity of the main image =  $0.0044/0.1774 \times 100 = 2.4608\%$

The ratio of the intensity of the second parasitic image to the intensity of the main image =  $0.003567/0.17743 \times 100 = 2.0104\%$



# List of Symbols

$A$	Calibrated spectrum in radiance units
$A_{pix}$	Pixel area
$A_{po}$	scaling factor dependent on apodization
$b$	image distance
$C_{bins}$	number of pixels co-added
$c$	Speed of light
$C$	Coulomb
$CdTe$	Cadmium Telluride
$cm_y, cm_z$	Haidinger fringe center
$CH_4$	Methane
$CO_2$	Carbondioxide
$C_s$	Specific detector element capacity
$d$	pixel pitch
$DC$	Interferogram DC
$E$	Energy
$E_{ph}$	Photon energy
$f$	focus
$F_f$	Frame frequency
$fr$	frame index
$Ge$	Germanium
$HgCdTe$	Mercury Cadmium Telluride
$HgTe$	Mercury Telluride
$h, v$	Horizontal and vertical pixel index
$h_p$	Planck's constant
$H_2O$	Water
$H_y, H_z$	Higher order shear
$InSb$	Indium antimonide
$I$	Interferogram
$I_D$	Dark current
$K_B$	Boltzmann constant
$KCl$	Potassium chloride
$L$	One sided interferogram length
$LN_2$	liquid Nitrogen
$lsb$	least significant bit
$L_p$	Spectral radiance
$M$	Modulation efficiency
$N$	Number of points
$Nb$	Detector quantization level
$N_p$	Number of electrons due to photon flux
$N_D$	Number of electrons due to dark current
$N_2O$	Nitrous oxide
$O_3$	Ozone

---

$\phi$	Phase
$q$	Electronic charge
$Q_{fw}$	Detector full well capacity
$R$	Reflectance
$r$	pixel distance from the optical axis
$R_D$	Detector response
$r_{det}$	Detector zero bias resistance
$R_{inst}$	Instrument response
$S$	Spectrum
$sh_y, sh_z$	Shear value
$T$	Temperature
$t_{int}$	Detector integration time
$t_{iint}$	Interferogram recording time
$U$	Detector ROIC voltage
$u_v$	Zero bias voltage
$V_J$	Johnson noise voltage
$W$	Wedge angle
ZnSe	Zinc selenide
$\alpha$	Off-axis angle
$\Pi$	Box function
$\otimes$	Convolution
$\llcorner$	Dirac comb
$\epsilon$	Emissivity
$\eta$	Detector quantum efficiency
$\lambda$	Wavelength
$\nu$	Noise
$\Sigma_1$	Detector lower cutoff wavenumber
$\Sigma_2$	Detector upper cutoff wavenumber
$\sigma$	Wavenumber
$\tau$	Transmission
$\phi$	Photon flux
$\Omega$	Solid angle
$\Delta x$	Sampling interval of an interferogram
$\delta\sigma$	Sampling interval of a spectrum

# List of Abbreviations

<b>ADC</b>	analog to digital converter
<b>AIM</b>	AIM Infrarot-Module GmbH
<b>AR</b>	anti-reflective
<b>BB</b>	blackbody
<b>BBC</b>	cold blackbody
<b>BBH</b>	hot blackbody
<b>bif</b>	Braut-resampled interferogram
<b>CAD</b>	Computer-aided design
<b>cub</b>	cuboid
<b>CM</b>	Chemistry mode
<b>CMOS</b>	Complementary metal oxide semiconductor
<b>DFT</b>	Discrete Fourier transformation
<b>DM</b>	Dynamics mode
<b>EM</b>	Electromagnetic
<b>EMC</b>	Electromagnetic compatibility
<b>ESMVal</b>	Earth System Model Validation campaign
<b>ESS</b>	equidistant space sampling
<b>ESSenCe</b>	The ESA Sounder Campaign 2011
<b>ETS</b>	equidistant time sampling
<b>FCE</b>	fringe count error
<b>FEE</b>	front end electronics
<b>FFT</b>	Fast Fourier Transform
<b>FOV</b>	field-of-view
<b>FPA</b>	focal plane array
<b>FSV</b>	Forman Steel and Vanasse
<b>FT</b>	Fourier transformation
<b>FTS</b>	Fourier Transform Spectrometer
<b>FWHM</b>	full width at half maximum
<b>FZJ</b>	Forschungszentrum Jülich
<b>GLORIA</b>	Gimballed Limb Observer for Radiance Imaging of the Atmosphere
<b>GPS</b>	Global Positioning System
<b>HALO</b>	High Altitude and Long Range Research Aircraft
<b>HITRAN</b>	High-resolution Transmission Molecular Absorption Database
<b>IDCA</b>	Integrated Detector Cooler Assembly
<b>IDL</b>	Interactive Data Language
<b>IFM</b>	interferometer
<b>IFTS</b>	imaging Fourier transform spectrometer
<b>ILS</b>	instrument line shape
<b>IMK</b>	Institute for Meteorology and Climate Research
<b>IMU</b>	inertial measurement unit
<b>iIMCU</b>	iMAR inertial measurement and control unit
<b>INS</b>	inertial navigation system

---

<b>IR</b>	infrared
<b>IRO</b>	infrared objective
<b>K01_F02</b>	Campaign 01, flight 02
<b>K03_F14</b>	Campaign 03, flight 14
<b>K03_F20</b>	Campaign 03, flight 20
<b>KIT</b>	Karlsruhe Institute of Technology
<b>KOPRA</b>	The Karlsruhe Optimized and Precise Radiative transfer Algorithm
<b>LMI</b>	length measuring interferometer
<b>LPE</b>	liquid-phase epitaxy
<b>lsb</b>	least significant bit
<b>lut</b>	lookup table
<b>LWIR</b>	long-wavelength infrared
<b>MCT</b>	Mercury Cadmium Telluride
<b>MDB</b>	Myasishchev Design Bureau
<b>MEMS</b>	Micro-Electro-Mechanical System
<b>MI</b>	Michelson interferometer
<b>MIPAS</b>	Michelson Interferometer for Passive Atmospheric Sounding
<b>MIPAS B2</b>	Michelson Interferometer for Passive Atmospheric Sounding - Balloon
<b>MIPAS Envisat</b>	Michelson Interferometer for Passive Atmospheric Sounding - Environmental Satellite
<b>MIPAS STR</b>	Michelson Interferometer for Passive Atmospheric Sounding - STRatospheric aircraft
<b>MOPD</b>	maximum optical path difference
<b>NEP</b>	noise equivalent power
<b>NESR</b>	noise equivalent spectral radiance
<b>NL</b>	nonlinearity
<b>oac</b>	off-axis correction
<b>OLAF</b>	Optimierte Level1 Auswertung für Fernerkundung
<b>OPD</b>	optical path difference
<b>PBL</b>	planetary boundary layer
<b>ppm</b>	parts per million
<b>PRT</b>	Platinum resistance thermometer
<b>PV</b>	photo voltaic
<b>QCL</b>	quantum cascade laser
<b>ref.</b>	reference
<b>rms</b>	root-mean-square
<b>ROA</b>	Detector zero bias resistance-area product
<b>ROIC</b>	Readout Integrated Circuit
<b>sci/scr</b>	imaginary/real part of the complex calibrated spectra
<b>SCU</b>	Stabilization Control Unit
<b>SNR</b>	signal-to-noise
<b>spi/spr</b>	imaginary/real part of the phase corrected spectra
<b>SRU</b>	spectral radiance units
<b>stx</b>	statistics table
<b>SWS</b>	stare while scan
<b>TACTS</b>	Transport and Composition in the Upper Troposphere/Lowermost Stratosphere campaign
<b>TEC</b>	Thermo-Electric cooler
<b>UTLS</b>	Upper Troposphere and Lower Stratosphere
<b>VHG</b>	volume holographic grating
<b>ZPD</b>	zero path difference

# List of Figures

1.1.	Schematic view of the global structure of the troposphere and lower stratosphere of the earth's atmosphere. . . . .	2
1.2.	Forward calculated spectra showing several trace gases at 20 km altitude for a mid latitude July standard atmosphere in the spectrally detectable range of GLORIA . . . . .	3
2.1.	A 2D diagram showing the ray propagation in a two port Michelson interferometer. . . . .	6
2.2.	Blackbody interferogram and its corresponding spectrum from measurement data. . . . .	8
2.3.	A ray diagram showing projections for the on-axis and an off-axis pixel. . .	11
2.4.	A 2D plot showing the Haidinger fringe pattern over the FPA. . . . .	12
3.1.	Block diagram showing some of the target sources and different components of GLORIA which are in the path of the IR and the reference laser signal. .	13
3.2.	Bottom view of the GLORIA instrument. . . . .	14
3.3.	A CAD drawing illustrating the GLORIA instrument. . . . .	15
3.4.	A 2D diagram showing the ray propagation through the different optical components in GLORIA. . . . .	16
3.5.	Inside view of the spectrometer showing different components of the GLORIA interferometer. . . . .	16
3.6.	Front view of the spectrometer showing different components. . . . .	17
3.7.	Energy band diagram of a p-n junction. . . . .	19
3.8.	Reference laser diode setup for the GLORIA interferometer. . . . .	20
3.9.	3D model of GLORIA blackbody and its optical surface. . . . .	21
3.10.	Block diagram for the electronic unit in GLORIA. . . . .	22
3.11.	Architecture of read-out electronic system for GLORIA. . . . .	23
3.12.	A schematic illustration of the measurement geometry of GLORIA and other FTS instruments. . . . .	24
3.13.	HALO research aircraft with GLORIA in the belly pod. . . . .	25
4.1.	Interferogram maximum plotted for a given pixel of several <i>cub</i> files from laboratory measurements. . . . .	29
4.2.	The real and the imaginary part of the radiometrically calibrated spectrum for a single pixel for one <i>cub</i> file . . . . .	31
5.1.	Experimental setup used for the direct blackbody measurements with the detector. . . . .	34
5.2.	2D Noise and the corresponding histogram distribution for detector II/1. . .	35
5.3.	2D response and the corresponding histogram distribution for detector II/1. .	36
5.4.	2D NEP and the corresponding histogram distribution for detector II/1. . .	37

5.5. Histogram plots showing the noise and the response distribution of pixels for detector bias voltages of 1.24 V, 1.32 V and 1.40 V . . . . .	38
5.6. Histogram plot showing the noise and the response distribution of pixels for detector temperatures of 50 K, 55 K and 62 K . . . . .	38
5.7. Blackbody spectrum measured at detector temperatures of 50 K, 55 K and 62 K. . . . .	39
5.8. The relative change of the spectra for detector temperatures of 55 K and 62 K with respect to the measurement at 50 K. . . . .	40
5.9. 2D NEP for detector II/1a and histogram distribution for detector II/1 and II/1a. . . . .	41
5.10. Histogram and 2D NEP plot for cold blackbody for detector II/1 and detector II/2 for 256×256 detector pixels. . . . .	42
5.11. Histogram and 2D NEP plot for cold blackbody for detector II/1 and detector II/2 for 128×128 detector pixels. . . . .	44
5.12. Distribution of the bad pixels based on the radiometric criterion for detector II/1 and II/2. . . . .	44
5.13. Interferogram DC plot of a blackbody source measured at different integration time and a linear fit of the DC values. . . . .	46
5.14. Linearized DC plotted with respect to the measured DC. . . . .	47
5.15. Blackbody spectrum plot before and after the nonlinearity correction for a single pixel (129,154) of detector II/1. . . . .	48
5.16. Blackbody spectrum plot before and after the nonlinearity correction for a single pixel (129,155) of detector II/1. . . . .	49
5.17. Interferogram DC plots of a blackbody source measured at different integration time for two pixels of detector II/1. . . . .	49
5.18. Mean signal of a blackbody spectrum in the range between 20 cm <sup>-1</sup> and 400 cm <sup>-1</sup> without and with a nonlinearity correction plotted for detector II/1. 50	
5.19. Mean signal of a blackbody spectrum in the range between 20 cm <sup>-1</sup> and 400 cm <sup>-1</sup> without and with a nonlinearity correction plotted for detector II/2. 51	
5.20. Percentage of pixels plotted against the mean signal of the blackbody spectrum in the range between 20 cm <sup>-1</sup> and 400 cm <sup>-1</sup> before and after performing the nonlinearity correction for detector II/1 and detector II/2. . . . .	51
5.21. Distribution of the bad pixels based on the nonlinearity criterion for detector II/1 and detector II/2. . . . .	52
5.22. Block diagram of a detector pixel and a simplified detector readout electronics. 55	
5.23. The DC plot showing measurement and theoretically calculated values for detector II/2 using a 128×128 pixel array for a cold and a hot blackbody at 219 K and 258.5 K, respectively. . . . .	57
5.24. The noise plot shows measured and theoretically calculated values for detector II/2 using a 128x128 pixel array for a hot blackbody at 258.5 K. . . . .	58
5.25. The instrument response curve for a single pixel of detector II/2. . . . .	60
5.26. Transmittance curve for GLORIA. . . . .	61
5.27. 2D plots showing the modulation efficiency and the instrument response. . . . .	62
5.28. Detector response for a single pixel of detector II/2. . . . .	63
5.29. Detector quantum efficiency for a single pixel of detector II/2. . . . .	64
5.30. 2D distribution of the cutoff wavenumber plotted over the 48×128 pixel array. 65	
5.31. The theoretical values of the NESR plotted as a function of detector integration time at 1000 cm <sup>-1</sup> . . . . .	66
5.32. NESR plot from on-ground (pre-flight) measurements with GLORIA blackbody as scene compared with the modeled values. . . . .	67
5.33. Mean NESR plotted over the 64×128 pixels of detector II/2 and the corresponding histogram for a scene with blackbody at 287 K. . . . .	68

5.34. NESR plot from ESSenCe flight K01_F02 looking at the atmosphere as scene compared with the modeled values. . . . .	69
5.35. Mean NESR plotted over the $48 \times 128$ pixels of detector II/2 and the corresponding histogram looking at the atmosphere as scene. . . . .	69
5.36. NESR plot from TACTS flight K03_F20 looking at the atmosphere as scene and compared with the modeled values. . . . .	70
5.37. Mean NESR plotted over the $48 \times 128$ pixels of detector II/1 and the corresponding histogram looking at the atmosphere as scene. . . . .	71
5.38. The image of the four IR blackbody point sources over the GLORIA detector for an instrument temperature of $-55.6$ °C . . . . .	72
5.39. Zoom plots of the four main images of the infrared blackbody source on the GLORIA detector. . . . .	73
5.40. Zoom plot of the image of the central infrared blackbody on the GLORIA detector and the ensquared energy diagrams for all four images plotted for a squared area for three temperatures. . . . .	74
5.41. Through focus spot diagram for focused and different defocused IRO positions. . . . .	75
5.42. Ensquared energy diagram plotted for a squared area with a spot simulated for three instrument temperatures. . . . .	76
5.43. Intensity plot showing the main image and the parasitic images of the four point sources over the detector array. . . . .	78
5.44. The intensity distribution of main image and two parasitic images over the detector pixel array. . . . .	79
5.45. Ray propagation through the beamsplitter showing multiple reflections and transmissions at its surface. . . . .	80
6.1. The line position distribution of a $\text{N}_2\text{O}$ line at $1150.9099$ $\text{cm}^{-1}$ plotted over the detector array. . . . .	84
6.2. Measurement setup with GLORIA being placed inside the thermal-vacuum chamber. . . . .	87
6.3. Simulated $\text{N}_2\text{O}$ spectrum without noise generated using KOPRA and realistic parameters for the GLORIA instrument. . . . .	88
6.4. The line intensity and line position differences between the HITRAN values and the $\text{N}_2\text{O}$ lines simulated by using KOPRA are plotted against $\text{N}_2\text{O}$ line indices . . . . .	89
6.5. A measured $\text{N}_2\text{O}$ line spectrum before and after zero filling plotted as a function of wavenumber. . . . .	91
6.6. A measured $\text{N}_2\text{O}$ line spectrum and its first order derivative plotted as a function of wavenumber. . . . .	92
6.7. The spectral calibration parameters plotted for different zero filling terms using the zero filling method of line finding. . . . .	93
6.8. The standard deviation of the line position values for $128 \times 128$ pixels plotted for the $\text{N}_2\text{O}$ lines with a SNR of 12 for the strongest line in the range between $1140$ $\text{cm}^{-1}$ and $1200$ $\text{cm}^{-1}$ . . . . .	96
6.9. The optical axis (h,v) position variation with the movement of the infrared objective on its axis. . . . .	97
6.10. Atmospheric spectrum plot for a single pixel from flight K01_F02 . . . . .	98
6.11. The spectral calibration parameters calculated using the selected atmospheric lines of set 1 forward direction data from flight K01_F02. . . . .	99
6.12. The line position distribution over detector array before and after performing the spectral calibration and the number of pixels used. . . . .	101

6.13. The standard deviation of the selected CO <sub>2</sub> line position distribution over the detector array plotted against their respective line positions and a 2D distribution of the signal-to-noise ratio for the CO <sub>2</sub> line at 967.707 cm <sup>-1</sup> over the detector array. . . . .	102
6.14. Spectra (horizontal pixels binned) plot over the vertical pixel distribution after spectral calibration of flight (K01_F02) data. . . . .	102
6.15. Difference of the line position between set 1 and set 2 distributed over the detector array. . . . .	103
6.16. The spectral calibration parameters calculated using the selected atmospheric lines of set 1 and set 2 for forward and backward direction data from flight K01_F02. . . . .	104
6.17. The temperature drift of the reference laser diode due to the temperature drift of the interferometer. . . . .	105
6.18. The line position distribution over detector array before and after performing the spectral calibration and the number of pixels used. . . . .	106
6.19. Signal-to-noise ratio distribution for the CO <sub>2</sub> line at 967.707 cm <sup>-1</sup> over the detector array for deep space measurements performed during flight K03_F14.107	107
6.20. The spectral calibration parameters calculated using the selected atmospheric lines for the forward and backward direction data from flight K03_F14.108	108
6.21. Spectrally calibrated spectra from flight K03_F14 plotted for co-added pixels for two spectral ranges showing CO <sub>2</sub> and H <sub>2</sub> O lines. . . . .	109
6.22. Image distance plotted with respect to the varying beamsplitter temperature for a fixed IRO position. . . . .	111
6.23. Image distance plotted with respect to the IRO positions corresponding to the interferometer temperature of -51 °C . . . . .	112
6.24. A N <sub>2</sub> O spectrum for pixel (64,62) for the IRO placed at 280 count position. 114	114
6.25. The FWHM of the N <sub>2</sub> O lines in the spectral range between 1140 cm <sup>-1</sup> and 1205 cm <sup>-1</sup> calculated for pixel (64,62) from measurement data and plotted for five different IRO positions. . . . .	114
6.26. The FWHM of the N <sub>2</sub> O lines in the spectral range between 1240 cm <sup>-1</sup> and 1320 cm <sup>-1</sup> calculated for pixel (64,62) from measurement data and plotted for five different IRO positions. . . . .	115
6.27. A schematic diagram showing a possible path of the interferometer drive with the moving cube corner in GLORIA. . . . .	117
6.28. Haidinger fringe center variation over OPD for an interferometer temperature of -14 °C. . . . .	119
6.29. Shear variation over the OPD for an interferometer temperature of -14 °C. . 119	119
6.30. Shear variation over the OPD for several interferometer temperatures. . . . 120	120
6.31. The shear variation over the OPD before and after making the shear adjustment for the instrument temperature of -65 °C. . . . .	121
6.32. The Haidinger fringe center variation over the OPD for an interferometer temperature of -65 °C. . . . .	122
6.33. The shear variation over the OPD for an interferometer temperature of -65 °C.122	122
6.34. The shear frequencies for measurements performed at an interferometer temperature of -65 °C. . . . .	123
6.35. Frequency plot in the direction of interferometer drive movement for an interferometer temperature of -65 °C. . . . .	124
6.36. Shear frequencies for measurements performed at variable interferometer velocities with the interferometer at room temperature. . . . .	125
6.37. A zoom of the shear frequencies for measurements performed at interferometer velocities of 0.549 cm/sec with the interferometer at room temperature. 127	127

A.1. Schematic diagram of the optical components and its alignment in GLORIA interferometer. . . . .	144
A.2. Transmission curve of the optical components used in GLORIA interferometer.	145
B.1. Ray propagation through the beamsplitter showing multiple reflections and transmissions at its surface. . . . .	147



# List of Tables

3.1.	AIM detector parameter specifications. . . . .	19
3.2.	Typical setting for the GLORIA measurement parameter for an observer at 15 km. . . . .	24
5.1.	Parameters relevant for the determination of the radiometric properties of the detector. . . . .	34
5.2.	The parameters used for the comparison of the radiometric properties of detector II/1 and II/2 . . . . .	42
5.3.	Coefficients of the polynomial fit for performing a nonlinearity correction following the second approach. . . . .	48
5.4.	Parameters for the NESR evaluation from spectrally resolved measurement	67
6.1.	Line position difference for the zero filling method using several zero filling terms. . . . .	94
6.2.	Spectral parameters from simulated spectrum without and with noise. . . .	95
6.3.	The line position and intensity of the selected CO <sub>2</sub> lines from the HITRAN database used for the spectral calibration of the data measured during flight. 98	
6.4.	Mean and standard deviation of the spectral calibration parameters calculated using the selected atmospheric lines from flight K01_F02. . . . .	100
A.1.	Properties of the optical components used in GLORIA. . . . .	143
B.1.	Position of the spurious images for variable parameter. . . . .	150



# Acknowledgements

I take this opportunity to acknowledge the help and moral support extended to me for the successful completion of this thesis. I would like to express my sincere thanks to all people who believed in me and helped me in different ways in making this strenuousness work feasible.

First of all, I sincerely thank Prof. Dr. Herbert Fischer for giving me the opportunity to work in this interesting field of science. I would also like to thank him for the discussions, timely suggestions, support and encouragement he has given to me throughout my Ph.D. work. I would also like to thank him for the critical proofreading of my thesis.

I would like to thank Prof. Dr. Johannes Orphal who agreed to be my second referee. I would also like to thank him for the valuable discussions, his encouragements and for proofreading my thesis.

My special thanks go to my direct supervisor Felix Friedl-Vallon for his excellent support and supervision throughout my Ph.D. work. His sound words of advice, his in-depth knowledge about instruments and his willingness to engage intellectually in the problems will ever remain fresh in my memory and will continue to give me inspiration for the future years to come. Also, I would like to thank Anne Kleinert for helping with the programming, data handling and processing and various other aspects of Fourier transform spectroscopy (FTS). Her scholarly insight improved my study and mended the content to this research work. I have learned a lot from both of you. Thanks for showing me the way and guiding me through when I was stuck in scientific problems. Thanks for taking the time to proofread my thesis and give constructive critical comments and suggestions. Also, I thank you both for supporting me in having a smooth start in Karlsruhe and adapting to the German lifestyle.

Next, I would like to thank the members of my working group at IMK for their continuous support and the friendly and pleasant work atmosphere. Big thanks to Thomas Gulde, Guido Maucher, Erik Kretschmer, Christof Piesch, Hans Nordmeyer, Christian Sartorius, Thomas Latzko, Friederike Graf, Olga Suminska-Ebersoldt and Michael Höpfner for sharing their in-depth knowledge in the respective fields of FTS. Additional thanks goes to Thomas G., Guido, Christian, and Friederike for proofreading specific sections of my thesis. Special thanks go to Hermann Oelhaf for his timely suggestions, support in the course of my work, discussions, comments and especially for proofreading my thesis. Furthermore, I also want to thank Wolfgang Woiwode and Gerald Wetzel for the discussions on spectroscopy and level2 retrieval methodology. I would also like to thank Frank Hase for the helpful discussions we had during the past years on various topics of my work. I would like to thank the other members of the team who have worked for a short term in the GLORIA project. Specially, I would like to mention Markus Streit and Tobias Feger for the discussions. Special thanks also go to Andreas Ebersoldt (IPE) for his support with electronics and Christian Schmitt (IAI) for his support with the JIFB viewer. I would also like to thank our mechanical workshop team for their continuous support; they have

provided everything necessary even on a very short notice whenever it was needed in the laboratory. Namely to mention Alexander Streili and Benjamin Riexinger.

I would also like to give thanks to the GLORIA team members from Forschungszentrum Jülich and Bergische Universität Wuppertal. Special thanks go to Tom Neubert for his support with the data acquisition electronics, Tobias Guggenmoser and Jörn Ungermann for their support with the data processing. I thank the other colleagues for the group discussions, support with the problems related to the instrument and data analysis.

I will be failing in my duty if I forget to name our institute secretary Astrud Wiessner for her immense enthusiasm and willingness to help at all times with the official paper works. I would also like to thank the other secretaries, Derya Göce, Mara Kasubke and Laura Olbrich for helping me with the campus north official work.

I would also like to express my gratitude to my friends at KIT and Karlsruhe for their companionship. Specially - Fabio Cismondi and Irene Meliciani, Tobias Schieferdecker, Babak Nasr, Subho Dasgupta and Alakananda Khastagir, Arindam Dasgupta, Chilla Malla Reddy, Mohammad Abdullah Al Faruque and Nahid Chowdhury, Iryna and André Loges, Nigel and Stefanie Smale, Swarup Chauhan, Soumya Bera and a lot of others whose name I have not mentioned here: You all are present in my heart and I thank you very much for being with me at all times.

I would like to profusely thank Anika Menchen for being there by my side, supporting and encouraging me in many ways during the last years. Next, I would thank my seniors Chayan Sengupta, Vikram Pakrashi and Bidisha Ghosh who had an immense contribution in my education during the school and college days, also thanks for the continuous encouragement you are still giving to me. Additionally thanks to Anika, Arindam, Vikram and Bidisha for proofreading my thesis. I would also like to thank all my teachers for giving me education and knowledge. I would also like to thank all my friends in India. Especially Shashank Shekhar, Ayan Sengupta and Ranjan Biswas; very special thank goes to my aunty, Nandini Bakshi, who has supported me in numerous ways. Thanks to all of you for being with me and supporting me such that I could reach until this platform.

Last but not least, I take it an honor to express my deep sense of gratitude to my family who always gave me moral support and encouragement. All my achievements are possible because of them. A special thank goes to my brother, Rajesh Kumar Sha, for his constant support, suggestions and counseling. He always has been my role model, my hero of real life. Big thanks also go to my bhabhi-ji, Roushani Sha and to my bhatijaa and bhatiji, Ayush and Moushami, for their loving support. I am grateful to the sacrifices my father, my mother and my brother Rajesh, made to support my education. This work would not have been possible without their priceless sacrifices for which I will remain grateful every single day of my life. Thank you.